MULTIDISCIPLINARY CENTER FOR EARTHQUAKE ENGINEERING RESEARCH

A National Center of Excellence in Advanced Technology Applications

ISSN 1520-295X

Experimental Investigation and Retrofit of Steel Pile Foundations and Pile Bents Under Cyclic Lateral Loadings

by

A.A. Shama, J.B. Mander, B.B. Blabac and S.S. Chen
University at Buffalo, State University of New York
Department of Civil, Structural and Environmental Engineering
Ketter Hall
Buffalo, NY 14260

Technical Report MCEER-01-0006

December 31, 2001

This research was conducted at the University at Buffalo, State University of New York and was supported by the Federal Highway Administration under contract number DTFH61-92-C-00106.

Experimental Investigation and Retrofit of Steel Pile Foundations and Pile Bents Under Cyclic Lateral Loading

by

Ayman A. Shama[1], John B. Mander[2], Blaise B. Blabac[3] and Stuart S. Chen[4]

Publication Date: December 31, 2001
Submittal Date: March 30, 2000

Technical Report MCEER-01-0006

Task Number 106-E-5.4

FHWA Contract Number DTFH61-92-C-00106

1 Structural Engineer, Parsons Transportation Group Inc., New York; Former Graduate Research Assistant, Department of Civil, Structural and Environmental Engineering, University at Buffalo, State University of New York
2 Professor and Chair of Structural Engineering, University of Canterbury, New Zealand; former Associate Professor, Department of Civil, Structural and Environmental Engineering, University at Buffalo, State University of New York
3 Former Graduate Research Assistant, Department of Civil, Structural and Environmental Engineering, University at Buffalo, State University of New York
4 Associate Professor, Department of Civil, Structural and Environmental Engineering, University at Buffalo, State University of New York

MULTIDISCIPLINARY CENTER FOR EARTHQUAKE ENGINEERING RESEARCH
University at Buffalo, State University of New York
Red Jacket Quadrangle, Buffalo, NY 14261

Preface

The Multidisciplinary Center for Earthquake Engineering Research (MCEER) is a national center of excellence in advanced technology applications that is dedicated to the reduction of earthquake losses nationwide. Headquartered at the University at Buffalo, State University of New York, the Center was originally established by the National Science Foundation in 1986, as the National Center for Earthquake Engineering Research (NCEER).

Comprising a consortium of researchers from numerous disciplines and institutions throughout the United States, the Center's mission is to reduce earthquake losses through research and the application of advanced technologies that improve engineering, pre-earthquake planning and post-earthquake recovery strategies. Toward this end, the Center coordinates a nationwide program of multidisciplinary team research, education and outreach activities.

MCEER's research is conducted under the sponsorship of two major federal agencies, the National Science Foundation (NSF) and the Federal Highway Administration (FHWA), and the State of New York. Significant support is also derived from the Federal Emergency Management Agency (FEMA), other state governments, academic institutions, foreign governments and private industry.

The Center's FHWA-sponsored Highway Project develops retrofit and evaluation methodologies for existing bridges and other highway structures (including tunnels, retaining structures, slopes, culverts, and pavements), and improved seismic design criteria and procedures for bridges and other highway structures. Specifically, tasks are being conducted to:

- assess the vulnerability of highway systems, structures and components;
- develop concepts for retrofitting vulnerable highway structures and components;
- develop improved design and analysis methodologies for bridges, tunnels, and retaining structures, which include consideration of soil-structure interaction mechanisms and their influence on structural response;
- review and recommend improved seismic design and performance criteria for new highway systems and structures.

Highway Project research focuses on two distinct areas: the development of improved design criteria and philosophies for new or future highway construction, and the development of improved analysis and retrofitting methodologies for existing highway systems and structures. The research discussed in this report is a result of work conducted under the existing highway structures project, and was performed within Task 106-E-5.4, "Dependable Strength and Ductility of Steel Pile Bents" of that project as shown in the flowchart on the following page.

This research investigated the performance and retrofit of bridge pile-to-cap connections that are representative of construction in the eastern and central United States. Simplified theoretical concepts were developed to predict the connection behavior under different lateral and axial load patterns. These concepts were then compared to rigorous finite element analysis that validated the simplified limit theories. On the basis of these theories, design guidelines and retrofit strategies for these connections were proposed.

SEISMIC VULNERABILITY OF EXISTING HIGHWAY CONSTRUCTION
FHWA Contract DTFH61-92-C-00106

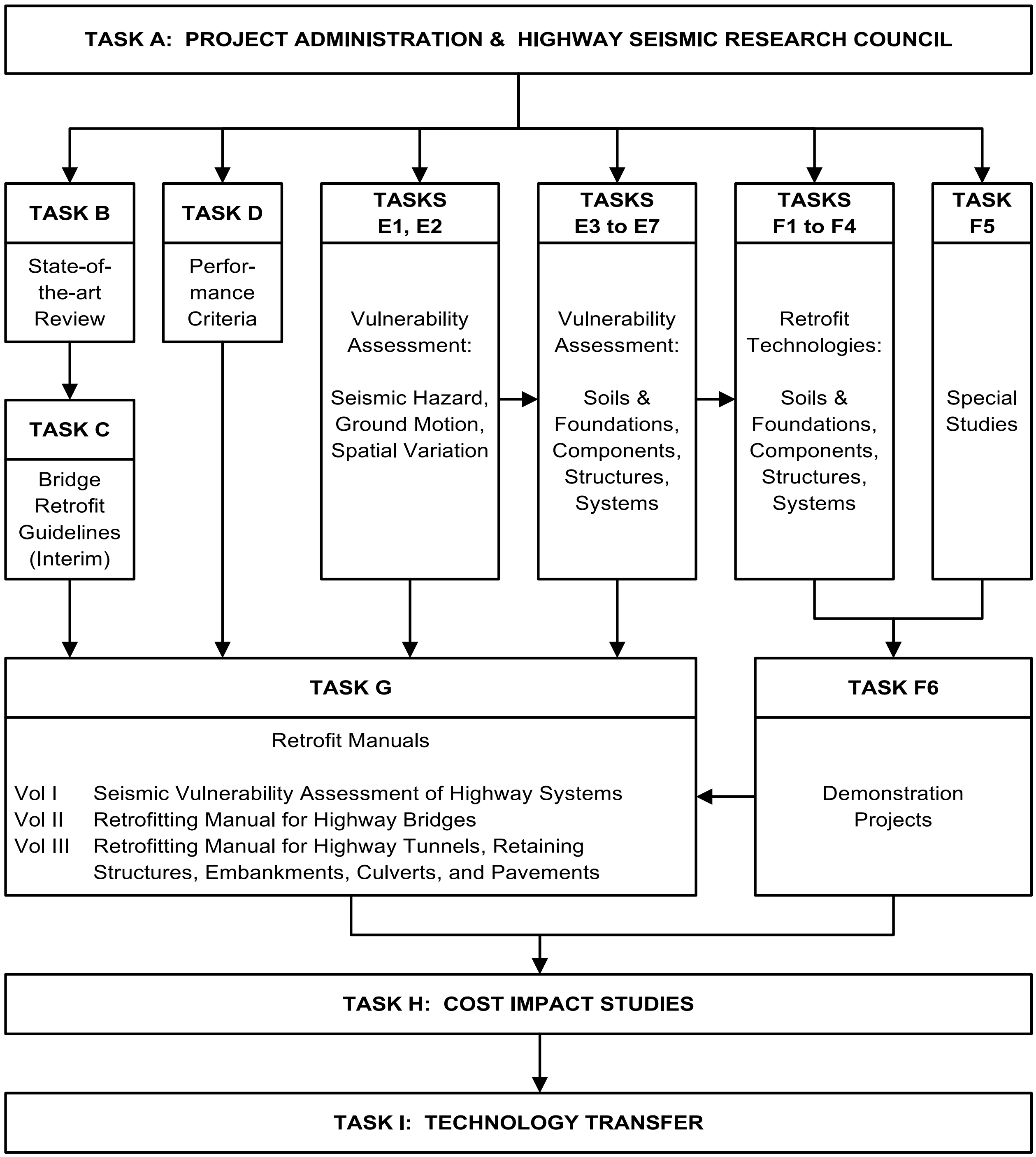

ABSTRACT

This research is concerned with the seismic performance of pile-to-pile cap connections. Two perspectives are considered. The first is the seismic vulnerability of existing pile cap connections, where the embedment depth of the pile inside the cap beam is small. Secondly, is the seismic design requirements for strong cap beam-to-pile connections for new construction and retrofit of existing structures.

To achieve these perspectives, two theories were developed. The first theory is based on the ultimate capacity of the concrete cap beam and is used to predict the performance of as-built connections. The second theory, which is a cracked elastic theory assumes a linear distribution for stresses along the connection embedment depth, and hence is applicable for the seismic design requirements of new and/or retrofitted connections. Three-dimensional finite element models were developed, to validate the predictions of the cracked elastic theory.

The initial experimental program consisted of testing seven as-built specimens under different loading conditions to evaluate the seismic vulnerability of existing connections. The results of the experiments agreed with the predictions of the post-ultimate theory. A second experimental program was conducted to evaluate the performance of specimens retrofitted in accordance with the theoretical models developed in this study. The results of the second series of experiments validated the proposed retrofit strategy.

The results of analytical approach, which is based on fiber element analysis, for predicting the performance of these specimens under lateral load was compared favorably to the experimental results. Finally, a fatigue-life model based on a simplified approach was developed and showed satisfactory agreement with the available experimental results.

ACKNOWLEDGEMENTS

This research was carried out in the Department of Civil, Structural and Environmental Engineering at the State University of New York at Buffalo. The first author conducted the experimental study on the as-built and retrofitted pile foundation specimens, as well as the weak axis and retrofitted pile bent specimens, the computational and fatigue modeling as part of his Ph.D. studies under the supervision of the second author. The third author conducted the strong axis experiments on the pile bents and developed part of the ultimate strength theory, under the supervision of the fourth and second authors, respectively.

Financial support is gratefully acknowledged from the Multidisciplinary Center for Earthquake Engineering Research through contract with the Federal Highway Adminstration

The assistance of the technicians Messrs Cizdziel, Pitman, Salehi and Walch of the Department of Civil Engineering Seismic Research Laboratory are gratefully acknowledged. Former graduate student Doug Shaffer is thanked for his help in the construction of the pile foundation specimens and also for his assistance in the construction of its retrofit. Mrs. Debra Kinda is thanked for typing the manuscript.

TABLE OF CONTENTS

TABLE OF CONTENTS (Cont'd)

TABLE OF CONTENTS (Cont'd)

TABLE OF CONTENTS (Cont'd)

TABLE OF CONTENTS (Cont'd)

LIST OF FIGURES

LIST OF FIGURES (Cont'd)

Section 3

LIST OF FIGURES (Cont'd)

LIST OF FIGURES (Cont'd)

LIST OF FIGURES (Cont'd)

LIST OF FIGURES (Cont'd)

LIST OF FIGURES (Cont'd)

Figure Title Page

LIST OF TABLES

Section 1
Introduction

1.1 BACKGROUND

As a result of the disastrous consequences of earthquakes in the last several decades, there has been an increased perception not only about the performance of different structures during an earthquake but also about how to control the damage to these structures during seismic events. Bridges are very important structures that are required to be serviceable after an earthquake to provide access to other critical services such as fire stations and hospitals.

Many bridges in the country were designed and constructed before the development of modern seismic design codes and standards. They were designed to sustain static and wind loads only. Accordingly, some of these bridges may be vulnerable to damage during earthquakes. This certainty was revealed by the indigent performance of some bridges during the 1964 Alaska earthquake (Kachadoorian 1968). During that earthquake, 69% of the bridges located in south central Alaska were severely damaged or destroyed. The substructures of most of these bridges were either wood or steel pile bents. A photograph of the damage that occurred to steel pile bents of two of these bridges is shown in figure 1.1. Earthquake damage to piles has been noticed also during the 1964 Nigata Earthquake (JNEEC 1965). It was observed that in several occasions piles were damaged at the top close to the connection with pile cap. Many bridge structures suffered severe damage during 1971 San Fernando earthquake. Damage included piers, foundations and embankments as well as superstructure span collapse. Since then, research has been focused not only to enhance the seismic performance of newly designed bridges but also to develop retrofit strategies for existing ones.

During severe ground motions, some critical regions in the structure, where plastic hinging occurs, experience inelastic deformations. If the design forces or deformations for these regions (capacity) are less than the seismic forces or deformations (demand) during a certain event, plastic hinging may occur.

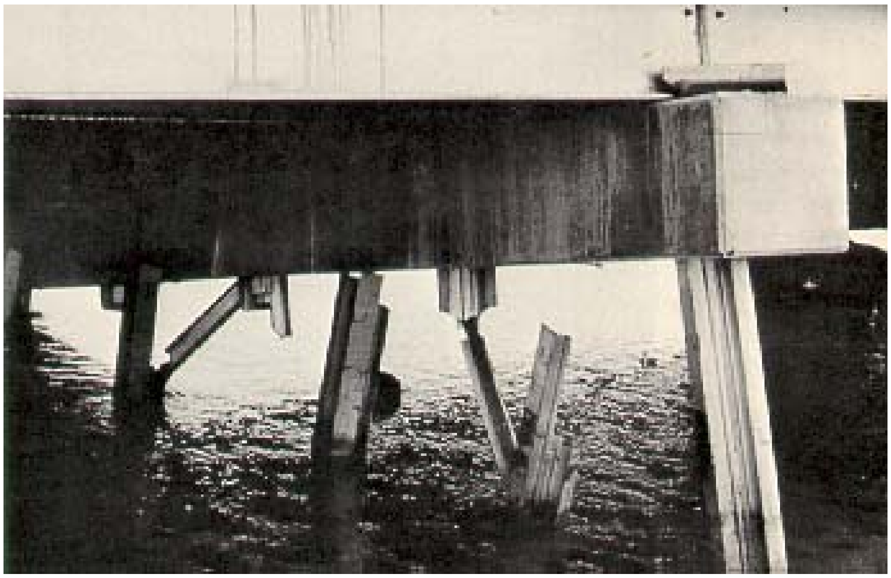

(a) Damage Occurred to Steel Pile Bent on Scott Glacier Bridge

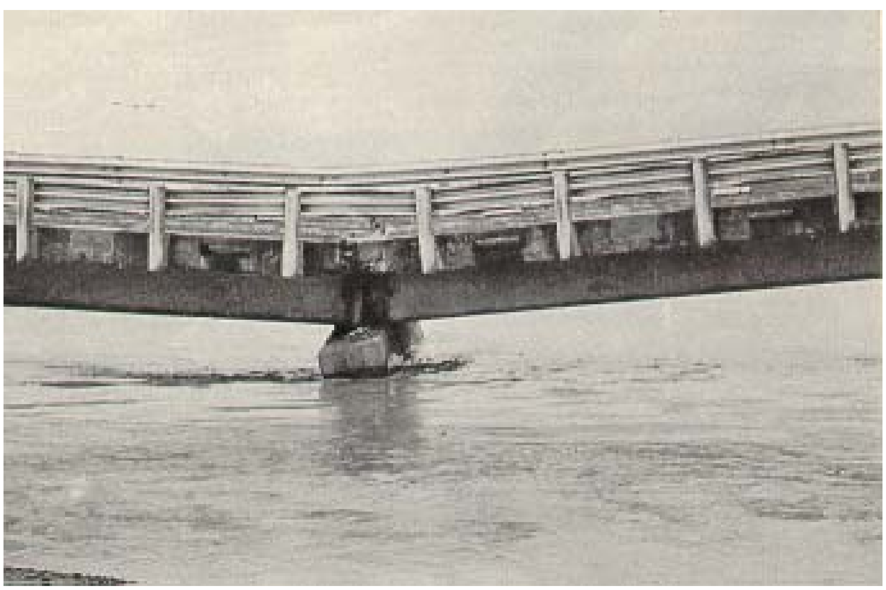

(b) Collapsed Bent and Deck of Copper River Bridge

Figure 1.1 Damage occurred to two bridges during Alaska Earthquake 1964

Basic plasticity principles dictate that these plastic hinges mostly occur at the connections between different elements within the structure. Figure 1.2 shows two locations in a bridge structure where these plastic hinges can take place. The first one is a typical pile bent, where the steel H-piles extend out of the soil directly to the pier cap. They are embedded approximately *300 mm* into the reinforced concrete cap beam. In this form of construction, the plastic hinge is anticipated to occur at the connection between the steel H-pile and the cap beam. In the second form of construction, which is a pile supported foundation, the plastic hinge can take place at the connection between the steel pile and the concrete pile cap. In both situations the local performance of the connection has a major effect on the overall performance of the structure. Therefore it is imperative to appraise the performance of these connections under cyclic loading through a comprehensive experimental program and to develop methods for its retrofit assessed by experiments to maintain its ductility during large cyclic drifts. The work presented herein is an effort to contribute towards both goals.

1.2 Overview Of Related Previous Work

Early research on single piles was directed mainly towards estimating their static load carrying capacity. Other parameters such as geometrical and mechanical pile and soil properties, type of piles, type of loading, and soil-pile-structure interaction were also investigated. However, little effort has been devoted towards the evaluation of the ultimate lateral resistance of laterally loaded piles or to assess the pile-to-pile cap connection performance under seismic or cyclic lateral load. Broms (1964) presented methods for the calculation of the ultimate lateral resistance of piles in cohesionless and cohesive soils. Satisfactory agreement was found between his work and available test data at that time. The effect of cyclic loading on the lateral performances of piles was investigated by Matlock et al (1978) and by Poulos (1982) who suggested that, for design purposes, the effects of cyclic lateral loading can be taken into account by modification of the static analysis of the pile. A common characteristic of all these studies, that they were localized on the behavior of the pile and pile-soil interaction rather than the pile-to-pile cap connection. Shafer and Williams (1947) investigated this connection. However, they tested the piles only under uniaxial compression

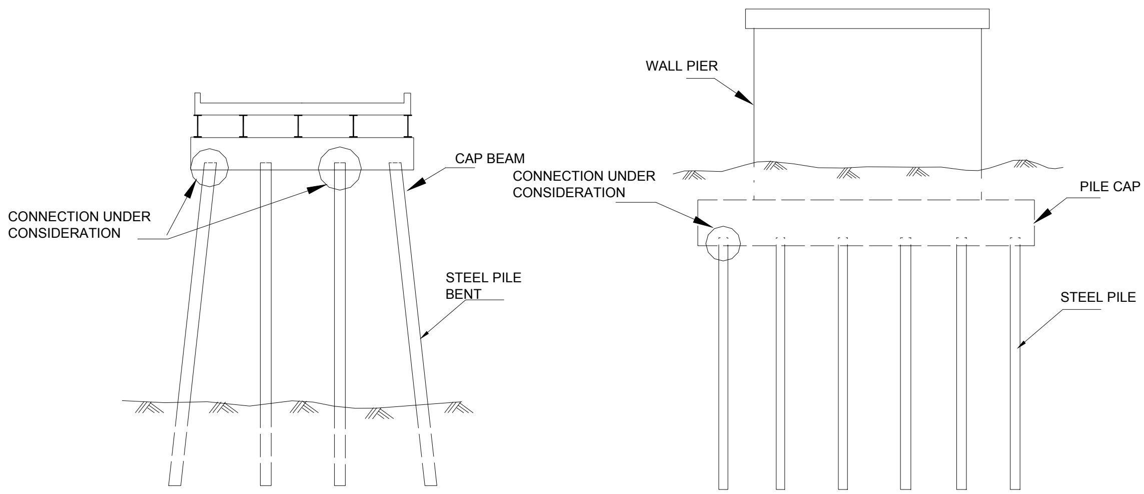

Figure 1.2 Critical Locations in a Bridge Substructure where Plastic Hinges can take Place

Load. Therefore their findings are not relevant to the study of cyclic lateral loading for which the behavior of the connection is dominated by the induced shear and bending moments.

A series of cyclic tests was conducted in New Zealand on prestressed concrete pile-to-cap connections (Joen and Park 1990). The results showed that well detailed prestressed concrete piles and pile-to-cap connections are capable of undergoing large post-elastic deformations without significant loss in strength when subjected to severe seismic loading.

Another significant study concerning pile-to-cap connection has been done in British Columbia, Canada (Steunenberg et al 1998) where a convenient design, for this connection, favored by the Ministry of Transportation and Highways of British Columbia has been successfully tested. This design consists of a steel anchorage plate embedded in the concrete pile cap. The plate is then welded to the pile top after placement in the field. The design is different than what is followed in the United States but it gives some insight for future design of this connection.

Chai and Hutchinson (1999) conducted an experimental program for bridge structures supported on single extended reinforced concrete pile shafts, considering the pile-soil interaction in their experiments. Four full scale 400mm diameter concrete piles with details representative of current Caltrans design. Their study showed that the depth to the plastic hinge within the soil decreases with an increase in the soil density and an increase in the above ground height.

A series of tests has been conducted at the University of Southern California (Xiao et al 1999) as a part of FHWA-MCEER Highway project, in order to investigate seismic behavior of bridge steel pile-to-pile cap connections representative of construction in California. Five full-scale H-shaped steel pile-to-cap connection subassemblies were tested during this experimental study. Two of the full-scale subassembly specimens were subjected to vertical cyclic load simulating axial forces in pile due to footing overturning during a seismic ground motion. Two other were loaded with cyclic lateral force and constant vertical load. It was found that the pile to-cap connection can sustain significant amount of moment.

Other relevant studies were devoted to strengthen structural steel connections embedded in precast concrete by additional reinforcement or by providing holes in the steel web for the concrete to enter (Rath, 1974). However, typical bridge pier piles do not employ these kinds of strength enhancements and must rely entirely on the bond and adhesion developed between the steel and concrete in the embedded region to resist the applied moments. The capacity of steel shapes used as brackets (Mattock and Gaafar, 1982) and coupling beams (Harries et al., 1993) was also investigated. The primary contribution of these articles has been in the use of the stress block approach in the embedded region to develop expressions for the theoretical resistance of the connections (Marcakis and Mitchell, 1980).

1.3 What Then Is Particularly New In This Study?

This research is devoted to study the seismic performance of bridge pile-to-cap connections that is representative of construction in the eastern and central United States. This problem was not tackled previously. Simplified limit state theories are developed to predict the connection performance under lateral loading. Based on these theories, design guidelines are suggested for these connections. Such an approach has not been formally proposed previously for seismic design of new bridge structures.

The conceptual elastic cap/elasto-plastic steel pile retrofit strategy proposed in this study is a new approach that was not addressed before. Moreover, employing wire rope for confining the plastic hinge zone within the concrete is a new and successful approach. The fatigue-life model proposed in the present study, for retrofitted connections, which is a function of the pile section dimensions is a new approach that can be used in future studies to predict the design fatigue-life of these connections under cyclic loading .

1.4 Scope And Objectives

The behavior and capacity of cyclically loaded, H-pile-concrete pile cap connections has received very little research. Retrofit strategies for these connections are still not assessed. Primarily designed for vertical loading, these structures may be susceptible to damage from cyclic lateral loading that would arise during seismic events.

The present work has three main objectives: (1) to explore and understand the performance of the pile-to-cap connection under cyclic loading; (2) to develop simple procedures for the retrofit of these connections and examine the validity of these procedures; (3) to provide the design engineer with sufficiently accurate theoretical principles, yet simple enough to be used in practice for predicting the behavior of these connections under different loading conditions.

In order to achieve these objectives, a theory is developed, based on bond and energy considerations, capable of predicting the expected moment capacity of the pile-to-pile cap connection. Theoretical predictions were assessed by experiments conducted on full-scale specimens designed to focus on the pile-to-cap connection in both strong and weak axis directions. Pile specimens were tested to failure under vertical loads using quasi-static reversed lateral cyclic loading to assess the effect of axial load-moment interaction on both interior (vertical) and exterior (battered) piles. In view of the performance of these specimens, a retrofit strategy was developed and applied to the specimens that performed faulty during the experiments. The retrofitted specimens were tested again to assess the developed retrofit procedure. On the basis of the experimental study, a seismic damage assessment criterion is proposed for bridge structures supported by piled foundations.

1.5 ORGANIZATION

The organization of this report: following this introductory section, the remaining sections are organized as follows. Section 2 presents an analysis of the potential plastic mechanism for pile bents and pile foundations, taking into account the effect of pile-soil interaction. Theories are developed for predicting the strength of the pile-to-pile cap connections based on elastic and inelastic concrete assumptions. The connection efficiency was determined in view of the developed theories. Section 3 describes the steps involved in the construction of the test specimens followed by the experimental setup that was developed to undertake full-scale tests on the pile-to-cap connections. This section also outlines the different methods that can be employed to accommodate the axial load variation for this kind of experiments. Section 4 presents results for the seven experiments performed to evaluate the seismic vulnerability of existing pile-to-cap connections. Section 5 presents the steps involved in the retrofit strategy proposed in this study and outlines the results of the experiments on the retrofitted specimens that performed poorly in the first series of experiments. Section 6 validates the theories developed in Sections 2 and 3 for predicting the lateral force displacement relationship and ductility ratio by comparing the experimental results with the results obtained utilizing these theories for different pile-to-cap connections. A fatigue theory is then developed in this section for the low cycle fatigue behavior of the specimens that failed in such failure mode. Section 7 presents a summary of the work reported herein, conclusions drawn from the theoretical and experimental aspects of this work, and recommendations for future research are given.

SECTION 2

THEORETICAL CAPACITY OF PILE-TO-CAP CONNECTIONS

2.1 INTRODUCTION

In this section, theories are developed to predict the capacity of pile-to-cap connections. The problem is treated first from a global point of view, where potential plastic mechanisms for pile bents and pile foundations are outlined. Admissible plastic mechanisms are postulated that include the effect of pile-soil interaction. This is followed by development of simplified theoretical concepts that look closely at the connection itself and predict its local behavior under different lateral and axial load patterns. The theory is then utilized to provide design guidelines and retrofit strategies for these connections. Finally, a comparison is made between the simplified limit theories with a rigorous finite element analysis.

2.2 GLOBAL PLASTIC MECHANISMS FOR PILES AND PILE BENTS

Figure 2.1 presents a steel pile bent and a postulated collapse mechanism for lateral (earthquake) loading. It is assumed that plastic hinges will take place somewhere within the embedded length of the pile. Determination of this location will be discussed in detail in the next subsection. If it is assumed here that any potential settlement for the pile group due to the working vertical loads has already taken place before reaching the state of this mechanism, then the vertical reaction of the piles do not perform any work. The external work done (EWD) by the lateral loading for a virtual (horizontal) displacement Δ (drift) can be expressed as:

$$EWD = F\Delta = C_C W\Delta = C_c W\theta H \tag{2.1}$$

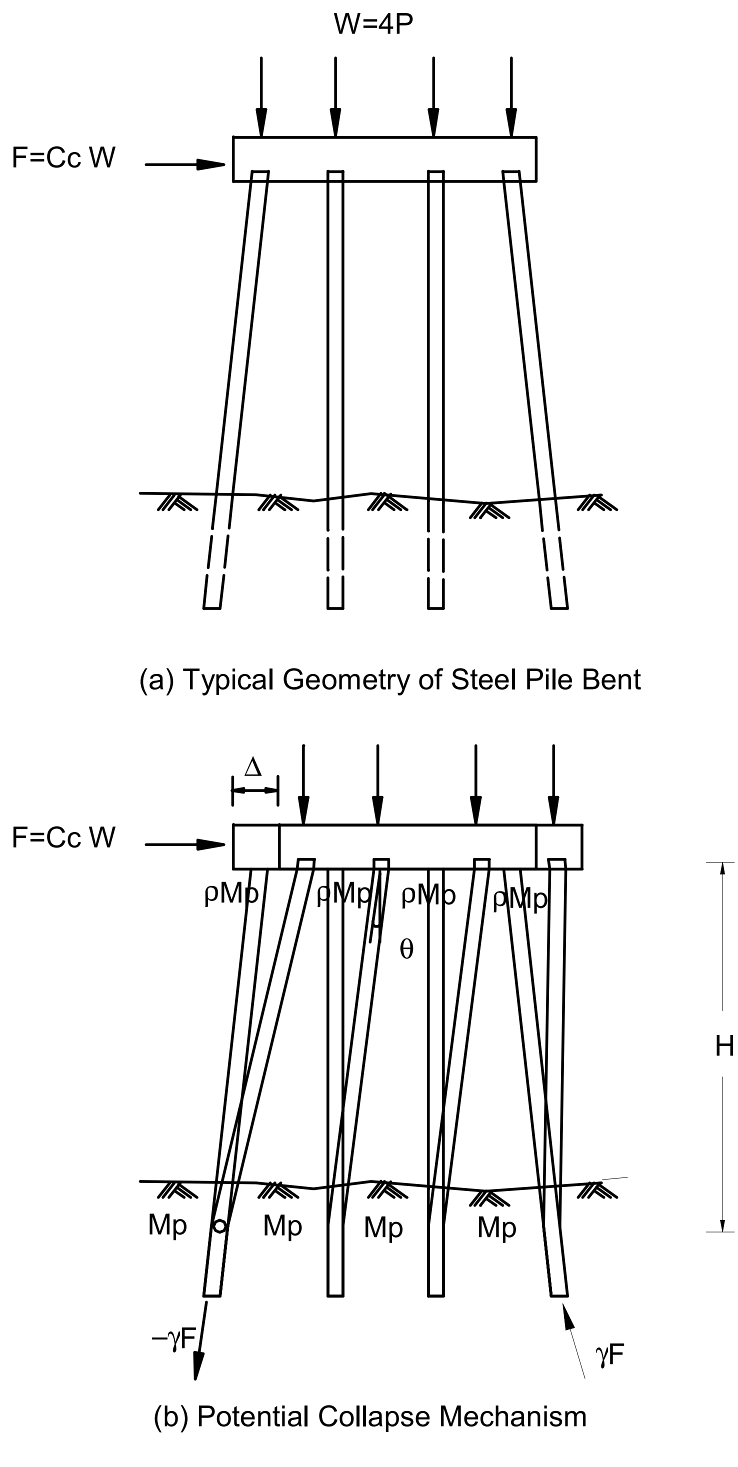

Figure 2.1 Potential Plastic Mechanism for Pile Bents

where F = the total lateral force on pile bent; W= the seismic weight of the superstructure; C_C = seismic base shear capacity coefficient; θ=rotation angle, and H = equivalent height of the pile between plastic hinges.

The internal work done (IWD) can be quantified as:

$$IWD = nM_P\theta(\rho + 1) \tag{2.2}$$

in which n = number of piles in the bent; M_P = plastic moment capacity of the pile section; and ρ = pile connection efficiency, expressed as the ratio of the nominal moment capacity of the concrete cap beam at the hinge location to the plastic moment capacity of the pile steel section. Note that for a hinge condition ρ = 0 and for a fully fixed condition $\rho \geq 1$.

Equating the external work done (2.1) with the internal work done (2.2), an expression for the base shear capacity of the bent can be evaluated as:

$$C_c = \frac{nM_P(\rho + 1)}{HW_t} \tag{2.3}$$

If it is assumed that the superstructure seismic weight is shared equally between the number of piles such that each of them carries an axial load P_e, the superstructure seismic weight can be expressed as:

$$W_t = nP_e \tag{2.4}$$

Substituting equation (2.4) in (2.3) gives:

$$C_c = \frac{M_p(\rho + 1)}{HP_e} \tag{2.5}$$

It should also be noted that, due to the additional axial thrust at piles, their plastic moment capacity is reduced. The following well-known moment-axial load interaction expressions for M_P according to ASCE 1971 can be utilized:

Strong axis bending:

For $0 \le P \le 0.15P_Y$

$$M_{PC} = M_P \tag{2.6}$$

For $0.15P_Y \le P \le P_Y$

$$M_{PC} = 1.18(1 - \frac{P}{P_Y})M_P \tag{2.7}$$

Weak axis bending: Neglecting the contribution of the web to the plastic capacity it can be shown that for weak axis bending:

$$M_{PC} = \left[1 - \left(\frac{P}{P_Y}\right)^2\right] M_P \tag{2.8}$$

Where M_{PC} = plastic moment capacity of piles including axial load effects.

2.3 PILE-SOIL INTERACTION REPRESENTATION

From equation (2.5) it is evident that the base shear capacity of the pile bent is dependent on the length between the hinges (H). The lower hinges in the bent are beneath the ground surface by some depth. In this subsection, it is the primary objective of studying the pile-soil interaction under ultimate load to estimate the distance between the two plastic hinges. The effective length is taken as the clear distance from the inflection point at the pile to the point of the connection between the steel pile and the concrete cap beam. For the purpose of investigating the soil-structure interaction, a single interior pile is examined, and the connection efficiency will be set to unity for simplicity. Two cases are considered: Case (1) where a pile is totally embedded in soil (pile foundation); and Case (2) where a pile extends above the soil (pile bent).

2.3.1Cohesionless soil

The following assumptions are made using the well-known approach adopted by Broms (1964b):

1. The active earth pressure acting on the back of the pile is neglected.
2. The distribution of passive pressure along the front of the pile is equal to three times the Rankine passive pressure.
3. The shape of the pile section has no influence on the distribution of the ultimate soil pressure or the ultimate lateral resistance.
4. The full lateral resistance is mobilized at the movement considered.
5. The piles are relatively long and hence, the ultimate lateral resistance will be governed by the plastic moment capacity of the pile section.

Brom's simplified assumption of ultimate soil resistance being equal to three times the Rankine passive pressure is based on limited empirical evidence from comparisons between predicted and observed ultimate loads. These comparisons suggest that the assumed factors of 3 may in some cases be conservative, as the average ratio of predicted to measured ultimate loads is about two thirds.

Case (1): Pile Foundation:

According to the aforementioned assumptions one is able to apply the theory of virtual work to the pile mechanism with soil reactions figure 2.2a and b. It is assumed, for simplicity, that the pile is embedded in a uniform homogeneous layer of soil. The external work done on one pile is:

$$\mathrm{EWD} = \mathrm{FH}\theta \tag{2.9}$$

Where F = the lateral load acting on pile, H = the distance between the two plastic hinges. The internal work done on the pile and soil is:

$$\mathrm{IWD} = 2\mathrm{M}_{\mathrm{p}}\theta + \frac{3}{2}\gamma \mathrm{K}_{\mathrm{P}}\mathrm{H}^{2}\mathrm{H}_{0}\mathrm{d}_{\mathrm{P}}\theta + 0.5\gamma \mathrm{K}_{\mathrm{P}}\mathrm{H}^{3}\mathrm{d}_{\mathrm{P}}\theta \tag{2.10}$$

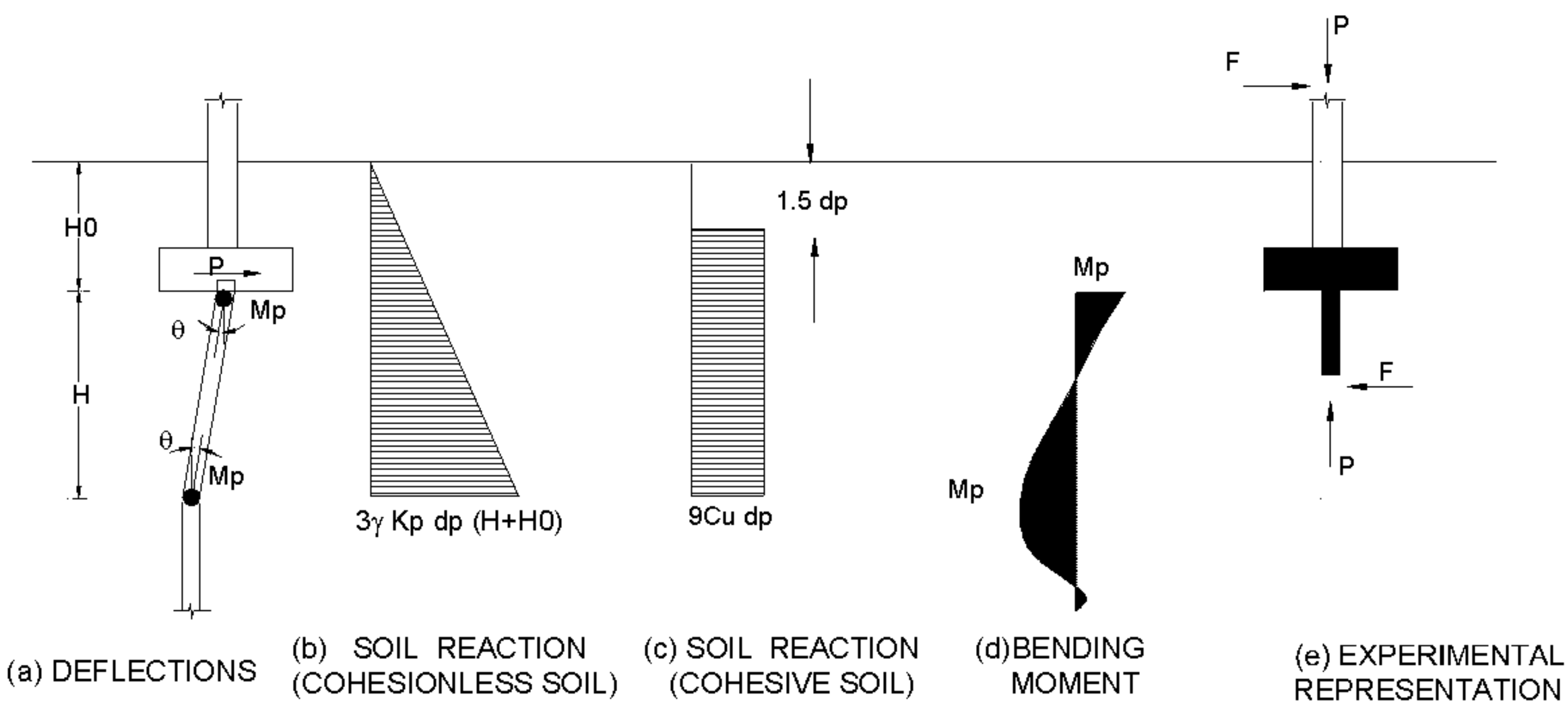

Figure 2.2 Soil Structure-Interaction Representation in Plastic Mechanism of Pile Foundations

in which H_0 = The embedded depth of the cap beam; d_P = the depth of the steel pile section; θ = the plastic rotation of the pile; γ = the unit weight of the soil considered; and K_P = Rankine coefficient of passive earth pressure evaluated as:

$$K_P = \frac{(1+\sin\phi)}{(1-\sin\phi)} \qquad (2.11)$$

where ϕ = the angle of internal friction for the cohesionless soil.

Equating the external work done equation (2.9) to the internal work done equation (2.10), a value for the shear carried by one pile can be obtained as follows:

$$V = \frac{2M_P}{H} + 1.5\gamma K_P d_P H H_0 + 0.5\gamma K_P d_P H^2 \qquad (2.12)$$

According to the upper bound theorem of collapse, the minimum value of V is required to obtain the correct mechanism. Minimizing equation (2.12) with respect to H as follows:

$$\frac{dV}{dH} = 0 = -\frac{2M_p}{H^2} + 1.5\gamma K_p d_p H_0 + \gamma K_p d_p H \qquad (2.13)$$

Upon rearrangement of equation (2.13) this gives:

$$2M_p = 1.5\gamma K_p d_p H_0 H^2 + \gamma K_p d_p H^3 \qquad (2.14)$$

Dividing equation (2.14) by d_p^4 and rearranging gives the following dimensionless expression:

$$\frac{2M_p}{d_p^4 \gamma K_p} = 1.5\left(\frac{H_0}{d_p}\right)\left(\frac{H}{d_p}\right)^2 + \left(\frac{H}{d_p}\right)^3 \qquad (2.15)$$

Further simplification of equation (2.15) leads to the following expression for the normalized distance between plastic hinges H/d_p:

$$\left(\frac{H}{d_p}\right) = \left[\frac{\left(\dfrac{2M_p}{\gamma K_p d_p^4}\right)}{1 + \dfrac{1.5\left(H_0 / d_p\right)}{\left(H / d_p\right)}}\right]^{1/3} \tag{2.16}$$

Now defining the shear span aspect ratio as $\frac{L}{d_p} = \frac{M_p}{Vd_p}$ one obtains:

$$\frac{L}{d_p} = \frac{M_p}{Vd_p} = \frac{M_p}{2\dfrac{M_p d_p}{H} + 1.5\gamma K_p d_p^2 H H_0 + 0.5\gamma K_p d_p^2 H^2} \tag{2.17}$$

Further simplification of equation (2.17) gives:

$$\frac{L}{d_p} = \frac{H / d_p}{2 + \dfrac{\gamma k_p d_p{}^4}{2M_p}\left(\dfrac{H}{d_p}\right)^3\left(1 + 3\dfrac{H_0 / d_p}{H / d_p}\right)} \tag{2.18}$$

Equation (2.18) can be used in conjunction with equation (2.12) to obtain the effective length L. This is illustrated through the following numerical example.

<u>Example</u> Consider a pile-to-cap connection with an embedded depth for the cap equals 2.5 m. It is assumed that the pile is driven in loose silty sand (unit weight = 15.5 kN/m^3, angle of internal friction = 20^0). The HP (10x42), a section extensively used in pile foundation construction, is

considered. Equation (2.12) was then employed to evaluate the shear carried by the pile V for a wide range of H values and the relationship is plotted in figure 2.3, where H was normalized by dividing by d_p. A minimum value of V = 289.3 kN is obtained from this relationship with a corresponding value of $H/d_p = 12$. The value of H/d_p was then substituted in equation (2.18) to obtain the normalized effective length L/d_p. For the soil properties and pile steel section assigned, the effective length was determined as 864mm.

The above procedure was employed to determine the normalized distance between the plastic hinges H/d_p corresponding to the minimum value of V. Two HP steel sections, HP 10x42, and HP 12x63, usually used in practice were utilized for this study. Some cases representing different probable pile-soil conditions were considered for each section. The charts shown in figure 2.4 illustrate these cases. The distribution of the 72 values of H/d_p obtained from this analysis is portrayed in figure 2.5. As can be seen the distribution is approximately lognormal with median and coefficient of variation of 13 and 0.32, respectively. The median value was implemented in equation (2.16) and a simplified expression for the normalized distance between plastic hinges can be obtained as:

$$\left(\frac{H}{d_p}\right) = \left[\frac{\left(\dfrac{2M_p}{\gamma K_p d_p^4}\right)}{1 + 0.12\left(H_0 / d_p\right)}\right]^{1/3} \tag{2.19}$$

If equation (2.19) is substituted in equation (2.18), a general equation for L/d_p can be obtained as:

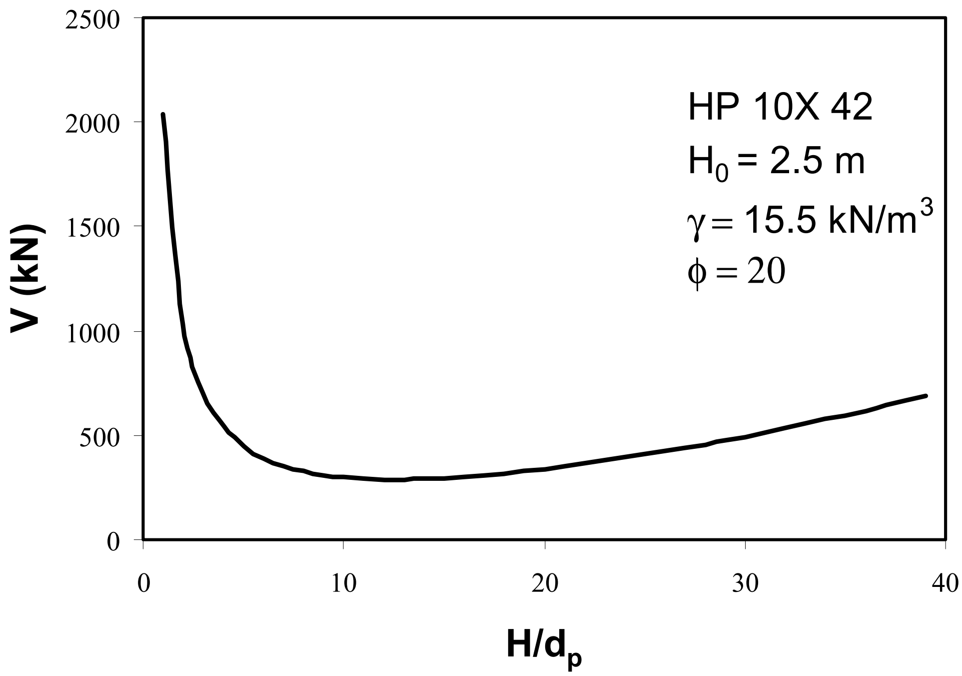

Figure 2.3 Evaluation of the Minimum Value of the Shear Carried by Pile and the Corresponding Value of the Distance between Plastic Hinges

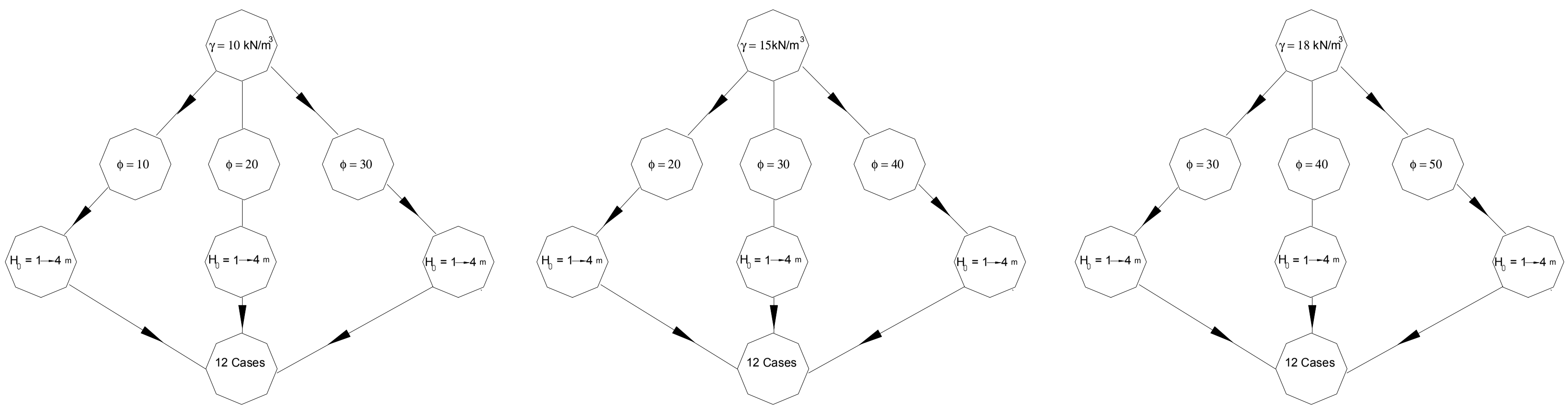

Figure 2.4 Charts illustrating the Number of Cases used to determine an Average Value for H/d_p

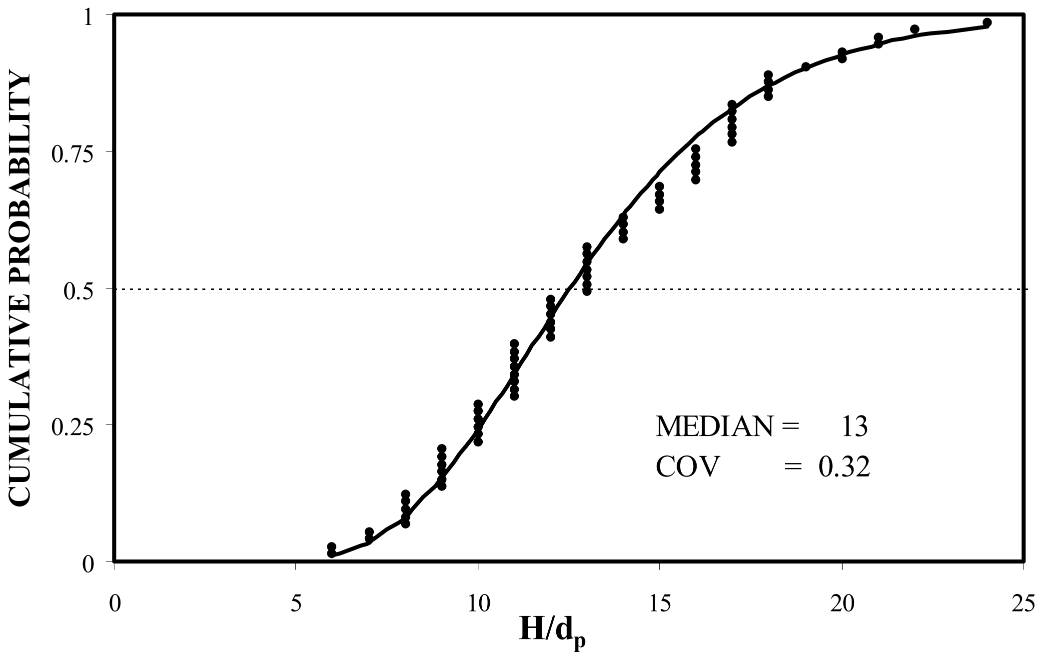

Figure 2.5 Lognormal Distribution of the Distance between Plastic Hinges for Different Pile-Soil Conditions

$$\frac{L}{d_p} = \frac{\frac{1}{3}\left(\frac{2M_p}{\gamma K_p d_p^4}\right)^{1/3}}{\left[2\left(1+0.12\,{}^{H_0}\!/_{d_p}\right)^{1/3} + \left(1+0.12\,{}^{H_0}\!/_{d_p}\right)^{-2/3}\right]\left[\frac{1}{3} + \frac{\frac{H_0}{d_p}\left(1+0.12\,{}^{H_0}\!/_{d_p}\right)^{1/3}}{\left(\frac{2M_p}{\gamma K_p d_p^4}\right)^{1/3}}\right]} \tag{2.20}$$

Further simplification of equation (2.20) leads to:

$$\frac{L}{d_p} = \frac{K_{buried}}{3}\left(\frac{2M_p}{\gamma K_p d_p^4}\right)^{1/3} \tag{2.21}$$

where for non-buried foundations $K_{buried} = 1$, and for buried foundations

$$K_{buried} = \frac{\left(1+0.12\,{}^{H_0}\!/_{d_p}\right)^{2/3}}{\left(1+0.08\,{}^{H_0}\!/_{d_p}\right)\left(1+3\frac{H_0}{d_p}\left(\frac{1+0.12\,{}^{H_0}\!/_{d_p}}{\frac{2M_p}{\gamma K_p d_p^4}}\right)^{1/3}\right)} \tag{2.22}$$

The effect of the cap embedment depth on the effective pile length is illustrated for two HP sections in figure (2.6). The exact values for L/d_p are plotted as well as the values obtained using the simplified equation (2.21). It is shown that the pile effective length decreases with increasing the cap embedment depth. Also, there is a satisfactory agreement between the exact solution and equation (2.21)

Using the above procedure, the relationship of ${}^{L}\!/_{d_p}$ versus the internal angle of friction for various types of soils is plotted in figure (2.8a). These values represent shales, silty sand, and sandy gravel. The geometrical as well as the material properties of the 10X42 HP steel piles

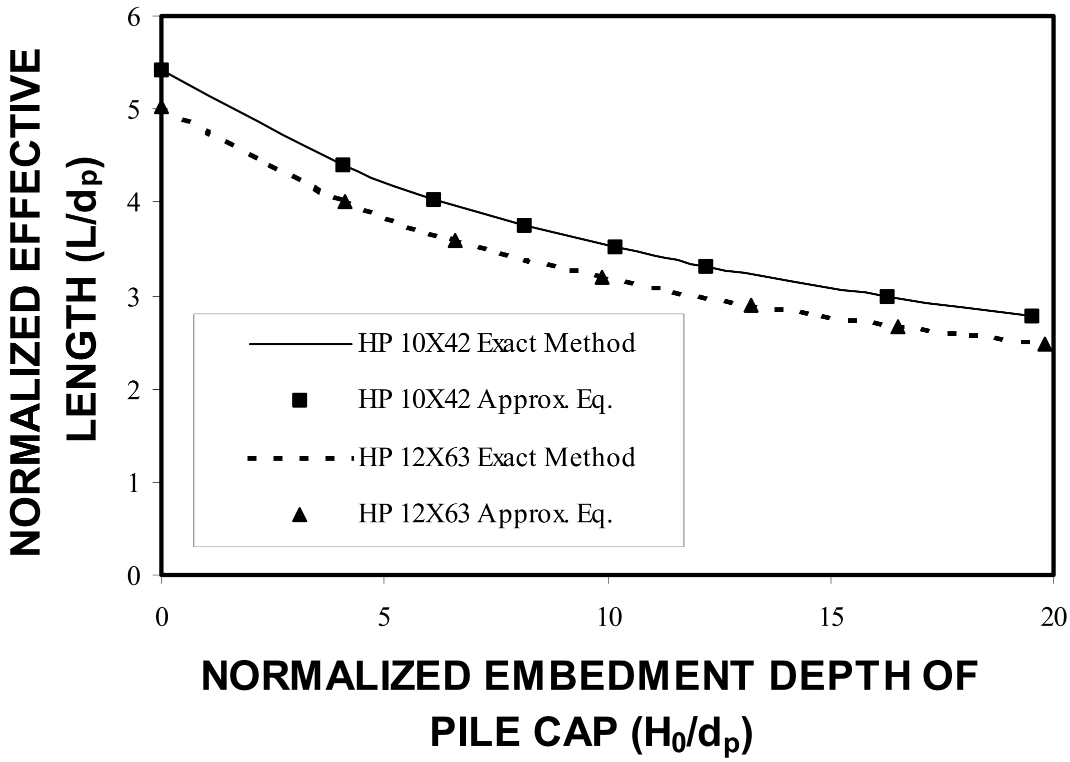

Figure 2.6 Relationship between the Pile Cap Embedment Depth and the Effective Length

was used in the development of these curves. A value of 2.5 m was assumed for H_0. Note from the figure that value of $\frac{L}{d_p}$ for pile foundations in cohesionless soils can range from $2\,d_p$ to $5\,d_p$. It can also be observed, that the effective length of piles increases with decreasing the internal angle of friction of soil.

Case (2): Pile bent:

The pile bent is a special case of the general pile foundation structure. According to figure 2.7, it will be assumed that the point of inflection lies in the middle distance between the two plastic hinges i.e. L=0.5H. Therefore, the goal is to determine the distance Z, defined as the depth within the soil to the plastic hinge. Applying the theory of virtual work for the mechanism shown in figure (2.7a), and (2.7b), the internal work done on the pile and soil is:

$$IWD = 2M_p\theta + \frac{1}{2}K_P\gamma d_P Z^3\theta \tag{2.23}$$

and the external work done taken same as equation (2.9) with H = h+Z:

$$EWD = F(h+Z)\theta \tag{2.24}$$

Equating the external work done equation (2.9) to the internal work done equation (2.24) therefore:

$$F = \frac{2M_p + 0.5K_p\gamma d_p Z^3}{(h+Z)} \tag{2.25}$$

The minimum value of P is required for an upper bound collapse. Therefore, minimize P with respect to Z, therefore:

$$\frac{2M_p}{(h+Z)^2} = \frac{1.5K_p\gamma d_p Z^2(h+Z) - 0.5K_p\gamma d_p Z^3}{(h+Z)^2} = \frac{K_p\,d_p\gamma Z^2(Z+1.5h)}{(h+Z)^2} \tag{2.26}$$

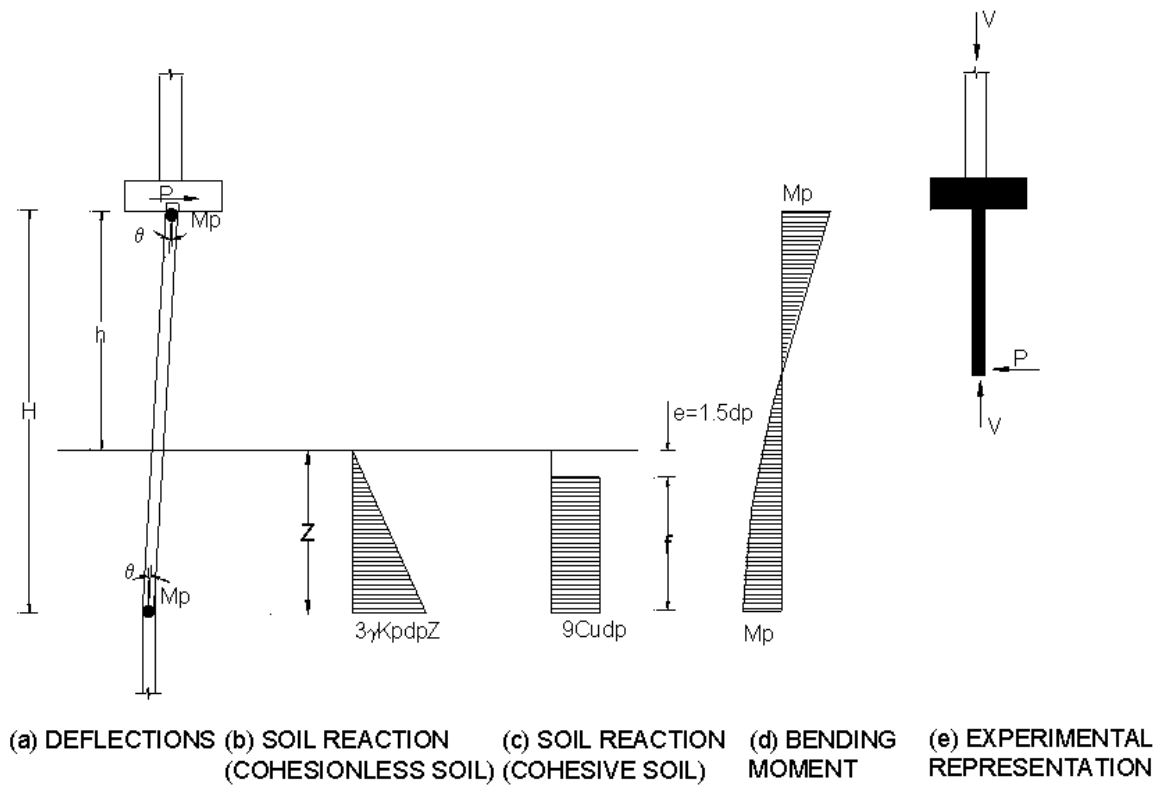

Figure 2.7 Soil Structure-Interaction Representation in Plastic Mechanism of Pile Bents

Further simplification of equation (2.26) gives:

$$Z^3 + 1.5hZ^2 - \frac{2M_p}{K_p \gamma d_p} = 0 \tag{2.27}$$

Therefore the normalized depth to maximum moment can be evaluated as:

$$\frac{Z}{d_p} = \left(\frac{2M_p}{\gamma K_p d_p^4} - 1.5 \frac{h}{d_p} \left(\frac{Z}{d_p} \right)^2 \right)^{1/3} \tag{2.28}$$

Equation (2.28) can be solved by fixed point iteration.

2.3.2 Cohesive soil:

According to Broms(1964a), it has been assumed that the lateral soil reaction is equal to zero to a depth of 1.5 pile depth and equal to 9.0 $C_U d_P$ below this depth, where C_U is defined as the cohesion of the soil considered, determined from undrained triaxial, direct shear or vane tests. The piles are relatively long and hence, the yielding of the pile section rather than failure of the surrounding soil governs the failure.

Case (1) Pile foundation:

Consider the plastic mechanism of the pile foundation shown with soil reactions in figure (2.2a) and (2.2c) and applying the theory of virtual work for this mechanism, therefore the external work done on the pile is taken same as equation (2.9). The internal work done on the pile and soil can be expressed as:

$$IWD = 2M_p \theta + \frac{9}{2} C_U d_P H^2 \theta \tag{2.29}$$

Equating the external work done (2.9) to the internal work done (2.29), the shear carried by one pile is determined as:

$$V = \frac{4M_P + 9C_U d_P H^2}{2H} \tag{2.30}$$

According to the upper bound theorem of collapse, the minimum value of V is required to obtain the correct mechanism. Consequently, minimizing equation (2.30) with respect to H, therefore an expression for the normalized distance between the plastic hinges can be obtained as:

$$\frac{H}{d_p} = \frac{2}{3}\left(\frac{M_p}{C_U d_p^3}\right)^{1/2} \tag{2.31}$$

Defining the shear span as $L = \dfrac{M_p}{V}$ one obtains:

$$L = \frac{M_p}{V} = \frac{M_p}{\left[\dfrac{2M_p}{H} + \dfrac{9}{2}C_U d_p H\right]} \tag{2.32}$$

Further simplification in terms of pile diameter d_p therefore:

$$\frac{L}{d_p} = \frac{1}{6}\left(\frac{M_p}{C_U d_p^3}\right)^{\frac{1}{2}} \tag{2.33}$$

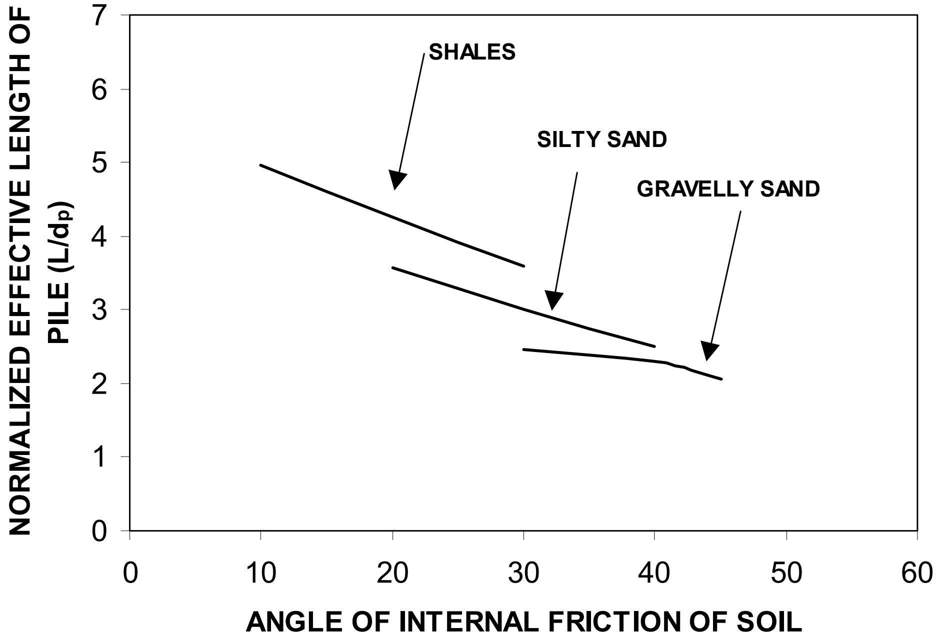

(a) Cohesionless Soil

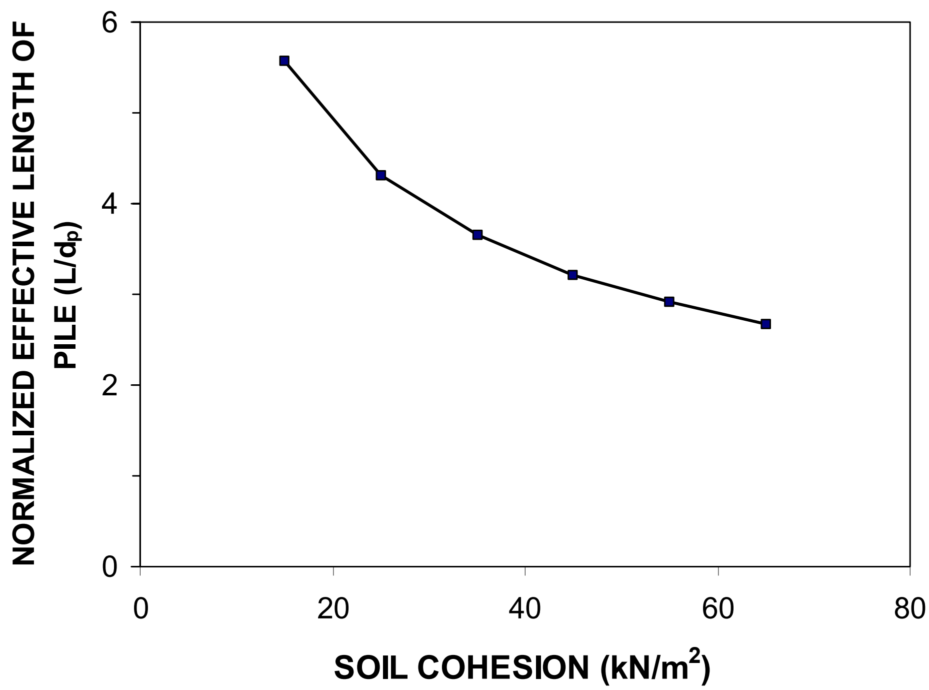

(b) Cohesive soils

Figure 2.8 Effect of Soil Parameters on the Effective Length of Pile specimens

The relationship between the cohesion of soil and the normalized effective length of the pile was evaluated using equation (2.33). The relationship is plotted in figure 2.8b. It can be concluded from that figure that the normalized effective length of the pile specimen (L/d_p) can vary from a value of $2d_p$ to $6d_p$ depending on the soil parameters used.

Case (2) Pile Bent:

The principle of virtual work for the plastic mechanism shown in figure (2.7a) with soil reactions in (2.7c) is adopted:

$$EWD = P(h + f + e)\theta \qquad (2.34)$$

in which, h= the clear distance from the plastic hinge at pile-to-cap connection to the soil surface, e= soil depth where the lateral soil reaction equals zero, and f = the embedded depth to the second plastic hinge excluding e. The internal work done on the pile and soil can be expressed as:

$$IWD = 2M_p\theta + \frac{9}{2}C_U d_P f^2\theta \qquad (2.35)$$

Equating the external work done equation (2.34) to the internal work done equation (2.35) gives:

$$P = \frac{2M_P + 4.5C_U d_P f^2}{(h + f + e)} \qquad (2.36)$$

Minimizing this expression with respect to f gives:

$$4.5C_U d_p f^2 + 9C_U d_p f(h + e) - 2M_p = 0 \qquad (2.37)$$

Solving equation (2.37) for f and adding e, an expression for Z can be obtained as:

$$Z = (h + e)\left[\sqrt{1 + \frac{0.44M_P}{C_U d_P (h + e)^2}} - 1\right] + e \qquad (2.38)$$

Results of the analyses of pile bents in cohesionless and cohesive soils suggests that a typical depth to maximum moment lies in the range $3\,d_P$ to $9\,d_P$, depending on the soil properties used in the calculation. As an approximation a value of $5\,d_P$ is used in the present study.

2.4 PILE-TO-CAP CONNECTION EFFICIENCY-ELASTIC BEHAVIOR FOR CAPACITY DESIGN

An objective of the present study is to determine the strength and ductility of pile-to-cap connection under highly plastic drifts, and hence provide retrofit methodologies for improving the seismic performance of this connection. The plastic crushing moment capacity of the concrete cap beam as well as the plastic moment capacity of the steel pile control the performance of the connection under high drifts. As steel is more ductile than concrete, failure of the connection under severe seismic drifts is expected to occur when the concrete stress reaches its crushing capacity, while the steel pile section is still capable to absorb more energy. Consequently, connection efficiency is defined as:

$$\rho = \frac{M_j}{M_P} \tag{2.39}$$

where M_j = moment capacity of the concrete-pile connection (joint); and $M_p = f_y Z_p$ = nominal moment capacity of the pile. If $\rho > 1$ then plastification in the pile is expected, whereas if $\rho < 1$ damage to the connection is expected.

In what follows, using basic principles, it will be focused on developing two theories for the evaluation of the connection efficiency. The theories are developed for strong axis bending direction and the same approach can be used for the weak axis direction.

2.4.1 Pre-Damaged Efficiency Based on Cracked Elastic Theory

The following assumptions are made in the analysis:

1. Both concrete bending and compressive stresses along the embedment depth of the steel section will counteract the lateral applied load.
2. The stresses and strains, at any load stage, continue to be closely proportional i.e. the stress distribution along the embedment depth is linear.
3. The stresses develop at the back face of the connection are small enough to be considerably negligible during the analysis.

4. The overall behavior of the connection will be governed by the concrete compressive stress at the extreme fiber in the front face of the connection.

The mechanism based on these assumptions is shown in figure 2.9. According to the last assumption, an expression for the compressive stress of the concrete can be written at the extreme fiber in the front face of the connection in terms of the stress blocks (shown in figure 2.9) as follows:

$$-\frac{V}{A}-\frac{M_j}{S_x}\geq -f_c \tag{2.40a}$$

whereupon rearranging:

$$f_c \geq \frac{V}{b_f l_{emb}}+\frac{6M_j}{b_f {l_{emb}}^2} \tag{2.40b}$$

in which f_c = the allowable concrete compressive stress at the extreme fiber in the front face of the connection; V= the applied lateral load; b_f = the flange width of the steel pile section; l_{emb} = embedment depth of the steel pile section inside the concrete cap beam; and M_j = the nominal moment capacity of concrete.

The applied lateral load can be expressed as:

$$V = \frac{M_j}{L^*} \tag{2.41}$$

where L^* = the distance from the point of application of the lateral load to the neutral axis of the joint. Substituting equation (2.41) in (2.40) gives:

$$f_c \geq M_j \left(\frac{1}{L^* b_f l_{emb}} + \frac{6}{b_f l_{emb}{}^2} \right) \tag{2.42}$$

Solving for the joint moment gives:

$$M_j \leq \frac{f_c b_f l^2{}_{emb}}{\left(6 + \frac{l_{emb}}{L^*} \right)} \tag{2.43}$$

Introducing the connection efficiency ρ as defined in equation (2.39), therefore:

$$\rho = \frac{f_c b_f l_{emb}{}^2}{f_y Z_P (6 + \frac{l_{emb}}{L^*})} \tag{2.44}$$

Where, f_y = the yield stress of the steel pile section, Z_p = the plastic modulus of the steel pile section approximately can be expressed as:

$$Z_p \approx t_f b_f d_p \tag{2.45}$$

in which t_f = the pile steel section flange thickness; and d_P = the pile steel section depth.

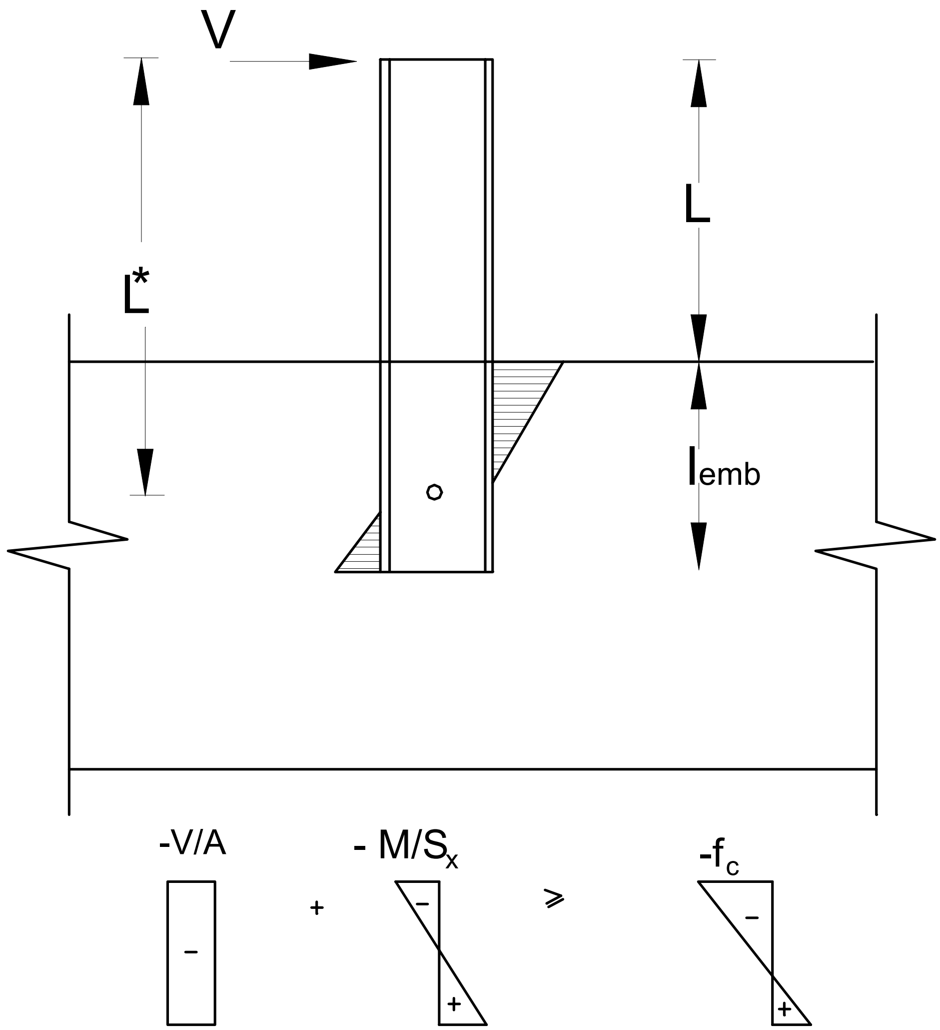

Figure 2.9 Stress Distribution for Cracked Elastic Theory

Therefore the connection efficiency can be quantified as:

$$\rho = \frac{\left(\frac{f_c}{f_y}\right)\left(\frac{d_P}{t_f}\right)\left(\frac{l_{emb}}{d_P}\right)^2}{\left(6 + \frac{l_{emb}}{L^*}\right)} \tag{2.46}$$

l_{emb} / L^* can range from 0.1, for the case of pile bents, to 0.5 for pile foundations. Taking an average value of 0.3 and substitute in equation (2.46) an expression for the elastic (pre-crushing) efficiency is obtained:

$$\rho = 0.16\left(\frac{f_c}{f_y}\right)\left(\frac{d_p}{t_f}\right)\left(\frac{l_{emb}}{d_p}\right)^2 \tag{2.47}$$

By inverting equation (2.47) one can obtain a design expression for determining the required embedment length

$$\frac{l_{emb}}{d_p} = \sqrt{\left(\frac{\rho}{0.16}\right)\left(\frac{f_y}{f_c}\right)\left(\frac{t_f}{d_p}\right)} \tag{2.48}$$

At section overstrength $f_{su} = \rho f_y$ with $\rho = 1.6$. Adopting a value of $f_c = 0.85 f_c^{'}$ and substituting into the above equation gives:

$$\frac{l_{emb}}{d_p} = 3.4\sqrt{\left(\frac{f_y}{f_c^{'}}\right)\left(\frac{t_f}{d_p}\right)} \tag{2.49}$$

2.4.2 Design Requirements with the Cracked Elastic Theory

It is of great interest for practicing engineers to use simple and transparent approaches to achieve their design objectives. This concept can be applicable for the future designs and design code provisions for pile-to cap connections under lateral loads, using the theories presented in this study. The cracked elastic theory, a conservative theory for design, can be used as an upper bound. Developed for high strain levels, the post ultimate plastic theory, described in the next subsection, can be used as a lower bound for estimating the embedment depth for these connections due to horizontal loads.

The cracked elastic efficiency is governed by the compressive stress at the extreme fiber of the front face of the connection. Therefore, design requires determination of the stress level at the concrete surface, after selecting the appropriate embedment depth. Figure 2.10 presents relationships between the normalized embedment depth and the pre-damaged efficiency, for an allowable stress of $f_c = 0.85f_c^{'}$. Using this stress ensures that premature concrete crushing will not occur. If an efficiency of $\rho = 1.6$ is adopted for design, (this value allows for connection overstrength) then the required embedment depth can be found.

2.5 A Theoretical Validation Of The Cracked Elastic Design Assumptions

2.5.1 Finite Element Modeling of Pile-to-Cap Connection

During the last four decades the finite element method has been developed and improved to become applicable for most of the civil and structural mechanics problems, and also extended to cover different areas such as mechanical and aerospace engineering. The evolution in the last two decades of computer hardware capabilities conferred this method more popularity among the engineering community. Basically, the finite element analysis of a continuum consists of three steps:

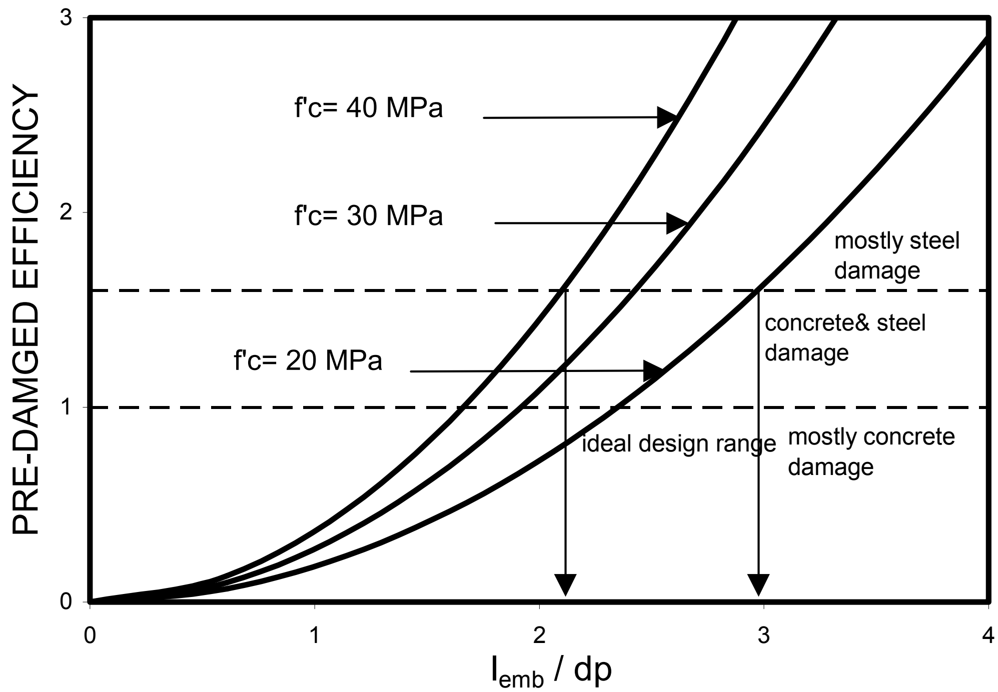

Figure 2.10 Pre-Damaged Efficiency for Different Compressive Strength

Structural idealization, whereby the continuum is idealized as an assemblage of a number of discrete elements connected at the nodes only

(i) Specifying the relation between the internal displacements of each element and its nodal displacements. This is done by using a displacement function to specify the pattern in which the element is to deform. On the basis of this displacement function, one can derive the element stiffness matrix which relates the element nodal forces to the element nodal displacements.

(ii) The structural analysis of the idealized assemblage of discrete elements. This analysis is carried out by the standard matrix stiffness procedure.

Although, classified as an approximate method for structural analysis, the finite element method proved its efficiency in idealizing different physical problems with satisfactory convergence. In the following pages, the cracked elastic theory developed earlier in this section will be validated by comparing its results to the finite element method.

2.5.2 Model Description

Two models were developed for comparison with the cracked elastic theory developed herein. The first model, denoted here as model 1, represents a short exterior pile with a *300 mm* embedment depth in a concrete pile cap. The dimensions of the pile and pile cap are same as those of pile specimen P1 which will be described in detail in section 4. Therefore the length, width and height of the pile cap were taken as *1450 mm*, *1000 mm, and 900 mm* respectively. Fixed boundary conditions were assigned to all the nodes at the interior edge surface to be consistent with the experimental setup, where that edge was anchored to the laboratory strong floor by means of an anchoring beam. The lever arm for that model was taken as *785mm* from the concrete surface to conform to the experiment. The direction of the lateral load for this model was set so that the bending be along its strong axis.

The second model denoted as model 2 represents a long interior pile loaded along its weak axis bending. Geometry and boundary conditions of that model are consistent with pile specimen W1 (details of this test specimen is given in section 4). The length of the concrete beam (*2400mm*) was taken equal to the distance where the concrete specimen was anchored to the laboratory strong floor. Fixed boundary conditions were assigned to all the nodes at the edge surfaces in both ends where it was anchored to the floor. The width and the depth were taken as 700mm and 600 mm respectively. The lever arm for this model was taken as *2616mm.* The geometrical properties of the steel section were taken as HP10X42, for the two models.

2.5.3 Types of Elements

Finite element meshes for the two models were generated using the FE analysis package PATRAN version 7.6 (PDA Engineering), and the finite element analyses were performed using the ABAQUS code version 5.7 (Hibbitt, Karlsson, and Sorensen, Inc.). An 8-node linear brick element of the type C3D8 was used to limit the computational time to a reasonable extent. 82.5X82.5X80 mm brick elements were used for the concrete cap beam in model 1. The same dimensions, except for the thickness were assigned to the steel section. 18270 nodes and 13260 elements were used for model one. In the region surrounding the steel section and extending 623 mm from both sides, 45X45X60 mm brick elements were used to model the concrete cap beam in model 2. The length of the element, however, was increased to 144.25 mm for the regions beyond 623mm from both sides. 7856 nodes and 5989 elements were used for model two. Typical FE meshes of model one, and two are shown in figures 2.11, and 2.12.

Contact gap elements of the type GAPUNI were used to model the steel-concrete interaction during loading. These contact elements were necessary to transfer the lateral forces properly from the steel pile to the concrete beam during loading, and hence leading to the appropriate distribution of stresses along the embedment depth. Each gap element allows for contact between two nodes. One node is located on the steel section and the other one is located in the same location on the concrete beam. Therefore, each gap element was defined by specifying the two nodes forming the gap and providing geometric data defining the initial state of the gap. In the present study the initial state of the gap was set to zero, that is the surfaces are initially bonded. The contact pressure-clearance relationship used in the present study is shown in figure 2.13. When the two nodes of one element are in contact, any contact pressure can be transmitted between them. The nodes separate if the contact pressure reduces to zero. Separated

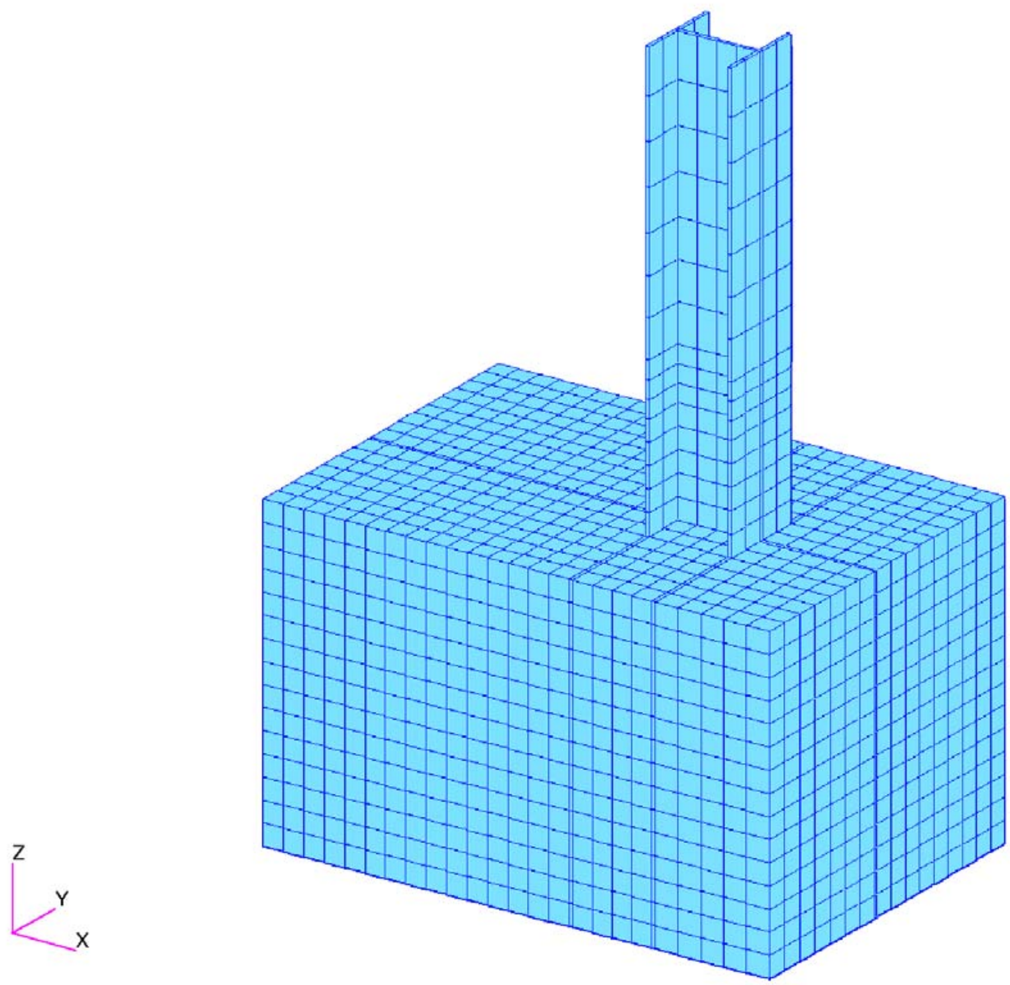

Figure 2.11 FEM Model 1 Short Exterior Pile

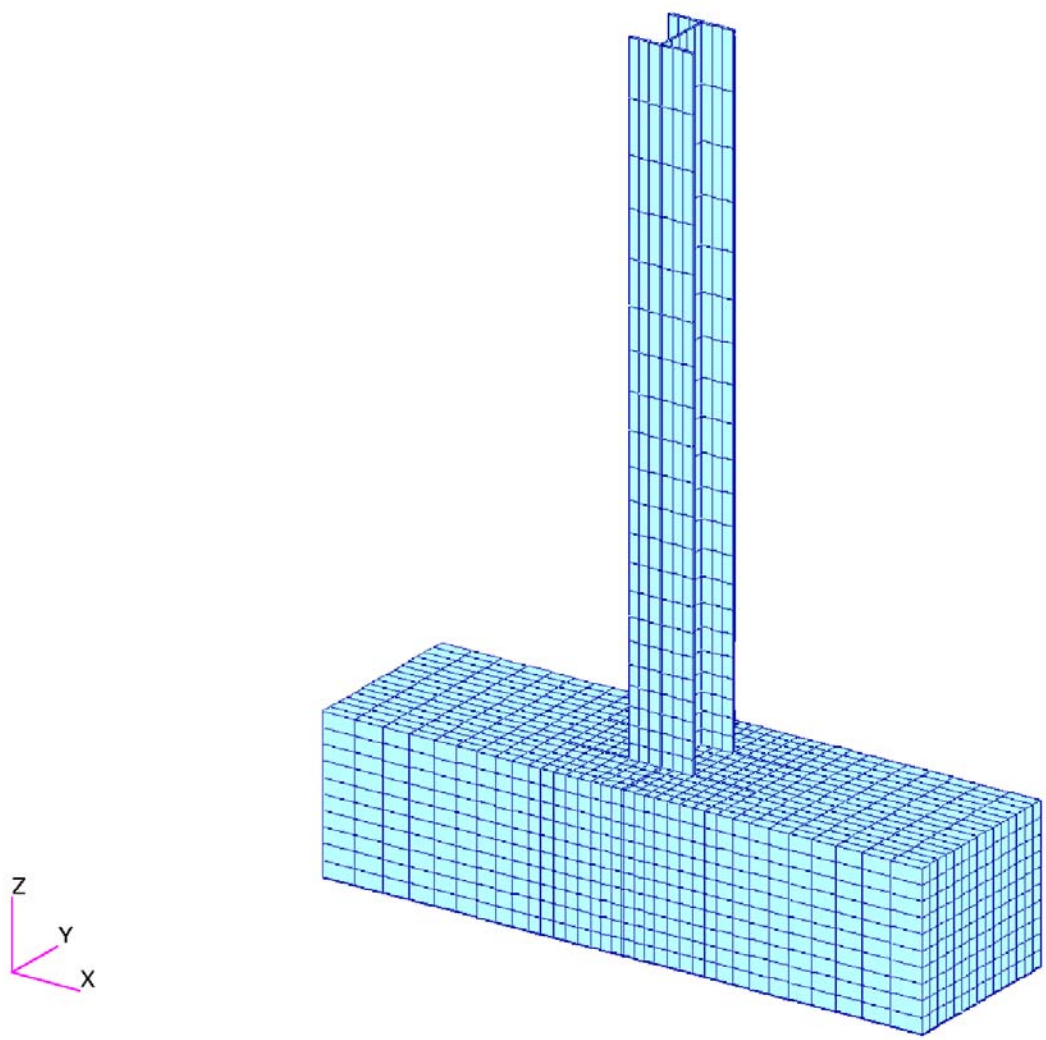

Figure 2.12 FEM Model 2 Long Interior Pile (Weak Axis)

nodes come into contact when the clearance between them reduces to zero. A friction property is associated with each gap element. This friction property controls the slipping of the surfaces, in contact, relative to each other. In the present study the basic Coulomb friction model was used to represent the friction between the interacting surfaces. On the basis of this model, the two contacting nodes can carry shear stresses up to a certain magnitude across their interface before they start sliding relative to one another. The Coulomb friction model defines this critical shear stress at which sliding of the surfaces starts as fraction of the contact pressure between the surfaces. The user specifies this fraction known as the coefficient of friction. Several values for the coefficient of friction were tried in the present study. It was observed that increasing the coefficient of friction results in a slight decrease of the compressive stresses of concrete along the embedment depth. Consequently, a value of 0.6 was used in this study for the coefficient of friction. A total number of 180 gap elements was used to represent the contact between the steel section and the concrete beam for model one. This number was 330, and 234 for model two and three respectively.

2.5.4 Material Constitutive Models

2.5.4.1 Steel Pile Model

The material properties used for the steel material in the elastic phase are as follows: modulus of elasticity = 200000 MPa, Poisson ratio = 0.28 and yield stress = 315 MPa. Those values are equal to those obtained from the coupon test of the HP 10X42 steel section. The results of this test are discussed in detail in section 3. The plastic behavior of the steel material was modeled using the classical metal plasticity mode in ABAQUS. This model uses Mises yield surface with associated plastic flow and isotropic hardening.

2.5.4.2 Concrete Beam Model

The material properties used for concrete are as follows: compressive strength after 28 days = 40 MPa, plastic strain at failure = 0.002, and Poisson ratio = 0.18. The Modulus of elasticity of

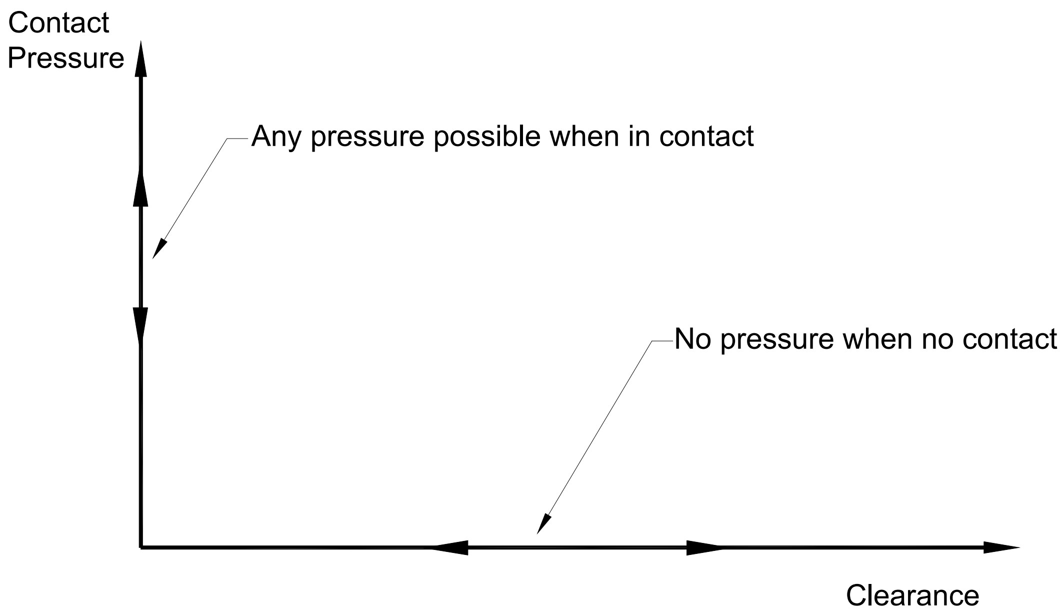

Figure 2.13 Pressure-Clearance Relationship for Contact Elements (after Hibbit, Karlsson & Sorensen Inc., 1997)

concrete was determined according to the following equation (ACI-318):

$$E_c = 4700\sqrt{f_c^{'}} \qquad \text{MPa} \tag{2.50}$$

in which E_c = Modulus of elasticity of concrete, and $f_c^{'}$ = concrete compressive strength. For the present study, a concrete strength of $f_c^{'} = 40$ MPa was assumed.

The compressive and cracking response of concrete that are incorporated in the ABAQUS concrete model are illustrated in figures 2.14, and 2.15. When concrete is loaded in compression, it initially exhibits elastic response. As the stress is increased, some irrecoverable inelastic straining occurs and the response of the material softens. The failure domain in compression is completed when an ultimate stress is reached whose analytical formulation is written in terms of the equivalent pressure stress and the Von Mises equivalent deviatoric stress. Cracking is assumed to occur when the stress reaches a failure surface that is called the crack detection surface. The model is characterized by tension stiffening post-failure behavior to represent the post-cracking softening of concrete.

For the present study, the concrete cap beams are characterized by little reinforcement. Therefore, the tension stiffening was defined in terms of a maximum displacement at which a linear loss of strength after cracking gives zero stress. The determination of this maximum displacement was based on an energy approach in which the concrete's brittle behavior is characterized by a stress-displacement response rather than a stress-strain response. One can refer to the ABAQUS 5.7 theory manual for more details about this formulation. For the present study, this maximum displacement was taken as *0.5 mm*. This value is well above the default value used in ABAQUS (*0.1mm*). However, it was adequate to avoid early divergence problems of the nonlinear algorithm that may prevent the progress of the solution at early stages.

Defined as small tensile strength material, concrete has a residual capability of transmitting shear forces in the presence of cracking. This is the effect of a rough crack configuration due to

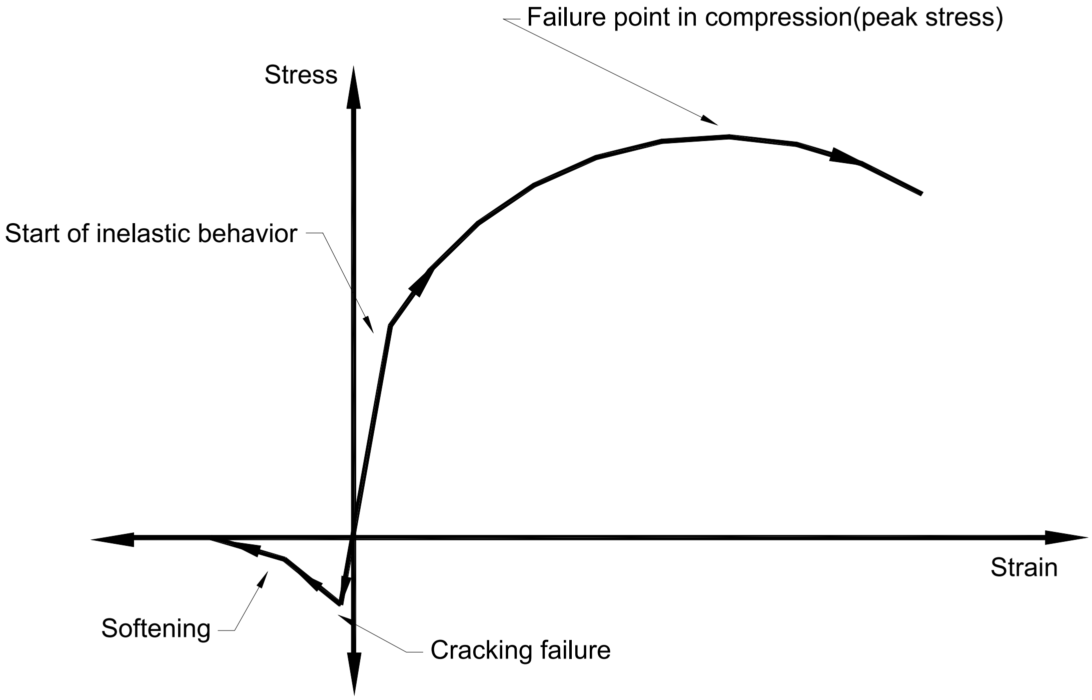

Figure 2.14 Uniaxial Behavior of plain Concrete (after Hibbit, Karlsson & Sorensen Inc., 1997)

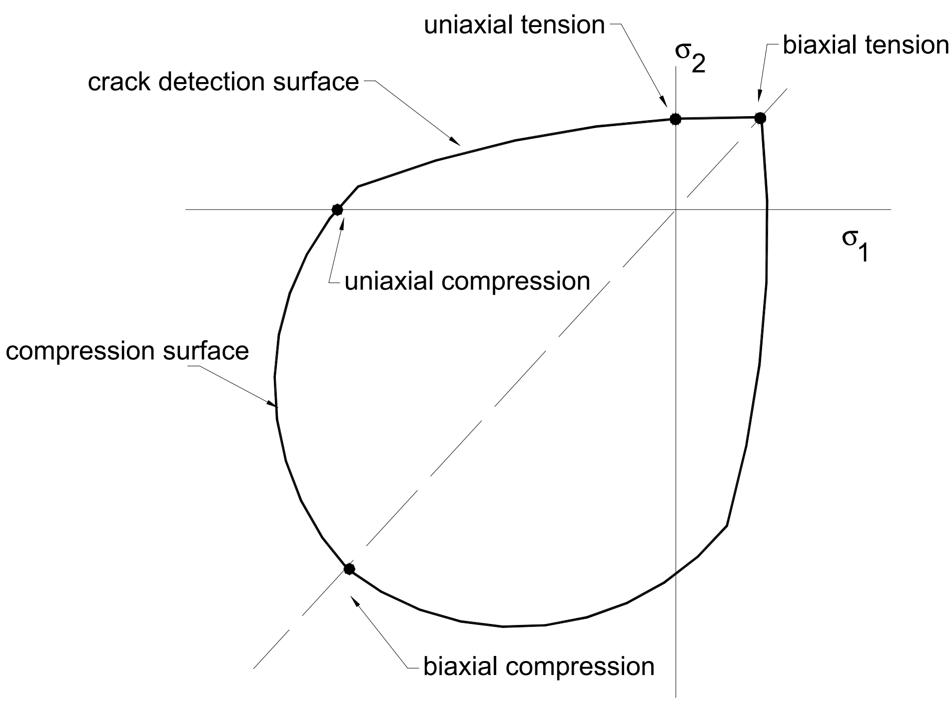

Figure 2.15 Yield and Failure Surfaces in Plane Stress (after Hibbit, Karlsson & Sorensen Inc., 1997)

aggregate interlock. From a computational point of view, this phenomenon is taken into account in ABAQUS by means of the so-called shear retention option, which specify the reduction in the shear modulus as a function of the opening strain across the crack. In the present study full shear retention was assumed, as the overall response is not strongly dependent on the amount of shear retention.

Two more values needed to be specified for the concrete model to define the shape of the failure surface. These values are the ratio of the ultimate biaxial compressive stress to the uniaxial compressive ultimate stress, and the ratio of the uniaxial tensile stress to the uniaxial compressive stress at failure. These values were taken as 1.16 and 0.1 respectively.

2.5.5 Nonlinear Analysis Algorithm

Although from first appearances the models look simple, but they are considered highly nonlinear problems. Nonlinearities in such models arise from the nonlinear material concrete in addition to the boundary nonlinearities i.e. contact and friction. In fact, accompanying both the friction and the concrete material model usually causes some divergence problems specially when cracks start to take place. In order to avoid premature reductions of the time increments, the number of equilibrium iterations for a residual check and the number of equilibrium iteration for a logarithmic rate of convergence check were set to 50 and 70 respectively. It is recommended for severely discontinuous problems to increase these two parameters on the CONTROLS option. The line search algorithm was used to avoid divergence of the solution in the early iterations. The analysis was conducted in load control. For such problems, it is preferable to use a direct user-specified fixed time incrementation with very small time increments rather than using the automatic time incrementation by ABAQUS.

2.5.6 Comparison of Results with the Cracked Elastic Theory

Comparisons between the FEM models with the cracked elastic theory are in terms of the compressive stress at the concrete surface and the distribution of stresses along the steel-concrete interface. Equation (2.43) can be rearranged and written in the following form:

$$f_c \geq \frac{M_0\left(6 + \frac{l_{emb}}{L^*}\right)}{b_f l_{emb}{}^2} \qquad (2.51)$$

in which $M_0 =$ the applied moment by the lateral load. Equation (2.51) is compared to the two FEM models in terms of the compressive stresses at the concrete surface, and the distribution of stresses along the embedment depth.

Model 1 was analyzed under a *120 kN* lateral load. Taking into consideration that the lever arm of this specimen was taken as *785mm.* Therefore the applied moment can be quantified as *94.2 kNm.* Substituting this value in equation (2.51), therefore the compressive stress at the concrete beam surface can be obtained as 26 MPa. Contour plots, from the ABAQUS program, of the compressive stresses for this model are shown in figure 2.16. One can observe that the distribution of stresses along the flange width is not uniform. Consequently, the comparison is made in terms of the average stresses along the flange width. The distribution of the compressive stresses along the flange width ranged from 6 MPa at the flange edge to 36 MPa at the center. An average value of 20 MPa can be taken for the compressive stress at the concrete surface. This value agrees reasonably with the theoretical formula proposed in this study.

Figure 2.17 illustrates the distribution of stresses for model 2 under *10 kN* lateral loading. As mentioned earlier the lever arm of this case was taken as *2616 mm,* which results in *26.2 kNm* applied moment at the connection. Again the distribution of stresses along the steel pile depth is not uniform. Note that a major part of the section depth had a 9 MPa stress. Equation (2.51) is used, after replacing b_f with d_p in the denominator to estimate the theoretical compressive stress at the interface. The theoretical compressive stress was quantified as 7 MPa. This value compares favorably with the values obtained from the finite element analysis.

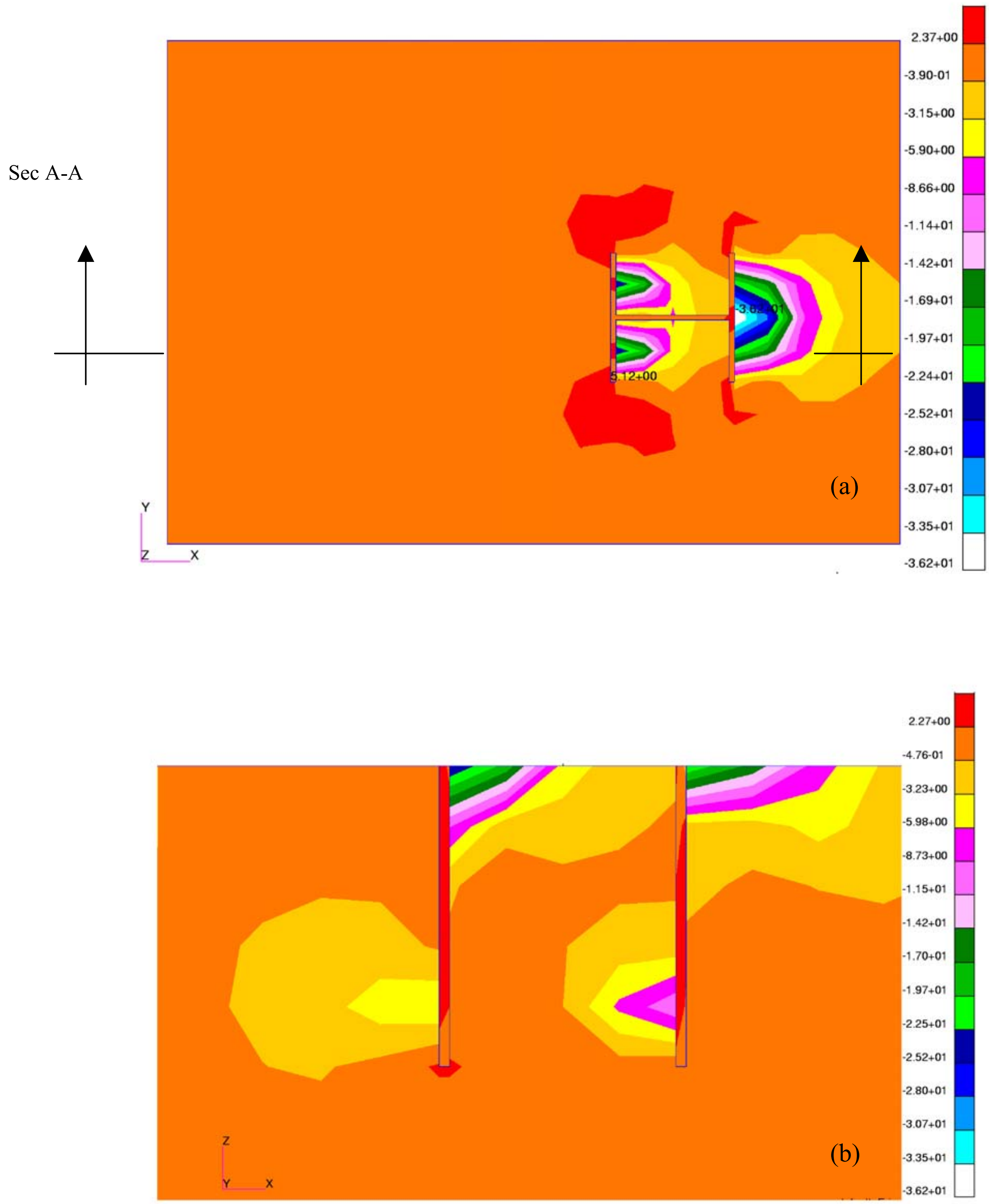

Figure 2.16 Compressive Stress Contours in MPa for Model 1 (a) Stress Contours along the flange width, and (b) Stress Contours along the embedment depth section A-A

On the basis of the stress contours along the steel-concrete interface, the distribution of the compressive stresses is plotted for the two models in figure (2.18). The two figures agree with the linear of stress assumption for the cracked elastic theory. The figures indicate also that the stresses generated at the back face of the connection are very diminutive compared to the linear stresses along the front face, and hence assess the assumptions implemented in the elastic cracked theory. Note that the applied lateral loads for the two FE cases studied here were enough to induce cracking within the damaged elasticity concrete model in ABAQUS.

2.6 PILE CAP CONNECTION EFFICIENCY-INELASTIC BEHAVIOR FOR SEISMIC VULNERABILITY ANALYSIS

The plastic theory presented here is an attempt to develop a rational analytical model capable of predicting the connection efficiency based on the ultimate capacity of the concrete cap beam. The theory accounts for the strength deterioration of the concrete due to reversed cyclic loading, and hence, evaluates the connection efficiency at different lateral load stages. It also accounts for the axial as well as the lateral load applied to the pile. The following assumptions are made:

1. The lateral load level is high enough so that stresses and strains are no longer proportional.
2. The equivalent rectangular stress distribution can be used to represent the parabolic distribution of the stresses along the sides of the connection.
3. Same values for the average concrete stress ratio α and the stress block depth factor β will be assigned for the two stress blocks at the front and back face of the connection.
4. The connection has already experienced many cycles of loading, and hence the stress block depth factor can be taken as equal to unity (Mander et al 1998).

In this case, the moment is resisted by bearing between the steel flange and the concrete and by end bearings through the flange on the compression side. A friction force along the slip surfaces provides additional resistance, which acts in the opposite direction of the movement. This mechanism and the resulting idealized stress blocks are shown in figure 2.19. According to the third and fourth assumptions, one is able to divide the rectangular stress block at the front

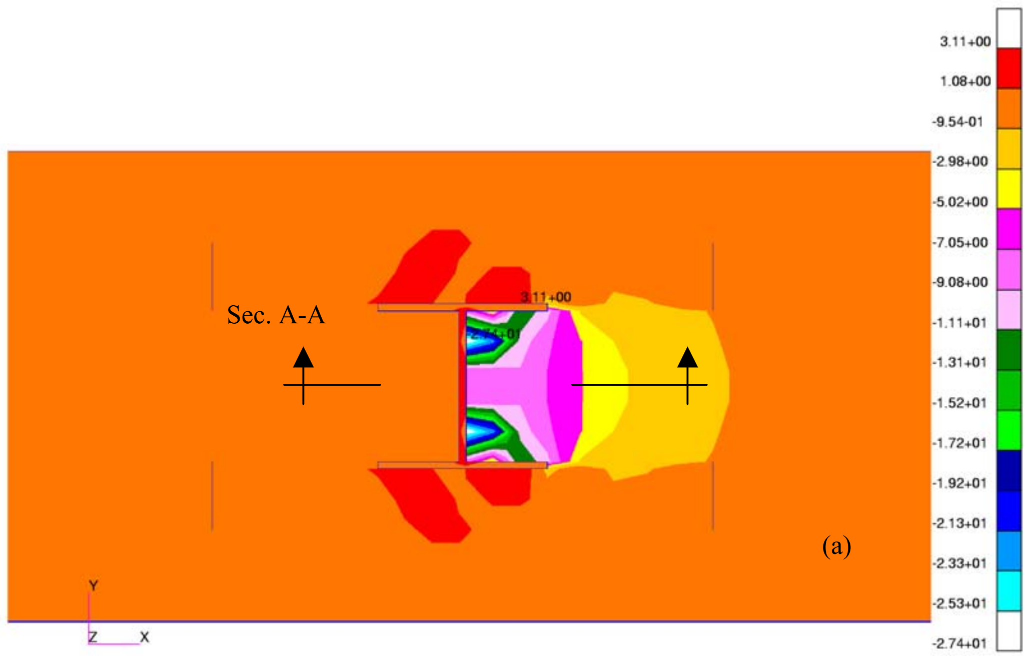

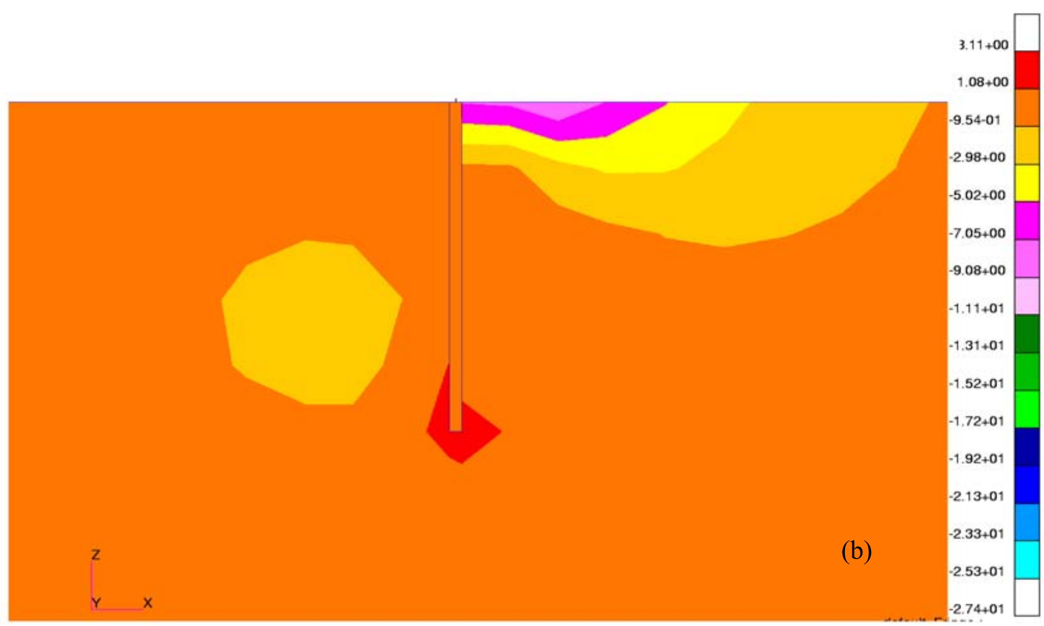

Figure 2.17 Compressive Stress Contours in MPa for Model 2 (a) Stress Contours along the flange width, and (b) Stress Contours along the embedment depth section A-A

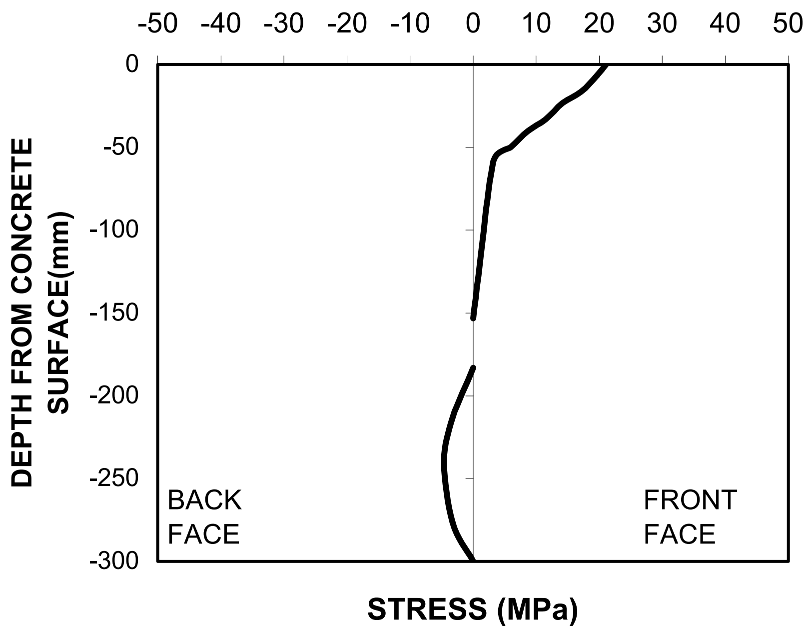

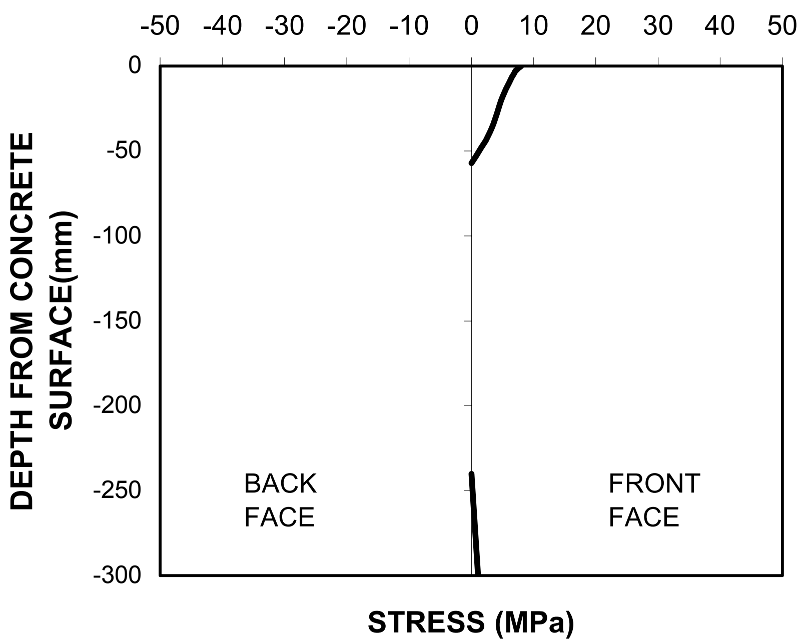

Figure 2.18 FEM Distribution of Compressive Stresses along the embedment Depth (a) Model 1, and (b) Model 2

face of the connection to two stress blocks as shown in figure 2.19a. The stress block force C_m of the front face as well as an equal force from the stress block at the back face will counteract the applied moment. The force C_h of the lower stress block at the front face will resist the applied lateral force F. The force C_m is quantified as:

$$C_m = \alpha\beta f'_c b_f a \tag{2.52}$$

and the force C_h that will resist the lateral load (shear):

$$C_h = \alpha\beta f'_c b_f (l_{emb} - 2a) \tag{2.53}$$

Summing the forces in the horizontal direction gives:

$$F = C_h \tag{2.54}$$

Combining equations (2.53) and (2.54), then solving for the stress block height a:

$$a = \frac{l_{emb}}{2} - \frac{F}{2\alpha\beta f'_c b_f} \tag{2.55}$$

Summing the forces in the vertical direction, therefore:

$$C_V = P - \mu F \tag{2.56}$$

Equation (2.52) through (2.56) can be used to evaluate the friction forces F_d and F_u as:

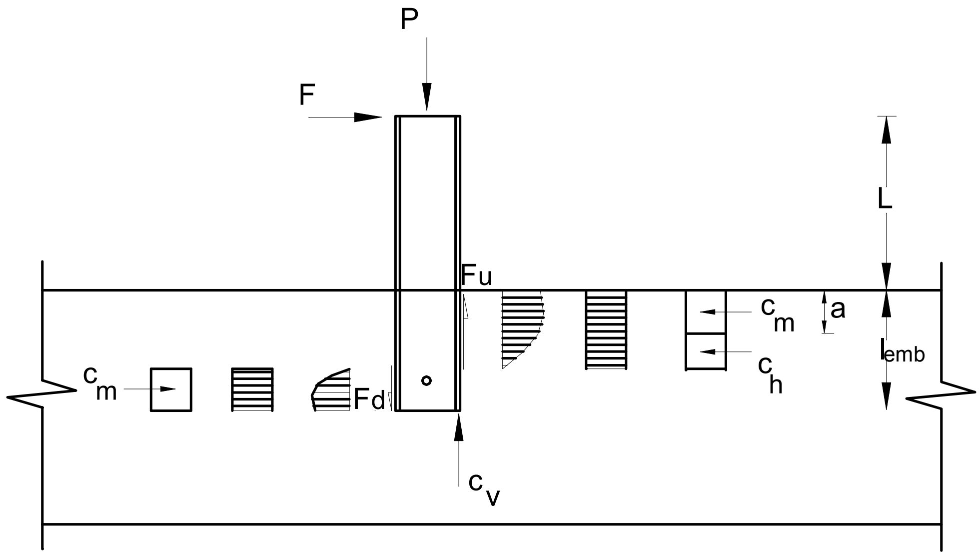

(a) Basic Mechanism

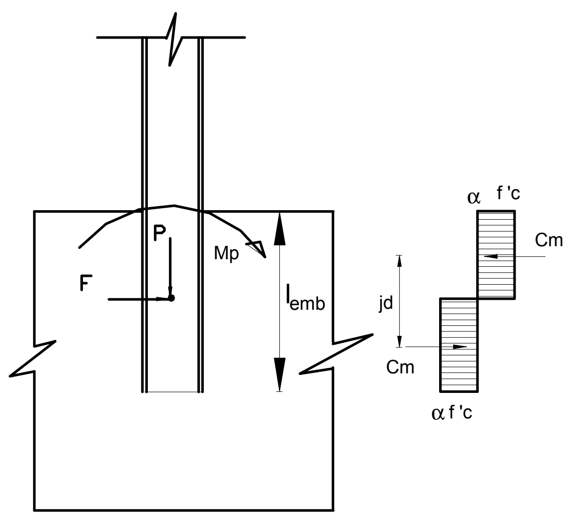

(b) Simplified Mechanism for the Distribution of l_{emb}

Figure 2.19 Mechanisms and Stress Distribution for Plastic Theory

$$F_d = \frac{1}{2}\alpha\beta\mu f_c' b_f l_{emb} - \frac{\mu F}{2} \tag{2.57}$$

and

$$Fu = \frac{1}{2}\alpha\beta\mu f_c' b_f l_{emb} + \frac{\mu F}{2} \tag{2.58}$$

Summing the moments about the instantaneous center of rotation:

$$F(L + l_{emb} - a) = C_m (l_{emb} - a) + (C_V + F_u + F_d)\left(\frac{d_p}{2}\right) + C_h\left(\frac{l_{emb}}{2} - a\right) \tag{2.59}$$

Substituting equations (2.52) through (2.58) into the above equation and simplifying, therefore:

$$\frac{1}{2}F^2 + \alpha\beta f_C' b_f \left(\mu d_p + 2L + l_{emb}\right) F - \left(\alpha\beta f_c' b_f\right)^2 \left(\frac{Pd_p}{\alpha\beta f_c' b_f} + \frac{l_{emb}{}^2}{2} + \mu l_{emb} d_p\right) = 0 \tag{2.60}$$

Solving this quadratic equation for F gives:

$$\frac{F}{\alpha\beta f_c' b_f d_p} = \left(\mu + \frac{2L}{d_p} + \frac{l_{emb)}}{d_p}\right)\left(1 \pm \sqrt{1 + \frac{2\left(\frac{Pd_P}{\alpha\beta f_c' b_f} + \frac{l_{emb}{}^2}{2} + \mu l_{emb} d_p\right)}{\left(\mu d_p + 2L + l_{emb}\right)^2}}\right) \tag{2.61}$$

Expanding the square root term in the above equation using the binomial theorem permits further simplification, and by taking only the negative root leads to the following expression for the lateral force F:

$$F = \frac{\alpha\beta P + \alpha\beta f_c' b_f d_p \left[\frac{1}{2} \left(\frac{l_{emb}}{d_p} \right)^2 + \mu \frac{l_{emb}}{d_p} \right]}{\mu + 2\left(\frac{L}{d_p} \right) + \left(\frac{l_{emb}}{d_p} \right)} \tag{2.62}$$

in which d_p = depth of the H-pile section; b_f =width of the H-pile section; l_{emb} = embedment depth into the concrete cap; α = average concrete stress ratio; and β = stress block depth factor. The residual moment capacity of the connection is given by:

$$M_j = F(L + l_{emb} - a) = Fd_p \left[\left(\frac{L}{d_p} \right) + \frac{1}{2} \left(\frac{l_{emb}}{d_p} \right) + \frac{F}{2\alpha\beta f_c' b_f d_p} \right] \tag{2.63}$$

Substituting the value of F from equation 2.62 into equation 2.63 and simplifying gives:

$$M_j = \frac{0.5\alpha\beta f_c' b_f d_p{}^2 \left[\frac{f_y A_P}{f_c' b_f d_p} \left(\frac{P}{P_y} \right) + \frac{1}{2} \left(\frac{l_{emb}}{d_p} \right)^2 + \mu \left(\frac{l_{emb}}{d_p} \right) \right] \left[\frac{f_y A_P}{f_c' b_f d_p} \left(\frac{P}{P_y} \right) + 4 \left(\frac{L}{d_p} \right)^2 + 2\mu \left(\frac{L}{d_p} \right) + 2\mu \left(\frac{l_{emb}}{d_p} \right) + 4 \left(\frac{L}{d_p} \right) \left(\frac{l_{emb}}{d_p} \right) + \frac{3}{2} \left(\frac{l_{emb}}{d_p} \right)^2 \right]}{\left[\mu + 2\left(\frac{L}{d_p} \right) + \left(\frac{l_{emb}}{d_p} \right) \right]^2} \tag{2.64}$$

Introducing the connection efficiency definition and substituting in equation 2.64, the post-ultimate efficiency is evaluated as:

$$\rho = \frac{\frac{0.5\alpha\beta f_c' b_f d_p{}^2}{f_y Z_P} \left[\frac{f_y A_P}{f_c' b_f d_p} \left(\frac{P}{P_y} \right) + \frac{1}{2} \left(\frac{l_{emb}}{d_p} \right)^2 + \mu \left(\frac{l_{emb}}{d_p} \right) \right] \left[\frac{f_y A_P}{f_c' b_f d_p} \left(\frac{P}{P_y} \right) + 4 \left(\frac{L}{d_p} \right)^2 + 2\mu \left(\frac{L}{d_p} \right) + 2\mu \left(\frac{l_{emb}}{d_p} \right) + 4 \left(\frac{L}{d_p} \right) \left(\frac{l_{emb}}{d_p} \right) + \frac{3}{2} \left(\frac{l_{emb}}{d_p} \right)^2 \right]}{\left[\mu + 2\left(\frac{L}{d_p} \right) + \left(\frac{l_{emb}}{d_p} \right) \right]^2} \tag{2.65}$$

in which; A_P= cross-sectional area of the H-pile section; f_y=the yield stress of the steel material, P_y= the axial yielding load of the H-pile; Z_P= the plastic section modulus of the H-pile; f'_c= the compressive strength of concrete; and μ= coefficient of friction between the steel and concrete.

It is of great significance to investigate the connection efficiency at different values of $\alpha\beta$. Based on piecewise stress-strain model, Mander et al (1998) suggested three equations for $\alpha\beta$, taking into account the concrete deterioration at late load stages. The first equation is used for strains $\varepsilon_{cu} < \varepsilon'_c$:

$$\alpha\beta = \left[1 + \frac{(1-x)^{n+1}}{(n+1)x} - \frac{1}{(n+1)x}\right] \tag{2.66}$$

Where $n = \frac{E_c \varepsilon'_c}{f'_c}$, x= $\frac{\varepsilon_{cu}}{\varepsilon'_c}$, E_c= modulus of elasticity of concrete, ε_{cu} = the maximum fiber strain in concrete, and, ε'_c= the strain corresponding to the compressive strength f'_c.

The second equation is used for $\varepsilon_{cu} \le \varepsilon'_c \le \left(\varepsilon'_c + \frac{0.8}{z}\right)$

$$\alpha\beta = \left(\frac{n}{(n+1)x}\right) + \left(1 - \frac{1}{x}\right)(1 - 0.5z\varepsilon_{cu}(x-1)) \tag{2.67}$$

The third equation is used when $\varepsilon_{cu} \ge \left(\frac{0.8}{z}\right) + \varepsilon'_c$

$$\alpha\beta = \left(\frac{n}{(n+1)x}\right) + \frac{0.48}{z\varepsilon_{cu}} + 0.2\left(1 - \frac{x_0}{x}\right) \tag{2.68}$$

Where z = slope of the descending branch of stress-strain curve of concrete given as, $z = 6.8f'_c$, and $x_0 = \frac{0.8}{z\varepsilon'_c} + 1$.

Equations 2.66 through 2.68 are plotted in figure 2.20a. Three significant values for $\alpha\beta$ can be adopted from that figure. First, at a value of $\alpha\beta$ =0.72 and ε_{cu} = 0.003, case of conventional lateral load, the connection has its full capacity, consequently, the efficiency can be taken as a maximum. Only slight damage due to some crushing will be noticed for this implied level of concrete strain.

Secondly, after applying loading at moderately large drifts, the maximum concrete strain can be estimated as ε_{cu} = 0.014. A corresponding value of $\alpha\beta$ =0.36 is obtained, that is one-half of the initial value. Thirdly, at a strain of 0.055 a value of $\alpha\beta$=0.24 is obtained; one third the maximum. These second and third strain levels represent moderate and heavy damage to the connections, respectively.

By applying the above criteria , the efficiency for different damage levels is observed. This result is evidenced in figure 2.20b where the ratio l_{emb}/d_p was plotted versus the connection efficiency for the three values of $\alpha\beta$. The figure shows that the connection will initially survive under conventional lateral loads, because ρ >1. But because the member will exhibit hardening so that M > M_j, then further damage will occur.

The relationship of ρ for various values of P/P_y and L/d_p is expressed graphically in figure 2.21. It can be concluded from that figure, that for values of $L/d_p \geq 2$, the post-ultimate connection efficiency ρ, remains essentially constant. Therefore substituting this value into equation 2.61 leads to the following simplified expression of ρ:

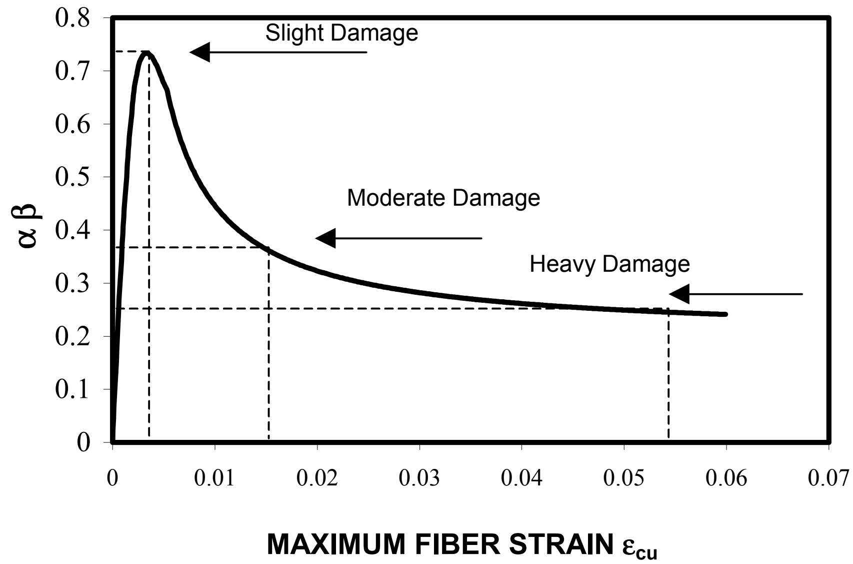

(a) Stress Block Parameters Concrete Strain Relationship

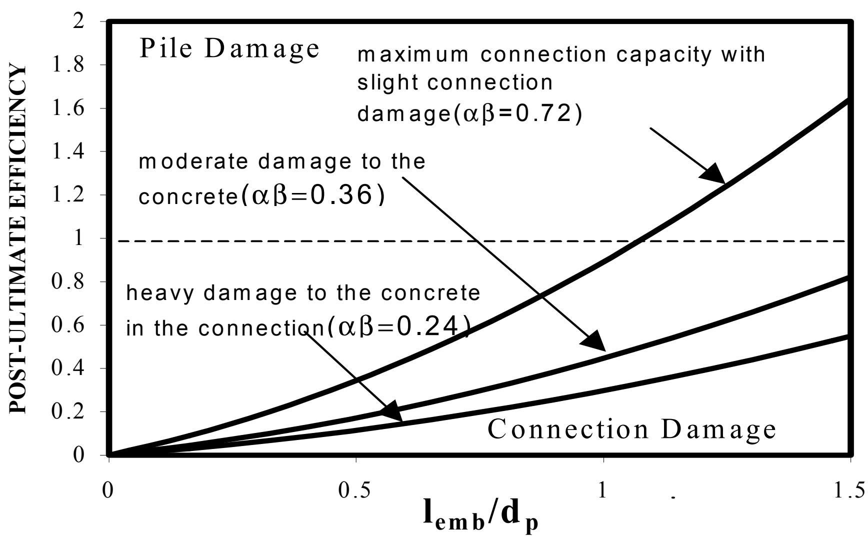

(b) Efficiency in terms of stress Block Parameters

Figure 2.20 Relationship between the Post-Ultimate Efficiency and the Concrete Stress Block Factors

$$\rho=\frac{\dfrac{0.5\alpha\beta f_c' b_f d_p^{\,2}}{f_y Z_P}\left[\dfrac{f_y A_P}{f_c' b_f d_p}\left(\dfrac{P}{P_y}\right)+\dfrac{1}{2}\left(\dfrac{l_{emb}}{d_p}\right)^2+\mu\left(\dfrac{l_{emb}}{d_p}\right)\right]\left[\dfrac{f_y A_P}{f_c' b_f d_p}\left(\dfrac{P}{P_y}\right)+\dfrac{3}{2}\left(\dfrac{l_{emb}}{d_p}\right)^2+(8+2\mu)\left(\dfrac{l_{emb}}{d_p}\right)+4\mu+16\right]}{\left[\left(\dfrac{l_{emb}}{d_p}\right)+\mu+4\right]^2} \qquad (2.69)$$

Substitution with $\mu = 0.6$, l_{emb}=*300mm* for as-built connections, and properties of section 10x42 in equation (2.65) leads to:

$$\rho = \frac{\alpha\beta}{2}\left[1.5\frac{f_c' b_f d_p^2}{f_y Z_p} + \left(\frac{P}{P_y}\right)\left(\frac{A_p d_p}{Z_p}\right)\right] \qquad (2.70)$$

The connection efficiency was evaluated, for different values of $\alpha\beta$, using the exact equation (2.65), the approximate equation (2.69), and the simplified equation (2.70). Results are shown in figure 2.22. Compared to the exact equation, the simplified equation is slightly conservative while the approximate equation gives results that are satisfactory. It is recommended that this equation (2.70) be used to analysis/seismic evaluation purposes.

Figure (2.23) presents some design guidelines for these connections under both horizontal and vertical loads, according to the plastic theory presented in this study. The figure indicates that the presence of the compressive vertical load increases (slightly) the efficiency of the connections. Conversely, tension uplift for exterior piles may reduce its efficiency for a certain lateral load. The figure suggests that the failure mode of all the pile-to-cap connections designed for *300mm* embedment will be a non-ductile concrete cap failure, as the average efficiency is 0.6.

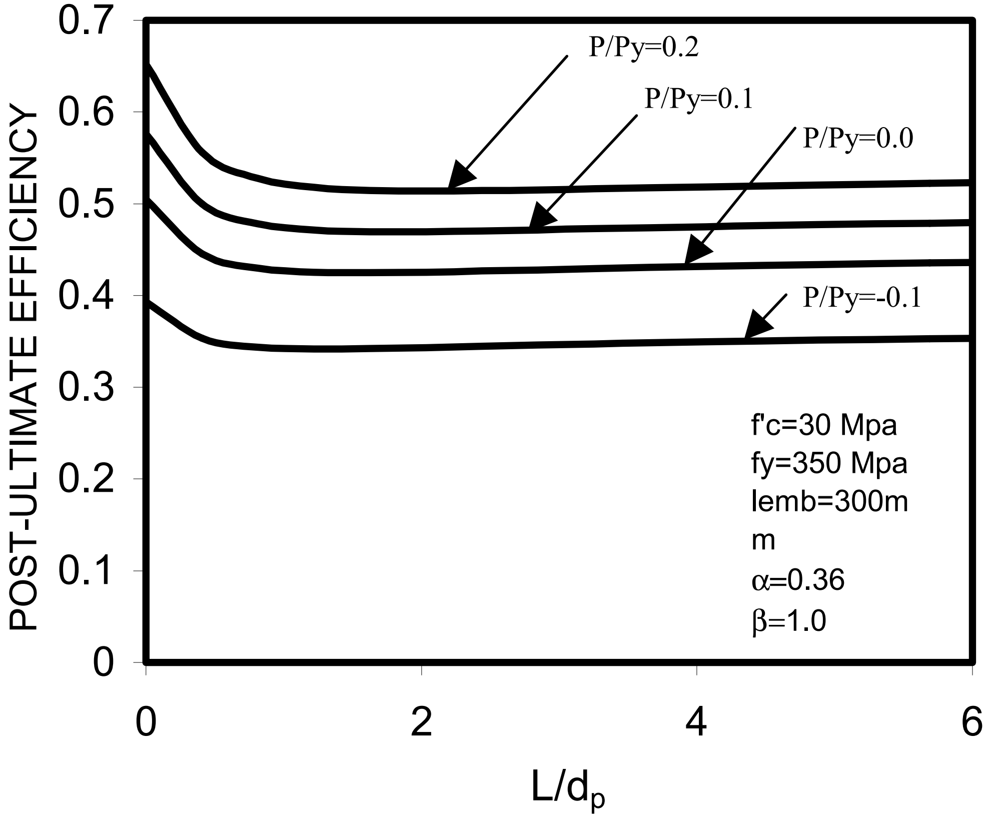

Figure 2.21 Effect of Effective length on the Post -Ultimate Connection Efficiency for As-Built Specimens

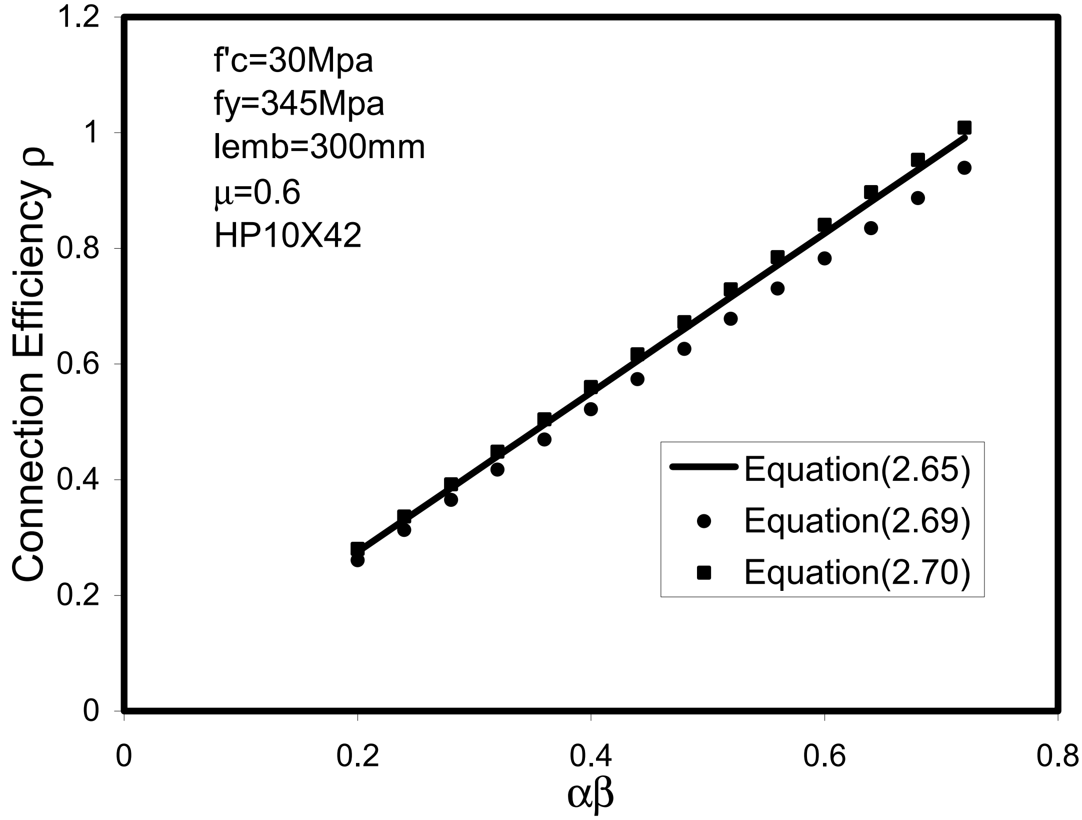

Figure 2.22 Connection Efficiency Stress Block Factors Relationship

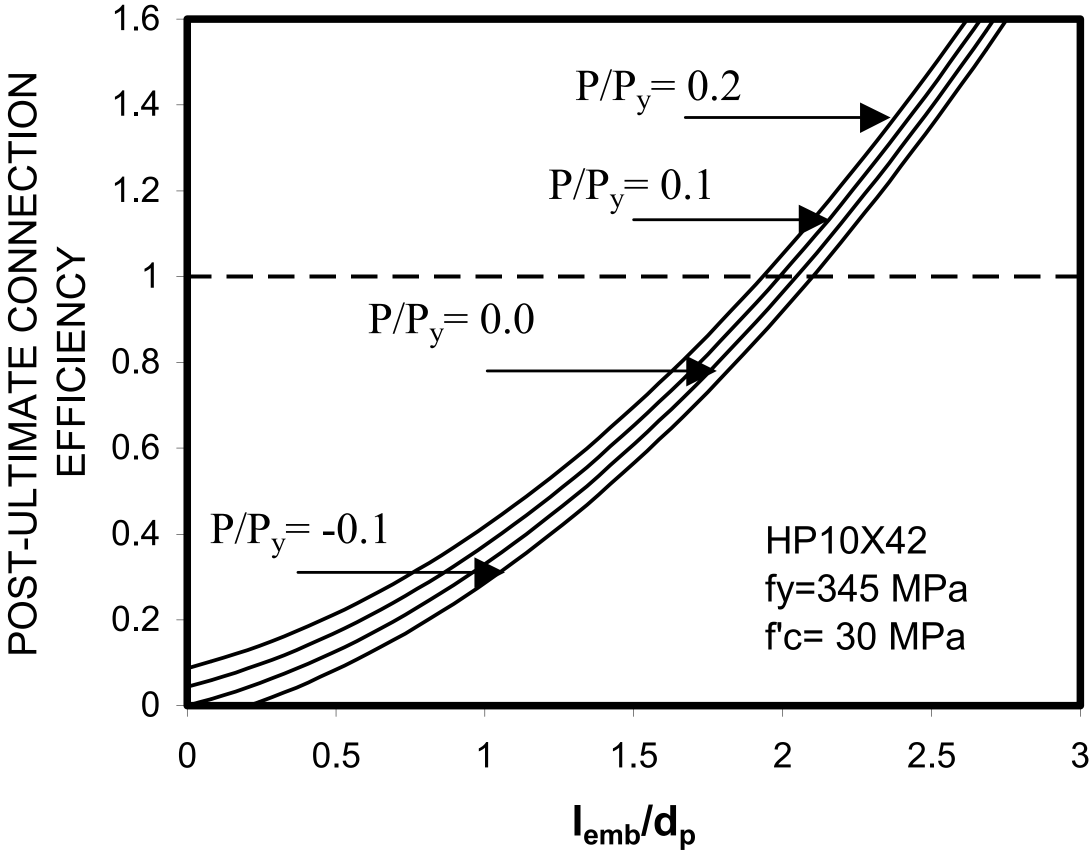

Figure 2.23 Post-Ultimate Connection Efficiency For Different Axial Load Levels

2.7 Retrofit Requirements and Design Philosophy

2.7.1 Retrofitting Needs

Based on design drawings collected from Ohio, North Carolina, and Louisiana State Departments of Transportation, the following observations were made concerning design and construction practice of pile-to-cap connections for both pile bents, and piled foundation structures:

(i) A 300 mm embedment depth for the pile into the cap is a common construction feature.

(ii) Cap beams are not provided with additional reinforcement to resist lateral loads.

(iii) Some minimal shear and confining reinforcement in the pile embedment region is used for the case of pile bents.

(iv) Some designs aligned the strong axis of the piles with the longitudinal axis of cap beam, while others used the weak axis.

(v) Most designs use battered exterior piles to increase the lateral resistance of the pile group.

The aforementioned observations suggest a possible vulnerability exists. One may expect cap beams to be damaged under the lateral loads that would arise during seismic events. To avoid damage, seismic strengthening of the pile-to-cap connection is necessary. Therefore, the goal is to develop practical and economical seismic retrofit measures to maintain a serviceable connection during earthquakes. Two basic approaches are available for the retrofit of these connections. The first approach is applicable only for steel pile bents. The second approach, however, is applicable for both pile bents and pile foundations. These approaches are:

1. Reduction of the seismic forces that can be developed in the cap beam during seismic events.
2. Increasing the cap beam strength to the level required to shift the plastic hinge location to the steel pile rather than the concrete cap. Hence, ensure better ductile connection that can possess large deformation capability and permit much more dissipation of seismic energy.

The first method can be achieved by connecting the bent piles with a link beam as shown in figure 2.24. The location of the link beam can be adapted so that the final moment at the connection will be less than both the nominal moment capacity of the concrete beam and the plastic moment capacity of the steel H-pile. The merit of this method is that it can be accomplished without traffic disruption. The approach has been used in California in the retrofit of Santa Monica Viaducts (Priestley et al 1997). This method will not be explored further here and is out the scope of the present study.

A conceptual elastic cap/elasto-plastic pile retrofit strategy, consistent with the second approach, is adopted in the present research. Two retrofit methodologies are presented using the two theories developed in the present study. These methodologies are illustrated in what follows.

2.7.2 Retrofit Methodology Based on Plastic Theory

A simplified version of the general plastic mechanism (figure 2.19b) will be adopted here. The additional retrofit depth needed could be evaluated through this mechanism. The design curves, in figure 2.23, based on the rigorous general model, can then be used to check this depth in terms of efficiency. In this mechanism it will be assumed that the stress block force couple C_m will resist the external applied moment to the connection. Therefore, the stress block force C_m can be evaluated as:

$$C_m = 0.5\alpha\beta f_c' b_f l_{emb} \tag{2.71}$$

and the lever arm can be determined as:

$$jd = l_{emb}(1 - 0.5\beta) \tag{2.72}$$

By assuming $\beta = 1$, then jd can be taken as 0.5 l_{emb}. The moment strength of the connection can now be determined as:

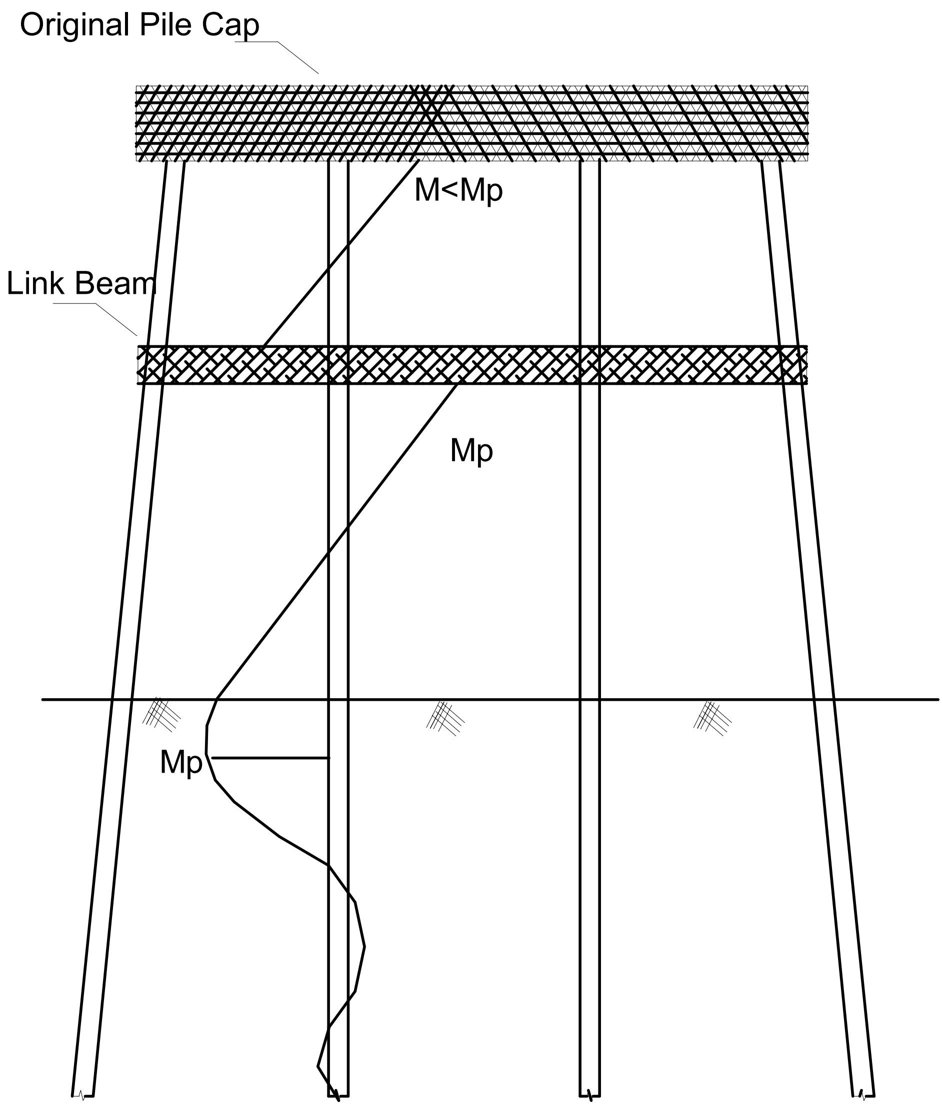

Figure 2.24 Retrofit of Steel Pile Bents with Link Beams

$$M_j = \phi C_m jd \tag{2.73}$$

Where ϕ = strength reduction factor. Substitute equation (2.71) and (2.72) in (2.73) therefore

$$M_j = 0.25\,\phi\alpha\beta f'_c b_f l_{emb}^{\ 2} \tag{2.74}$$

if $\alpha\beta$ is taken as 0.36 and ϕ =0.90, further simplification for equation (2.74) leads to:

$$M_j = 0.08 f'_c b_f l_{emb}^{\ 2} \tag{2.75}$$

To ensure that plastic hinges will not occur at cap beam, the following condition should be satisfied:

$$M_j \geq M_{po} \tag{2.76}$$

where M_{po} is the over strength plastic moment capacity of the steel H-pile section. Therefore:

$$0.08 f'_c b_f l_{emb}^{\ 2} \geq M_{po} \tag{2.77}$$

and hence

$$l_{emb} \geq \sqrt{\frac{12.5 M_{po}}{f'_c b_f}} \tag{2.78}$$

Further simplifications of equation (2.78) can lead to the following expression for the total embedment depth:

$$\frac{l_{emb}}{d_p} \geq 3.5\sqrt{\left(\frac{f_{su}}{f_c'}\right)\left(\frac{t_f}{d_p}\right)} \tag{2.79}$$

Therefore, the additional embedment depth needed is:

$$l_{ad} = l_{emb} - l_{ab} \tag{2.80}$$

where l_{ab} = the embedment depth for the as built structure.

The embedment depth obtained using the plastic theory in equation (2.79) is basically the same as the one obtained using the elastic theory in equation (2.49). This outcome is explained by considering the concrete stress strain relationship. The cracked elastic theory is based on the behavior of the concrete in the linear part of the curve. Consequently, it accounts for strains in the range less than 0.003. The plastic theory, however, accounts for the concrete deterioration and hence is based on the behavior of concrete after it reaches its compressive strength. Accordingly, it accounts for high strain levels in the range greater than 0.01. Taking into consideration these two assumptions, one can obtain a specific value of stress corresponding to these two values for the strain.

Additional design considerations are required to account for the effects of reversed cyclic loading. Under cyclic loading a gap is expected to occur at the pile flange-concrete interface. If the opening of that gap is not controlled, it may affect the hysteretic response of the connection, and hence its energy absorption. It is, therefore, necessary to provide sufficient horizontal reinforcing bars crossing the pile-concrete interface (see figure 2.25a). This steel can be chosen such that its area has a yield force equal to the plastic shear capacity of the pile section. Thus, the area of steel required is

$$A_s = \frac{V_p}{\phi f_{yh}} \tag{2.81}$$

Where, V_p = the shear capacity of the pile section, f_{yh} = the yield stress of reinforcing rebars. Horizontal stirrups are provided to counteract shear forces and to provide horizontal confinement

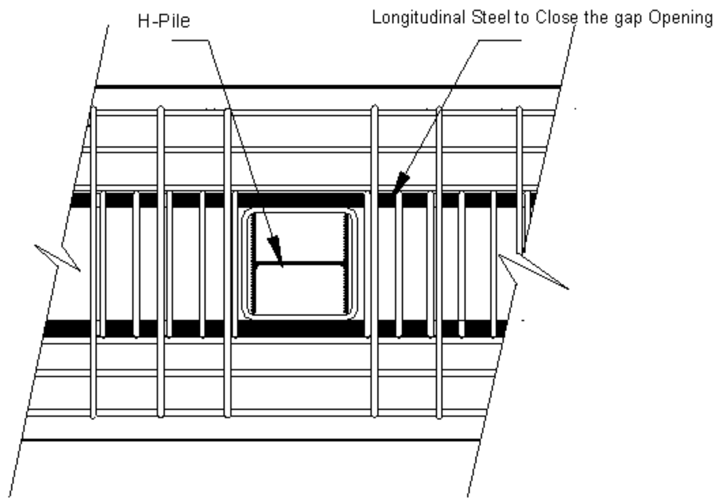

(a) Horizontal Bars Crossing the Pile-Concrete Interface

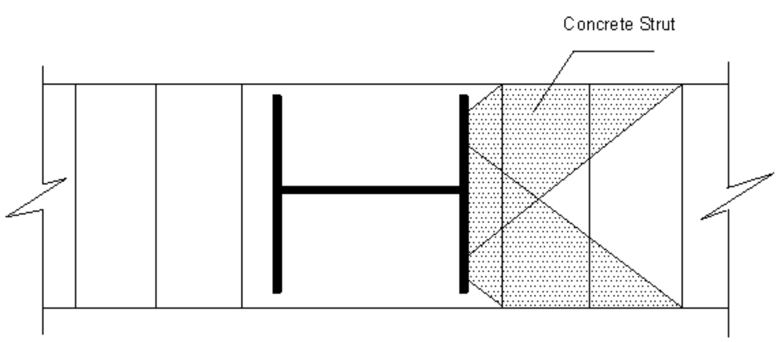

(b) Concrete Struts act at 45°to deliver shear forces to stirrups

Figure 2.25 Additional steel Required For The Retrofit of Pile bent-to-Cap Connection

or lateral load. Shear forces are assumed to provide a strut and tie actions. Concrete struts are assumed to act at 45^{o} to deliver the required shear force to a number of stirrups (figure 2.25b). The force in each hoop can be determined by the following equation:

$$V_{st} = \frac{0.50V_p}{n} \tag{2.82}$$

Assume all stirrups are yielded, therefore each one will carry a force of $A_v f_{yh}$, where A_v is the area of one stirrup, therefore:

$$A_v = \frac{V_{st}}{f_y} \tag{2.83}$$

2.7.3 Joint Shears and Direct Tensions

Additional reinforcement is required to prevent a gap beginning to open and subsequent spalling of concrete at edge piles under cyclic loading. Therefore, assume that the tension force in the steel rebars will resist the moment capacity of the connection, i.e. the plastic moment capacity of the steel H-pile section in figure 2.26, then

$$M_p = Tjd = \frac{2}{3}Tl_{emb} \tag{2.84}$$

and hence:

$$T = A_s f_{yh} = 1.5\frac{M_p}{l_{emb}} \tag{2.85}$$

Therefore the area of steel required can be quantified as:

$$A_s = \frac{1.5f_{su}Z_p}{f_{yh}l_{emb}}$$

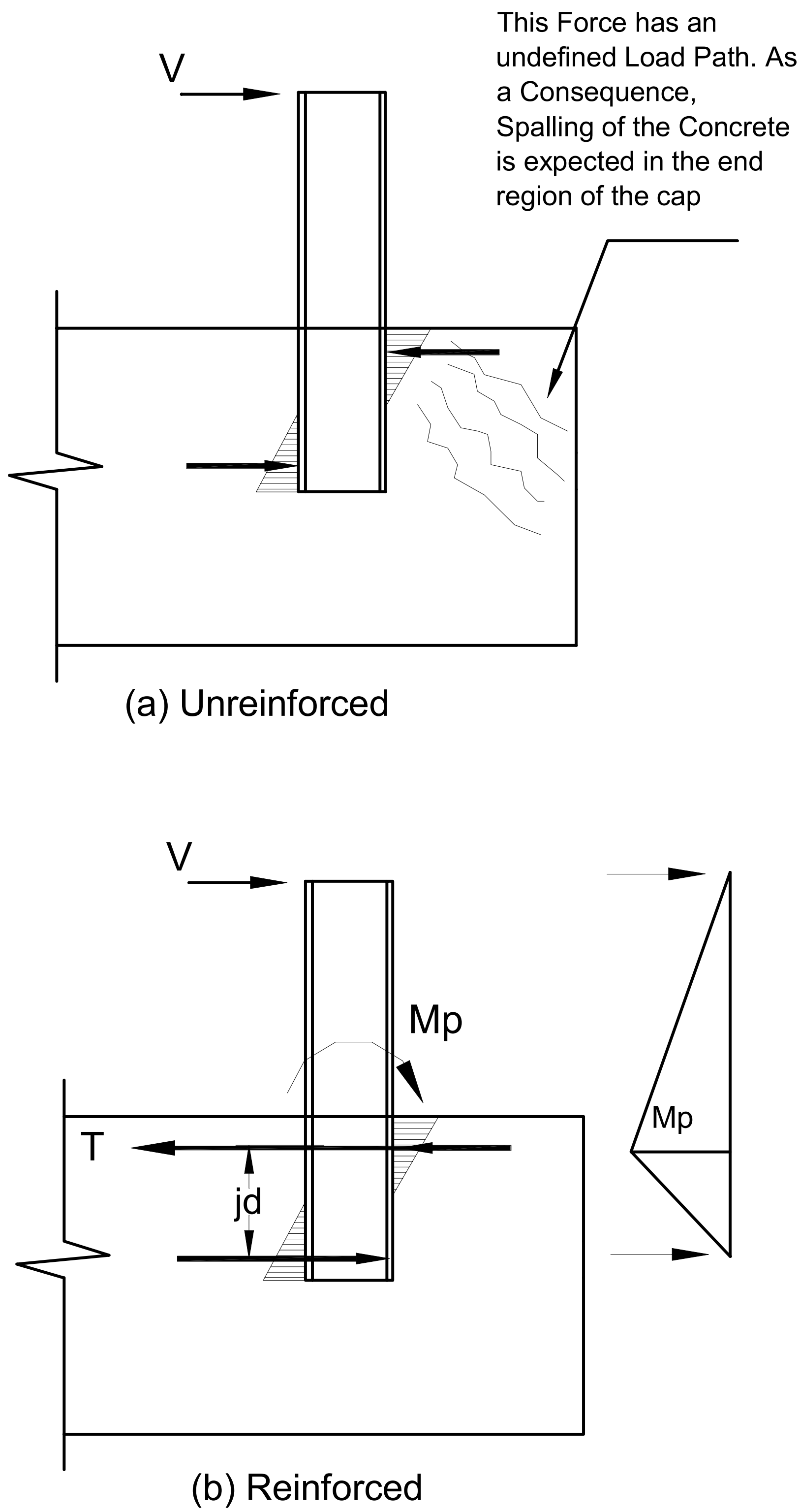

Figure 2.26 Steel Required for Edge Piles

in which f_{su} = the ultimate stress of the h-pile steel section that gives the overstrength demand $(Z_p f_{su})$.

2.8 Expected Performance Of The Substructure

A theory is developed to determine theoretically the behavior of the HP steel piles under monotonic loading. The theory and an algorithm to predict the lateral force-displacement relationship are summarized in what follows.

Consider a pile under forces and reactions in figure 2.27a. The total elastic displacement according to that load can be divided to two portions, lever arm elastic displacement, and elastic joint deformation. Hence, the total elastic displacement can be expressed as:

$$\Delta_e = \frac{M_{max} L^{*2}}{3EI} + \frac{M_{max}}{2EI} L_a L^* \tag{2.86}$$

in which Δ_e = the total elastic displacement; M_{max} = the maximum applied moment at critical section as shown in figure 2.27b; E and I = the modulus of elasticity and moment of inertia of the pile, L_a = the distance between points of reactions of the stress blocks within the embedded part, and L^* = the actual lever arm of the pile.

If the distribution of the plastic curvature along the plastic hinge in figure 2.27c can be approximated to two triangles, the plastic rotation can be quantified approximately as:

$$\theta_p = \frac{1}{2}\phi_p\left(1 - \frac{M_y}{M_{max}}\right)\left(L^* + L_a\right) \tag{2.87}$$

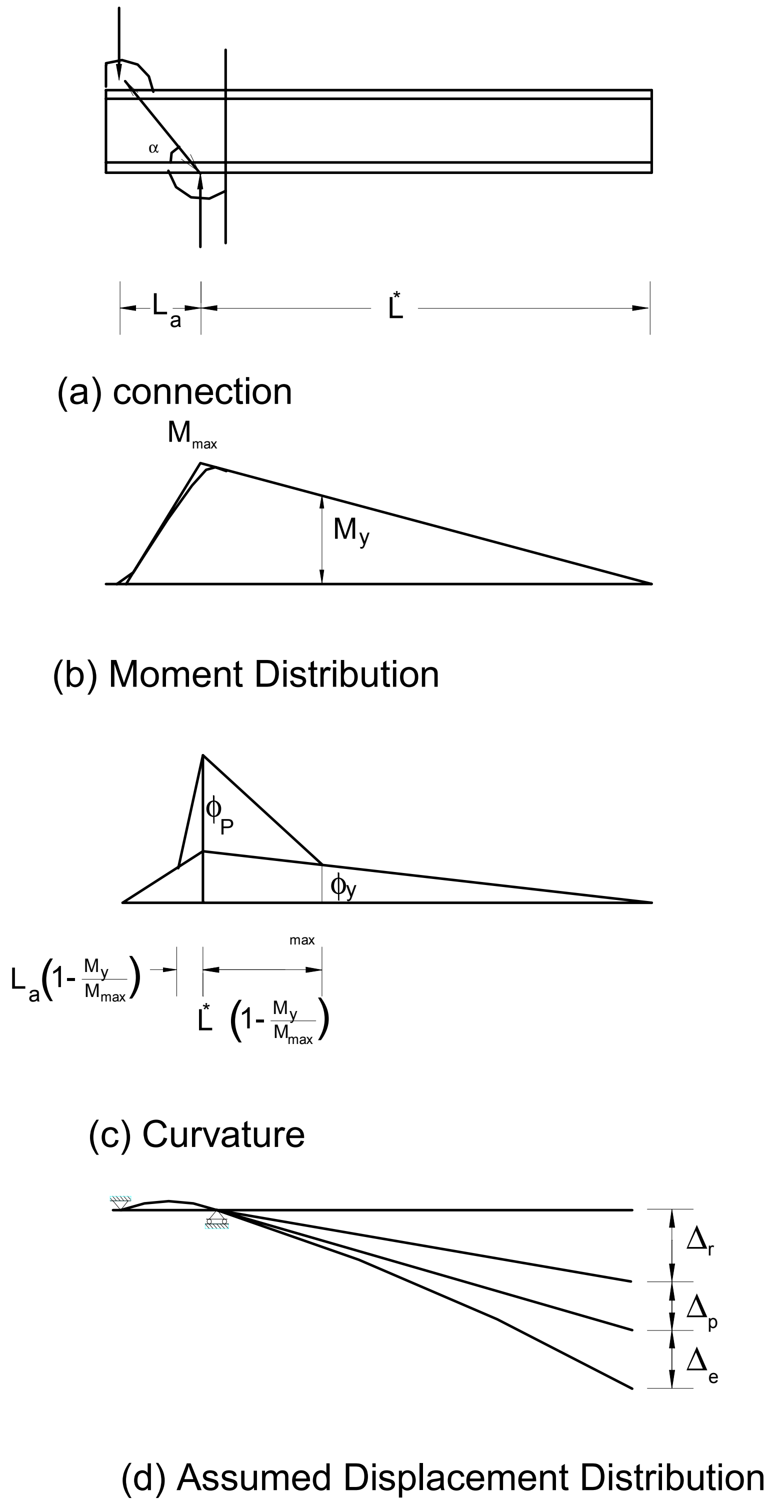

Figure 2.27 Assumed Distribution of Moments and Curvatures

where, ϕ_p = the plastic curvature corresponding to the applied moment; and M_y = the yielding moment of the HP steel section expressed as:

$$M_y = S_x f_y \tag{2.88}$$

where S_x and f_y are the elastic section modulus and the yield stress of the steel pile section. Therefore, the plastic deformation can be quantified as:

$$\Delta_p = \theta_p L \tag{2.89}$$

in which $\theta_p =$ the plastic rotation due to plastic deformation, and L is the length from the point of application of load to the concrete surface. Substitute equation (2.87) in (2.89) and simplify therefore the plastic deformation can be expressed as:

$$\Delta_p = \frac{\phi_p}{2} L^2 \left(1 - \frac{M_y}{M_{max}}\right)\left(1 + \frac{l_{emb}}{L}\right) \tag{2.90}$$

where, l_{emb} = the embedment depth of the specimen. The plastic curvature corresponding to the applied moment can be obtained explicitly from the moment curvature relationship as shown in what follows.

2.8.1 Moment-Curvature Analysis

Moment curvature analysis has two objectives, to compare with experimental results, and to write an analytic polynomial function that describes the plastic portion of the M-ϕ diagram. That polynomial will be employed later in the determination of the plastic curvature corresponding to the applied moment.

The moment-curvature analysis of the steel section under combined axial load P and bending moment, M requires the section to be divided into a number of segments (figure2.28), and for the purpose of integration , each segment can be divided to a number of nodal points according to the integration scheme to be used for the evaluation of the force in each segment. For each segment, the strain within each node can be evaluated according to the following equation:

$$\varepsilon_{i,j} = \phi\, y_{i,j} + \varepsilon_0 \tag{2.91}$$

where ε_0 = the strain at the centroidal axis, $\varepsilon_{i,j}$ = the strain at node i located at segment j, and $y_{i,j}$ = the distance from node i to the centroidal axis of the section. Hence, for a given strain profile, the stresses can be determined for each segment from which the axial load P and the bending moment M on the section can be calculated as follows:

$$P = \sum_{I=1}^{n} f_{S_{i,j}} A_{S_{i,j}} \tag{2.92}$$

$$M = \sum_{i=1}^{n} f_{S_{i,j}} A_{S_{i,j}} y_{i,j} \tag{2.93}$$

where n = number of segments, $f_{S_{i,j}}$ = the stress at node I located in segment j, and $y_{i,j}$ = the distance from the centroidal reference axis to the node i. In the present study, the strain-hardened relation proposed by Chang and Mander (1994) was employed to express the stress as a function of strain:

$$f_s = \frac{E_s \varepsilon_s}{\left\{1 + \left|\dfrac{E_s \varepsilon_s}{f_y}\right|^{10}\right\}^{0.1}} + \frac{1 + \mathrm{Sgn}(\varepsilon_s - \varepsilon_{sh})}{2}(f_{su} - f_y)\left[1 - \left|\frac{\varepsilon_{su} - \varepsilon_s}{\varepsilon_{su} - \varepsilon_{sh}}\right|^{\kappa}\right] \tag{2.94}$$

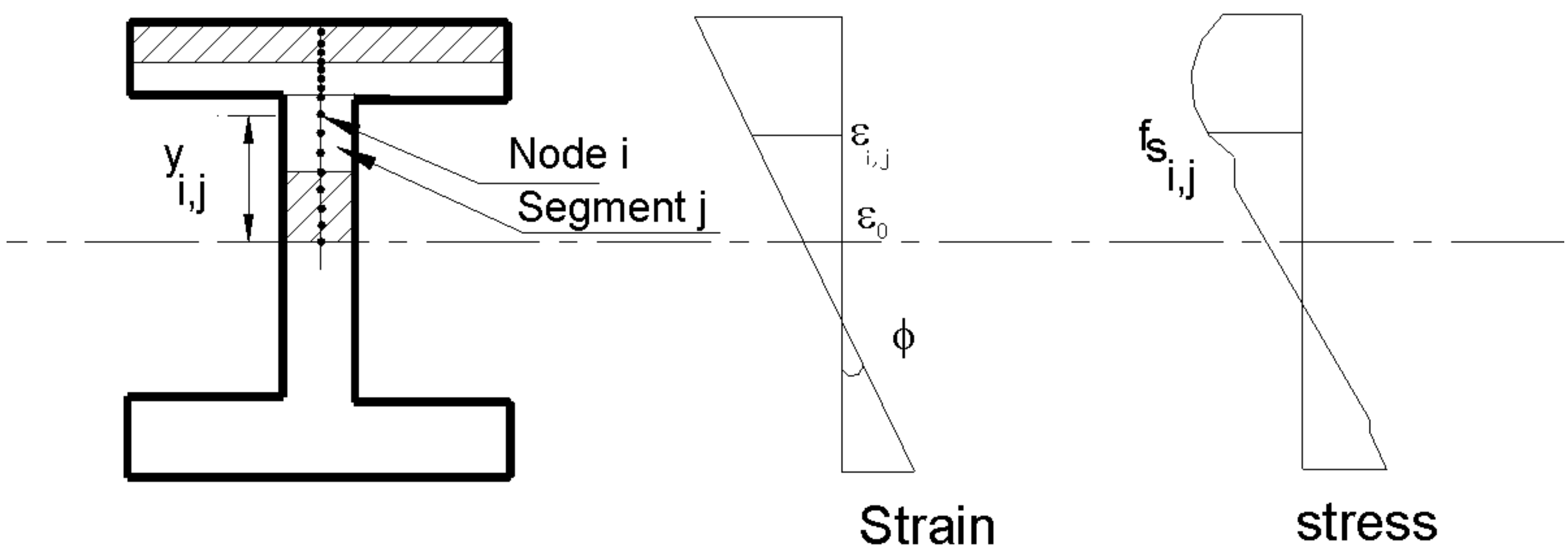

Figure 2.28 Integration Scheme for Moment Curvature Analysis

where the power κ is given by the ratio of the initial strain hardening modulus and the secant modulus between initial strain hardening point (f_y, ε_y) and the ultimate stress (f_{su}, ε_y):

$$\kappa = E_{sh} \frac{\varepsilon_{su} - \varepsilon_{sh}}{f_{su} - f_y} \tag{2.95}$$

in which, E_s = Young's modulus, ε_s = strain for any specified curvature value, f_y = yield stress of steel, ε_{sh} = strain-hardening strain, ε_{su} = strain at ultimate stress, and E_{sh} = strain-hardening modulus.

Solution of equations (2.91) and (2.92) simultaneously requires an iterative procedure where incremental forces (ΔM, ΔP) are related to incremental deformations ($\Delta\phi$, $\Delta\varepsilon_0$) by the instantaneous section stiffness, thus:

$$\begin{bmatrix} \Delta M \\ \\ \Delta P \end{bmatrix} = \begin{bmatrix} E_T I & E_T Z \\ \\ E_T Z & E_T A \end{bmatrix} \begin{bmatrix} \Delta\phi \\ \\ \Delta\varepsilon_0 \end{bmatrix} \tag{2.96}$$

The section stiffness coefficients E_TA and E_TZ are determined as follows:

$$E_T A = \sum_{i=1}^{n} E_{s_{i,j}} A_{S_{i,j}} \tag{2.97}$$

$$E_T Z = \sum_{i=1}^{n} E_{s_{i,j}} A_{S_{i,j}} y_{S_{i,j}} \tag{2.98}$$

where $E_{S_{i,j}}$ = current modulus of elasticity of the ith node within the jth segment , instateneous across the section.

Based upon the the theory presented , the solution algorithm can be summarized in the following steps:

(i) To the value of previous solution (ϕ_{n-1}) add the increment to give the new section curvature ϕ_n

(ii) From the out of balance force ΔP from previous step (if any) find the change in centroidal strain

$$\Delta\varepsilon = \frac{\Delta p - E_T Z \Delta\phi}{E_T A} \tag{2.99}$$

Therefore

$$\varepsilon_{0_n} = \varepsilon_{0_{n-1}} + \Delta\varepsilon_0 \tag{2.100}$$

(iii) For the new strain profile, calculate the new axial load P_n; and moment M_n using equations (2.92) and (2.93)

(iv) Determine the effective stiffness coefficients $E_T A$ and $E_T Z$ using equations (2.97) and (2.98).

(v) Check for out of balance force:

$$\Delta P = P_{target} - P_n \tag{2.101}$$

if the absolute value of ΔP is greater than a certain specified tolerance go to step (ii) otherwise go to step (i).

Proceeding with the above algorithm with different incremental values for curvature, a moment curvature relationship can be evaluated. Such a relationship for HP 10X42 section is shown in figure 2.30a.

With reference to the local x, y axis shown in figure 2.29, the plastic portion of the moment curvature relationship can be expressed as a polynomial :

$$y = ax^n \tag{2.102}$$

where x and y are determined as follows:

$$x = \phi_{pu} - \phi_p \tag{2.103}$$

in which ϕ_{pu} = the curvature at ultimate moment, and ϕ_p = curvature at the applied moment M.

$$y = \frac{M_{pu}}{M_y} - \frac{M}{M_y} \tag{2.104}$$

where M_{pu} = the ultimate moment of the HP steel section can be expressed as:

$$M_{pu} = f_{su} Z_p \tag{2.105}$$

where f_{su}, and Z_p are the ultimate stress and plastic modulus of the HP steel pile respectively. Solving for the coefficient a in equation (2.102) when ϕ_p = 0, and M =M_y gives:

$$a = \frac{\frac{M_{pu}}{M_y} - 1}{\phi_{pu}{}^n} \tag{2.106}$$

Substituting equation (2.106) into (2.93) a moment-plastic curvature equation can be written in terms of the global axes:

$$M = M_{pu} - (M_{pu} - M_y)\left(1 - \frac{\phi_p}{\phi_{pu}}\right)^n \tag{2.107}$$

Inverting this relationship gives the plastic curvature as a function of moment:

$$\phi_p = \phi_{pu}\left[1 - \left(\frac{M_{pu} - M}{M_{pu} - M_y}\right)^{\frac{1}{n}}\right] \tag{2.108}$$

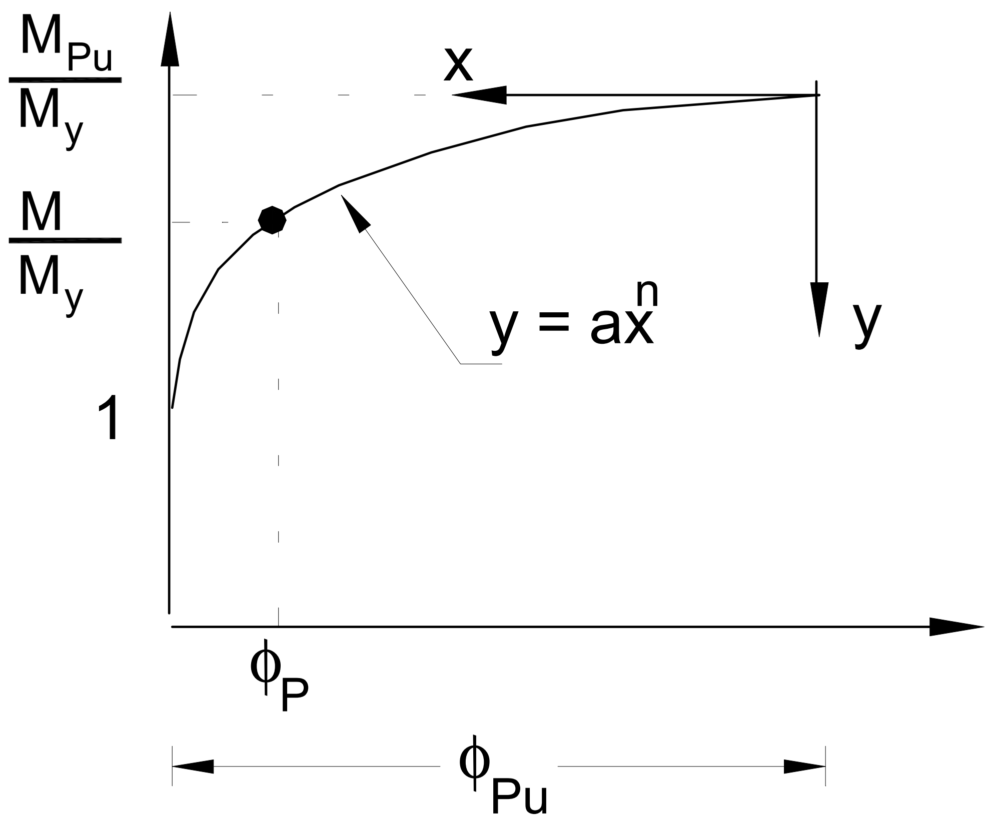

Figure 2.29 Idealization of the Plastic Portion of the Moment-Curvature Curve as a Polynomial

The parameter n can be found by examining several slopes(EI values) on the graph such that :

$$n = \frac{EI_T}{EI_{sec}} \tag{2.109}$$

where EI_T = initial (tangent) slope at the onset of plastification, and EI_{sec} = the secant slope between the start and finish of the plastic section of the moment curvature performance given by:

$$EI_{sec} = \frac{M_{pu} - M_y}{\phi_{pu} - \phi_y} \tag{2.110}$$

Alternatively, the parameter n was evaluated using an iterative procedure, where a preliminary value was proposed for n, and the plastic portion of the M-ϕ curve was generated using the computational algorithm described, and the same curve was calculated using equation (2.108). A specified tolerance was set so that the difference between different values at both curves would not exceed it. The whole process was resumed until the specified tolerance was achieved at all points within the curves. Figure2.30b portrays the plastic portion of the M-ϕ relationship for a HP 10x42 section using the computational algorithm, and using equation (2.104).

The steps involved in evaluating the force-deformation relationship can now be summarized as follows:

Part A:

Perform moment-curvature analysis using the computational algorithm, from which the value of M_{pu}, ϕ_{pu} and n can be determined, or use simplified values.

Part B:

1. Calculate the moment at critical section as a function of the incremental curvature using the moment-curvature algorithm.
2. Determine the elastic displacement using equation (2.86)
3. Determine the plastic curvature as a function of the applied moment using equation (2.108)
4. Determine the plastic displacement using equation (2.90).
5. The total displacement can be obtained as:

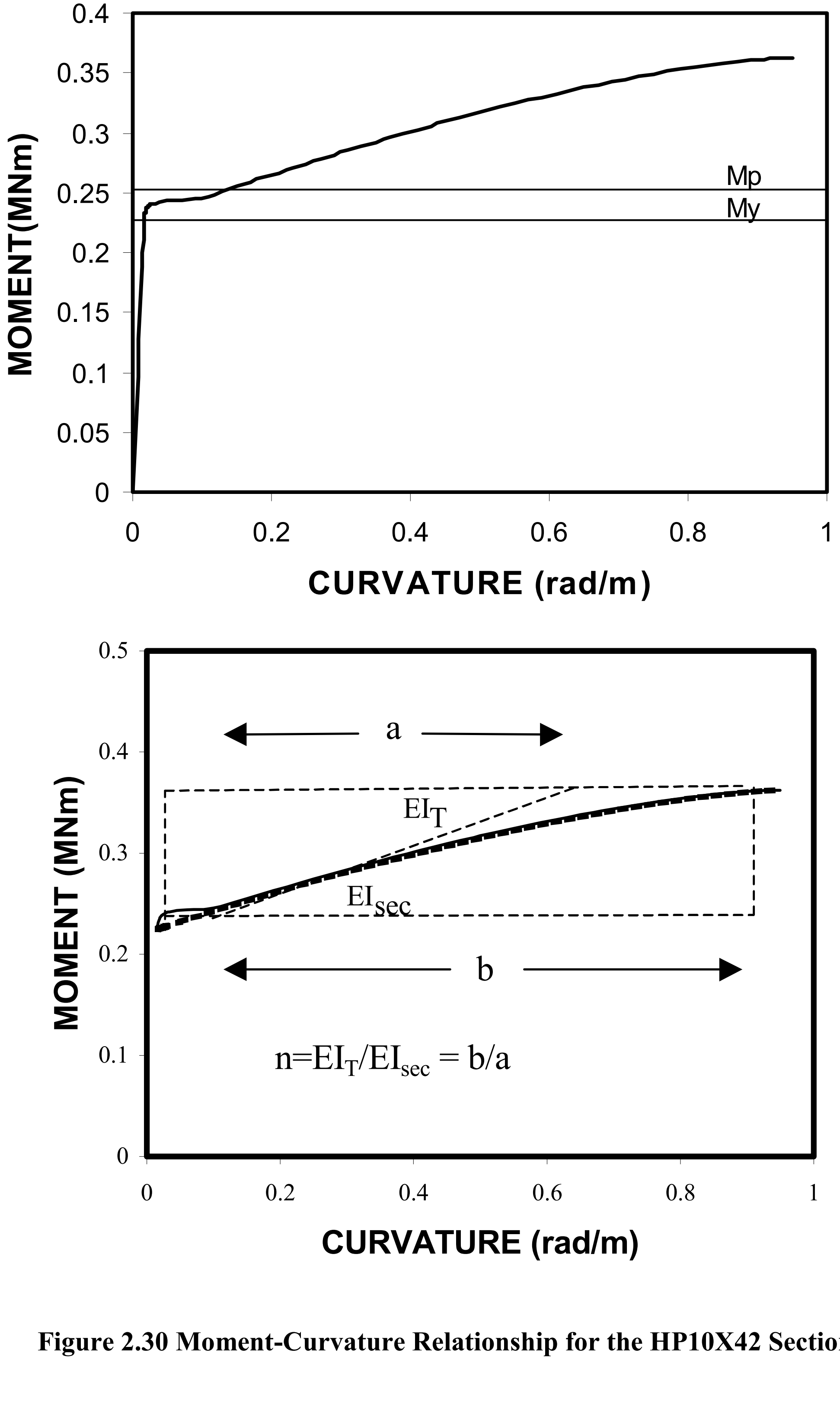

Figure 2.30 Moment-Curvature Relationship for the HP10X42 Section

$$\Delta = \Delta_p + \Delta_e \tag{2.111}$$

7. Determine the lateral force .
8. Choose a new extreme value for the strain, and resume steps from 1 to 7.

The results from the method presented in this section are compared to the experimental results in detail in section 6.

2.9 Theoretical Fatigue Model

Consider the pile under forces and reactions in figure 2.27. If the distribution of the plastic curvature along the plastic hinge can be approximated to two triangles, the plastic rotation can be quantified as:

$$\theta_p = 0.5\phi_p\left(1 - \frac{M_y}{M_{max}}\right)\left(L + d_p \cot\alpha\right) \tag{2.112}$$

where M_y = the yielding moment of the HP steel section; M_{max} = the maximum applied moment; L= clear distance from point of load application to the cap beam surface; l_{emb} = embedment depth of the steel pile into the cap; α = inclination angle for the strut that carries the reaction forces along the embedment depth, can be taken 45^0 and ϕ_p = plastic curvature corresponding to the maximum applied moment , which can be expressed for strong axis bending as:

$$\phi_p = \frac{2\varepsilon_{ap}}{d_p} \tag{2.113a}$$

and for weak axis bending as:

$$\phi_p = \frac{2\varepsilon_{ap}}{b_f} \tag{2.113b}$$

where ε_{ap} = the plastic strain amplitude for the steel section.

The rest of this fatigue-life derivation will be outlined for strong axis specimens; the same approach can be used for weak axis specimens. Substituting equation (2.113) into (2.112) gives:

$$\theta_p = \varepsilon_{ap}\left(1 - \frac{M_y}{M_{max}}\right)\left(\frac{L}{d_p} + \cot\alpha\right) \tag{2.114}$$

A low-cycle fatigue relationship between plastic strain amplitude and fatigue life for uni-axial loaded steel bars was suggested by Mander et al (1994) as the following expression:

$$\varepsilon_{ap} = 0.08\left(2N_f\right)^{-0.5} \tag{2.115}$$

where N_f = the number of reversals to incipient fatigue failure. Substituting equation (2.115) into (2.114), a relation between the plastic rotation and the number of reversals ($2N_f$) can be expressed as:

$$\theta_p = 0.08\left(1 - \frac{M_y}{M_{max}}\right)\left(\frac{L}{d_p} + \cot\alpha\right)\left(2N_f\right)^{-0.5} \tag{2.116}$$

The maximum applied moment can be expressed in terms of the ultimate moment, yield moment, and plastic curvature using equation (2.107)

$$\frac{M_{max}}{M_y} = \frac{M_{pu}}{M_y} - \left(\frac{M_{pu}}{M_y} - 1\right)\left(1 - \frac{\phi_p}{\phi_{pu}}\right)^n \tag{2.117}$$

where the constant n can be evaluated using equations (2.109) and (2.110) as:

$$n = \frac{E_{sh} I_{xx} \phi_{pu}}{M_{pu} - M_y} \tag{2.118}$$

in which E_{sh} = strain hardening modulus; ϕ_{pu} = ultimate plastic curvature; and I_{xx} = strong axis moment of inertia of the section.

Assuming for an I-beam shape the thin web does not contribute significantly to strength, then the yielding moment of the section can be expressed approximately as:

$$M_y = f_y \frac{I_{xx}}{0.5d_p} \approx f_y \frac{b_f d_p^2}{6}\left[1-\left(1-\frac{2t_f}{d_p}\right)^3\right] \approx f_y b_f d_p t_f \tag{2.119}$$

where f_y = the yield stress of the steel pile; b_f = the steel section flange width; t_f = the steel section flange thickness; and d_p = the steel section depth.

The ultimate moment M_{pu} can be determined in a similar fashion as:

$$M_{pu} = f_S Z_x \approx f_{su} \frac{b_f d_p^2}{4}\left[1-\left(1-\frac{2t_f}{d_p}\right)^2\right] \approx f_{su} b_f d_p t_f \tag{2.120}$$

where Z_x = the steel section plastic modulus and f_{su} = ultimate strength of the steel section. Thus from equations (2.119) and (2.120) there is an approximate equivalence between moment overstrength capacity and the stress-strain curve parameters as follows:

$$\frac{M_{pu}}{M_y} \approx \frac{f_{su}}{f_y} \tag{2.121}$$

Substituting equation (2.121) into (2.117) gives:

$$\frac{M_{max}}{M_y} = \frac{f_{su}}{f_y} - \left(\frac{f_{su}}{f_y}-1\right)\left(1-\frac{\varepsilon_{ap}}{\varepsilon_{su}}\right)^n \tag{2.122}$$

Substituting equation (2.121) into (2.118) and further simplification gives:

$$n = \frac{E_{sh}\ \varepsilon_{su}}{f_{su} - f_y} \tag{2.123}$$

Adopting the values obtained from coupon test of the specimens where E_{sh} = 2430 MPa, ε_{su} = 0.15, f_{su} = 475 MPa, and f_y = 315MPa, then from equation (2.123) n = 2.3.

2.9.1 Low-Cycle Fatigue Capacity Evaluation Algorithm

The theory developed in the preceding section is employed to evaluate the low cycle-fatigue capacity of the connections. The procedure is summarized in the following steps:

(i) For the considered steel section, choose the number of cycles $2N_f$.

(ii) Calculate the plastic strain amplitude using the fatigue rule proposed in equation (2.115).

(iii) Determine the plastic curvature using equation (2.113).

(iv) Determine the normalized yielding moment $\frac{M_y}{M_{max}}$ of the connection using equation (2.122).

(v) Determine the plastic rotation θ_p corresponding to the number of cycles $2N_f$ using equation (2.116).

(vi) Go to step (i) and change the value of N_f and resume steps from (ii) to (v).

2.9.2 Suggested Simplified Cyclic Based Fatigue Relationship

A further approximation of the fatigue-life can be made and one can use equation (2.122) to eliminate the term $\left(1 - \frac{M_y}{M_{max}}\right)$ in equation (2.116) as follows:

$$\left(1-\frac{M_y}{M_{max}}\right)=\frac{\frac{M_{max}}{M_y}-1}{\frac{M_{max}}{M_y}} \tag{2.124}$$

substituting equation (2.122) into (2.124) and simplifying therefore:

$$\left(1-\frac{M_y}{M_{max}}\right)=\frac{\left(\frac{f_{su}}{f_y}-1\right)-\left(\frac{f_{su}}{f_y}-1\right)\left(1-\frac{\varepsilon_{ap}}{\varepsilon_{su}}\right)^n}{\frac{f_{su}}{f_y}-\left(\frac{f_{su}}{f_y}-1\right)\left(1-\frac{\varepsilon_{ap}}{\varepsilon_{su}}\right)^n} \tag{2.125}$$

Further simplification of equation (2.125) leads to:

$$\left(1-\frac{M_y}{M_{max}}\right)=\frac{1-\left(1-\frac{\varepsilon_{ap}}{\varepsilon_{su}}\right)^n}{\frac{\frac{f_{su}}{f_y}}{\left(\frac{f_{su}}{f_y}-1\right)}-\left(1-\frac{\varepsilon_{ap}}{\varepsilon_{su}}\right)^n} \tag{2.126}$$

By using binomial expansion and further simplification, therefore:

$$\left(1-\frac{M_y}{M_{max}}\right)=\frac{n\frac{\varepsilon_{ap}}{\varepsilon_{su}}}{2+n\frac{\varepsilon_{ap}}{\varepsilon_{su}}} \tag{2.127}$$

Further simplification of equation (2.127) and substitution into (2.116) gives :

$$\theta_p = 0.08\left(\frac{n}{2}\frac{\varepsilon_{ap}}{\varepsilon_{su}}\right)\left(\frac{L}{d_p}+\cot\alpha\right)(2N_f)^{-0.5} \tag{2.128}$$

Substituting (2.115) into (2.128) and taking ε_{su} = 0.15, n = 2.3 gives the following rotation-life relationship

$$\theta_p = 0.05\left(\frac{L}{d_p} + \cot\right)(2N_f)^{-1} \tag{2.129}$$

This result is both interesting in its implication and useful in its outcome. Note that the fatigue exponent is -1. This means that a constant amount of energy is required leading to fatigue fracture. By multiplying both sides of equation (2.129) by $2N_f$ the cumulative plastic drift can be obtained by rearranging equation (2.129) as:

$$\sum\theta_p = (2N_f\theta_p) = 0.05\left(\frac{L}{d_p} + \cot\alpha\right) \tag{2.130}$$

The fatigue-life model proposed in this section is compared to the experimental results of the specimens that exhibited fatigue failure during the experiments and the results are presented in detail in section 6.

2.10 CLOSURE

In this section, potential plastic mechanisms for pile bents and pile foundations were analyzed. The effect of pile-soil interaction was considered within this plastic mechanism. Several parameters that affect the distance between the plastic hinges, for cohesionless and cohesive soils, were studied. This was followed by development of two theories to identify the connection efficiency. A conceptual elastic cap/elasto-plastic pile retrofit strategy was proposed. On the basis of this strategy, a method for the evaluation of the retrofitted connection performance was suggested. Results from 3-D FEM models compare favorably with the cracked elastic theory; the former validating the latter. A method was proposed for the connection performance under lateral loading . This method can be employed to predict the experimental back-bone curves of these connections under cyclic loading. Finally, a fatigue life model based on a simplified approach is developed.

SECTION 3
EXPERIMENTAL SYSTEM

3.1 INTRODUCTION

The experimental program involved in the present study consisted of two phases. The first phase was concerned with the evaluation of the strength and ductility capability of steel pile-to-concrete cap connections subjected to cyclic loading. In the second phase, an experimental study was performed to assess the retrofit strategy proposed in this study.

This section describes the development of experimental procedures and setup necessary to conduct the tests on full-scale specimens. The design of test specimens is explained first followed by a description of the construction of each specimen. The test rig and the associated instrumentation for each experiment are then described.

3.2 TEST SPECIMENS DESIGN

On the basis of the plastic mechanisms considered in Section 2 an experimental setup was devised for both pile foundations and pile bents. Figure 3.1 illustrates the procedure used to determine the physical modeling configuration for a prototype steel pile bent foundation. The shaded portions of this figure show the boundary conditions, which end at the inflection points in both the pile and cap beam. Extracting this shaded portion and inverting it, a test specimen is formed when anchored to the laboratory strong floor. The plastic mechanism study, for pile bents in cohesionless and cohesive soils, dictates an average value of $5\,d_p$ for the depth to the second plastic hinge within the soil. Based on the available drawings for this kind of bridge an average extended length of the pile above the soil is taken as *4.75m.* Accordingly, for the HP10X42 steel

(a)

(b)

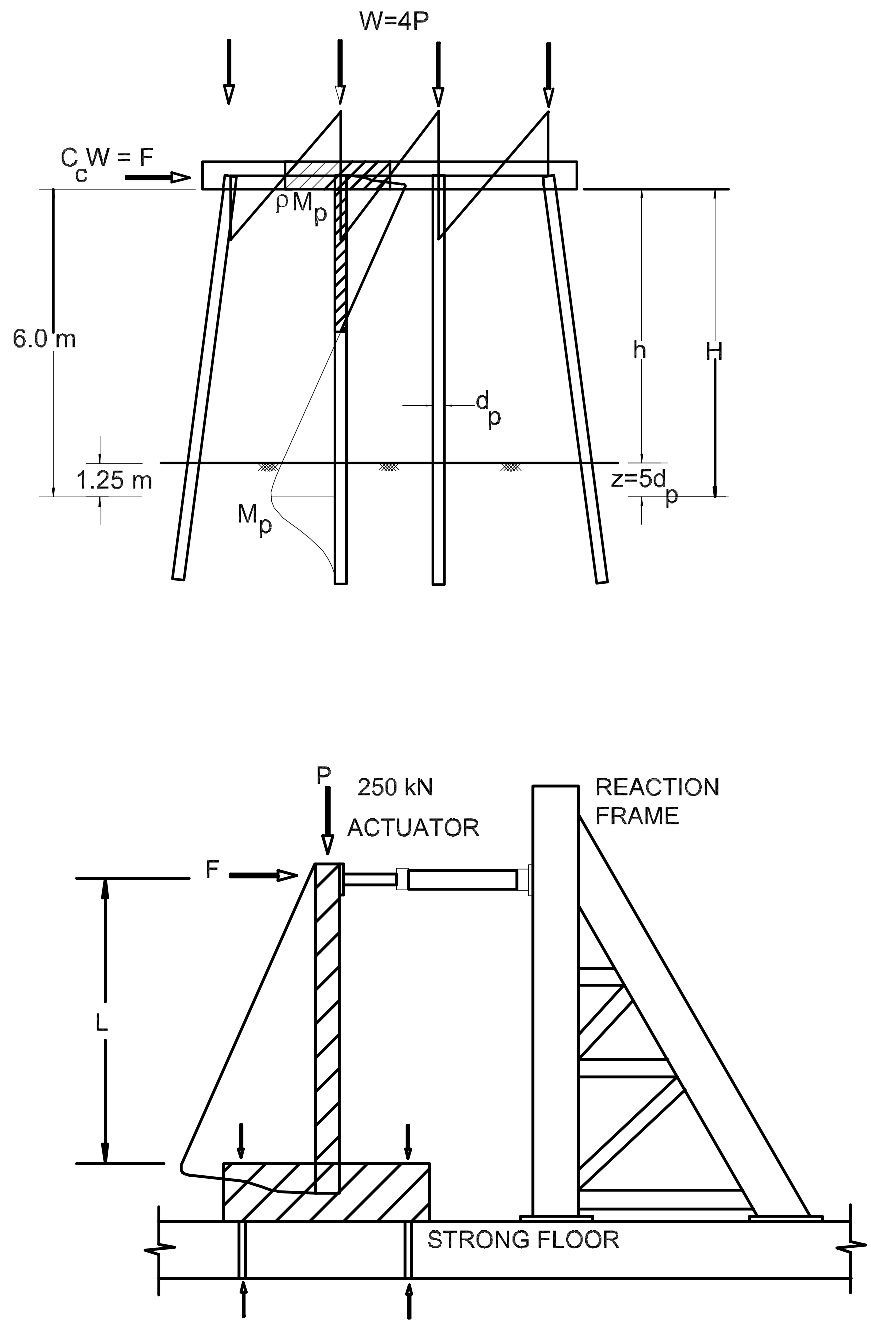

Figure 3.1 Physical Modeling Rationale for Pile Bents: (a) Typical Geometry of a Steel Pile Bent, and (b) Physical Model of Pile to Cap Connection

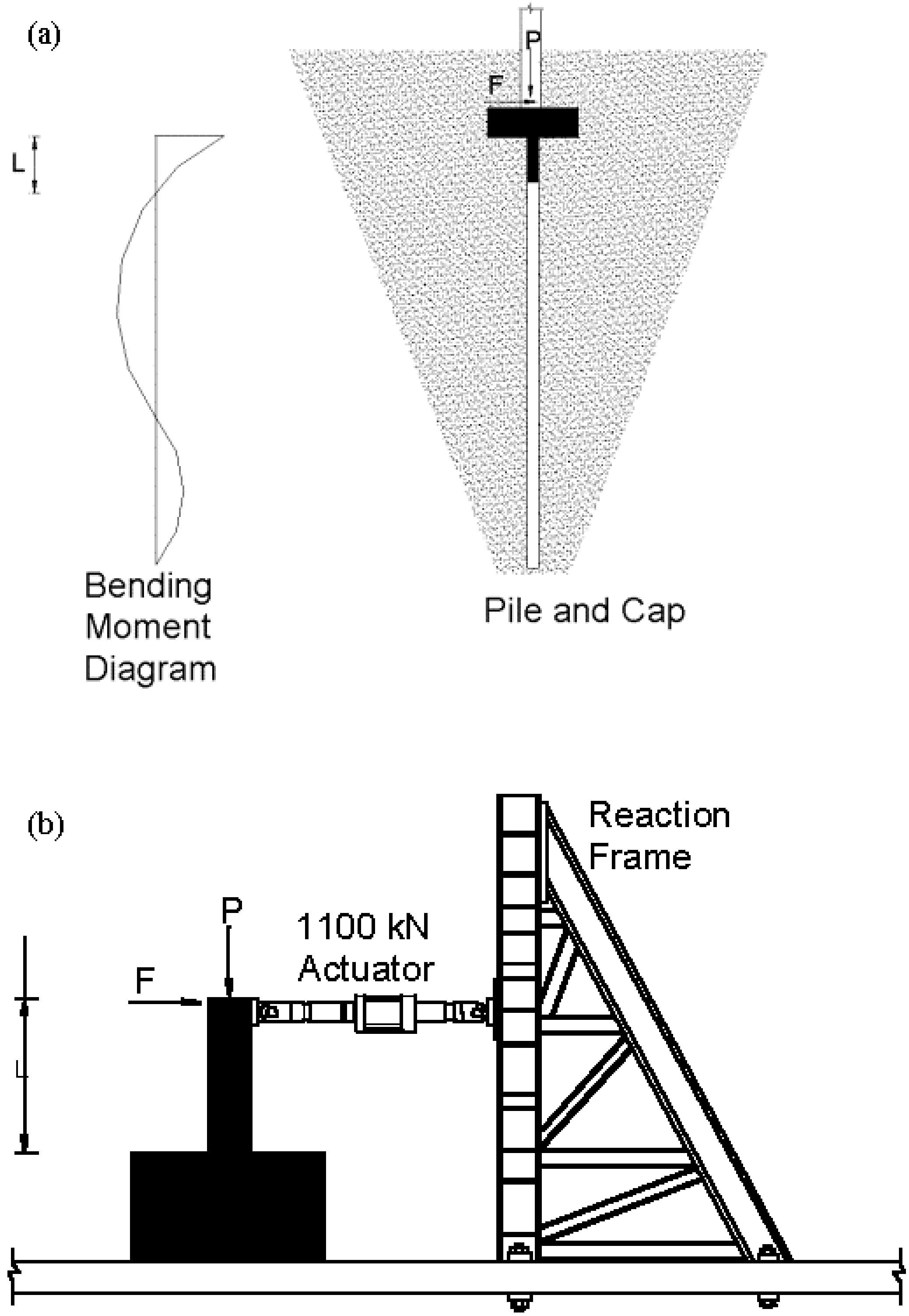

Figure 3.2 Physical Modeling Rationale for Pile Foundations: (a) Typical Geometry of Pile ,and (b) Physical Model of Pile-to- Pile-Cap Connection

section employed in the experimental study, the cantilever length of the pile bent experiments was taken as *3m*. The same rationale is used for pile foundation experiments (see figure 3.2) where the plastic mechanisms for these structures in cohesionless and cohesive soils suggests an average value of $3\,d_p$ for their effective length L. Consequently, the cantilever length of the pile foundation experiments was taken as *0.785m.* Axial loads are applied to the specimens by a vertical actuator acting via a lever beam system, while lateral loads are applied directly at the theoretical inflection point of the column.

3.3 Axial Load Accommodation

The axial gravity loads according to the setup designed were applied to the specimen by a vertical actuator through the lever beam system shown in figure 3.3. This setup is always adequate for interior piles testing. Exterior piles are usually exposed to additional vertical thrust during cyclic loading. The vertical thrust may add up to the total compressive gravity load on the pile or may cause tension uplift, according to the direction of the horizontal load. It is possible to accommodate the effect of tension uplift in the laboratory by various methods discussed below.

Consider the steel pile bent subjected to lateral load in figure 3.4a. For a total horizontal force of F, overturning equilibrium requires that:

$$T = \frac{3}{2}\frac{FL}{B} \tag{3.1}$$

where F= the horizontal applied load; B = the distance between the centerline of the adjacent piles; L= pile bent length and T= tension tie down force to restrain overturning. Therefore the total applied vertical load on an exterior pile can be written as:

$$P_v = P_g + T \tag{3.2}$$

where P_g = the gravity load on pile. Defining the ratio:

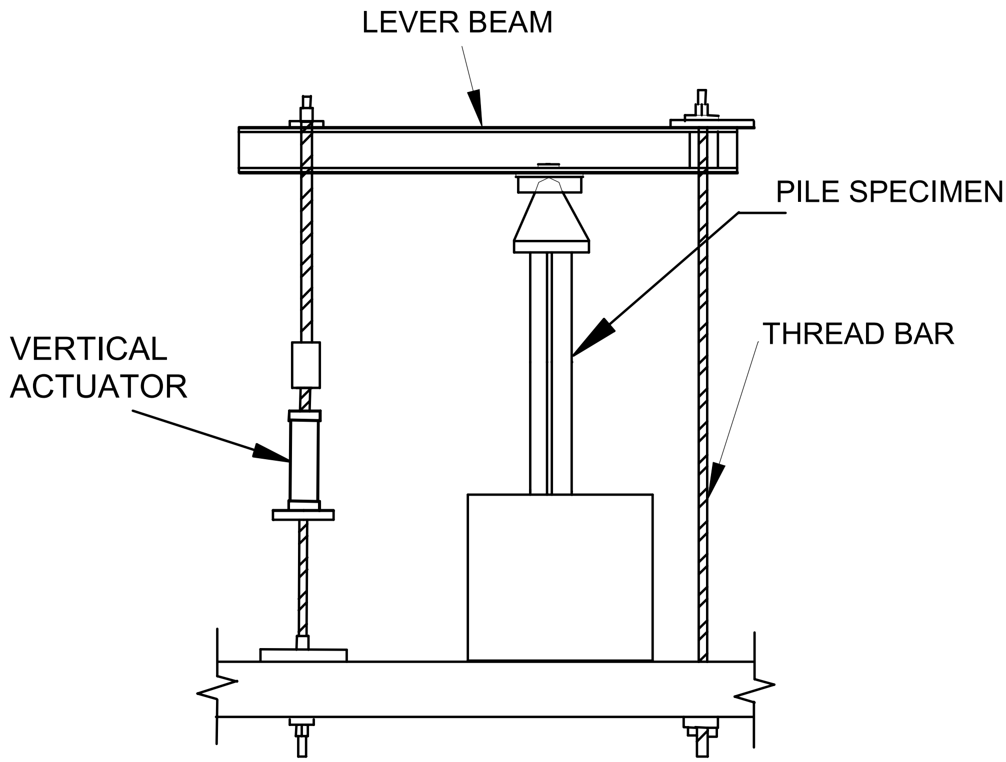

Figure 3.3 Gravity Load Accommodation In Laboratory

(a)

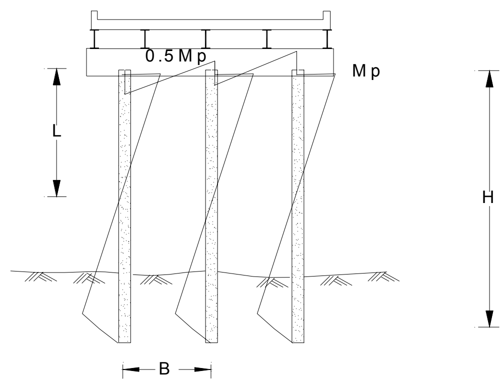

(b)

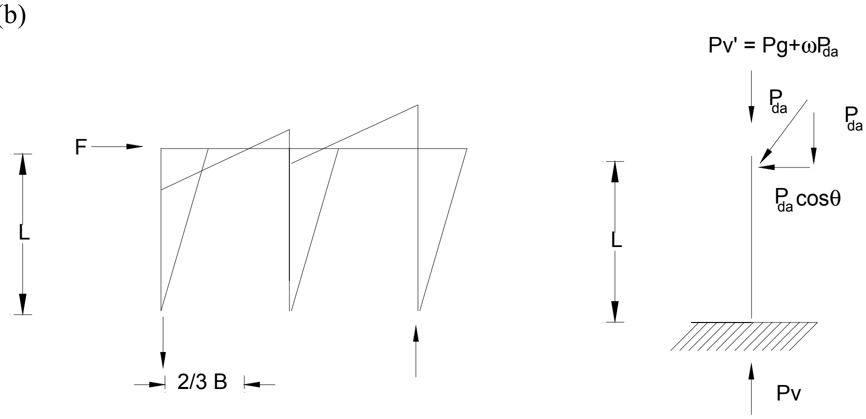

Figure 3.4 Axial Load Accommodation For Exterior Piles: (a) Pile Mechanism, (b)Portal Frame Idealization, and (c) Test Specimen

$$\upsilon = \frac{T}{F} = 1.5\frac{L}{B} \tag{3.3}$$

and substituting equations (3.1) and (3.3) in equation (3.2) gives:

$$P_v = P_g + \upsilon F \tag{3.4}$$

in which P_v = the total applied vertical load on the exterior pile; P_g = the gravity load on pile; and υ = coefficient relating the additional vertical force to the horizontally applied load.

Consider now a laboratory modeling for this physical situation. There are three possible experimental setups to carry out the additional tensile uplift, these are explained in what follows:

Method 1: Inclined Actuator:

One possible setup to carry out the additional tensile uplift is to fully incline the horizontal actuator to account for both the horizontal load F and the additional vertical thrust T. In this case the angle of inclination necessary is:

$$\theta_d = \tan^{-1} \upsilon \tag{3.5}$$

The axial load P_g is applied through the vertical actuator and is held constant to simulate the constant gravity load (figure 3.3). The total reaction force in the pile specimen is the sum of the two actuator components:

$$P_v = P_g + P_{da} \sin\theta_d \tag{3.6}$$

where P_{da} = force applied by inclined actuator. The main advantage of this setup is that it can directly accommodate vertical force changes including tension uplift.

However, in most cases, one may be restricted to another angle θ_a that is dictated by the space available in the laboratory.

Method 2: Horizontal Actuator with Variable Vertical Force:

One way to overcome the laboratory space limitation problem is to use a horizontal actuator operating in displacement control and the vertical actuator operating in load control. The variable axial load can be accommodated as follows:

$$P_v = P_g + \omega P_{ha} \tag{3.7}$$

where ω= a proportionality factor that adjusts the fraction of load transferred from the lateral actuator to the vertical actuator and P_{ha} = force applied by horizontal actuator.

Method 3: Hybrid Setup:

The previous two methods can be combined to obtain the third approach which can be applied under any laboratory room restriction. In this setup the horizontal actuator is inclined with the available angle θ_a and operates in displacement control. The vertical actuator operates in load control through an algorithm that relates its load to the inclined actuator load. This can be demonstrated in what follows.

The vertical prototype applied load can be expressed as:

$$P_v = P_g + \upsilon F = P_{v'} + P_{da} \sin\theta_a \tag{3.8}$$

where θ_a = available inclination angle to fit the space in the laboratory; and $P_{v'}$ = the force transferred from the vertical actuator to the specimen, can be quantified as:

$$P_{v'} = P_g + \omega P_{da} \tag{3.9}$$

The horizontal applied load can be evaluated as:

$$F = P_{da} \cos\theta_a \tag{3.10}$$

By substituting equations (3.8) and (3.9) into (3.7) and simplifying, an expression for the coefficient ω is obtained:

$$\omega = \upsilon \cos\theta - \sin\theta \tag{3.11}$$

Therefore the vertical actuator force P_{va} can be evaluated as:

$$P_{va} = \lambda P_{v'} \tag{3.12}$$

where λ = coefficient to account for the effect of the lever beam. To operate the vertical actuator according to the relationship of equation (3.11), the actuator analog control system required input from the load cell of the lateral actuator. This load cell value is then multiplied by the value ω. A fixed offset is employed by the vertical actuator controller to account for the gravity load.

The aforementioned procedure was employed in the experiments conducted for the present study. The lateral actuator was inclined for exterior piles in pile bent experiments to θ_a = 24^0, and for pile foundation experiments this angle was set to 44^0.

3.4 MATERIAL TESTS

Four steel coupons were cut from the pile flanges for the evaluation of its material properties. The specimens were constructed according to the ASTM standard dimensions for tension testing of metallic materials. A tension test was conducted for each specimen in an axial MTS 445 kN closed-loop servocontrolled hydraulic test system figure 3.5. The results of the stress-strain behavior for each specimen are shown in figure 3.6. However, the plots do not represent the entire loading history of the coupon test. In order to prevent damage to the extensometer, it was necessary to remove it prior to fracture of the specimen. Therefore, the

Table 3.1- Results of Flange Steel Coupon Tests

Specimen Number	Yield Strength (MPa)	Ultimate Strength (MPa)	E_s (GPa)	E_{sh} (MPa)	ε_{sh}
1	315	485	199	2430	0.0112
2	315	471	197	2270	0.0109
3	317	465	190	2390	0.0117
4	314	477	185	2630	0.0118
Average	315	475	193	2430	0.0114

Figure 3.5 Photograph Showing Coupon Specimen under Tension Test

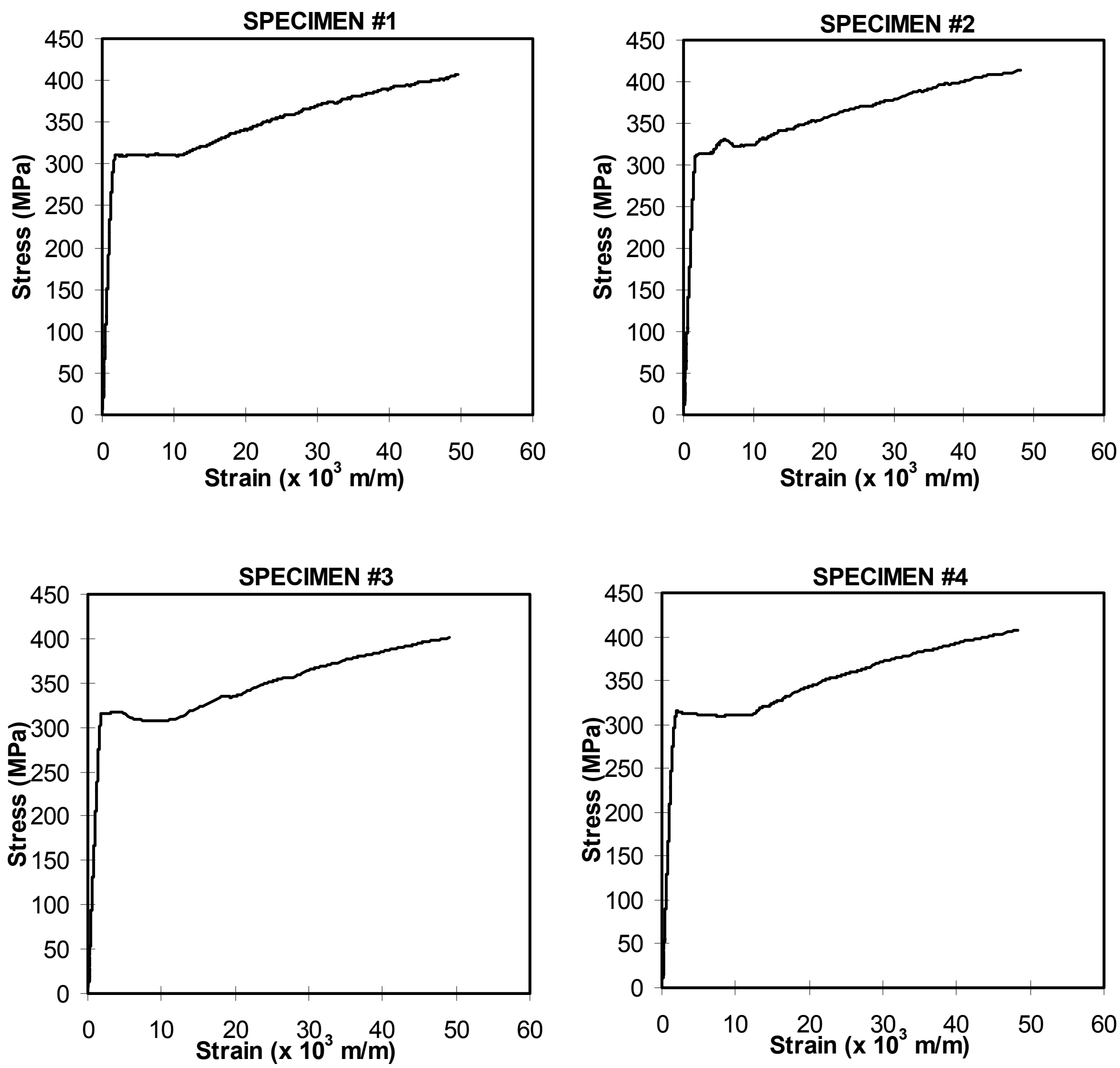

Figure 3.6 Coupon Test Results

ultimate strength of the steel was computed using the ultimate load on the coupon not the final value on the plot. Other steel properties derived from these tests are shown in table 3.1.

The ultimate compressive strength of the concrete was determined from the results of three *150mm x 300mm-cylinder* tests. Results for the various stages during the experimental program conducted in the present study are shown in table 3.2.

3.5 CONSTRUCTION OF TEST SPECIMENS

The test specimens were constructed with ready-mix concrete, with a specified 28-day concrete strength of 32 *MPa* and Grade 60 *(414 MPa)* steel reinforcement. The *HP*10x42 piles were obtained from a local pile driving company. The piles had experienced driving stresses but were otherwise unused. Typical pile driving procedure involves driving the pile to the required depth, then cutting the exposed length to achieve the proper height. The sections left over from this operation were employed as test specimens for this study.

3.5.1 Strong Axis Bending Specimens

Three pile specimens were used for this experimental study. However, instead of fabricating three separate pile-to-pile cap specimens, all three piles were embedded into the same pile cap at different spacing. Several vertical ducts made of *38mm* PVC pipe were built into the pile cap in order to provide access for anchor bolts. By using certain combinations of these ducts, the anchor points for the specimen could be changed to allow the piles to be tested individually.

The resulting test specimens consisted of a full-size cap beam with three HP *10x42* piles as shown in figure 3.7. The selected piles are typical of what is commonly used in construction practice. The arrangement of the longitudinal and transverse reinforcement, the embedment length of the pile, and the cross-sectional area of the pile cap are typical dimensions taken from design drawings of representative structures. The longitudinal reinforcement on the pile side of the cap beam consists of a pair of *28 mm* diameter (#9) bars spaced at 125 mm centers on each side of the

Table 3.2 Results of 150mmx300mm Cylinder Tests

Test ID	Spec. #	28 Day Comp. Strength (MPa)
Strong Axis Bending Pile Bent Specimens	1	32.4
	2	41.7
	3	37.3
	$f_c^{'}$	37 MPa
Pile bent Specimens Tested Along Weak Axis Bending & Pile Foundation Specimens Tested Along Strong & Weak Axes Bending	1	31.8
	2	28.6
	3	30.2
	$f_c^{'}$	30 MPa
Retrofit For Pile Bents Tested Along Strong Axis Bending	1	32.3
	2	30.7
	3	31.30
	$f_c^{'}$	32 MPa
Retrofit for Pile Foundation Specimens Tested Along Strong & Weak Axes Bending	1	33.5
	2	31.3
	3	32.4
	$f_c^{'}$	32 MPa

$f_c^{'}$ = Average compressive Strength of Three Specimens

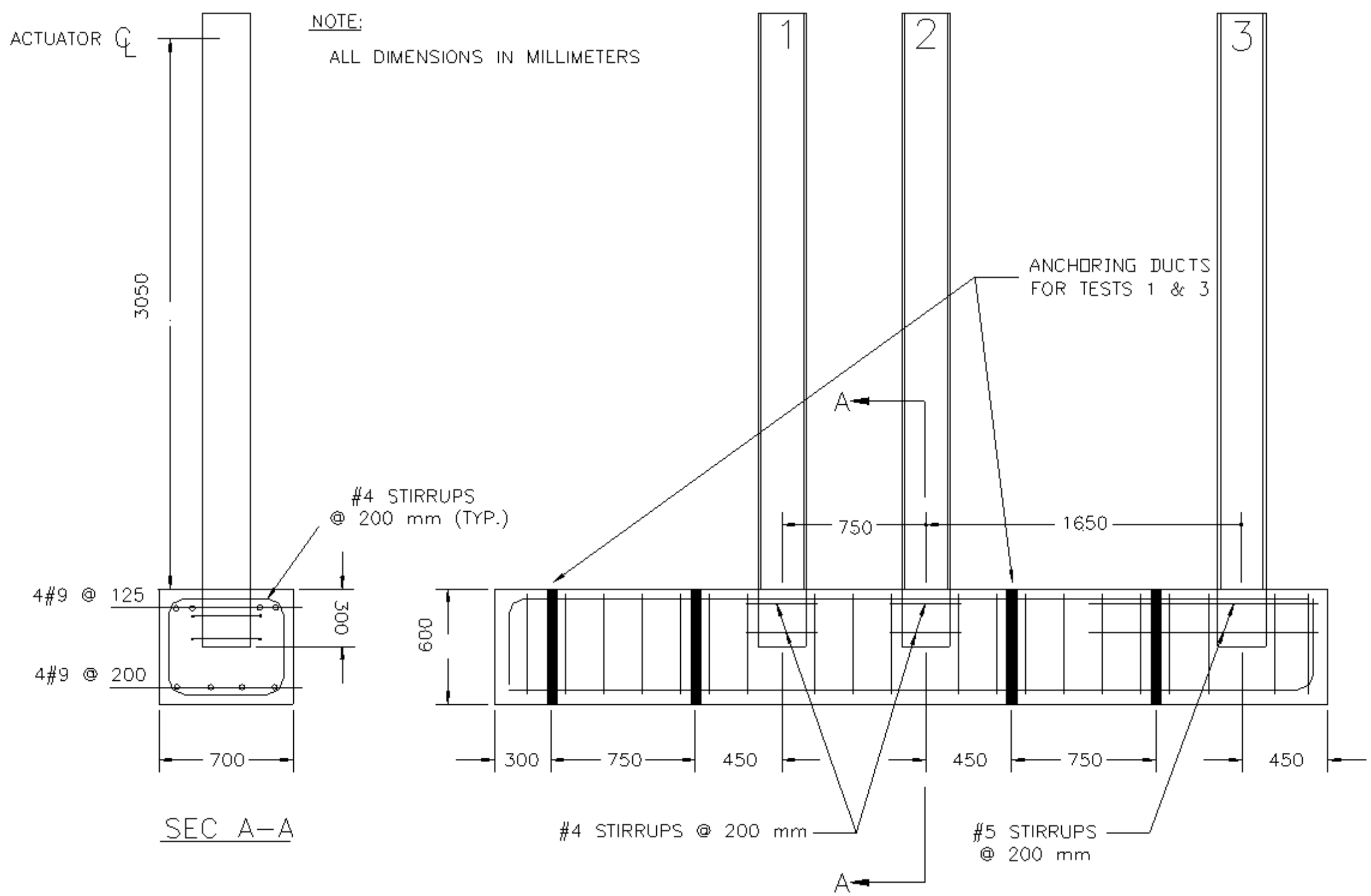

Figure 3.7 Geometry and Reinforcement For Strong Axis Pile Bent Specimen

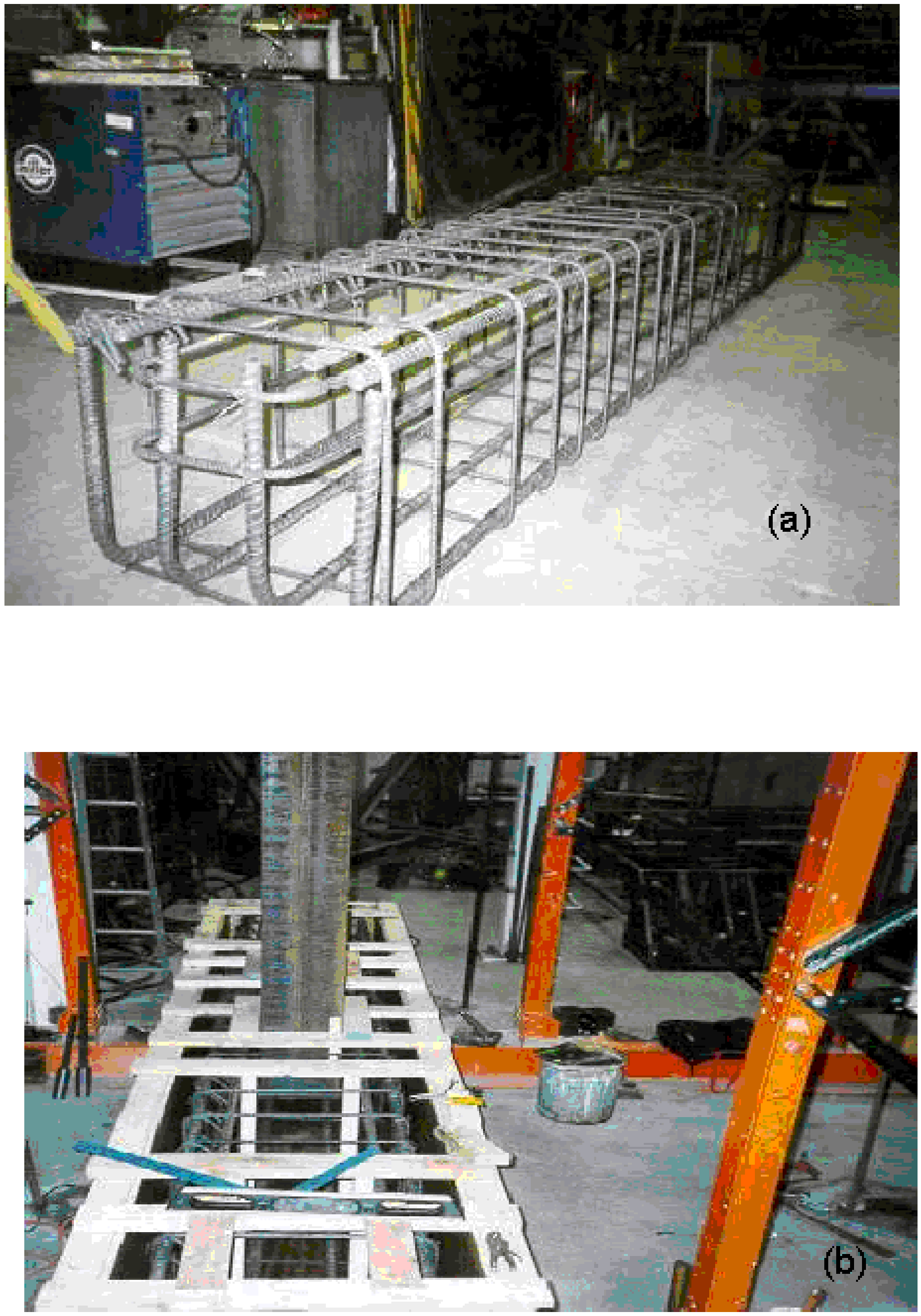

Figure 3.8 Construction Photos for Strong Axis Specimens (a) Reinforcement Cage, and (b) Formwork

embedded pile. The bottom row consists of four *28 mm* diameter (#9) bars equally spaced at 200 mm. The longitudinal bars were hooked at the ends to provide additional confinement of the concrete at the extremities of the beam. Shear reinforcement consisting of *12 mm* diameter (#4) stirrups were placed approximately *200 mm* apart along the length of the cap beam, with appropriate gaps at the pile locations. Confining reinforcement for interior piles consisted of two *12 mm* diameter (#4) stirrups with a *200 mm* spacing over the embedment length. The exterior piles utilized two *16 mm* diameter (#5) hoops which enclosed the aforementioned hooked longitudinal bars and were extended past the pile a distance equal to the development length of the *16 mm* diameter (#5) bar. Photographs of the reinforcement cage for this specimen are shown in figure 3.8.

During construction of the pile cap beam, the H-piles were supported by a steel framework, which maintained the load and proper alignment of the pile in the cap beam while the concrete cured. For each test, high alloy prestressing (DYWIDAG) threadbars were inserted through the anchoring ducts and into the laboratory strong floor. The bars were then prestressed to provide the necessary foundation reactions. Following a test, the pile was remounted back in its location, using the framework and any damage to the concrete cap beam was repaired prior to retrofitting.

3.5.2 Pile Bents Tested Along the Weak Axis of Bending

The same design reinforcement and specimen dimension used for preparing the strong axis bending cap beam specimen were also utilized for the construction of the weak axis bending specimen. Two pile specimens were used for this experiment study representing an interior pile with a constant axial load and an exterior pile with a varying axial load.

The upper longitudinal reinforcement of the cap beam consisted of two *28 mm* diameter (#9) bars spaced at *125 mm*. The bottom row consisted of four *28 mm* diameter (#9) bars equally spaced at *200 mm*. The stirrups consisted of *12 mm* diameter (#4) hoops spaced at *200 mm* along the length of the cap beam. The confining reinforcement consisted of two 12 mm diameter (#4) stirrups spaced at 150 mm along the embedment depth of the pile.

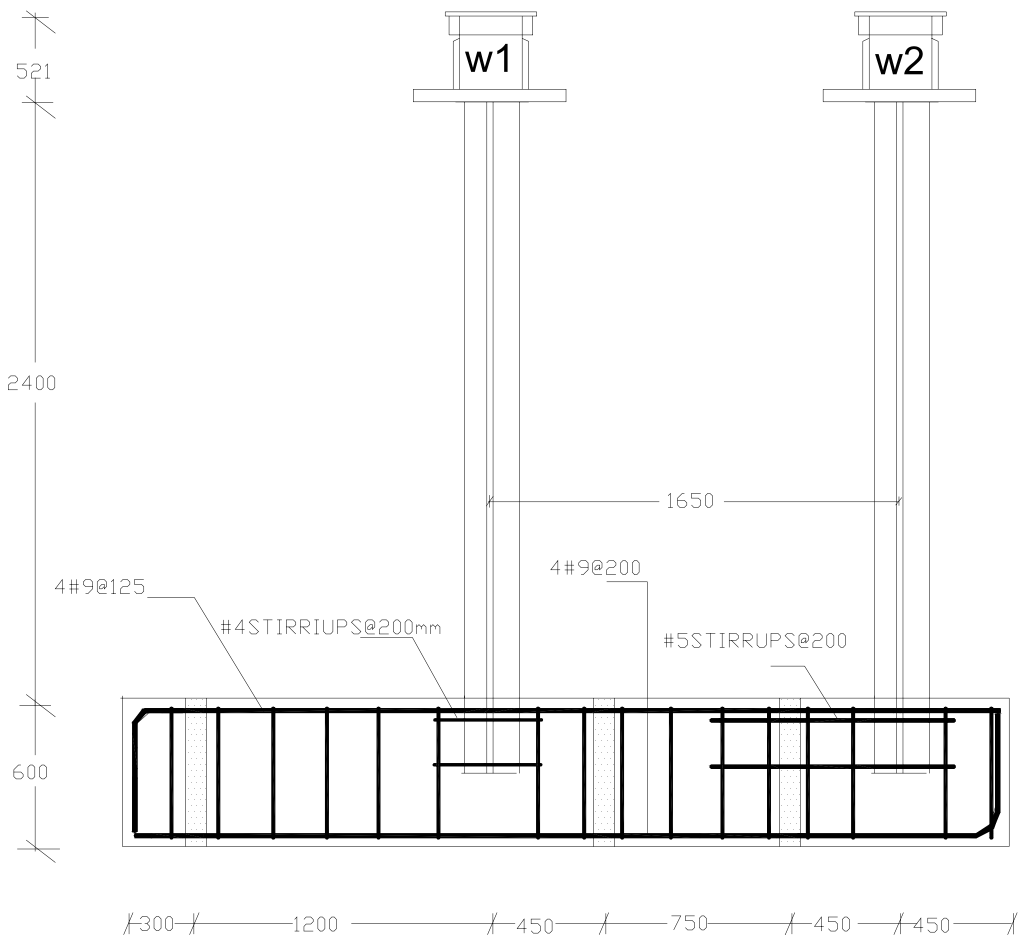

Figure 3.9 Reinforcement and Geometry of Weak Axis Experiment Specimen

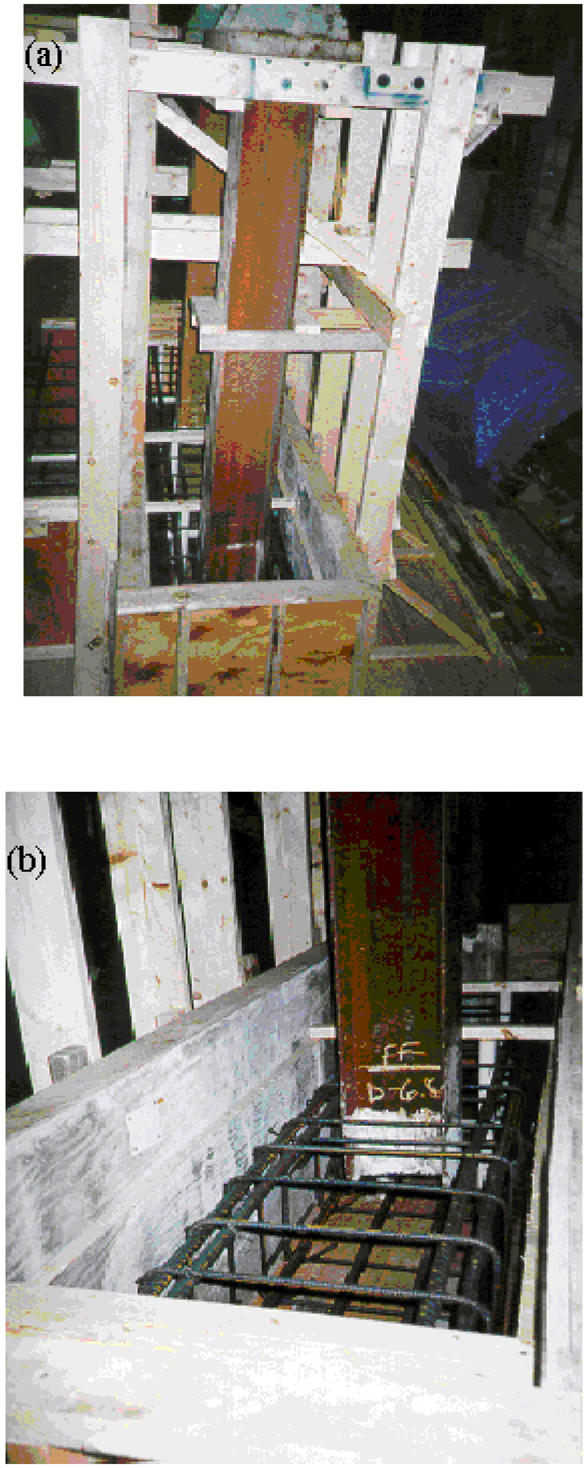

Figure 3.10 Photos of Weak Axis Specimens during construction showing: (a) Formwork, and (b) Reinforcement Cage

The pile specimens were provided with the bearings shown in figure 3.9, to provide the rotation adequacy for the lever beam relative to the pile, during the test through its sole plate, and to preserve more lever arm. The cap beam was supplied with six vertical ducts made of *38 mm* PVC pipe. Combinations of these ducts provided four anchor points, to attach the cap beam to the laboratory strong floor. High alloy prestressing (DYWIDAG) threadbars were used to post-tension the reinforced concrete cap beam portion of the specimen to the laboratory strong floor.

During the construction of the wooden boxing for the pile cap beam, a wooden framework was also constructed to keep up the proper alignment of the pile in the cap beam while the concrete is poured in. Photographs for this wooden framework as well as the construction of the specimen are shown in figure 3.10.

3.5.3 Pile Foundation Specimens

Figure 3.11a illustrates a typical piled foundation prototype for an exterior bridge foundation, taken from design drawings of FHWA. As shown in the figure, an exterior pile in a pile group can be exposed to seismic load along its strong and weak axes directions. Moreover, the tension uplift during cyclic loading may be a major factor that can affect its performance. Based on this criterion, the experimental program for the piled foundation in this study included testing two exterior piles along the strong and weak axes. On the basis of the prototype (Figure 3.11), one cap beam was constructed to accommodate both cases. Some slight modifications were introduced to the model as follows.

Although the bridge foundation design shown in figure 3.11 utilized one layer of mesh reinforcement at the bottom of the foundation, some other drawings utilized an additional layer at the top. Consequently, for the present study, two layers were used in the design of model specimen.

The hatched area in figure (3.11c) was employed to design the model specimen. Therefore the transverse steel was welded to a L2XL2X3/8 angle to achieve the continuation adequacy purposes of the steel in that direction (see figure 3.12).

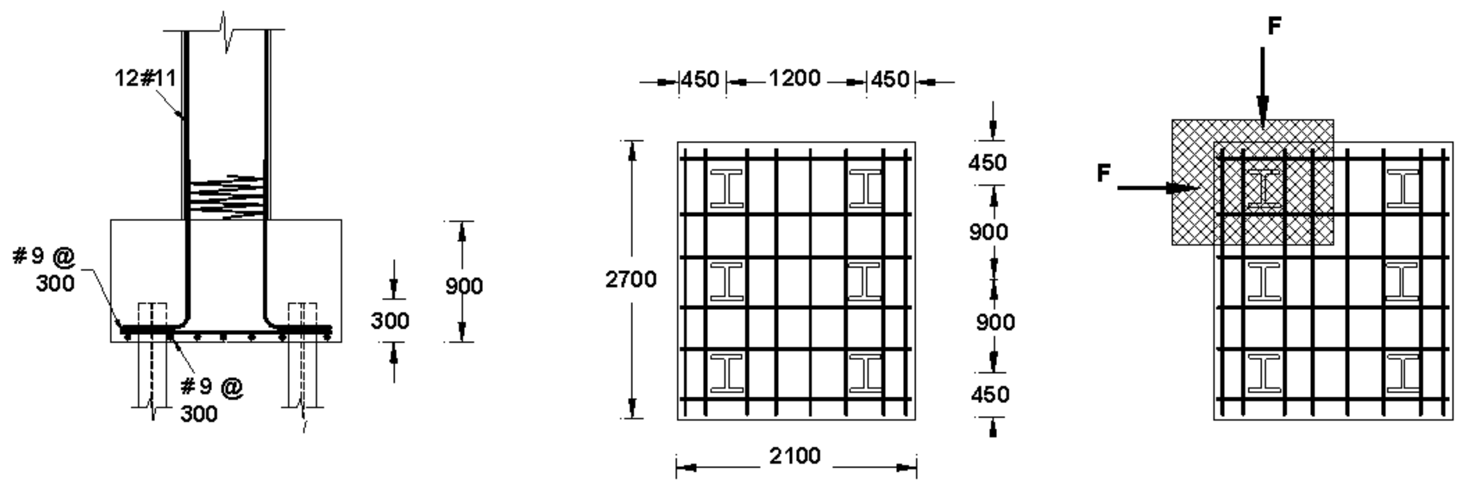

(a) Typical Bridge Foundation Prototype

(b)Plan View of Pile Group

(c) Shaded Portion Shows how Specimen was Devised

(b)Dimensions in mm

Figure 3.11 Bridge Prototype and Rationale used for devising the Model

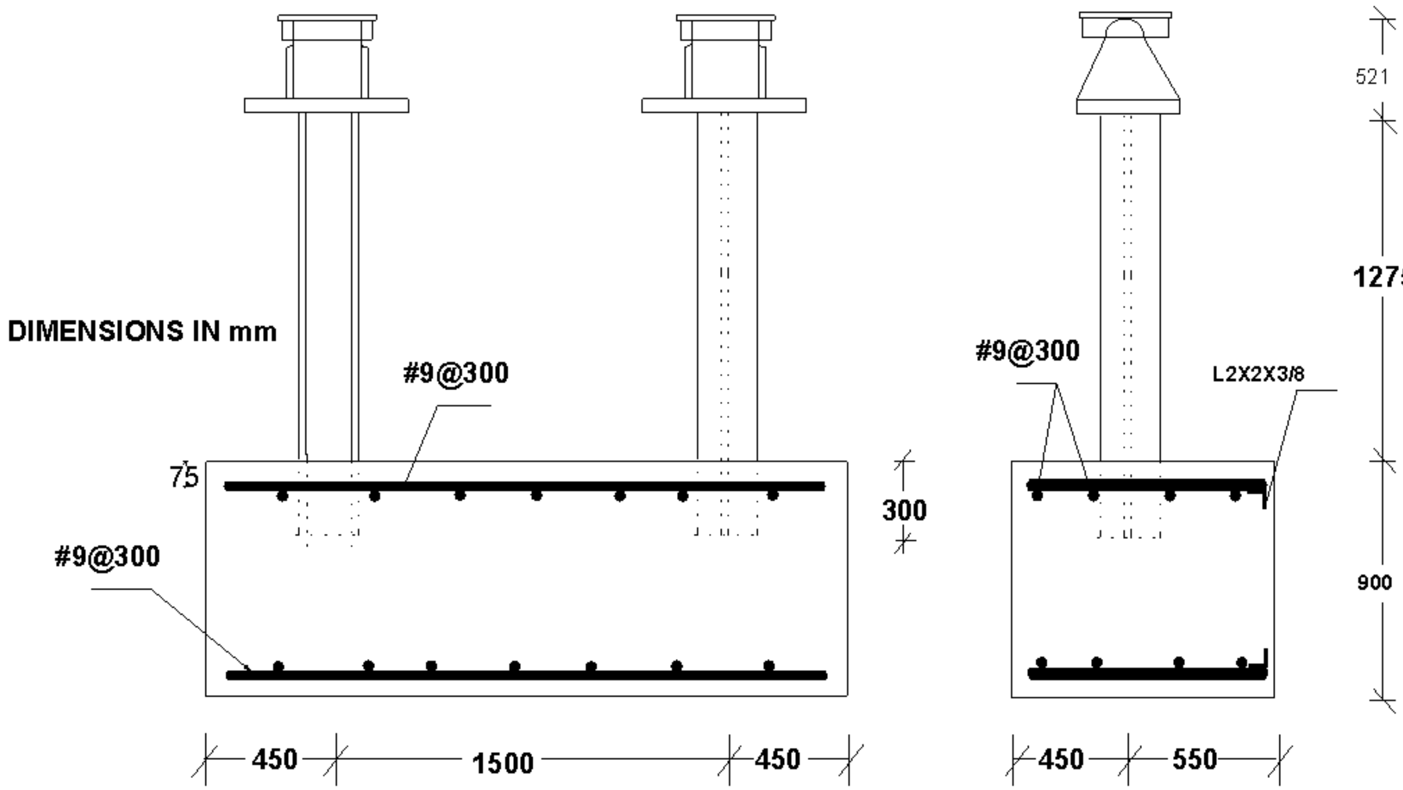

Figure 3.12 Geometry and Reinforcement of Pile Foundation as Built Specimens

It was decided to anchor the specimen to the laboratory floor using high alloy prestressing (DYWIDAG) threadbars that would be inserted through an anchor beam. Therefore, in designing the specimen, only horizontal ducts made of 38mm PVC pipe were built into the pile cap for the purpose of lifting the specimen during transferring from the workshop to the test setup location.

The pile specimens were provided with the same type of bearings used for the pile bent weak axis experiment, for the same purposes mentioned earlier. Photographs of the construction of this specimen are shown in figure 3.13.

3-6 EXPERIMENTAL SETUPS

3.6.1 Pile Bent Experiments

The test rig employed for these experiments is shown in figures 3.14 and 3.15. The specimens were anchored to the strong floor to provide restraint against both translational and uplift during testing. Lateral load was provided by a *250kN* capacity $\pm 300mm$ stroke MTS servo-controlled hydraulic actuator. This actuator, which was operated in displacement control, was attached directly to the pile with a pin connection, for the strong axis experiments, allowing rotation about only one axis, as shown in figure 3.15(a). It was, however, attached to the rocker bearing above the pile, in the case of weak axis experiments, through an adapter section, as shown in figure3.15 (b) to provide additional lever arm length. The other end of the actuator was bolted to a rigid reaction frame. The test rig did not employ any bracing to actively prevent out-of-plane motion of the pile. However, the pin connection at the pile provided adequate passive restraint against these undesirable displacements.

Figure 3.13 Construction of the Pile Foundation Specimen Showing: (a) Formwork, and (b) Reinforcing Cage

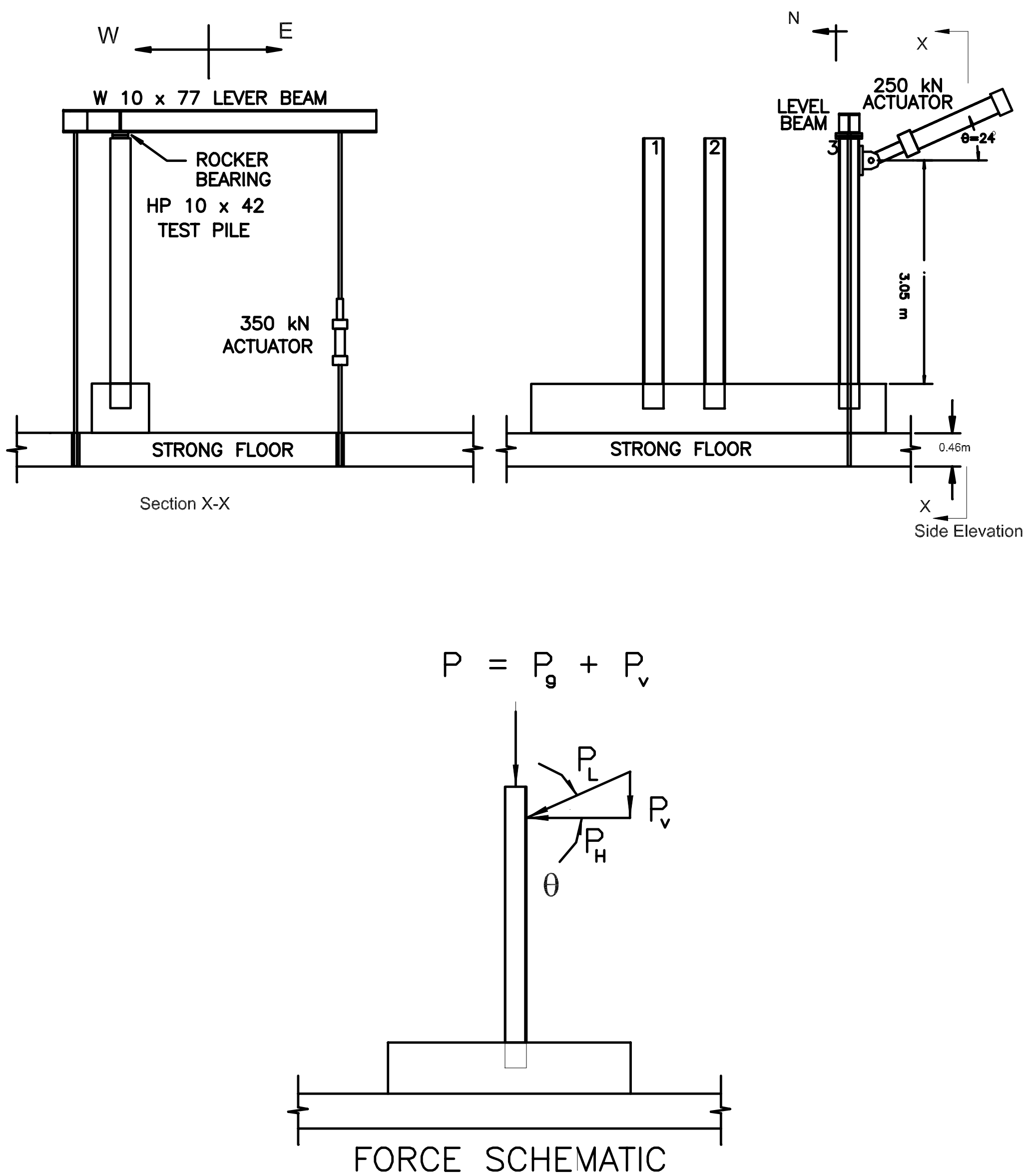

Figure 3.14 Test rig For Pile Bent Specimens

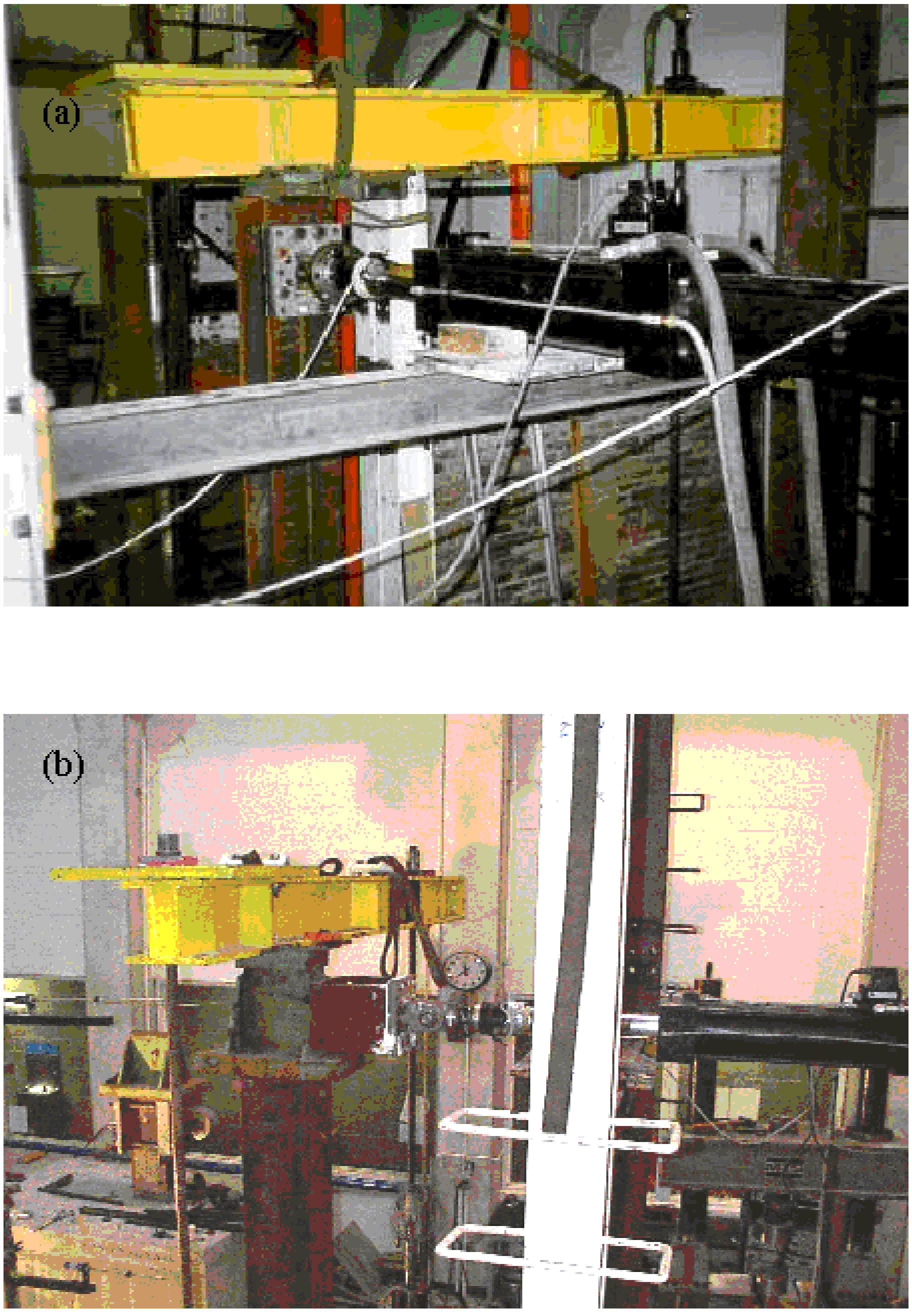

Figure 3.15 Pinned Connection of The Lateral Actuator to The Pile Bent Specimen: (a) Strong Axis Experiment, and (b) Weak Axis Experiment

Axial load was provided by a *350kN* capacity $\pm$*50mm* stroke Parker servo-hydraulic actuator operated in load control. The actuator load was applied to the pile through a *W10X77* lever beam, shown in figure 3.15(b). A *32mm* diameter high strength prestressing (DYWIDAG) threadbar provided the reaction at the other end of the lever beam. Both this bar and the actuator were anchored to the strong floor with rocker bearings that allowed the lever beam to move with the pile during the course of the tests. The constant gravity load was taken as 200 kN resulting in the following relationship according to equations (3.9) and (3.12):

$$P_{va} = \frac{3}{16} P_{v'} = (37.5 + 0.609 P_{da}) \text{ kN}$$

In case of strong axis experiments, a rocker bearing assembly was also located between the pile and lever beam. This bearing allowed the lever beam to rotate relative to the pile while transmitting the necessary load. The sole and web plates of the bearing used for weak axis experiments were employed for the same purpose. The testing procedure employed a quasi-static, cyclic lateral load that followed a sinusoidal wave form. An MTS 436 Controller was used for the hydraulic supply providing the frequency control for the test. MTS 406 Controllers were used for each actuator.

3.6.2 Pile Foundation Experiments

Figure 3.16 illustrates the test rig employed for the testing of the as built specimens. Lateral load was provided by an *1100kN* MTS hydraulic actuator anchored to the reaction frame at an angle of 42.5^0 to the horizontal and connected directly to the specimen. A photograph of the connection is shown in figure 3.17a. The vertical load due to gravity was provided by the *350kN* capacity $\pm$*50mm* stroke Parker servo-controlled hydraulic actuator, operated in load control and connected to the *W10X77* lever beam. The *W10X77* gravity load beam was anchored to the strong floor at one end using a *32mm* diameter DYWIDAG bar. The force in the 1100 kN actuator actively controlled the vertical actuator. The constant gravity load was taken as 135 kN. Therefore:

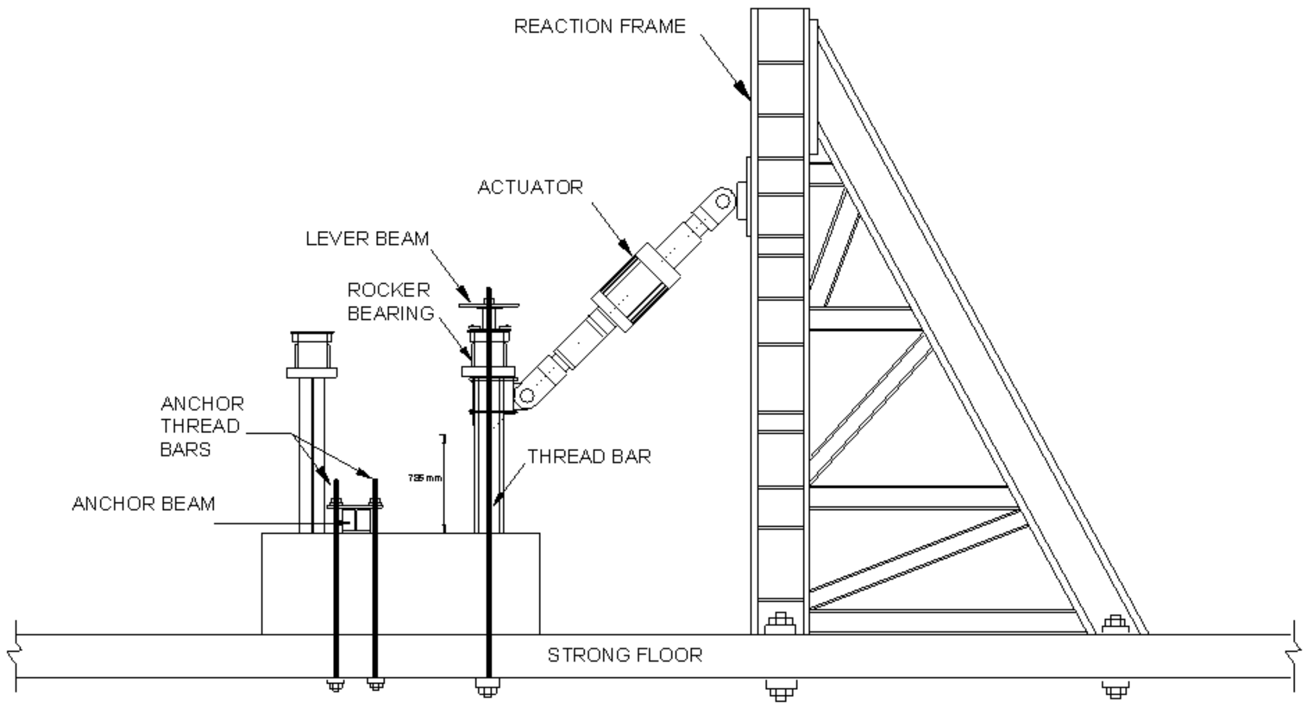

Figure 3.16 Test Rig Employed For As Built Pile Foundation Specimens

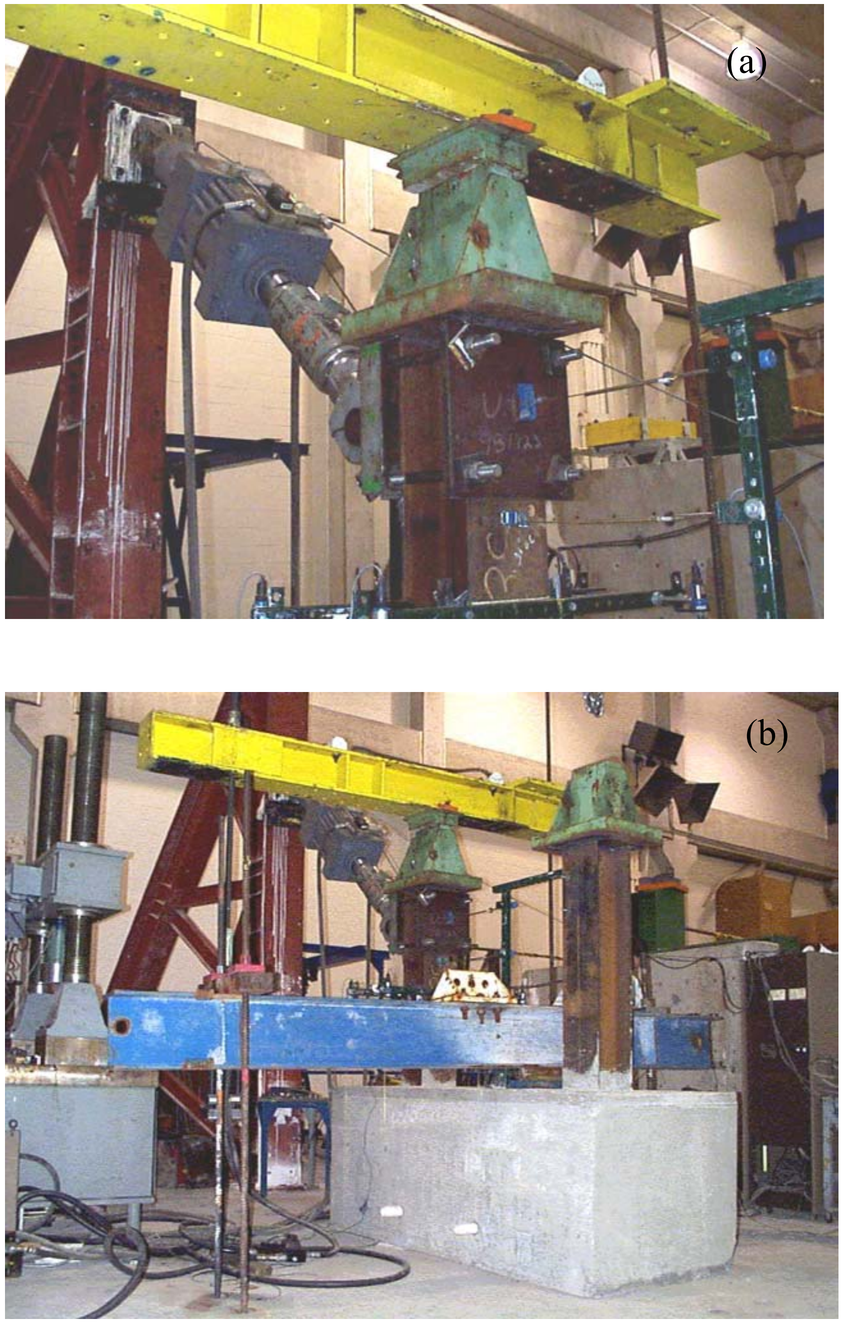

Figure 3.17 The Test Rig of the as Built Pile Foundation Specimens Showing : (a) Connection Between Actuator and Specimen, and (b) Anchor Beam

according to equations (3.9) and (3.12), the following relationship was used to control the vertical actuator

$$P_{va=}\frac{7}{16}P_{v'} = (59 + 0.121\ P_{da})\ \text{kN}$$

The vertical actuator increased the axial force in the column when the lateral actuator was pushing and decreased it during pull.

A *W10X88* steel beam was used to anchor the specimen to the strong floor to provide the sufficient restraint against translation and uplift during the tests. The beam was anchored at one end to the strong floor using two *25 mm* high alloy prestessing (DYWIDAG) threadbars. It was anchored from the other end to the strong floor using one *32mm* high alloy prestessing threadbar. The two *25mm* bars were prestressed to *90 kN* each. This prestressing force resulted in *480 kN* axial anchoring force on the specimen.

The test rig used for the as-built specimen was slightly modified for the retrofitted specimen. As shown in figure 3.18 the specimen is attached to the bearing to preserve the same lever arm before and after retrofit. On the basis of the retrofit philosophy adopted in this study, a ductile steel failure was expected. Accordingly, a maximum horizontal force was estimated as *490 kN* to yield the strong axis specimen. Therefore two additional keeper plates of *75mm* thickness were used to attach the actuator to the bearing. A picture of this connection is shown in figure 3.19a. Assuming a friction coefficient *0.3* between the specimen bottom and the laboratory floor, then the maximum vertical force necessary for anchoring this specimen is 1630 *kN*. Therefore for this setup four *32mm* high alloy prestessing threadbars were employed to anchor the specimen to the floor (figure 3.19b). Those bars were prestressed to a force of 310 *kN* each. The resulting anchoring force on the specimen was 1650 *kN*. Additional restraint precautions were added in the form of backup beam and backup plate to account for any uncertainty during the test. The laboratory reaction frame was prone to uplift due to the high uplift force that occurs when the diagonal actuator is pulling. Consequently, the same methodology adopted for anchoring the specimen to the laboratory floor was employed to impose additional axial force at

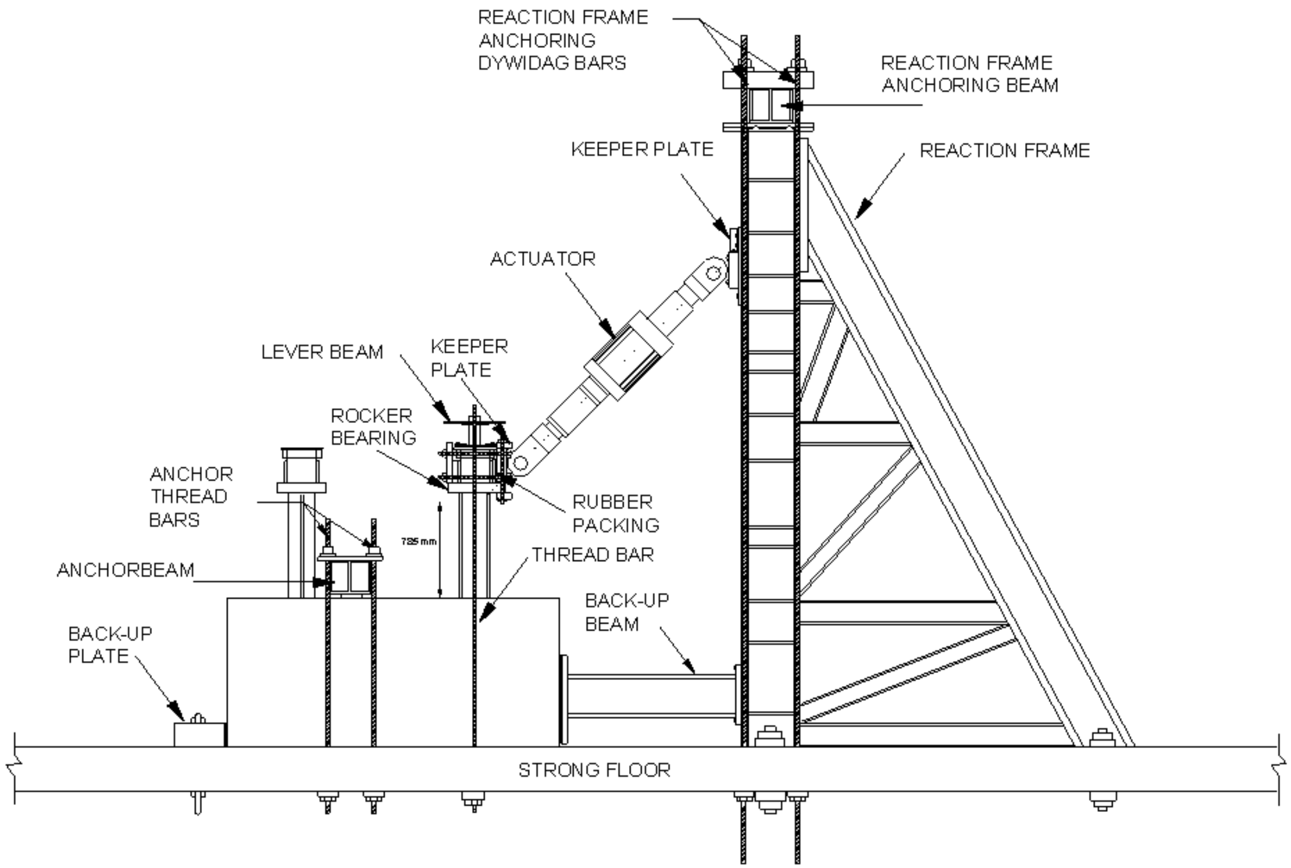

Figure 3.18 Test Rig Employed For Retrofitted Pile Foundation Specimens

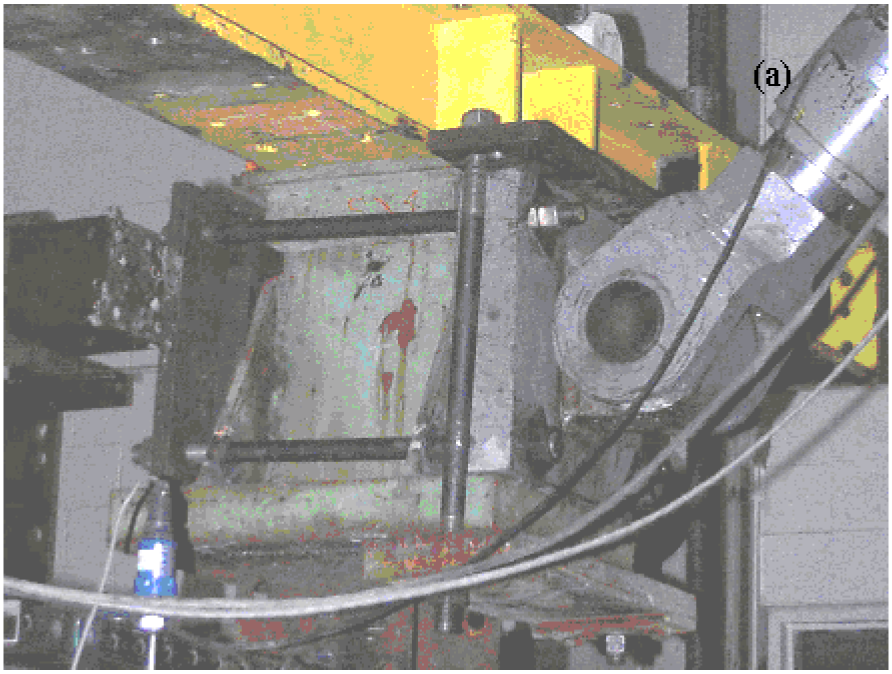

Figure 3.19 The Test Rig of the Retrofitted Pile Foundation Specimens: (a) Connection Between Actuator and Specimen, and (b) Anchor Beam Under Prestress

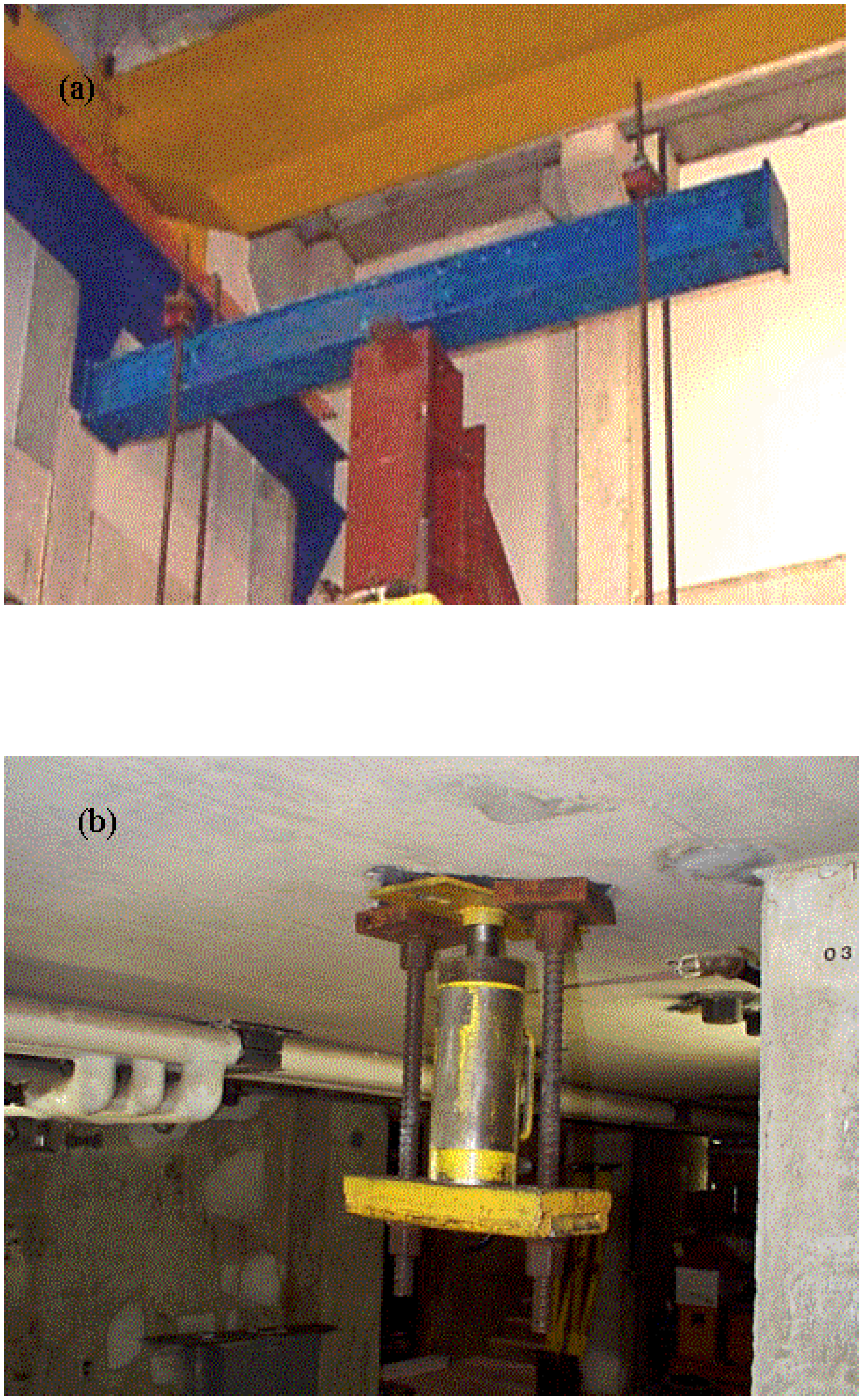

Figure 3.20 The Prestressing Process for the Reaction Frame: (a) Anchor Beam at the Top of the Reaction Frame with High Alloy Prestressing (DYWIDAG) Threadbars, and (b) Prestressing Process Below the Strong Floor

the top of the reaction frame. According to the inclination angle of the lateral actuator, *490 kN* uplift force is expected. Therefore, a W10X88 beam seated on a rocker bearing at the top of the reaction frame as shown in figure 3.20a was used with four *32 mm* high alloy prestressing threadbars to provide the necessary vertical force. In order to achieve this force the high alloy prestressing threadbars were prestressed to *360 kN* resulting in *720 kN* at the top of the reference frame. The prestressing process was conducted, as shown in figure 3.20b, below the strong floor.

3.7 INSTRUMENTATION DATA ACQUISITION AND PROCESSING

3.7.1 Instrumentation

The instrumentation used for the experiments consisted of sonic transducers and load cells as shown in figure 3.21. The Sonic Transducers (S-T) were MTS "Temposonics" model number DCTM-4002-1. The Sonic Transducers used for rotation measurements had a stroke of $\pm 102mm$, while for the measurement of lateral displacements for the pile bent experiments a $\pm 150mm$ stroke was used. Other Sonic Transducers used for pile foundation experiments had strokes of $\pm 102mm$, $\pm 150mm$, and $\pm 203mm$ for the lower, middle and upper location, respectively. The load cells were *500kN* and *650kN* devices supplied with the MTS and Parker actuators, respectively. Strain gauges were also used for the pile bent experiments they were Micro-Measurements CEA-06-125UW-120.

Sonic Transducers were also used to measure displacements of the pile specimens, as shown in figure 3.22. Three transducers were used for measuring the lateral displacements. They were placed at top, middle height and bottom of the specimen, 25mm above the concrete cap surface. The lowest transducer was designed to measure translation of the pile at the connection point. The top transducer was placed at the same height as the centerline of the lateral actuator. This instrument provided the input signal for the lateral actuator, which operated in "displacement control". The middle temposonic was located outside the potential plastic hinge zone and was used to gather additional displacement data for the pile. Pile foundation experiments employed an additional Sonic Transducer at the same height of the point of action of the inclined actuator. It was used to

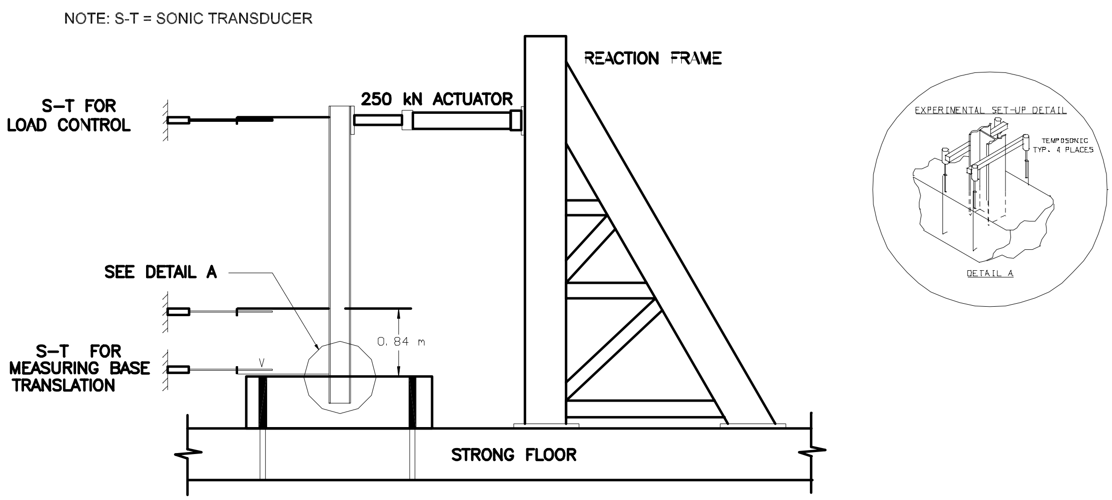

(a) INTERIOR PILE

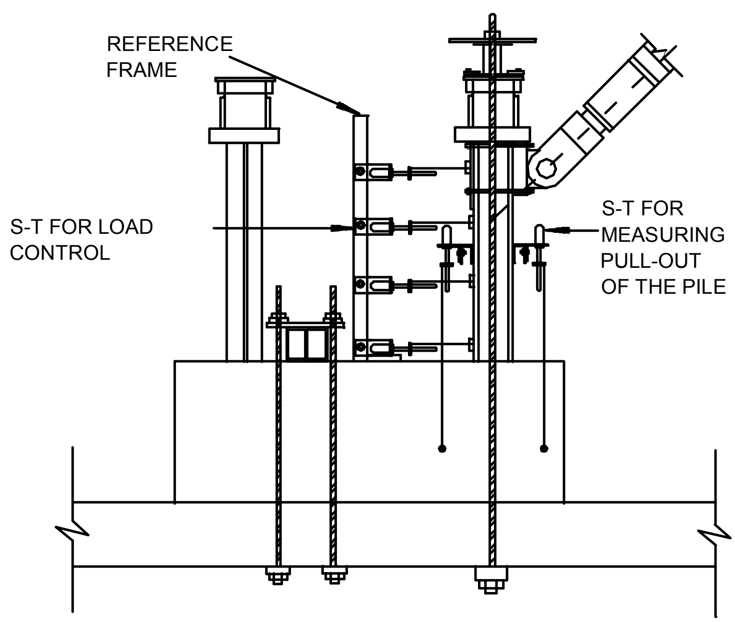

(b) EXTERIOR PILE

Figure 3.21 Instrumentation Configuration

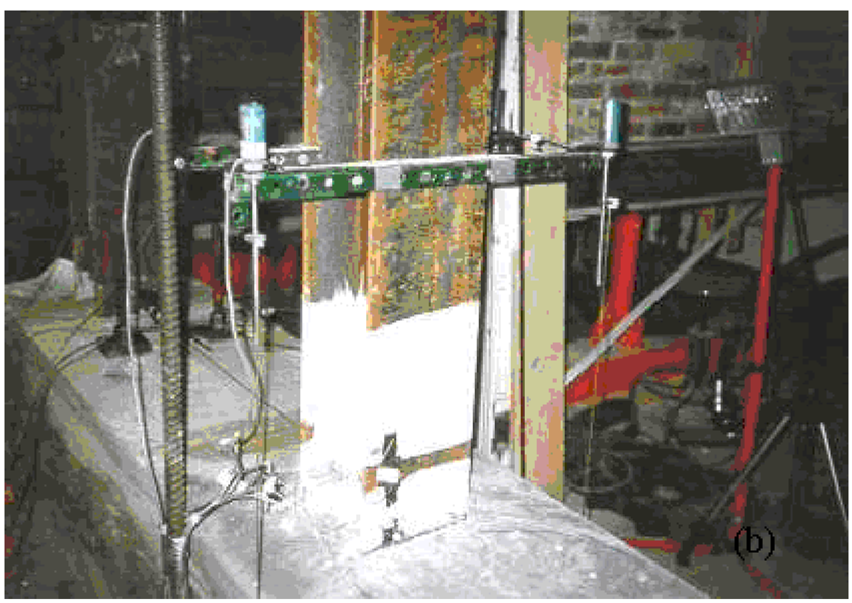

Figure 3.22 Instrumentation: (a) Lateral Displacement S-T, and (b) S-T for Measuring The pile Curvature and Pull Out

compare its outcome with the outcome from the displacement control sonic transducer. The middle sonic transducer was excluded from the pile foundation retrofitted specimen, as the length of the specimen was reduced to *686 mm*. All horizontal temposonics were mounted on a reference frame which was either anchored to the laboratory strong floor, or to the specimen.

Sonic transducers were also used to measure the rotation and "pull-out" of the pile, as shown in figure 3.22(b). Two tubular steel sections were clamped to the pile a distance of *610 mm* from the concrete pile cap surface. The sonic transducers were mounted at each end of the tubular reference frames providing a total of four instruments. During the test, the transducers measured linear translation, which could then be converted into rotation by accounting for the position of the transducer relative to the centerline of the pile. By taking the average of the four displacement values, it was possible to measure the vertical translation or "pull-out" of the pile relative to the cap beam.

3.7.2 Data Acquisition and Analysis

During the tests of the three pile specimens, an optim Megadac 5533A Data Acquisition system was used to collect and save the data in an ASCII format. The methods adopted in data analysis are outlined below.

The force and displacement data were obtained directly from the actuator load cell and the sonic transducers, respectively. The drifts were calculated using the relation:

$$\theta = \frac{\Delta}{L} \tag{3.13}$$

where, θ = the drift angle; Δ = displacement of top sonic transducer; and L= height of the pile measured from the cap beam surface to the transducer location at the centerline of the lateral actuator.

Curvatures and strains were calculated from:

$$\phi = \frac{\varepsilon}{L_P} \tag{3.14}$$

where:

$$\varepsilon = \frac{\Delta_p}{L_g} \tag{3.15}$$

in which Δ_p = the algebraic difference of the average readings of each pair of sonic transducers at each side of the pile; L_p = center-to-center distance between the transducers pairs measured along the longitudinal axis of the cap beam; and L_g = gage length.

Evaluation of Damping:

Effective damping (ξ_{eff}) in a structure can be viewed as a combination of equivalent viscous damping ξ_{eq}, and viscous damping inherent in the structure ξ_0 (assumed to be constant value of 0.05). The term ξ_{eq} represents the hysteretic damping provided by the nonlinear performance of the material and can be calculated as (Chopra 1995):

$$\xi_{eq} = \frac{1}{4\pi}\frac{E_D}{E_{so}} \tag{3.16}$$

where E_D = energy dissipated by damping (see figure 3.23), and E_{so} = maximum strain energy. According to figure 3.23a, E_D is evaluated as:

$$E_D = 4\Delta_y\Delta_{max}\left(K_0 - K_{eff}\right) \tag{3.17}$$

in which, Δ_y = yield displacement, Δ_{max} = maximum displacement, K_0 = initial stiffness, and K_{eff} = the secant stiffness (figure 3.23b) which can be written in terms of ductility ratio $\mu (= \Delta_{max} / \Delta_y)$ as:

$$K_{eff} = K_0 \left(\alpha + \frac{(1-\alpha)}{\mu} \right) \tag{3.18}$$

where $\alpha =$ post yield stiffness ratio. The maximum strain energy can be quantified as:

$$E_{so} = K_{eff} \frac{\Delta_{max}^2}{2} \tag{3.19}$$

Assuming an overall bi-linear response, as shown in figure 3.23a, the effective damping due to hysteresis can be determined by substituting equations (3.17) through (3.19) in equation (3.16) and rearranging, the equivalent viscous damping can be quantified as:

$$\xi_{eq} = \frac{2\eta}{\pi} \frac{(1-\alpha)\left(1 - \frac{1}{\mu}\right)}{(1 - \alpha + \mu\alpha)} \tag{3.20}$$

where η = efficiency factor defined as:

$$\eta = \frac{E_{cycle}}{E_{EPP}} \tag{3.21}$$

where E_{EPP} = the energy absorbed by a 100% perfect elasto-plastic system, defined according to the following relationship:

$$E_{EPP} = (F_n^+ + F_n^-)(x_p^+ + x_p^-) \tag{3.22}$$

where F_n^+ = the nominal capacity of the system in the push direction; F_n^- = the corresponding value in the pull direction; x_p^+ = the plastic component of the displacement in the push direction; and x_p^- = the corresponding value in the pull direction.

In the present study elastic-perfect plastic behavior will be assumed. Consequently, α is set to zero and equation (3.20) is simplified to:

$$\xi_{eq} = \frac{2\eta}{\pi}\left(1 - \frac{1}{\mu}\right) \tag{3.23}$$

The hysteretic energy absorbed by the system per cycle is given by:

$$E_{cycle} = \sum_{i=1}^{n}\left(\frac{F_i + F_{i-1}}{2}\right)(x_i - x_{i-1}) \tag{3.24}$$

where F_i = force in i-th step; and x_i = displacement of the same step.

The experimental effective viscous damping is defined according to UBC 1994 as:

$$\xi_{eff} = \xi_o + \xi_{eq} = \xi_o + \frac{1}{2\pi}\frac{E_{cycle}}{F_{max}\Delta_{max}} \tag{3.25}$$

where F_{max} = average of the maximum strength in the forward and reverse loading directions, and Δ_{max} can be evaluated as the average of the maximum displacement in both loading directions.

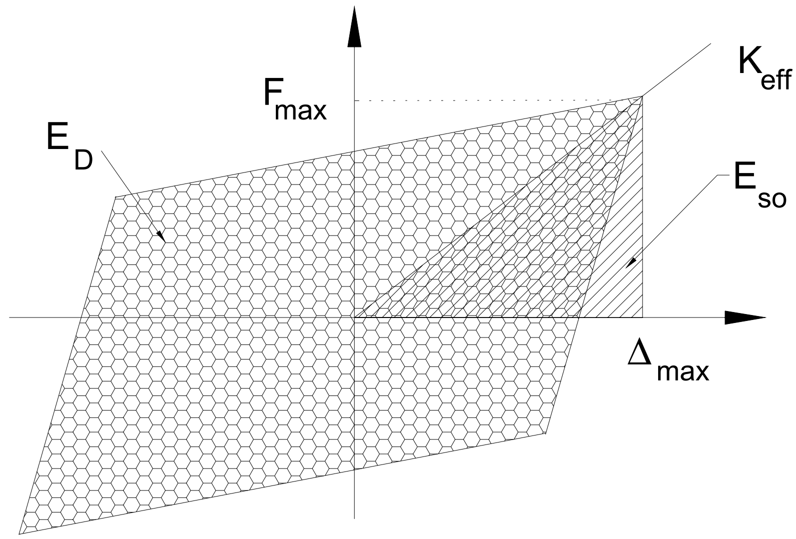

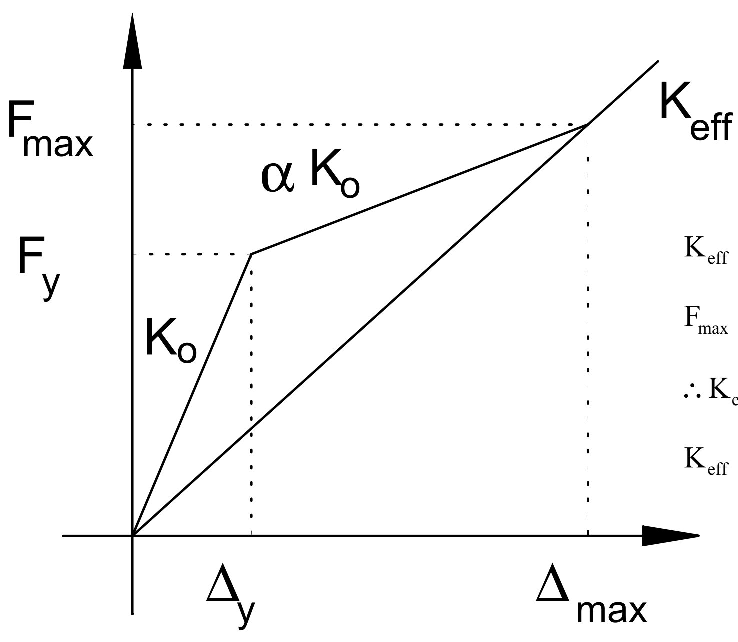

$$K_{eff} = \frac{F_{max}}{\Delta_{max}}$$

$$F_{max} = K_o \Delta_y + \alpha K_o \left(\Delta_{max} - \Delta_y\right)$$

$$\therefore K_{eff} = K_o \frac{\Delta_y}{\Delta_{max}} + \alpha K_o - \alpha K_o \frac{\Delta_y}{\Delta_{max}}$$

$$K_{eff} = K_o\left(\alpha + \left(1 - \alpha\right)/\mu\right)$$

Figure 3.23 Illustrating (a) Bilinear Representation of Cyclic Loops , and (b)Derivation of Effective Stiffness

Equation (3.20) and (3.25) are employed to evaluate the ductility ratio for different pile-to-cap connections tested in the present study. Details of these values will be discussed in the next two sections.

3.8 CLOSURE

In this section an experimental modeling strategy for steel H-pile-to-cap connections was outlined. The dimensions of the specimen were dictated by the anticipated translational plastic mechanism of the prototype. A method for simulating a variable axial load that accommodates the tension uplift conditions for exterior piles under lateral cyclic loads was presented. Through this method, the vertical actuator used to simulate the variable axial load is operated and controlled by the force output from the lateral actuator. The algorithm used to determine this relationship was described.

Coupon test results for the steel material used in the experiment as well as the 28 days compressive strength of the concrete used in the construction of all specimens were mapped. This was followed by, a description of the steps involved in the design, and construction of different test specimens.

The experimental test rigs, and instrumentation employed in all the experiments conducted through this study were explained through the aid of diagrams and photographs. Lastly, the methods used for analyzing and processing the experimental data were outlined.

SECTION 4
EXPERIMENTAL RESULTS FOR "AS-BUILT" SPECIMENS

4.1 SCOPE OF THE EXPERIMENTAL PROGRAM

This section outlines the experimental observations and results of the cyclic lateral load tests on the steel pile bents and pile foundation specimens. The main objective of these tests was to determine the performance of "as-built" specimens subjected to different cyclic loading regimes. These specimens are consistent with present "as-built" bridge practice in the eastern and central US.

Seven test specimens were investigated during this program to identify their seismic vulnerability. These specimens are as follows:

- Specimens S1: Strong Axis Interior Pile bent with No Axial Load.
- SpecimenS2: Strong Axis Interior Pile bent with Constant Axial Load.
- Specimen S3: Strong Axis Interior Pile bent with Constant Axial Load.
- Specimen W1: Weak Axis Interior Pile bent with Constant Axial Load.
- Specimen W2: Weak Axis Interior Pile bent with variable Axial Load.
- Specimen PS: Strong Axis Interior Pile foundation with variable Axial Load.
- Specimen PW: Weak Axis Interior Pile foundation with variable Axial Load.

Table 4.1 summarizes the axial loads and drift information for all the "as-built" specimens.

The experimental program consisted of testing the specimens at cyclic drift amplitudes which ranged from $\pm 0.5\%$ to 6%. Each of the specimens was tested for a minimum of two cycles per drift amplitude. Testing was conducted under displacement control where the specimens were first pushed then pulled. The command signal was provided by an analog function generator in the form of a positive sine wave with a cyclic period of one-minute.

Table 4.1 Characteristics of As-Built Test Specimens

Spec ID	Type	Gravity Load (kN)	Spec. Length (mm)	$\frac{M}{Vd_p}$	Lateral Actuator Angle θ	Vertical Axial Load Control	Total Axial Load	Max. Drift	Number of Cycles at Max. Drift
S1	Bent	0	3050	12.5	0	0	0	5%	2
S2	Bent	250	3050	12.5	0	250	250	6%	10
S3	Bent	200	3050	12.5	24	$200 + 3.27\ P_{da}$	200+4.02V	5%	10
W1	Bent	250	2616	10.5	0	250	250	6%	10
W2	Bent	200	2616	10.5	35	$200+2.72\ P_{da}$	200+4.02V	7.5%	8
PS	Foundation	135	785	3	43	$135+0.276\ P_{da}$	135+1.3V	6%	2
PW	Foundation	135	785	3	43	$135+0.276\ P_{da}$	135+1.3V	5%	5

S = Strong Axis Bending; W = Weak Axis Bending

PS = Piles, Strong Axis; PW = Piles, Weak Axis

V = $P_{da} \cos\theta$; M = Applied moment

4.2 General Observations

Pile Bent specimens (S1, S2, S3, W1, W2) behaved elastically prior to 2% drift. Pile bents oriented along the strong axis direction (S1, S2, S3) sustained higher drifts, and damage of the connection was concentrated mainly in the concrete cap beam. Pile bents tested along the weak axes bending (W1, W2) showed high performance in terms of ductility and energy absorption. Pile foundation specimens (PS, PW) behaved elastically prior to 0.5% drift and experienced fracture in the concrete cap in a brittle failure mode during the 2% drift .

To allow comparison of plots of the experimental results and the theoretical predictions, dashed lines representing the plastic moment capacity, and yield capacity are superimposed on the force -displacement plots. The theoretical yield and plastic moment capacities were defined using the well known relationships for bending moment:

$$M_y = V_y L = f_y S \tag{4.1}$$

and

$$M_P = V_P L = f_y Z_P \tag{4.2}$$

in which, f_y = the steel pile section yield stress; L = the lever arm; S = the steel pile section modulus; Z_P = the plastic modulus of the steel pile section; and V_p, V_y are the plastic and yield shear force, respectively. Those forces, however, were reduced or increased to account for the P-Δ for specimens tested under varying axial loads.

The experimental "yield" displacement is defined as an extrapolation to 1.0 V_p of the observed displacement at 0.75 V_p. The average value obtained from the forward and reverse directions of the first cycle of loading is used to define the experimental " yield " displacement.

4.3 Force-Displacement Results

4.3.1 Specimen S1: *Strong Axis Interior Pile with No Axial Load*

This specimen was tested under reverse cyclic lateral load along its strong axis; no vertical (axial) loads were applied to the pile. The loading was applied through a *250 kN* MTS servo-hydraulic actuator operated in displacement control, and mounted at a height of *3050 mm* above the concrete base surface. This was to investigate the likelihood of the pile "walking out" of its socket when the adhesive bond between the concrete in the cap beam and the steel pile was lost.

This specimen was tested with two reversed cycles at drift amplitudes of $\pm$ 0.5 %, $\pm$1%, $\pm$2%, $\pm$3% , $\pm$5% and with four reversed cycles at $\pm$4%. The most significant finding of this test was that even without axial load, the yield moment of the pile was exceeded and the plastic capacity of the section was nearly achieved (see figure 4.1). Yielding of the section first occurred just prior to the 2% drift level. At this point, damage to the connection was concentrated mainly in the pile with diagonal yield lines visible on the whitewashed flanges. Upon higher drifts, the damage occurred entirely in the concrete cap beam. Shear cracks formed in the concrete starting at the flange tips, emanating away from the pile at approximate 45^0 toward the edge of the beam. These cracks propagated down the side of the cap beam crossing each other about the mid-depth of the beam. The marked "pinching" of the force displacement plot is indicative of concrete crack propagation, which progresses by alternately opening and closing during the course of cyclic testing. Gaps formed between the face of the steel flanges and the adjacent concrete as the concrete crushed due to the high local bearing stresses. The "pinching" shown in figure 4.1 evidenced the significant cracking of the cap beam. The cracks opened and closed during the course of testing. On the pull side of the third cycle at the 4% drift level, a general shear failure occurred in the concrete on the tension flange side. The concrete near the flange became so loose that it could not provide sufficient bearing resistance for the flanges and the moment capacity dropped dramatically. Only two cycles at the 5% drift level were performed, as at that stage the loss of the connection strength was noticeable. A photograph of specimen S1 at the end of the test is shown in Figure 4.2.

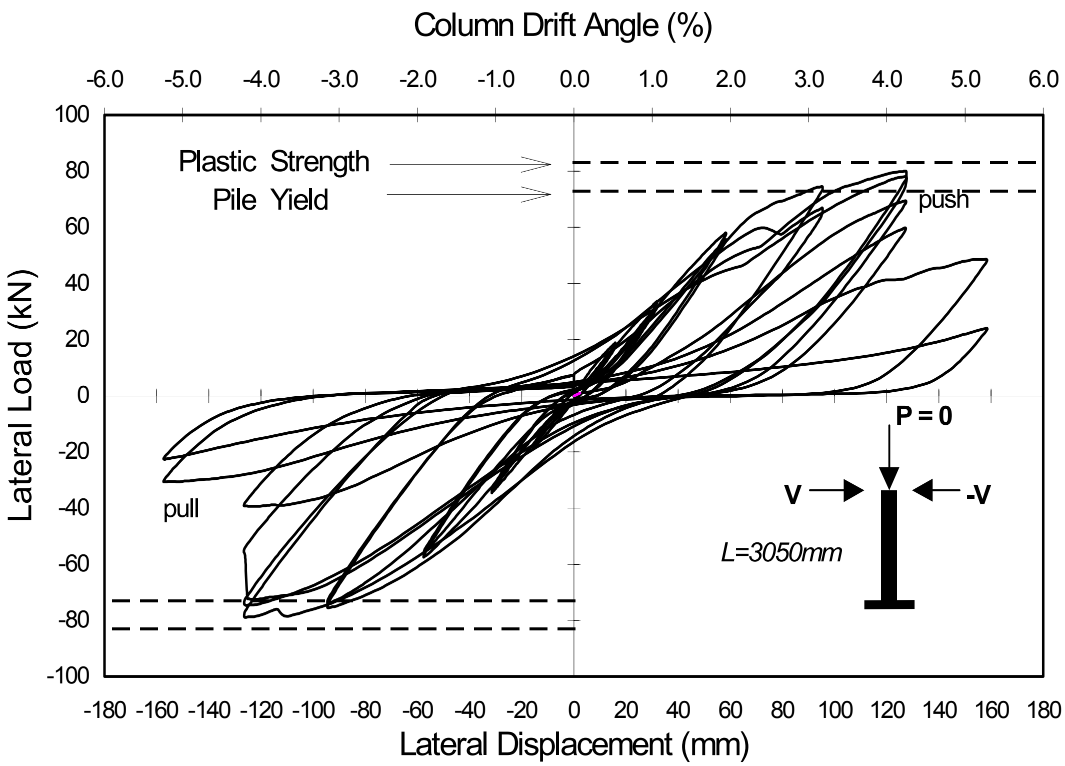

Figure 4.1 Pile Specimen S1: Lateral Load-Displacement Relationship

Figure 4.2 Connection S1 after Being Tested

4.3.2 Specimen S2: *Strong Axis Interior Pile with Constant Axial Load*

In addition to the lateral cyclic loading along the strong axis of the specimen, this specimen was also tested under a constant axial load. The 350 *kN* Parker servo-hydraulic actuator applied a constant axial load of 47 *kN* which was transferred through the lever beam arm action to the pile. This resulted in a *250 kN* axial force being transferred to the pile. This axial force is considered to be representative of the gravity load the bridge superstructure transfers to a steel pile within a bent. Specimen S2 was expected to perform somewhat better than specimen S1 as the axial load inhibited the "walk-out" phenomenon.

Specimen S2 was tested with two reversed cycles at drift amplitudes of $\pm 0.5\%$, $\pm 1\%$, $\pm 2\%$, $\pm 3\%$, $\pm 4\%$, $\pm 5\%$ concluding with ten cycles at $\pm 6\%$. The force-displacement behavior is shown in figure 4.3. The specimen behaved in an elastic manner prior to the 2% drift level at which point yielding occurred in the steel. Most of the deformation occurred in the steel pile for this test, and the gradual increase in capacity was attributed due to the steel strain hardening upon cyclic loading. Because the connection still had a large moment capacity remaining after the 5% drift test, it was decided to perform the constant, high amplitude test phase at the 6% drift level. Ten cycles were completed at 6% drift until failure in concrete was reached. A general observation for this specimen is that its hysteretic performance showed much more energy dissipation per cycle than specimen S1 (i.e. less "pinching of the hysteresis loop).

There was a balance between the moment capacity of the steel pile and the strength of the connection joint itself. Providing a compressive axial load increased the strength of the connection. The axial load effectively held the steel into the socket formed in the concrete, and created a moment opposing the overturning moment induced by the lateral load around the pile embedded tip. Once relative displacement occurred between the steel and concrete, the bond was rapidly reduced. The concrete surface at the interface was polished smooth by the slipping surfaces of the two materials (this effect was observed when the pile was removed following the test in order to repair the cap beam). While the adhesive bond remained intact and the connection strength

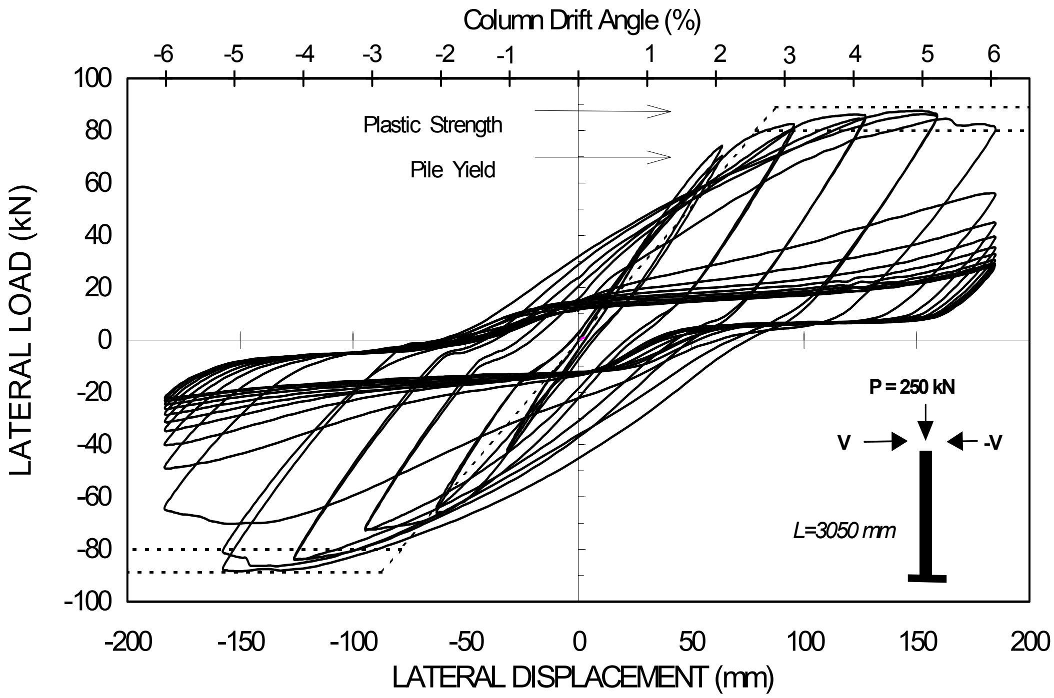

Figure 4.3 Pile Specimen S2: Lateral Load-Displacement Relationship

(M_j) exceeded the strength of the pile, the majority of the overall deformation arose primarily through ductile deformation of the steel. However, once the adhesive bond was lost, such that $M_j < M_p$, the rocking motion of the steel pile rapidly degraded the concrete, forming cracks which eventually failed the connection (see Figure 4.4). Even though the plastic moment capacity of the steel pile was achieved initially, significant cracking and spalling of the concrete pile cap beam occurred with continual cyclic loading and resulting in strength degradation.

4.3.3 Specimen S3: *Strong Axis Exterior Pile with Variable Axial Load*

Specimen S3 shown under load in Figure 4.5 was tested along the strong axis, under a variable axial load to investigate the effect of tension uplift on an exterior pile in a bent. The loading regime consisted of a *250 kN* MTS servo-hydraulic actuator inclined at 24^0 to the horizontal pushing downwards, together with a 350 *kN* Parker servo-hydraulic vertical actuator pulling downwards. The algorithm described in section 3.3 and governed by the equations shown in table 4.1 was employed to simulate the variable axial load during lateral cyclic loading.

This specimen was tested with two reversed cycles at drift amplitudes of $\pm 0.5\%$, $\pm 1\%$, $\pm 2\%$, $\pm 3\%$, $\pm 4\%$ concluding with ten cycles at $\pm 5\%$. The axial load varied between the net tensile force of *45 kN* to a net compressive force of *490 kN*, the axial load at zero displacement being *200 kN*. For the small axial loads of the pull direction, the pile behaved similarly to the first specimen, as shown in figure 4.6. Crack closure was strongly evident for the return cycles at the lower lateral load values. For the push direction however, the behavior more closely followed that of the second pile. Higher lateral loads were needed to achieve the same drift levels in comparison to the pull direction. Yielding of the steel was pronounced at the 2% drift level with a load plateau evident at higher drifts.

The second phase of testing consisted of ten cycles at 5% drift. Interestingly, very little strength degradation was seen for this phase of the test. This high ductility can be attributed to the limited cracking damage in the concrete cap beam. The cracks formed were

Figure 4.4 Connection S2 after Being Tested: Top shows the Gap created between the Steel Pile and Cap Beam; Bottom shows Side View

Figure 4.5 Specimen S3 under Test Along its Strong Axis

stable and did not propagate over a wide area, as in the first two tests (see the photograph of the specimen after test in figure 4.10). The slightly higher degree of confining reinforcement on the end of the cap beam, as compared to the interior piles, is responsible for maintaining the integrity of the concrete during the cyclic tests. Due to shortcomings of the test rig, the test of Pile Specimen 3 was not continued sufficiently to reach the ultimate failure capacity of the connection.

Figure 4.9 plots a lateral load-axial load interaction diagram for Specimen S3. The ultimate strength interaction relationships assumed for I-section shapes bending along its strong axis is:

$$\frac{F_{pc}}{F_p} = 1.18\left(1 - \frac{P}{P_y}\right) \tag{4.3}$$

in which F_{pc} = the lateral load capacity for a given axial load, P, F_p = the unmodified lateral load capacity given by $F_p = M_p / L$ where M_p =plastic moment capacity and L = cantilever column height of the pile. The experimentally observed result is the inclined line adjacent to the vertical axis. Evidently, a maximum vertical compression load of 490 *kN* and a tension load of *45 kN* were attained. The axial load required to yield the gross cross-section of the pile, P_Y, is 2510 *kN*.

4.3.4 **Specimen W1:** *Weak Axis Interior Pile with Constant Axial Load*

This specimen was tested to study the cyclic performance of interior piles oriented along the weak axis. The specimen was tested before under the same conditions as specimen S2. The lateral actuator was mounted at 2616 mm above the concrete base surface and connected to an adapter steel section, which was connected to the specimen. This specimen was expected to perform better than specimen S2, as the connection efficiency in this case is higher than in case of strong axis orientation. Figure 4.9a shows this specimen under test.

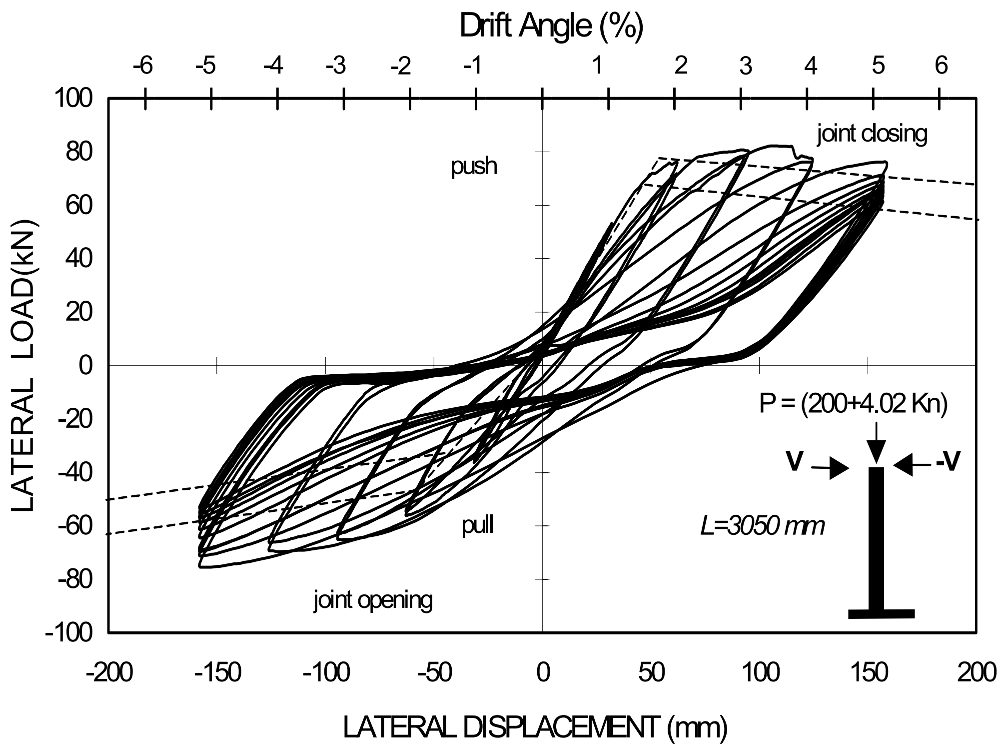

Figure 4.6 Pile Specimen S3: Lateral Load-Displacement Relationship

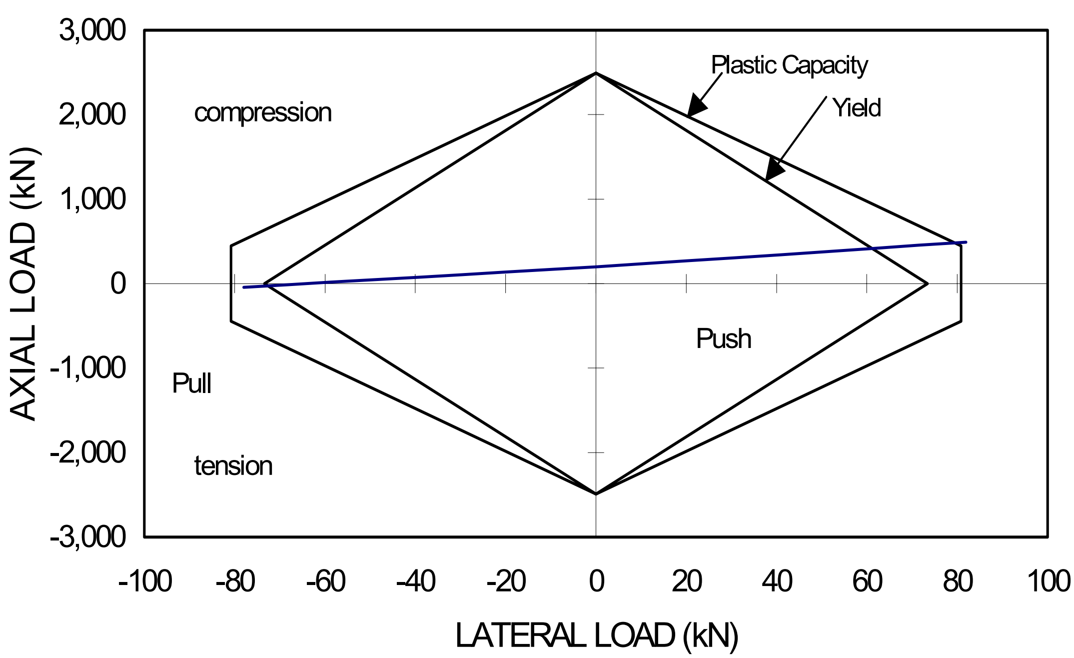

Figure 4.7 Experimental and Theoretical Lateral Load-Axial Load Interaction Diagram For Specimen S3

Figure 4.8 Connection S3 after Being Tested

Specimen W1 was tested with two reversed cycles at drift amplitudes of $\pm 0.5\%$, $\pm 1\%$, $\pm 2\%$, $\pm 3\%$, $\pm 4\%$, $\pm 5\%$ concluding with twelve cycles at $\pm 6\%$ drift. The steel performance rather than the concrete behavior governed the overall behavior of the connection. Therefore, the connection showed a perfect performance in terms of energy absorption and ductility (see figure 4.10).

The maximum lateral force attained for this specimen was 48 *kN,* and 46 *kN* in the push and pull directions, respectively. The expected performance of the steel material under cyclic loading was achieved during this experiment. Up to *2%* drift the specimen behaved in an elastic fashion. Yielding occurred first at the push of the first cycle of 3% drift, at the flanges, through a distance extended 100 *mm* above the concrete cap beam surface. This yielding extended to another *100 mm* during the *4%* and *5%* drifts. This was accompanied with a noticeable work hardening of the steel material. Local buckling was pronounced in both flanges during the pull of the second cycle of the *6%* drift. At this point it was noticed that the connection could undergo more cycles until the strength degradation of the steel material is achieved. Therefore, it was decided to carry out twelve more cycles of 6 *%* drift. Strength degradation was noticeable at the third cycle and continued through the rest of the cycles. A photograph of the connection after the test is shown in figure 4.11.

4.3.5 Specimen W2: *Weak Axis Interior Pile Under Variable Axial Load*

This specimen was tested along the weak axis under the same conditions as Specimen S3 to investigate the effect of tension uplift on exterior piles oriented on that direction. The specimen was less in height than specimen S3. Accordingly, the lateral actuator was mounted at an 35^0 angle, and the vertical actuator-lateral actuator load relationship was modified to accommodate the difference in inclination and achieve the same loading conditions as specimen S3. Figure 4.9b shows this specimen under test.

Figure 4.9 of Specimens W1 and W2 under Test Along their Weak Axes (a) Specimen W1, and (b) Specimen W2

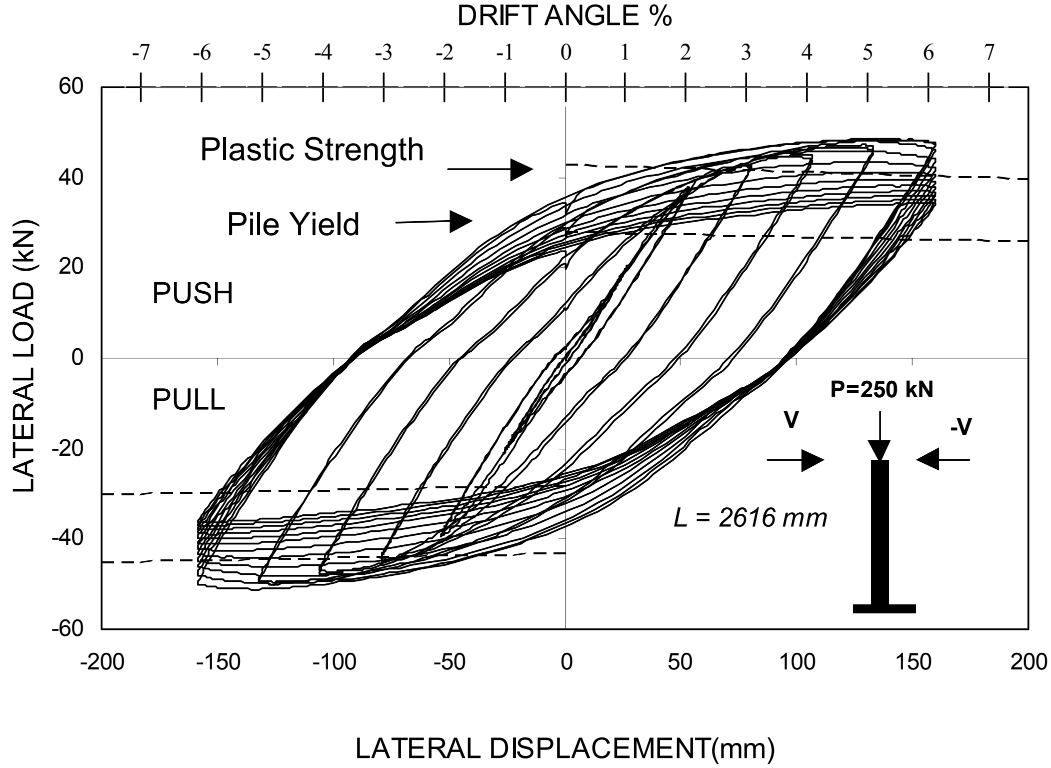

Figure 4.10 Pile Specimen W1:Lateral Load -Displacement Relationship

Figure 4.11 Connection W1 after Being Tested

The specimen was tested with two cycles of drift at levels of $\pm$ *0.5%,* $\pm$ *1%,* $\pm$ *2.5%,* $\pm$ *3.5%,* $\pm$ *5%,* $\pm$ *6%,* and 8 cycles at $\pm$ *7.5%* (see figure 4.12). The overall performance of the connection was governed by the steel behavior up to *6%* drift. Most of the deformation occurred in conforming to typical steel behavior. The maximum force attained in the push direction was *51kN*. The maximum pull force, however, was *64 kN*.

The specimen behaved in an elastic fashion prior to 2.5 % drifts. Yielding of the flanges, in the push direction, was noticeable at the first cycle of 2.5 %. This was characterized by some diagonal striations on the white washed flanges. During the *3.5%* drift these striations continued to spread in the flanges through a 150mm length above the concrete cap beam surface. As shown in figure 4.13, work hardening was observable to the end of the second cycle of the *5%* drift. At this drift level, yielding was noticeable over a distance of *350mm* from the concrete surface. Local buckling of the flanges took place during the push of the second cycle of the 6% drift. At this point it was obvious that strength degradation of the steel material started to occur. Two more cycles were tried at *7.5%* drift. Two Cracks appeared in the concrete, during the push of the first cycle at that drift, and emanated from the pile towards the transverse cap beam, and propagated down to the lower concrete cap beam surface. A sudden loss of strength took place in hysteretic loops companioning the crack growth, during the pull of this cycle. Other cracks emanated from these two basic cracks during the second cycle at 7.5% drift, and pinching of the loops was noticeable. Six more cycles were conducted at that drift level. The cracks opened and closed during the course of these drifts. It was obvious by the end of the sixth drift that the connection reached its ultimate capacity, and failure occured. Photographs of this connection after the experiment are shown in figure 4.15.

The ultimate strength interaction relationships for I-section shapes bending along its weak axis is governed by the following equation:

$$\frac{F_{pc}}{F_p} = \left[1 - \left(\frac{P}{P_y}\right)^2\right] \tag{4.4}$$

Figure 4.12 Specimen W2 Under 7.5% Drift During Testing

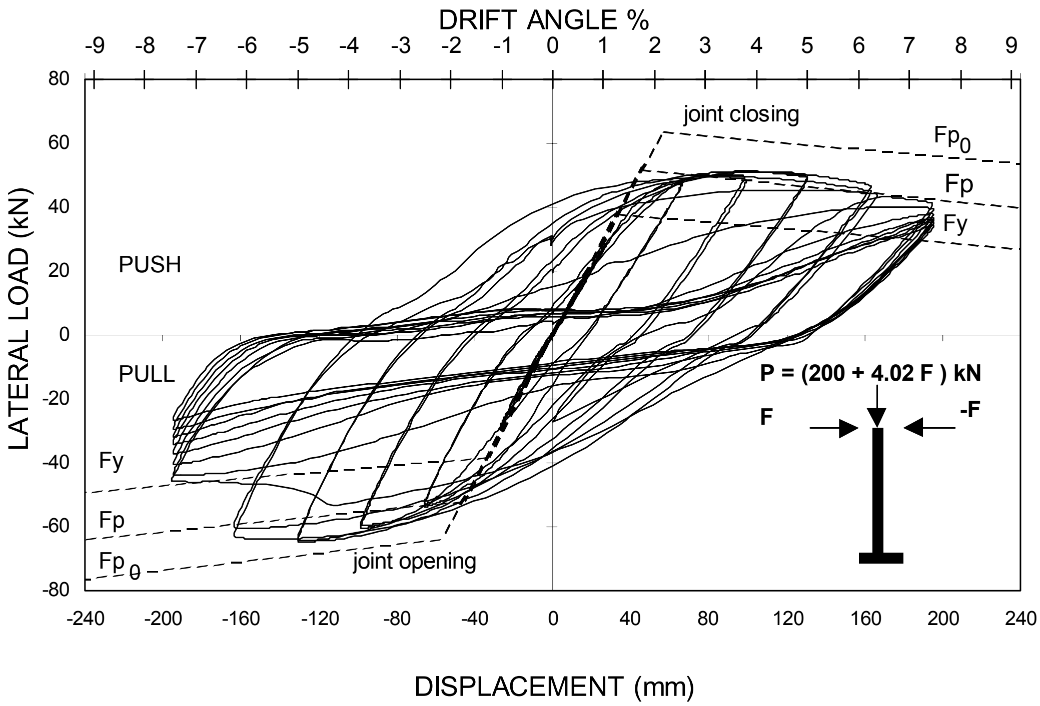

Figure 4.13 Pile Specimen W2: Lateral Load-Displacement Relationship

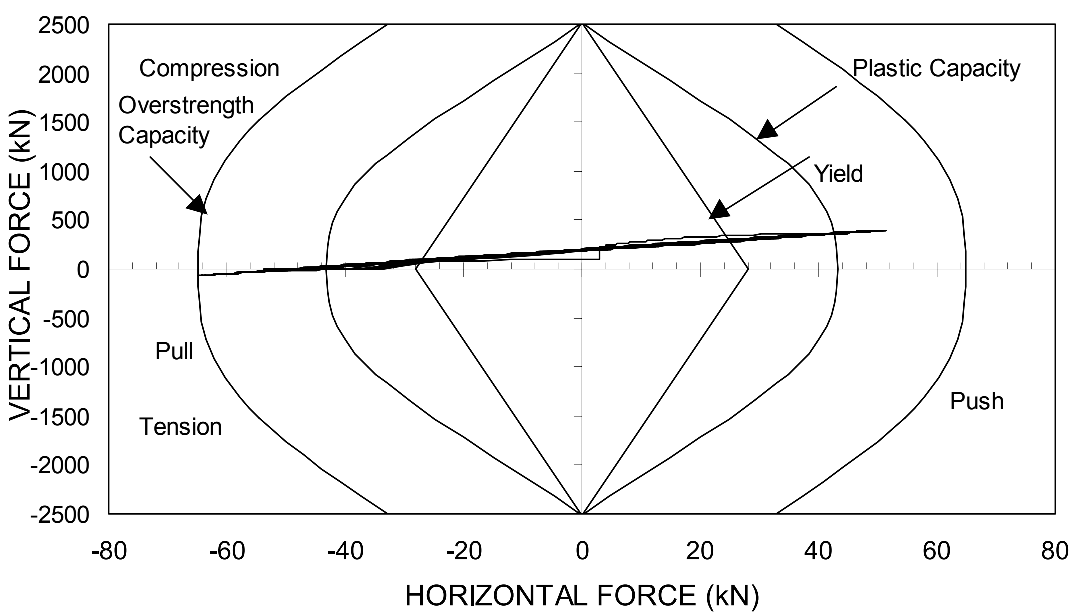

Figure 4.14 Experimental and Theoretical Lateral Load-Axial Load Interaction Diagram For Specimen W2

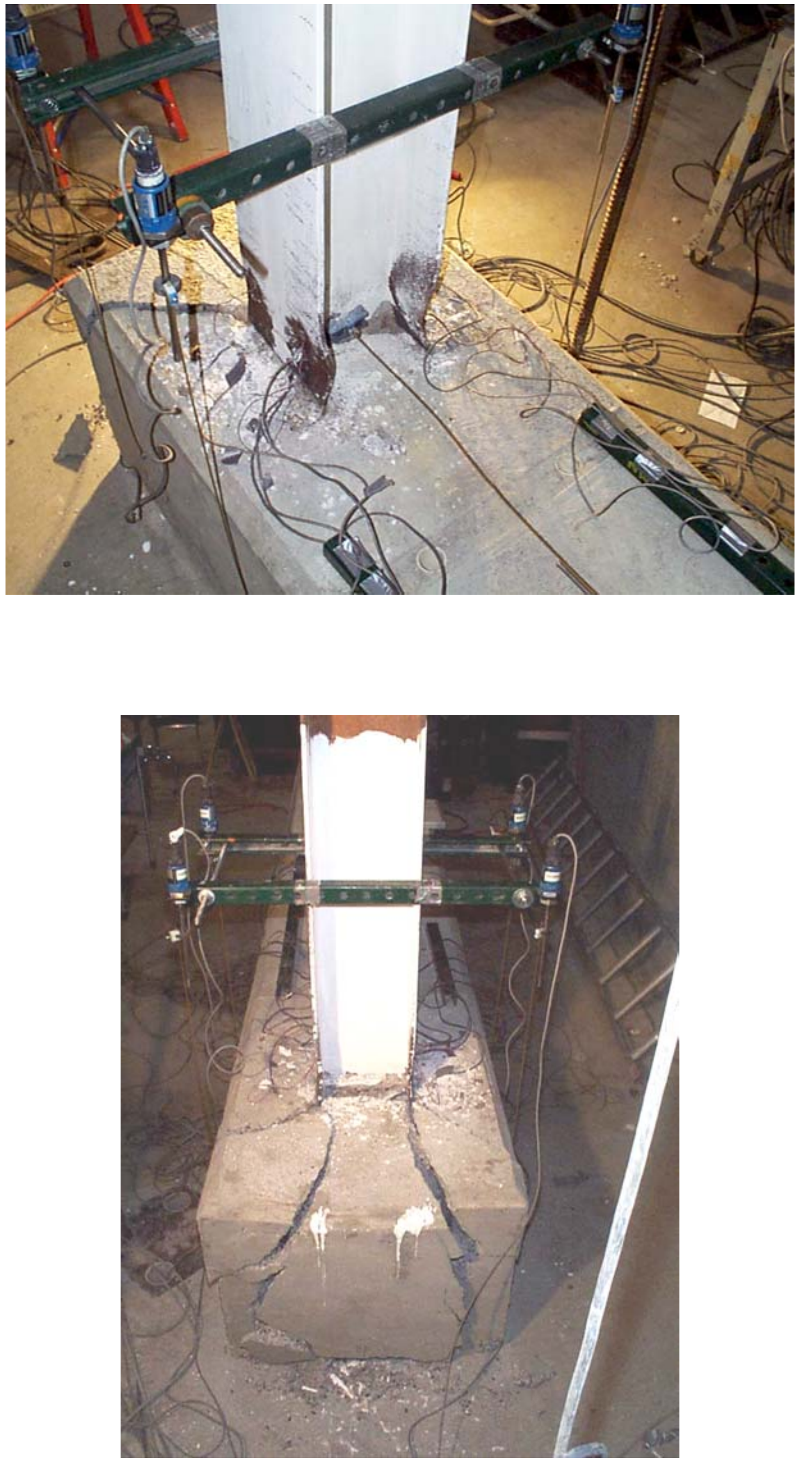

Figure 4.15 Damage Occurred to Connection W2 after Test.Top Photograph shows an end view. Lower Photograph Shows a side view including the damage occurred to the cap beam

Figure 4.14 plots a lateral load-axial load interaction diagram for Specimen W2. The maximum compression and tension forces 397 kN, and 65 kN respectively were achieved during the push of the first cycle at 6% drift companioning, the extreme work hardening of the steel material. This specimen showed a superior performance compared to specimen S3, tested under same conditions along the strong bending axis, as the maximum tension uplift force was higher in this case without any detectable walking out of the pile from the socket

4.3.6 Specimen PS : *Strong Axis Exterior Pile with Variable Axial Load*

Specimen PS represents an exterior pile foundation with a typical pile cap connection. The specimen was tested along its strong axis orientation with a variable axial load considered to be representative for this class of piles as shown in Figure 4.16a. The *1100 kN* MTS servo-hydraulic actuator operated in displacement control and mounted at an angle of 43^0 was used to induce the lateral load. The 350 kN Parker servo-hydraulic vertical actuator induced the variable axial load. Both actuator outputs are related to induce a total axial load governed by the equation shown in Table 4.1. The specimen had a clear height of *785 mm* $\left(\mathrm{M}/\mathrm{Vd}_{\mathrm{p}}=3\right)$ above the concrete base surface.

This specimen was tested with two reversed cycles at drift amplitudes of $\pm 0.25\%$, $\pm 0.5\%$, $\pm 1\%$, $\pm 2\%$, $\pm 3\%$, $\pm 4\%$ and 5% drift. It exhibited the most inferior performance among all other specimens tested during the course of this study. The 285 kN theoretical yield force of the steel pile section was not attained.

The specimen behaved linearly prior to the *1%* drift amplitude. A sudden brittle failure of concrete was pronounced at the push of the first cycle at the *2%* drift. This failure was characterized by two wide cracks formed in the concrete starting at the flange tips and propagated away from the pile towards the beam transverse edge to a *450 mm* distance above the concrete lower surface. During the second cycle at the *2 %* drift amplitude, a second transverse crack propagated along the beam transverse edge to connect the two points where the other two cracks stopped.

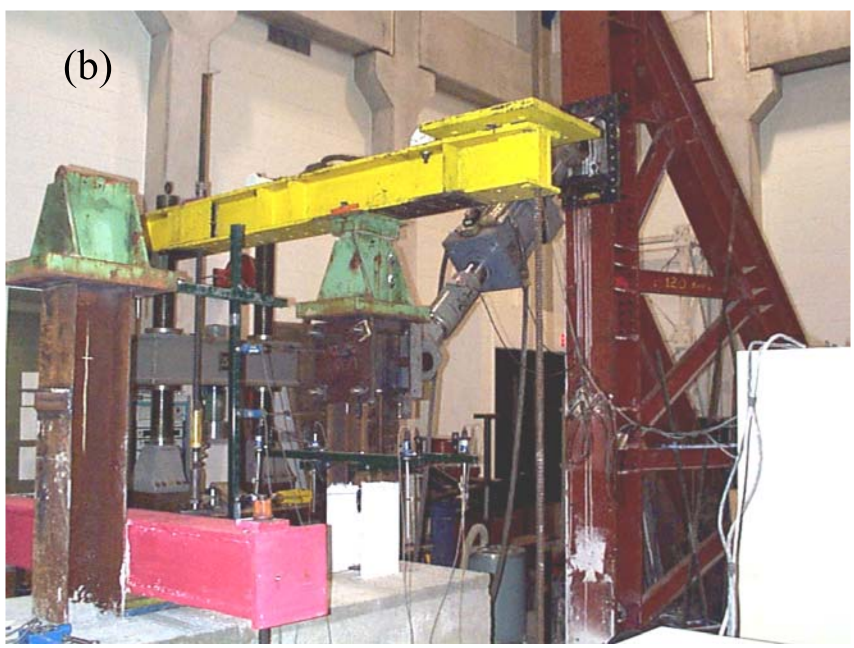

Figure 4.16 Specimen PS and PW under Test Along their Strong and Weak Axes (a) Specimen PS, and (b) Specimen PW

This failure was accompanied with a 30% loss of strength in the hysteretic load-displacement loops (see figure 4.17). Cracks widening growth continued during the course of the 3% drift and the opening of the cracks was noticeable during the push. The pinching shown in figure 4.17 evidenced the significant cracking of the pile cap. During the course of the 4% and 5% drifts, slipping of the steel section within the embedment zone was apparent as the pile walked out of the socket. Failure of the connection was evident by the end of the second cycle at *5%* drift. Photographs of this failure are shown in figure 4.19.

The theoretical as well as the experimental lateral load-axial load interaction relationships of this specimen are presented in figure 4.18. A maximum vertical compression load of *430 kN* and a tension load of *176 kN* were attained. The maximum tension uplift experienced during this experiment was during the pull of the first cycle of *2%* drift. Although the value of 176 *kN* tension was very large compared to the values attained for the pile bent experiments, this force, however, did not cause any slipping of the pile out of the concrete at the 2% drift. Slipping occurred later at 4% drift as a result of the breaking down of the bond between the steel and concrete.

4.3.7 Specimen PW : *Weak Axis Exterior Pile with Variable Axial Load*

Specimen PW was tested with two reversed cycles at drift amplitudes of $\pm 0.25\%$, $\pm 0.5\%$, $\pm 1\%$, $\pm 2\%$, $\pm 3\%$, $\pm 4\%$ and concluded with five reversed cycles at 5% drift. The overall connection behavior was governed by the steel performance up to the end of the *2%* drift test. The steel section flanges exhibited an inelastic behavior at the push of the first cycle during the 2% drift. This was characterized by visible yield lines, on the whitewashed compression flanges, along a distance of *159 mm* above the concrete cap surface. At 3% drift, during the pull cycle, a sudden brittle failure occurred, accompanied by a loss of strength of about 75 kN (see figure 4.20). Two wide cracks occurred in the concrete cap beam at the flange tips and emanated towards the transverse edge of the concrete beam. Loss of strength continued during the 4% drift test, when a second transverse crack propagated along the transverse edge to join the first crack at two points.

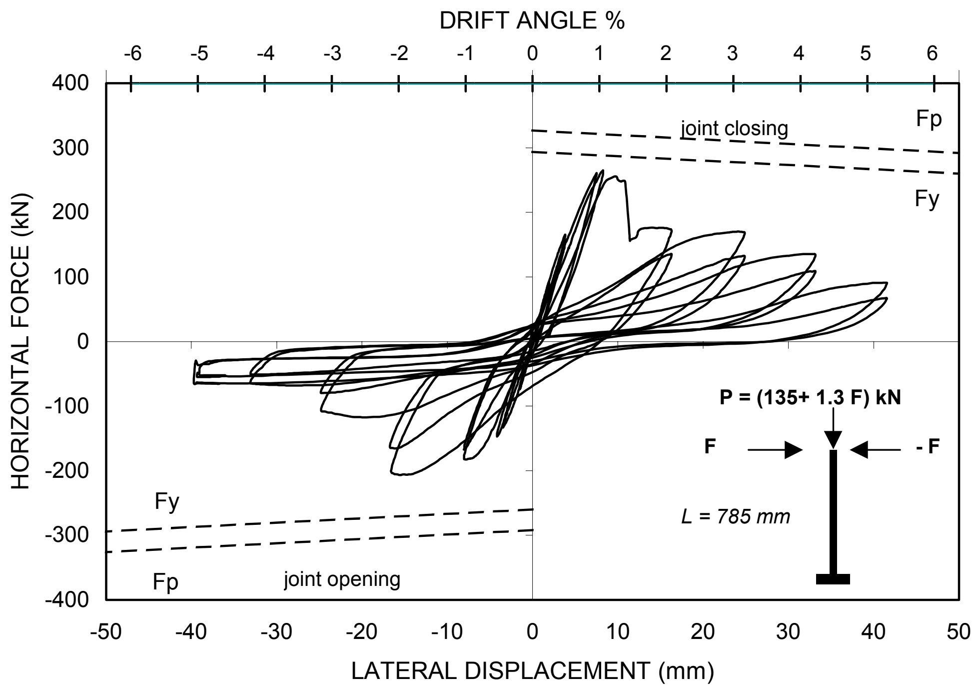

Figure 4.17 Pile Specimen PS Lateral Load-Displacement Relationship

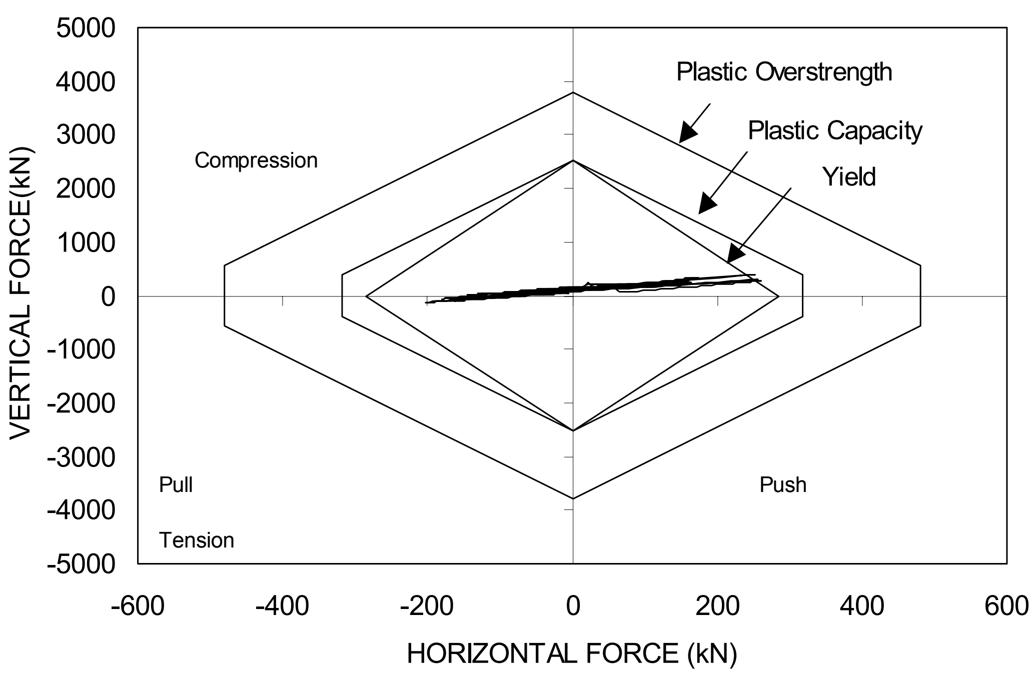

Figure 4.18 Experimental and Theoretical Lateral Load-Axial Load Interaction Diagram For Specimen PS

Figure 4.19 Connection PS after Being Tested. Top shows an end view including the damage occurred to the cap Beam.Lower Photograph shows a side view

It was decided to perform five more drifts at the 5% level. An obvious slipping out of the steel section from the concrete occurred during the pull of the first cycle of that test. This slipping was accompanied by centralization of cracks along the region of contact between concrete and steel. It was apparent, by the end of the fifth cycle at this drift, that the connection had no more resistance. Photographs of this specimen after failure are illustrated in figure 4.22.

Figure 4.21 plots the theoretical and experimental lateral load-axial load interaction diagrams for this specimen. The maximum tension uplift occurred during the pull of the second cycle at 2% drift. The maximum lateral force associated with this tension force was 167 kN. However, the concrete in the vicinity of the web was not cracked yet, and had a sufficient bearing resistance to sustain this uplift force. Accordingly, slipping of the pile out of the socket did not occur at that load level. It can be extracted from the figure that this specimen exhibited an average maximum overstrength factor of 1.17.

4.4 DISCUSSION OF EXPERIMENTAL RESULTS

The significance of the presence of the axial load on the experimental performance can be explored by comparing the behavior of specimens S1 tested without axial load and specimen S2 tested with constant 250 kN axial load. The first noticeable difference was the higher initial stiffness of the connection with axial load. Both specimens behaved in an elastic manner prior to to the 2% drift level at which point yielding occurred in the steel. However, more load was required for specimen S2 to reach this displacement. A general observation for this specimen is that its hysteretic performance showed more energy dissipation per cycle than specimen S1 (i.e. less "pinching of the hysteresis loop). The different behavior exhibited by these two test specimens illustrated the significant influence of axial load on the strength of the connection.

Due to their lesser strength, weak axis specimens showed a superior performance with respect to strong axis specimens. As an example, specimen W1, tested along its weak

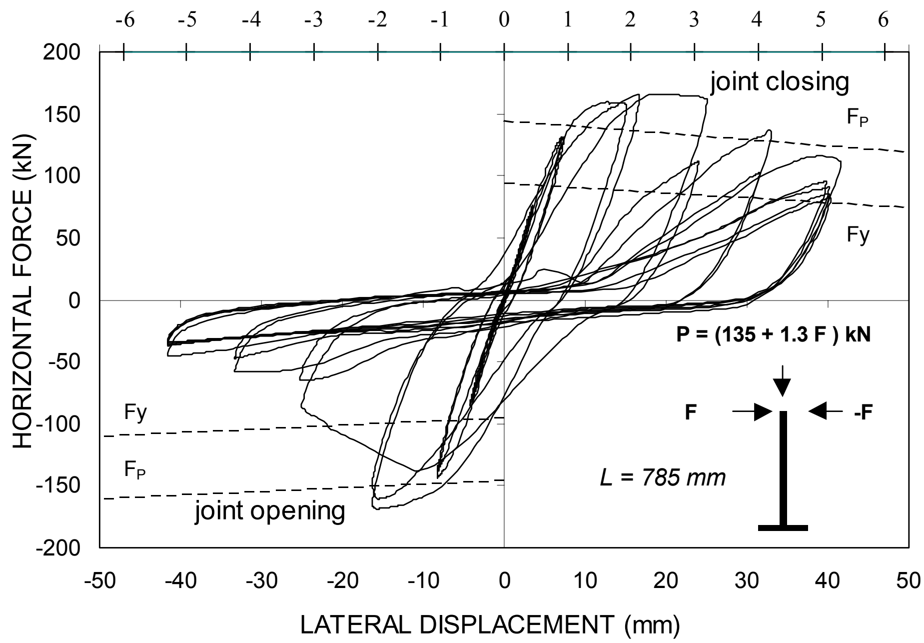

Figure 4.20 Pile Specimen PW :Lateral Load-Displacement Relationship

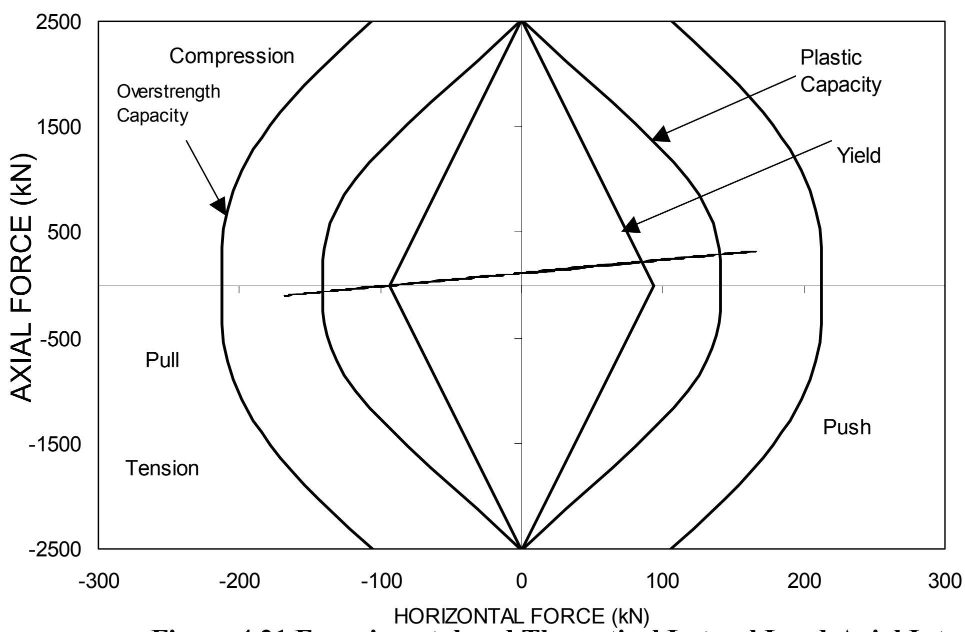

Figure 4.21 Experimental and Theoretical Lateral Load-Axial Interaction Diagram for Speimen PW

Figure 4.22 Damage occurred to Connection PW after Being Tested

axis bending with a constant compressive axial load of *250 kN,* behaved in a better manner than specimen S2 which was tested under the same conditions but along its strong axis. The steel performance rather than the concrete behavior governed the overall inelastic behavior of the connection. Compared to the maximum lateral force obtained for specimen S2 (88 *kN* in average) the maximum lateral force attained for specimen W2 was much less. Although the lever arm was less for this test than the strong axis test, the maximum force was 48 *kN,* and 46 *kN* in the push and pull directions, respectively.

Pile foundation specimens tested under varying axial loads showed a different performance than the pile bent specimens tested under similar conditions. The *786 mm* lever arm of these specimens was close to *0.25* of that of the pile bent specimens. Therefore, a shear failure mode was anticipated for such specimens. Both specimens PS and PW showed the most indigent behavior among other specimens tested through this experimental program. Specimen PW, however, exhibited better performance than specimen PS. Compared to specimen PS, specimen PW showed an improved performance, as the former did not exhibit any overstrength. This is attributed also to the lesser strength of this specimen, which is tested along its weak axis bending, than the strong axis-bending specimen PS.

A common failure in the form of damage to the concrete connection was obtained for specimens W2, PS, and PW. This failure was characterized by two wide cracks starting at the flange tips and emanating towards the concrete beam transverse edge. At higher drifts, a third transverse crack occurs on the transverse edge joining the two points where the other two cracks stopped.

A general observation for all the strong axis specimens that they failed in a non-ductile behavior due to damage in the concrete connection. Due to their lesser strength, the weak axis specimens, however, showed better performance. The connection efficiency, defined as the ratio of ultimate moment capacity of concrete pile connection to the nominal moment capacity of the steel pile, is used here for comparison. Adopting a

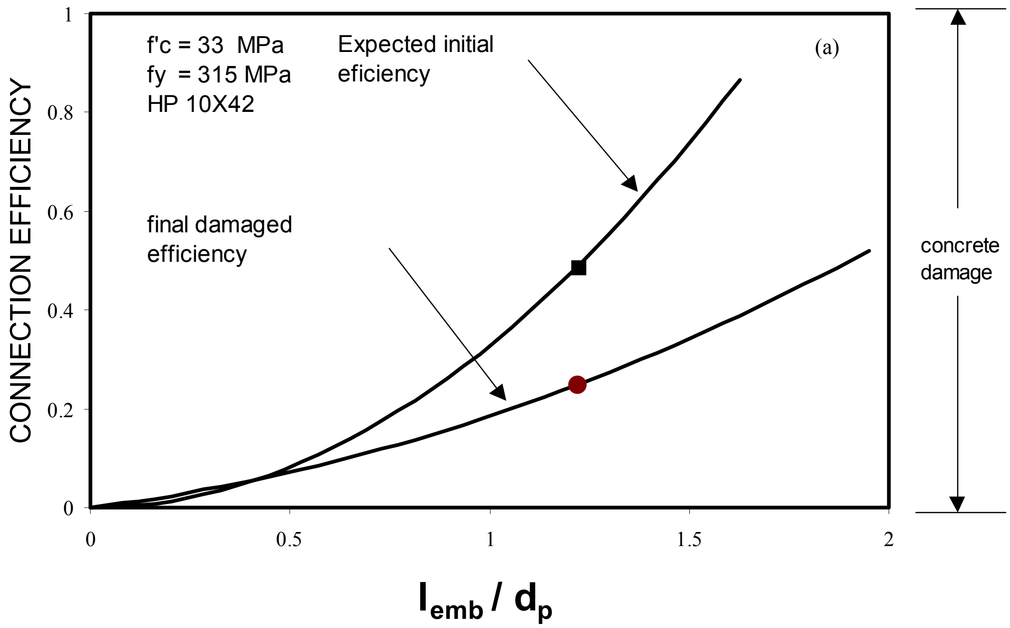

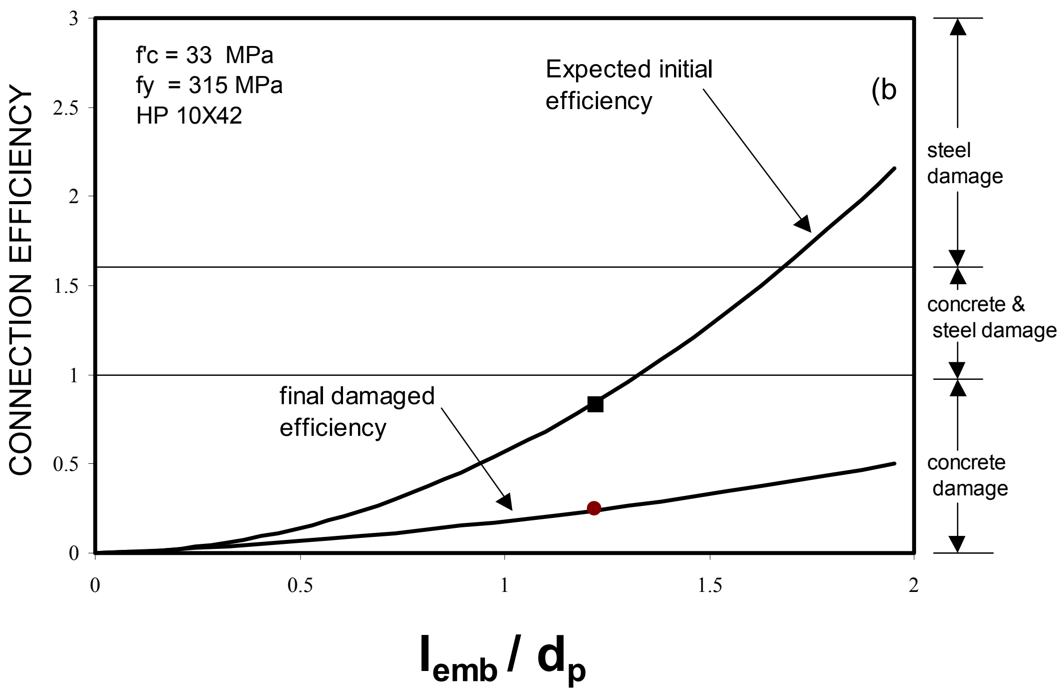

Figure 4.23 Comparison of Theoretical efficiency with Experimental Results: (a) Strong Axis Bending; and (b) Weak Axis Bending

value of $f_c = 0.85\ f_c^{'}$ and substituting in equation (2.47) the expected initial efficiency can be written as:

$$\rho_{ES} = 0.136\left(\frac{f_c^{'}}{f_y}\right)\left(\frac{d_p}{t_f}\right)\left(\frac{l_{emb}}{d_p}\right)^2 \tag{4.5}$$

The same approach used in deriving equation (4.5) was used to derive an equation for the elastic cracking efficiency for weak axis bending:

$$\rho_{Ew} = 0.255\left(\frac{f_c^{'}}{f_y}\right)\left(\frac{d_p}{t_f}\right)\left(\frac{l_{emb}}{b_f}\right)^2 \tag{4.6}$$

Figure 4.23 plots the relationship between the normalized embedment depth and the connection efficiency for both the strong and weak axis, using actual material and dimensional properties. The figure shows that strong axis specimens with embedment depth 300 mm would fail with damage mostly concentrated in concrete, which agrees well with what happened for strong axis experiments. The figure also shows that elastic efficiency for weak axis experiments are clod=se to unity which suggests initial damage in the steel section and then with the onset of strain hardening in the steel section the damage is expected to propagate into the concrete connection. This agrees well with what happened for specimens W2 and PW. The theory , however, was conservative in predicting the performance of specimen W1; this is presumed to be due to the in-situ concrete strength being greater than indicated by the test cylinders.

4.5 CLOSURE

The present section outlined the results of a series of experiments to determine the seismic vulnerability of existing pile-to-cap connections, characterized by small embedment depth of the pile inside the cap beam (*300mm*). Based on the results presented herein the following conclusions are drawn:

1. The experiments indicated that pile bent connections oriented along their strong axes bending failed in a non-ductile manner within the concrete pile cap. Therefore, these connections may be prone to damage under severe seismic loading, and hence, may be in need of retrofit.
2. Specimen S1, tested without considering any axial load exhibited the lowest performance among the pile bent specimens tested during the course of this experimental program.
3. Pile bent connections oriented along their weak axes of bending exhibited superior performance in terms of ductility and energy dissipation with respect to strong axis connections.
4. Pile foundation connections failed in the concrete beam in a non-ductile brittle shear mode.
5. The experiments demonstrated that predictions by both the cracked elastic and plastic theories give an adequate representation of the joint strength range.

SECTION 5
EXPERIMENTAL RESULTS FOR RETROFITTED PILE-TO-CAP CONNECTIONS

5.1 INTRODUCTION

Substructures consisting of either pile bents or pile foundations have been widely used in the construction of highway bridges throughout the United States. But the majority of these bridges were built two to three decades ago, when design of structures for current high seismic loads was not required. Moreover, the experimental study performed in this research on specimens simulating as-built substructures indicated that the pile-to-pile cap connection, a connection primarily designed for vertical loading, is very susceptible to damage from cyclic lateral loading. Therefore, in zones of moderate to high seismicity it is prudent to perform any properly designed seismic strengthening for this class of connection. It should be noted that a poorly conceived seismic retrofit might result in more disastrous consequences than if the structure had been left alone. Consequently, the primary focus of the retrofit scheme developed herein is to provide a more ductile connection that can possess a large deformation capability permitting dissipation of seismic energy in large earthquakes. Based on the experimental study on pile bents to cap connections tested along the weak axis of the pile group, it is evident that the pile-to-cap connections have an immense ductility capability, and thereby there is no need for retrofit. If, however, biaxial loading is of concern, then retrofit should be considered.

This section presents the experimental results of pile-to-cap connection that have been retrofitted with the aim of strengthening the shear-critical connection and ensuring plastification takes place only in the steel pile itself. This section first sets forth the seismic retrofit strategy in accordance with the design concepts advocated in section 2 and then goes on to present and compare the test results.

5.2 Construction of Retrofit

5.2.1 Strong Axis Bending Pile Bents

The embedment depth of the retrofitted specimen was determined using equation (2.79)

$$\frac{l_{emb}}{d_p} \geq 3.5\sqrt{\left(\frac{f_{su}}{f'_c}\right)\left(\frac{t_f}{d_p}\right)} \tag{5.1}$$

for a 35 MPa concrete and 315 MPa steel and using the dimensions of the HP 10X42 steel pile section, the total embedment depth was determined as 625 mm. The original specimen had an embedment depth = 300 mm. Therefore it was decided to use another 300 mm for the overlay depth.

The longitudinal reinforcement needed to close the anticipated gap between the steel section and the concrete cap beam during cyclic loading is determined according to equation (2.81):

$$A_s = \frac{V_P}{\phi f_{yh}} = \frac{0.6F_y d_P t_w}{\phi f_{yh}} = \frac{0.6x315.2x246x10.54}{0.85x413} = 1397mm^2.$$

$\therefore$ Use 4-25 mm diameter rebars (4#8, A_s = 1963 mm^2).

The size and number of stirrups that resist the shear force was determined by assuming 4 stirrups will resist the shear force. Therefore, according to equation (2.82)

$$V_{st} = \frac{0.50V_p}{n} = \frac{0.50x0.6x315.2x246x10.54}{4x1000} = 61.02kN$$

Substitute in equation (2.83)

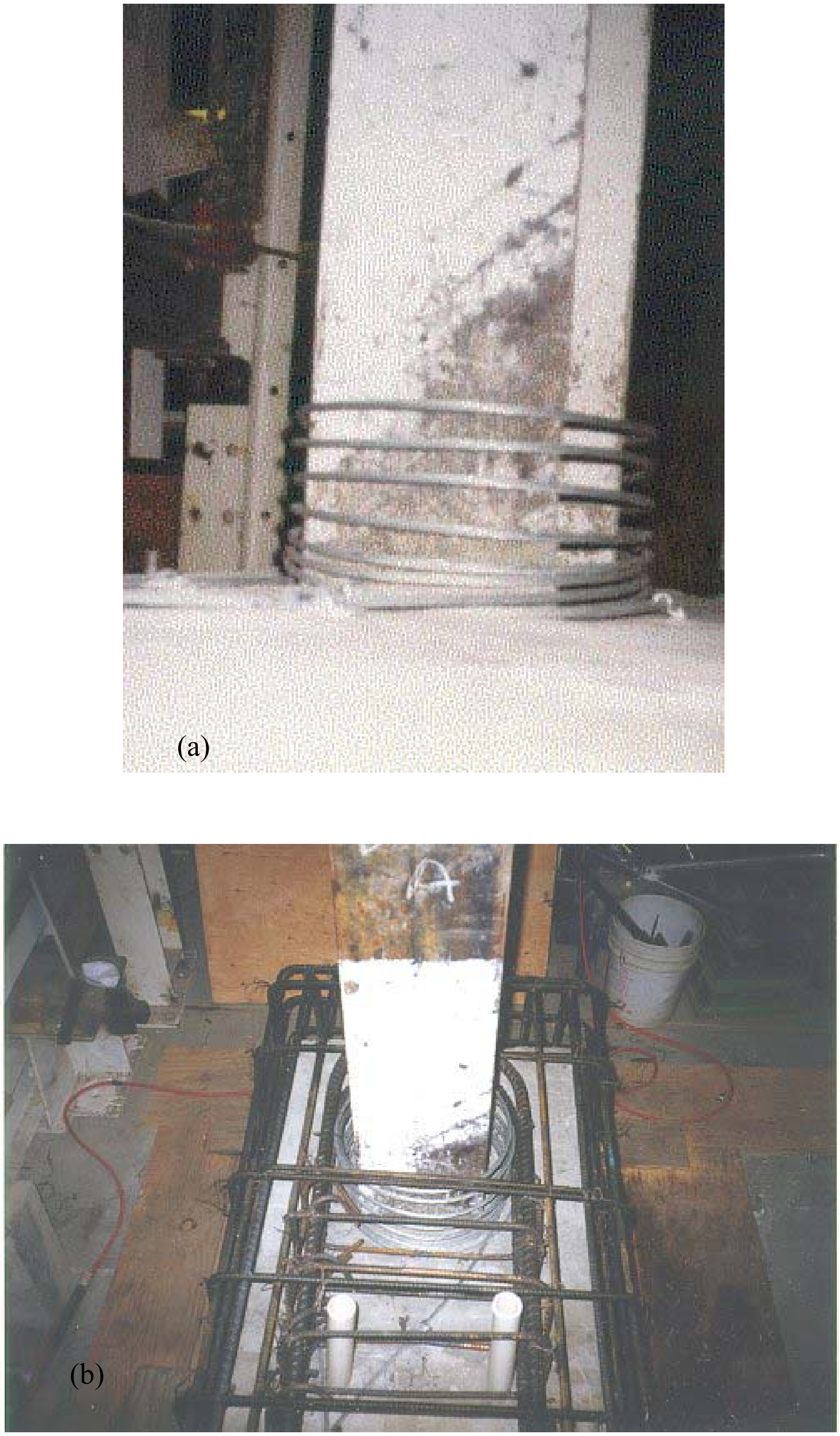

Figure 5.1 Wire rope used for joint confinement Specimen # S3 (a) Specimen after completing the wire rope confinement, and (b) Specimen after installing the main cap reinforcement

$$A_v = \frac{V_{st}}{f_y} = \frac{61.02x10^3}{413} = 148mm^2$$

$\therefore$ Use 12 mm diameter double leg stirrup ($A_s = 226\ mm^2$).

To ensure joint confinement, additional transverse reinforcement (9.5 mm diameter 1x7 galvanized wire rope) was added to the HP 10X42 steel pile along the overlay length, with a spiral pitch of 50 mm. A photograph of specimen #3 with wire rope wrapped in place is shown in figure 5.1 (a), and (b).

To facilitate the top-down pouring of concrete in an actual bridge, it was decided to increase the width of the pile cap by 100 mm on each side. The first series of tests showed that this increase in width would not enhance the cyclic performance of the specimen. The additional width is required for practical purposes where the pile cap will be in the inverted position in the actual bridge, and that extension of the width will facilitate the concrete placing and compaction during the casting process in the field. Additional reinforcement was provided in the form of # 4's rebars (13-mm diameter) every 150-mm for the longitudinal direction, for load distribution. Diagonal # 4 stirrups were used to improve joint shear resistance. The rest of the stirrups were three sided (U shaped) # 4's rebars. Figure 5.2 illustrates the reinforcing details for the pile bent retrofit at the connections.

The stages of construction are summarized as follows:

I. The wire rope was provided first, and wrapped as one part around the three specimens, finally it was fastened and attached to original concrete using a 13mm galvanized wire rope clamp.

II. The 4#8 rebars were then installed in place followed by the No. 4 (13-mm diameter) double leg stirrup as shown in figure 5.1b.

III. 7-16 mm diameter (7# 5) were provided as spacers along the two longitudinal sides of the specimen. Two 16 mm one hole galvanized straps were used to hold the spacer bars. The straps were attached to the sides of the original cap beam by 6 mm x 25mmx 9.5 mm sleeve concrete anchors drilled into the original concrete.

IV. The longitudinal # 4's rebars were fastened to the spacer bars by tie wires.

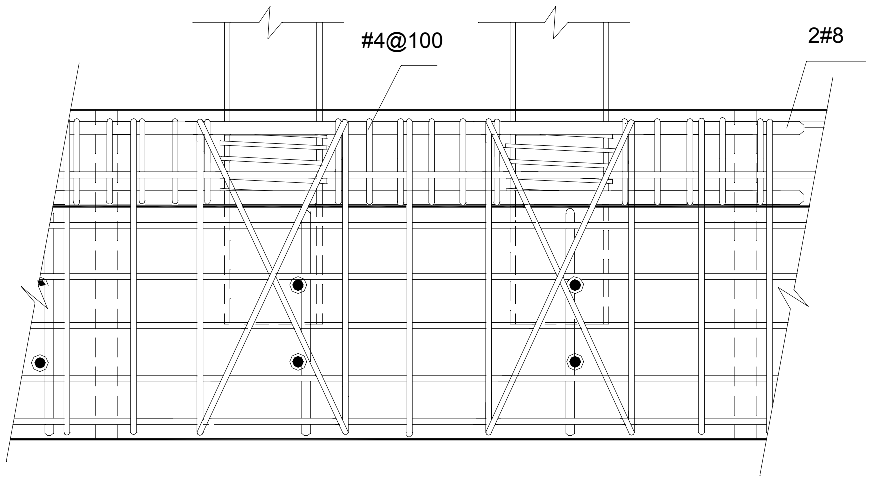

(a) Connections for specimens S1, and S2 (Elevation View)

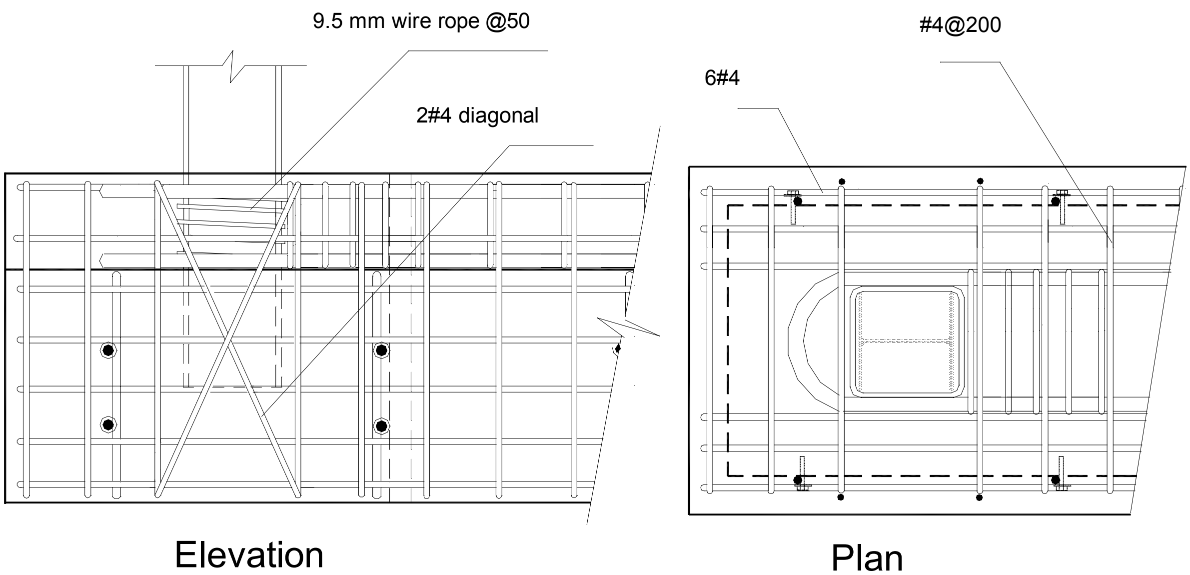

(b) Connection for specimen S3

Figure 5.2 Reinforcement Details For Connections ReS1, ReS2, and ReS3

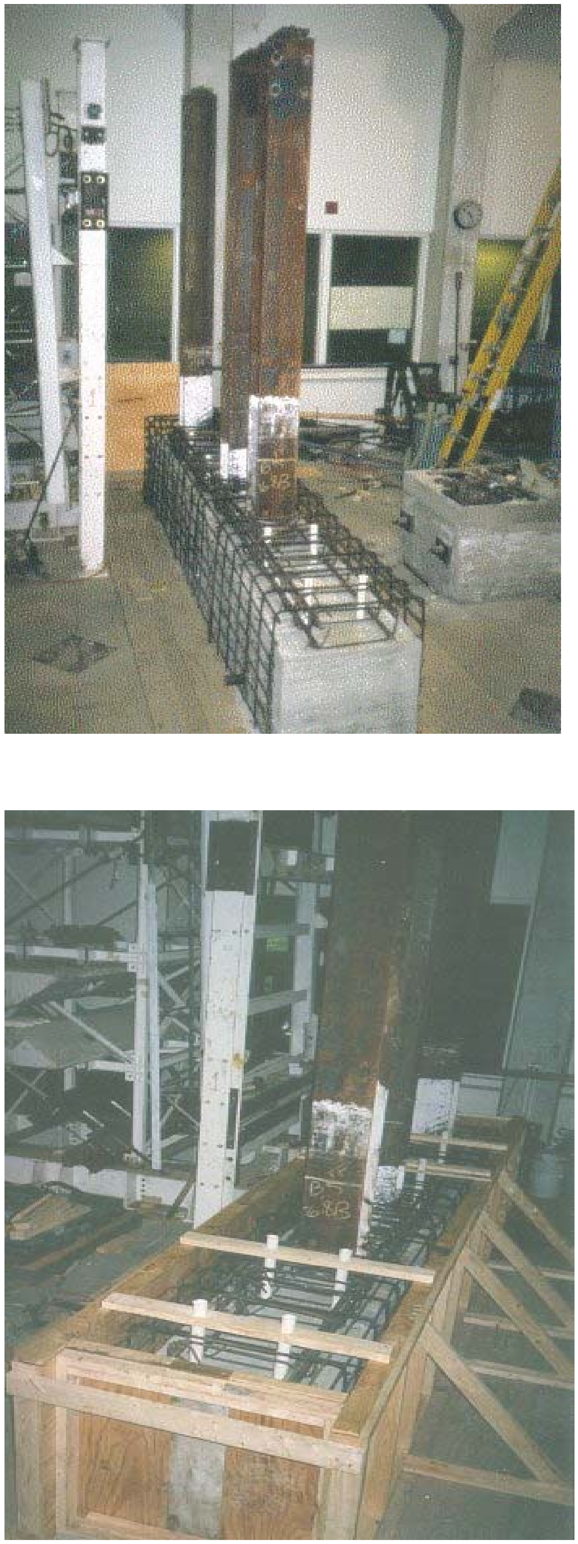

Figure 5.3 Construction of Specimen Retrofit: Top Shows the Reinforcing Cage; Bottom Shows the Formwork Prior to Pouring the Concrete.

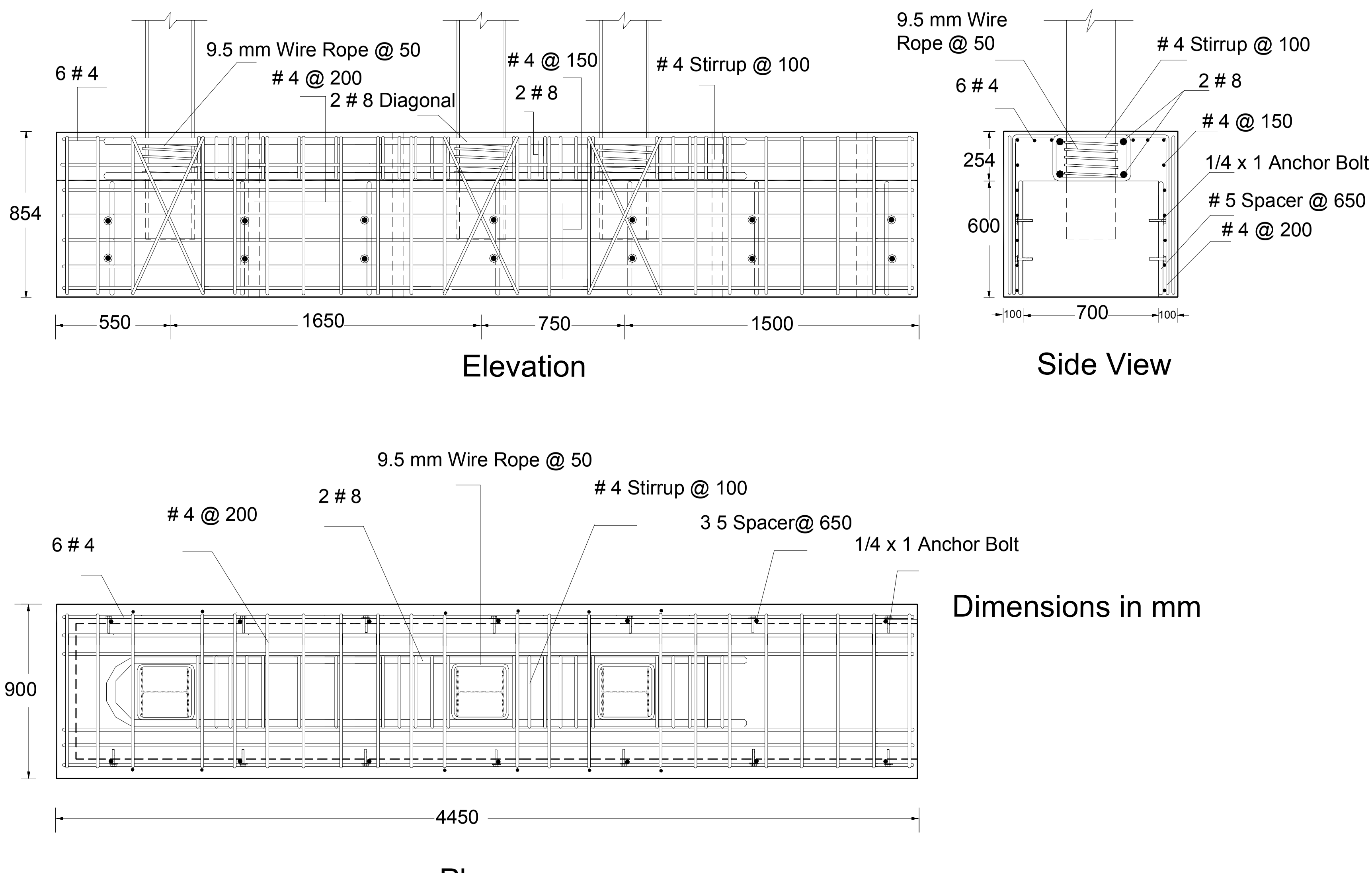

Figure 5.4 Geometry and Reinforcement For Strong Axis Pile bent Retrofitted Specimen

The U Shape stirrups were then attached to the longitudinal *# 4's* rebars using tie wires.

V. Finally the formwork was installed and the concrete poured.

Photographs of the stages of the retrofit construction are shown in figure 5.3 (a) and (b). The retrofitted specimen was constructed with ready-mix concrete. The ultimate compressive strength of the concrete was determined from the results of three 150X300 mm cylinder test. Results are shown in table 3.2. and (b). Figure 5.4 portrays different views for the retrofitted specimen with typical dimensions.

5.2.2 Pile-Pile Cap Specimens

Due to the sudden brittle failure of the as built specimens, a *462 mm* overlay length was taken for the retrofitting of these specimens. This results in a full embedment depth of 762 mm. According to equation (2.43), the nominal moment capacity of the connection can be expressed as:

$$M_j = \frac{f_c b_f l_{emb}^2}{\left(6 + \frac{l_{emb}}{L^*}\right)} \tag{5.2}$$

where, M_j = the nominal moment capacity of concrete; f_c = the concrete compressive stress at the extreme fiber in the front face of the connection; l_{emb} = the total embedment depth of the connection; L^* = the distance from the point of application of the lateral load to the neutral axis of the connection; and b_f = the flange width of the steel pile section. If it is assumed according to the retrofit strategy followed here that the plastic hinge would occur in the steel section. Therefore, f_c can be expressed as:

$$f_c = \frac{M_{P0}}{b_f l_{emb}^2}\left(6 + \frac{l_{emb}}{L^*}\right) \tag{5.3}$$

in which M_{p0} = the plastic moment capacity of the steel section expressed as:

$$M_{p0} = \phi_0 f_y Z_p \tag{5.4}$$

Substituting the new value for embedment depth in equation (5.3) therfore:

$$f_c = \frac{M_{P0}}{b_f l_{emb}^2}\left(6 + \frac{l_{emb}}{L^*}\right) = \frac{1.1x315x791000}{256x(762)^2}\left(6 + \frac{762}{1067}\right) = 12.3\,MPa$$

this value ensures that the stresses in the concrete along the embedment depth would be within the elastic range.

The longitudinal reinforcement required to prevent concrete spalling at the pile cap edges under cyclic loading is determined using equation (2.85).

$$A_s = \frac{1.5 f_{su} Z_p}{f_{yh} l_{emb}} = \frac{1.5x450x791000}{414x762} = 1777\,mm^2$$, assume 4 bars per pile d_{bar} = 24 mm.

Additional transverse reinforcement in the form of 9.5 mm diameter 1x7 galvanized wire rope was added to provide confinement for concrete along the overlay depth within the flanges of the pile (see figure 5.5).

Keeping in mind that pile cap foundations are usually constructed below the ground level, and during the retrofit of these foundations, soil will be excavated to the level of the overlay depth. Under these circumstances and to facilitate the concrete pouring and compaction, 300mm was added to the pile cap width at the edges.

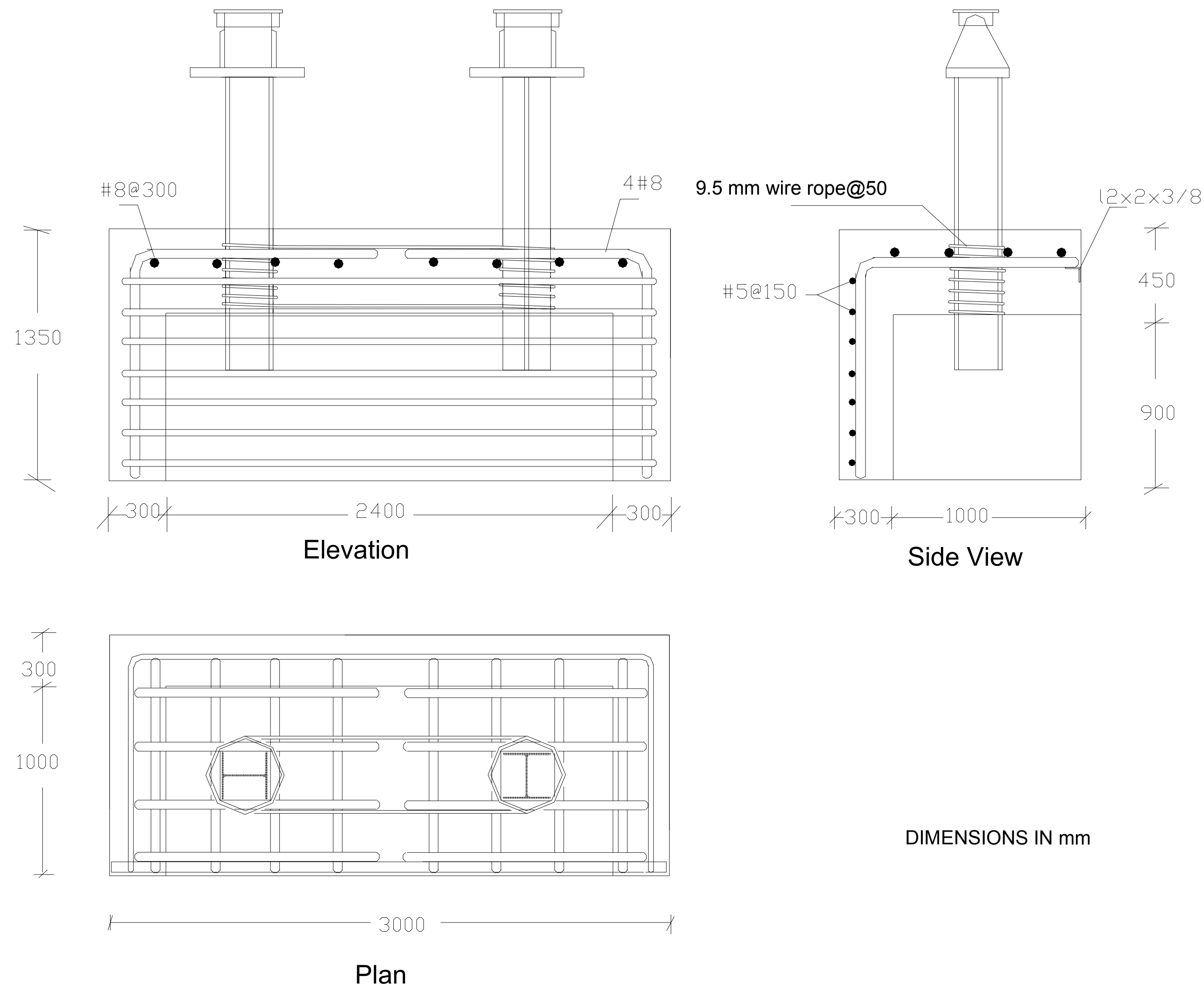

Figure 5.5 Geometry and Reinforcement For Pile Foundation Retrofit Specimen

Figure 5.6 Retrofit Construction of Pile Foundation Specimen, (a) Wire Rope set in place, and (b) Specimen after The Reinforcement was Accomplished

The construction of the retrofit in the lab was carried out in three steps,

1. The wire rope was wrapped around the two specimens then fastened and attached to original concrete using a 13mm galvanized wire rope clamp.
2. The main longitudinal L shaped *24mm* reinforcement was set in place and fastened together.
3. Additional longitudinal reinforcement consisting of *13 mm* rebars at *150 mm* was added to complete the reinforcing cage.
4. Finally the construction of the retrofit was concluded by setting the formwork in place and placing the concrete.

Photographs of the steps of the retrofit construction are shown in figure 5.6.

5.3 Scope Of Experimental Program

The experimental program for testing the retrofitted specimens was similar to the one used for as-built connections described previously in Section 4. For consistency, the same loading procedures were employed. Therefore, the specimens were tested in displacement control under incremental cyclic loading. Two cycles of drift at levels of $\pm 0.5\%$, $\pm 1\%$, $\pm 2\%$, $\pm 3\%$, $\pm 4\%$, $\pm 5\%$ and $\pm 6\%$ were applied. The quasi- statically displacement function was sinusoidal with a one-minute period per cycle. Table 6.1 summarizes the axial loads and drift information for each specimen tested in the retrofit study. During the load simulation for specimens ReS2, and ReS3 the vertical load was mistakenly underestimated. This resulted in the values shown in the table for the axial loads. These values were slightly less than those used for the as-built specimens. However, this did not affect the potential performance of the specimens, because it was observed during the first series of experiments for the as-built specimens, that specimens ReS2 and ReS3 performed somewhat better than specimen RES1, tested without any axial load. Consequently, testing specimens ReS2 and ReS3 in the second series of experiments with a reduced axial load would ascertain the retrofit methodology developed in this retrofit study.

Table 5.1 Test Program for Retrofitted Specimens

Spec. ID	Gravity Load (kN)	Lateral Actuator Angle θ	Vertical Axial Load Control (kN)	Total Axial Load (kN)	Max. Drift	No. of Cycles at Max. Drift
ReS1	0	0	0	0	5%	29
ReS2	150	0	150	150	6%	15
ReS3	120	24	$120+1.43\,P_{da}$	120+2.01V	5%	3
RePS	135	44	$135+0.22\,P_{da}$	135+1.27V	7%	0.5
RePW	135	44	$135+0.22\,P_{da}$	135+1.27V	5%	10

S = Strong Axis Bending W = Weak Axis Bending
PS = Piles, Strong Axis PW = Piles, Weak Axis
$V = P_{da} \cos\theta$

5.4 General Observations

All the specimens were subjected to quasi-static applied drift up to failure. Pile bent specimens possessed significant inelastic behavior beyond 2% drift. Pile foundation specimens exhibited inelastic performance beyond 0.5% drift. This was characterized by flaking of whitewash on both sides of the pile flanges.

A common form of failure mode was observed in specimens ReS1, and ReS2, where fracture occurred in the flange (at 5% and 6% drift), that was subjected to compression during joint closure (actuator pushing). The first cracks appeared at the flange, 120 mm above the retrofitted concrete cap surface. The flaw then propagated horizontally with additional drift to include the pile web. In the case of specimen ReS2, the flaw also propagated vertically in the flange on both sides of the web. This failure mode was accompanied with local buckling of the pile flanges in the hinge zone.

No noticeable cracks occurred in the reinforced concrete pile cap, except some minor cover spalling observed in the immediate vicinity of the pile web. It was also observed, that the gap which usually formed between the face of the steel flanges and the adjacent concrete, in the first series of tests for specimens ReS1, and ReS2, before retrofitting the cap beam, did not occur during the course of the second series of tests in specimens ReS1 and Res2. This corroborates the retrofit strategy proposed here.

It was decided to stop the test for specimens ReS3 at 3% drift before it reached failure due to out of plane motion of the pile at that drift.

During testing specimen RePS, one of the bolts connecting the actuator to the specimen was fractured. As a result , the experimental setup was dismantled and the test was stopped at the beginning of the 7% drift. The specimen, however, experienced severe local buckling without being fractured.

5.5 Force Deformation Behavior

5.5.1 Specimen *ReS1*

This specimen was tested without any axial load with two reversed cycles at drift amplitude of $\pm 0.5\%$, $\pm 1\%$, $\pm 2\%$, $\pm 3\%$, $\pm 4\%$, and concluded with 26 cycles at $\pm 5\%$. The complete hysteretic response of the specimen is shown in figure 5.7 . Yielding of the pile section first occurred just prior to the 2% drift level, characterized by some diagonal striations on the white washed flanges. Local buckling was initiated at the second cycle of 3% drift and continued to grow as the drift amplitude increased. Strain hardening was observed on the first cycle at 3% drift was attained. Beyond the 4% drift level, strength degradation of the steel material occurred as a result of the local buckling.

The specimen was exposed to a continued cycles of constant amplitude testing at 5% drift, through which strength degradation of the specimen continued. Finally on the 26^{th} cycle, a visible horizontal fatigue crack was observed at the flange subjected to compression when the lateral actuator is pushing. The flaw growth continued during the last three cycles and propagated horizontally to include part of the HP10X42 steel section web. Based on the crack initiation, and crack growth mechanism, it is evident that the failure of that specimen was due to low cycle fatigue. Photographs portraying such failure are shown in figure 5.8(a), (b).

5.5.2 Specimen ***ReS2***

Specimen ReS2 was tested under a constant axial load of *150 kN* with two reversed cycles at drift amplitude of $\pm$0.5%, $\pm$1%, $\pm$2%, $\pm$3%, $\pm$4%, $\pm$5% and concluded with 15 cycles at $\pm$6%. Figure 5.9 presents the force-deformation results.

This Specimen exhibited inelastic behavior prior to 2% drift and experienced work hardening in the pile steel material through both the 3% drift and the 4% drift cycles. Local buckling of the steel pile flanges started to occur, along a *250mm* distance above the cap beam concrete surface, during the second cycle at 4% drift. Strength degradation of the steel pile followed and was observable at the beginning of the 5% drift.

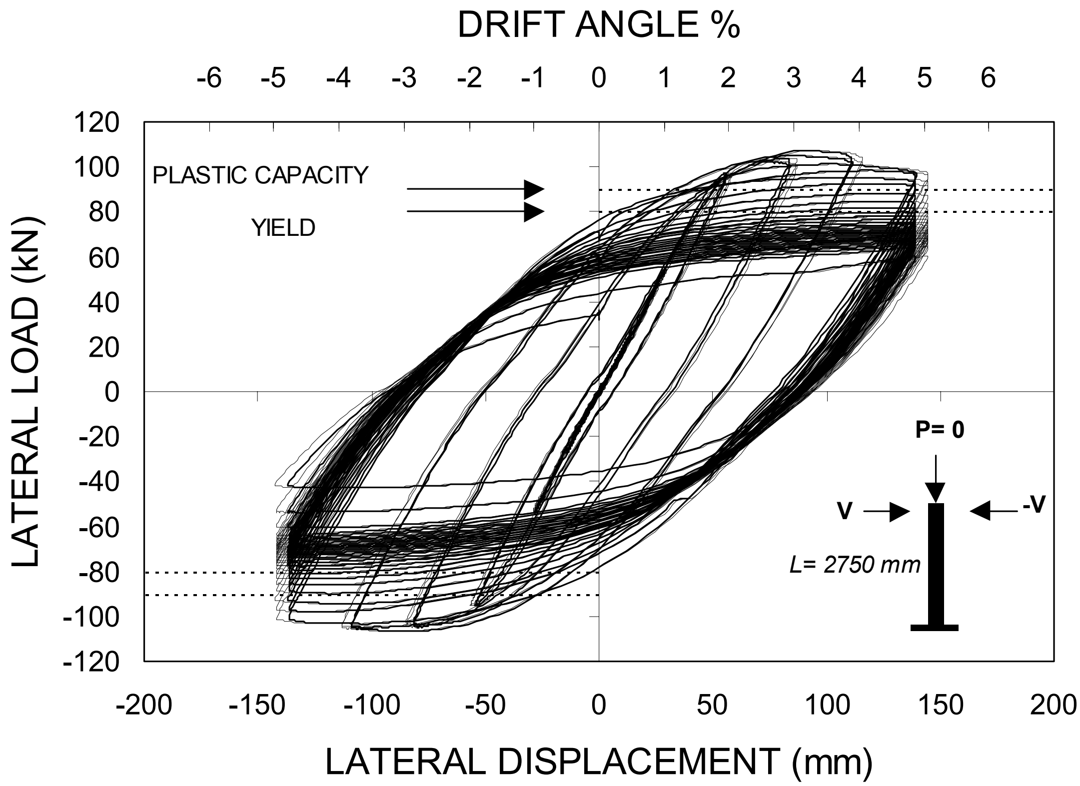

Figure 5.7 Performance of Specimen *ReS1* after Retrofit :Horizontal Force-Displacement Relationship

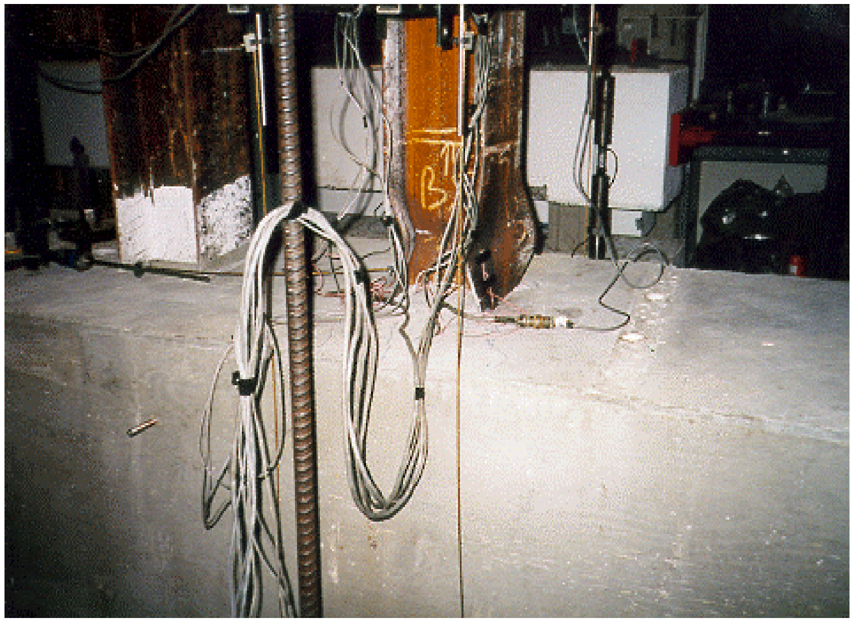

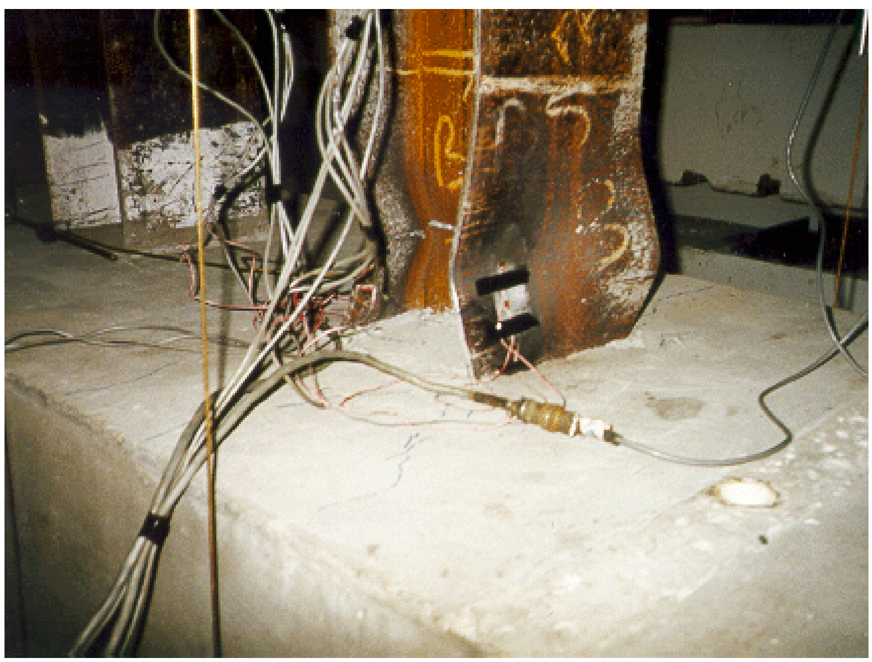

Figure 5.8 Specimen *ReS1* after Test. Top Photograph Shows a General Side View, Bottom Photograph Shows a Close-up View of the Flange Buckling

It was decided to perform a constant cyclic high amplitude test phase at the 6% drift level up to the fatigue failure of the specimen. A horizontal crack occurred at the compression flange after the 12th cycle was completed. The flaw continued to grow, propagating vertically both sides of the flange as well as horizontally in the web and fracture of the specimen was visible at the end of the 15th cycle. At that point the test was stopped. Photographs illustrating the fracture of specimen ReS2 due to low cyclic fatigue are shown in Figure 5.10a and 5.10b.

5.5.3 Specimen ***ReS3***

Specimen ReS3 was tested under variable axial load with two reversed cycles at each drift amplitude of $\pm 0.5\%$, $\pm 1\%$, $\pm 2\%$, $\pm 3\%$, $\pm 4\%$ concluding with 3 cycles at $\pm 5\%$. This specimen also satisfied the main objective of the conceptual elastic cap/elasto-plastic pile retrofit strategy proposed in this study.

The specimen behaved in an elastic manner prior to 2% drift. Yielding of the flanges in an area 250 mm above the added concrete surface was noticed through both the 2% and the 3% drifts and diagonal yield lines were visible on the whitewashed flanges. Strain hardening of the steel material also occurred during both the 2% and 3% drifts. Local buckling was initiated during the second cycle at 3% drift. This local buckling became more pronounced during the 4% drift and characterized by observable strength degradation in force displacement loops (see figure 5.11). Due to shortcomings of the test setup, the test of pile specimen ReS3 was not continued to reach the failure of the steel. Figure 5.12 plots the theoretical and experimental lateral load-axial load interaction diagrams for this specimen. The maximum tension uplift (296 kN) occurred during the pull of the second cycle at 4% drift. The maximum lateral force associated with this tension force was 117 kN. The specimen exhibited an average maximum overstrength factor of 1.17. A photograph of this specimen after the completion of testing is shown in figure 5.13.

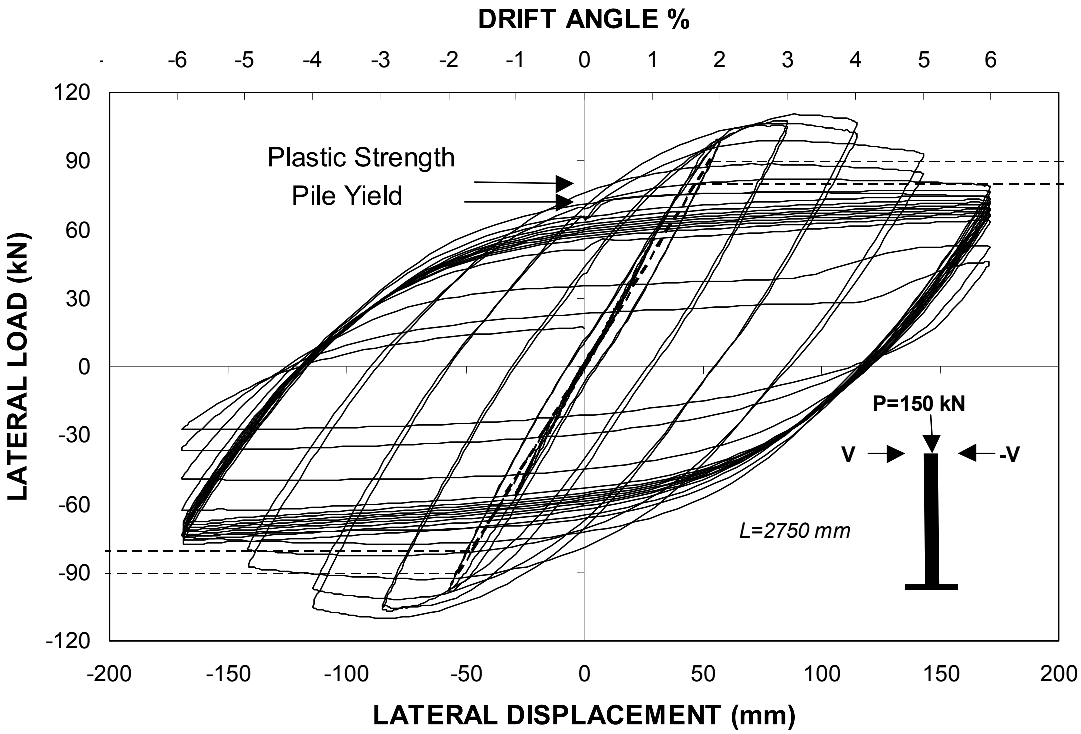

Figure 5.9 Performance of Specimen *ReS2* after Retrofit:Horizontal Force-Displacement Relationship

Figure 5.10 Specimen *ReS2* after Testing. Top Shows a Side View Including the Location of the Fatigue Crack. The Lower Photograph Shows an End View of the Specimen

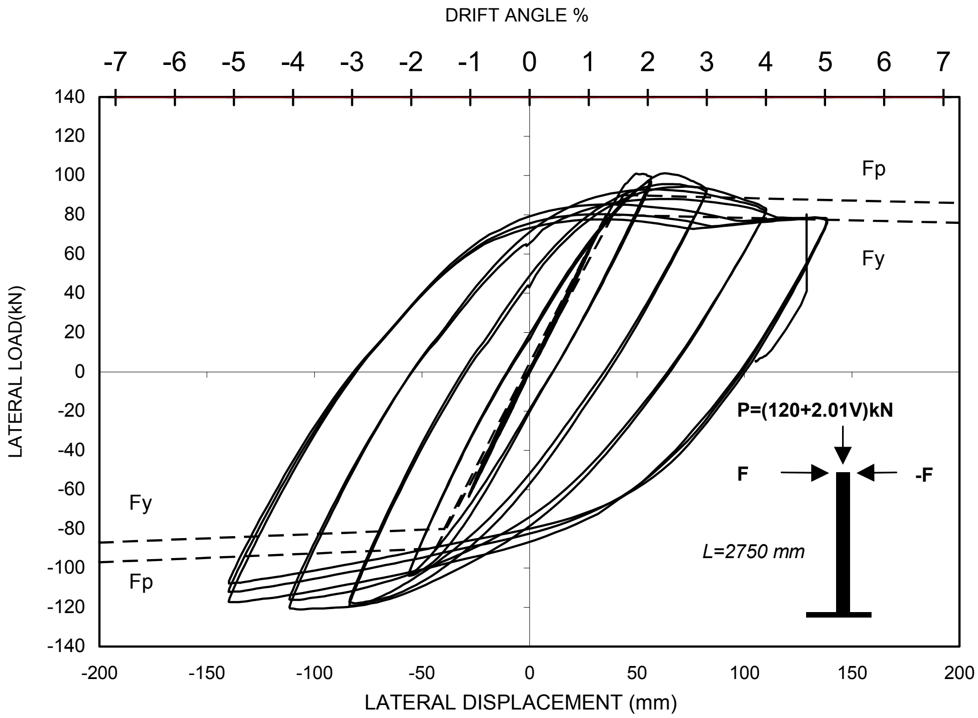

Figure 5.11 Performance of Specimen *ReS3* after retrofit :Horizontal Force-Displacement Relationship

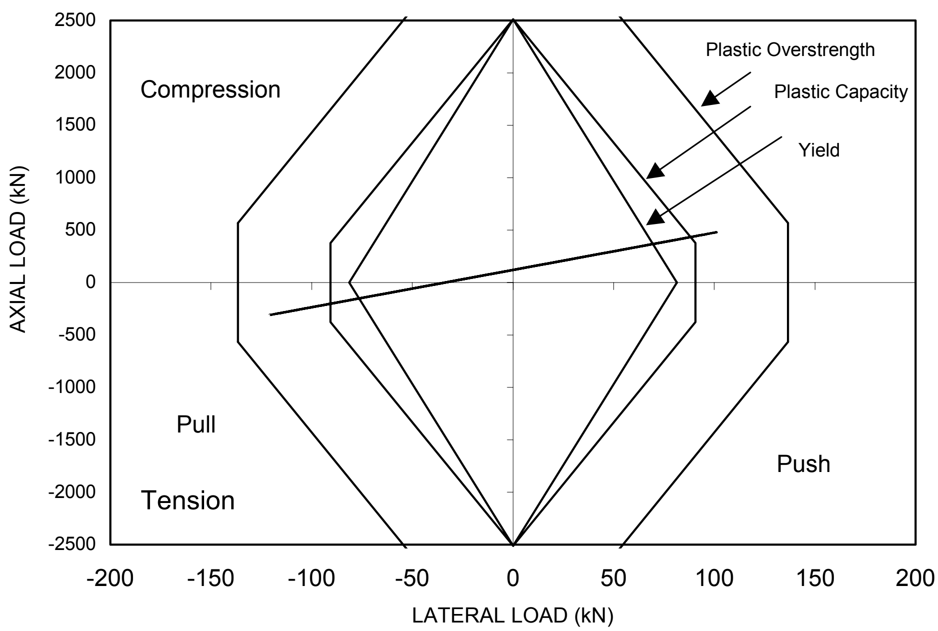

Figure 5.12 Experimental and Theoretical Lateral Load Axial Load Interaction Diagram For Specimen *ReS3* After Test

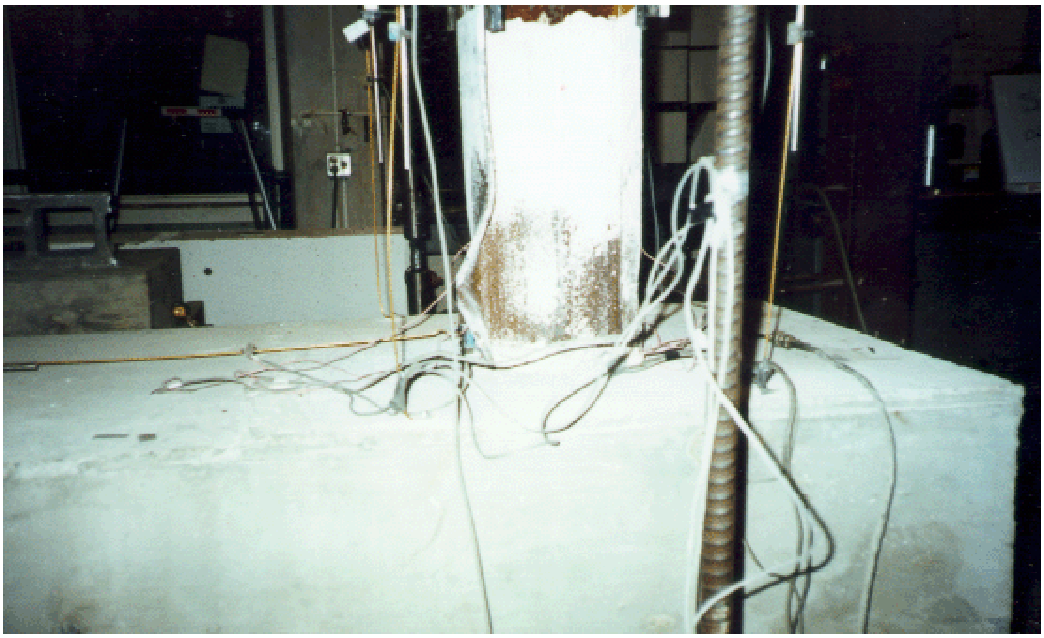

Figure 5.13 Specimens *ReS3* after Testing

5.5.4 Specimen *RePW*

Specimen RePW was tested under variable axial load with two reversed cycles at drift amplitude of $\pm 0.25\%$, $\pm 0.5\%$, $\pm 1\%$, $\pm 2\%$, $\pm 3\%$, $\pm 4\%$ concluding with 12 cycles at $\pm 5\%$. The specimen was tested up to 5% drift without any significant damage in the concrete cap beam. This behavior also validated the retrofit strategy proposed in this research. One should keep in mind that this specimen exhibited a brittle shear failure in the cap beam prior to retrofitting.

The overall performance of the connection was governed by the ductile behavior of the steel pile. The specimen behaved in an elastic manner up to 0.5% drift. Inelastic action on the section started to occur beyond this drift level. However, it was more pronounced during the push of the first cycle at 2% drift and continued through the 3% cycle. The diagonal striations on the white washed flanges extended to *200mm* distance above the concrete beam surface during the 3% drift and accompanied by a noticeable strain hardening of the steel material in the force-displacement loops (see figure 5.14).

Local buckling was initiated during the second cycle at 4% drift and exerted some strength degradation. Local buckling of both flanges continued to grow with the proceeding of loading at the first two cycles at 5% drift.

Ten more cycles were conducted at 5% drift, strength degradation of the steel material was more pronounced through these cycles. The test stopped after the Specimen completed 12 cycles at 5% drift. A photograph of the specimen after the test was completed is shown in figure 5.16.

Figure 5.15 plots the theoretical as well as experimental lateral load-axial load interaction diagram for this specimen. The maximum tension uplift (164 kN) occurred during the pull of the first cycle at 4% drift. The maximum lateral force associated with this tension force was 236 kN. This specimen exhibited an average maximum overstrength factor of 1.32.

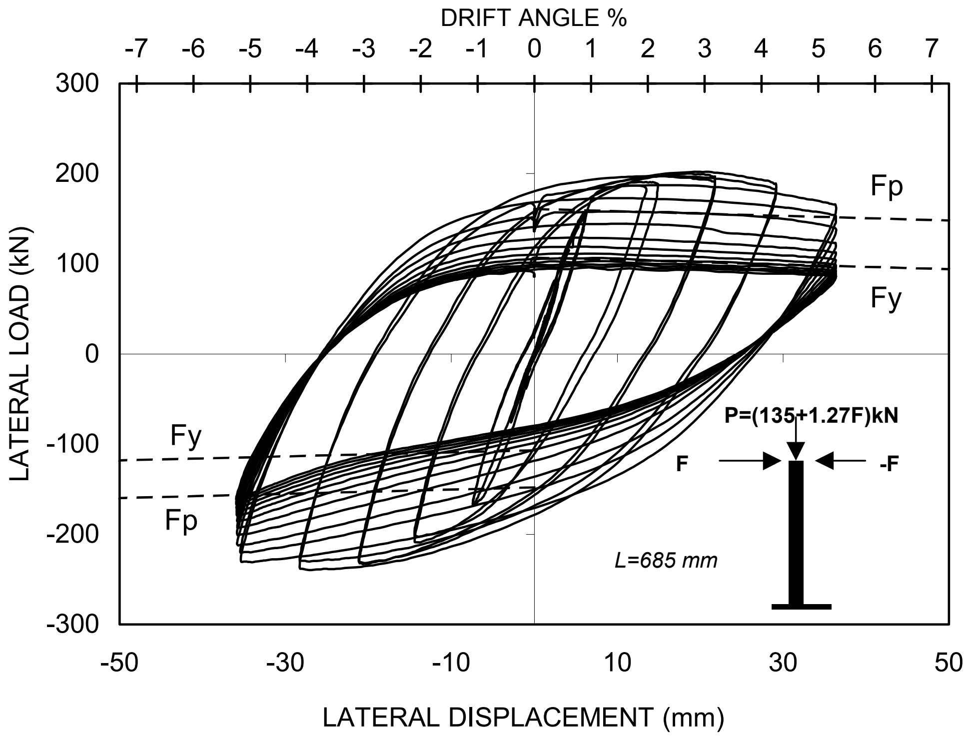

Figure 5.14 Performance of Specimen *RePW* after retrofit : Horizontal Force-Displacement Relationship

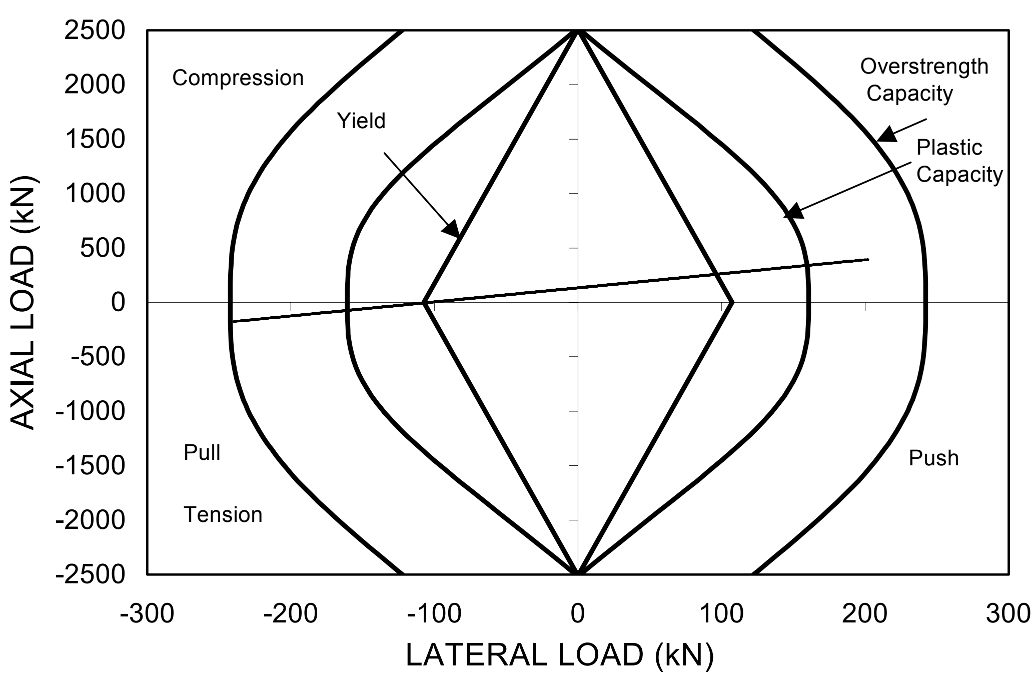

Figure 5.15 Experimental and Theoretical Lateral Load Axial Load Interaction Diagram For Specimen *REPW* After Retrofit

Figure 5.16 Photograph of Specimen *RePW* after Testing

5.5.5 Specimen ***RePS***:

Specimen RePS was tested under variable axial load with two reversed cycles at each drift amplitude of $\pm 0.25\%$, $\pm 0.5\%$, $\pm 1\%$, $\pm 2\%$, $\pm 3\%$, $\pm 4\%$, $\pm 5\%$ concluding with one cycle at $\pm 6\%$ and another half cycle at +7%. This specimen showed a ductile behavior in the steel pile with few insignificant cracks in the concrete beam cover in a small region surrounding the steel pile.

Due to shortcoming of the lateral actuator, the specimen did not attain the required displacement during the push of first cycle at 2% drift. This displacement, however was attained during the pull of this cycle. Another half cycle was tried manually at the same drift, then the experiment stopped temporarily to replace the malfunctioning lateral actuator with another actuator with the same specifications.

Yielding of the steel section of this specimen occurred prior to 1% drift level. The inelastic behavior of the pile was pronounced during the 2% drift. This was characterized by diagonal striations in both the white washed flanges and the web along a 125 mm distance above the concrete cap beam surface. These striations extended to a distance of *200 mm* above the concrete surface during the first cycle at 3% drift with strain hardening of the steel material being noticeable in the force-displacement loops.

Local buckling started to occur at the first cycle of the 3% drift, but it was very pronounced, along a distance of *200mm,* on the compressed flange, during the push of the second cycle at this drift. It was noticed that this local buckling did not happen on the other flange subjected to compression during the pull. This phenomenon was noticed also on the force-displacement plot (figure 5.17) where the softening happened in the flange subjected to compression in the push direction at the end of the 3% drift, while the flange on the other side was still in the strain hardening phase. This phenomenon continued through the two cycles at 4% drift.

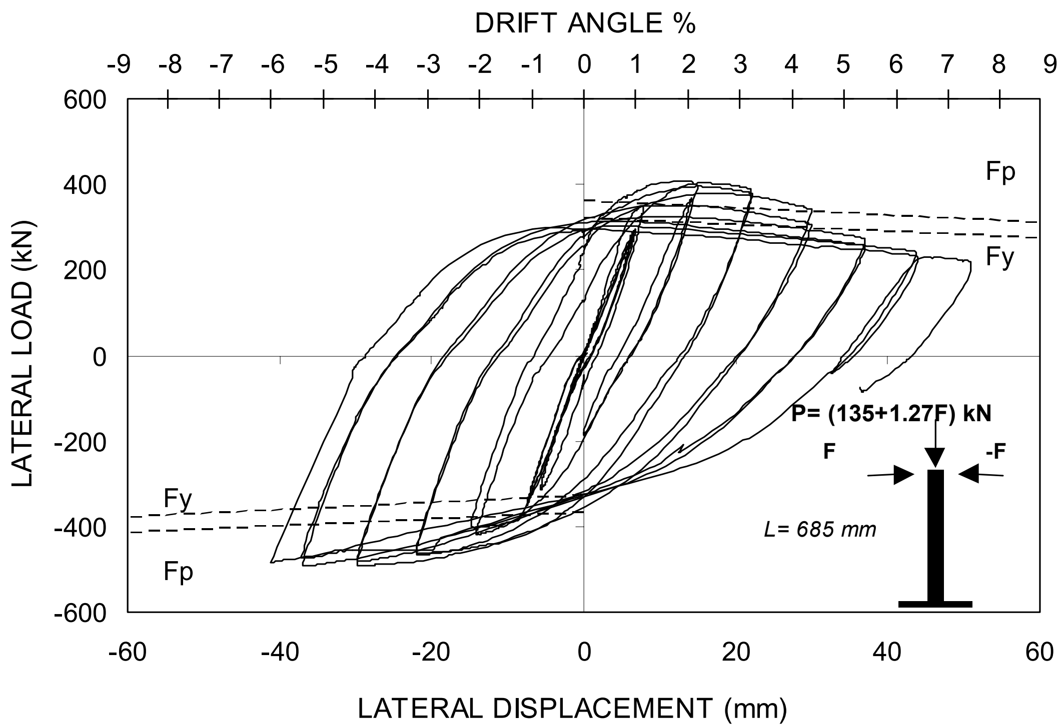

Figure 5.17 Performance of Specimen *RePS* after retrofit: Horizontal Force-Displacement Relationship

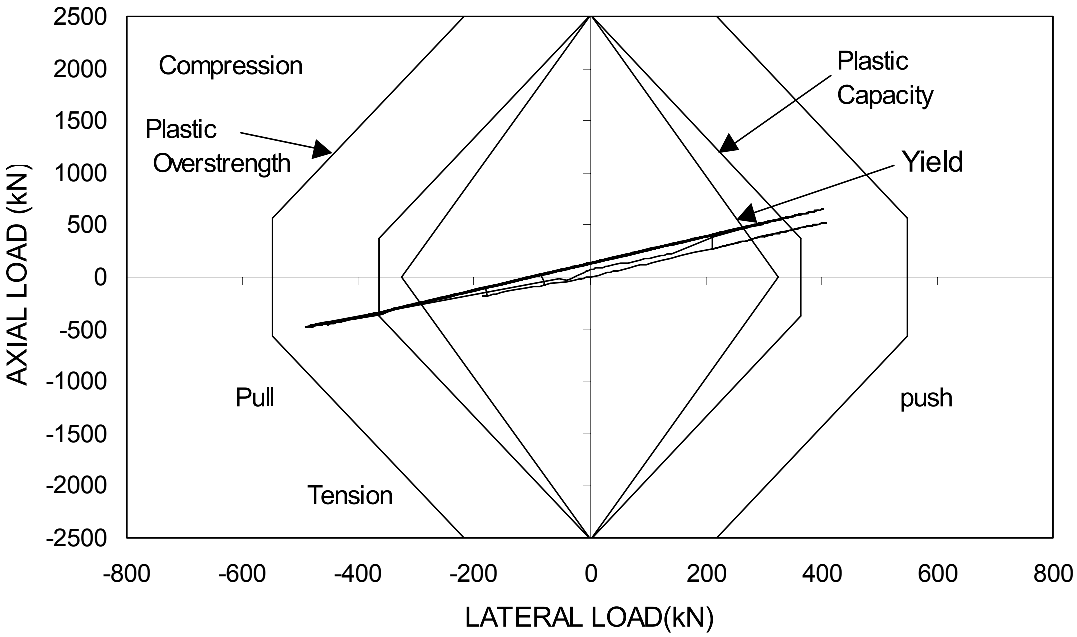

Figure 5.18 Experimental and Theoretical Lateral Load Axial Load Interaction Diagram For Specimen *RePS* After Retrofit

One of the four anchor bolts attaching the lateral actuator to the specimen at the bearing level yielded during the pull of the second cycle at 5% drift. The test stopped temporarily and this bolt was replaced. One cycle at 6% drift was carried out, however, two other anchor bolts attaching the lateral actuator to the specimen fractured suddenly by the end of this cycle. The test continued another half cycle at 7% drift and then stopped. The fracture of these bolts occurred as a result of their low cyclic fatigue because at the point of fracture, the steel pile was in the strength degradation phase and these bolts have already sustained higher forces during the strain hardening of the specimen. Photographs of the specimen after test are portrayed in figure 5.19.

Figure 5.18 shows the theoretical and experimental lateral load-axial load interaction diagrams for specimen RePS. The maximum tension uplift (467kN) happened during the pull of the second cycle at 4% drift. The maximum lateral force associated with this tension force was 482kN. The average maximum overstrength factor of this specimen is 1.18.

5.6 CLOSURE

The present section outlined the steps involved in the construction of the retrofit of the pile bents and the pile foundation specimens. The results of a series of experiments to determine the performance of the retrofitted specimens were then presented. Based on the results presented in this section the following conclusions are drawn:

(i) Compared to the as-built case, specimen ReS1 exhibited superior energy absorption and stable hysteretic response loops. This specimen exhibited two cycles, at 5% drift, with non ductile failure at the concrete cap beam, under same loading conditions, before it was retrofitted.

(ii) In the first series of tests for the as-built specimens, the presence of the axial load improved the hysteretic response of specimen S2 when compared to S1. However,

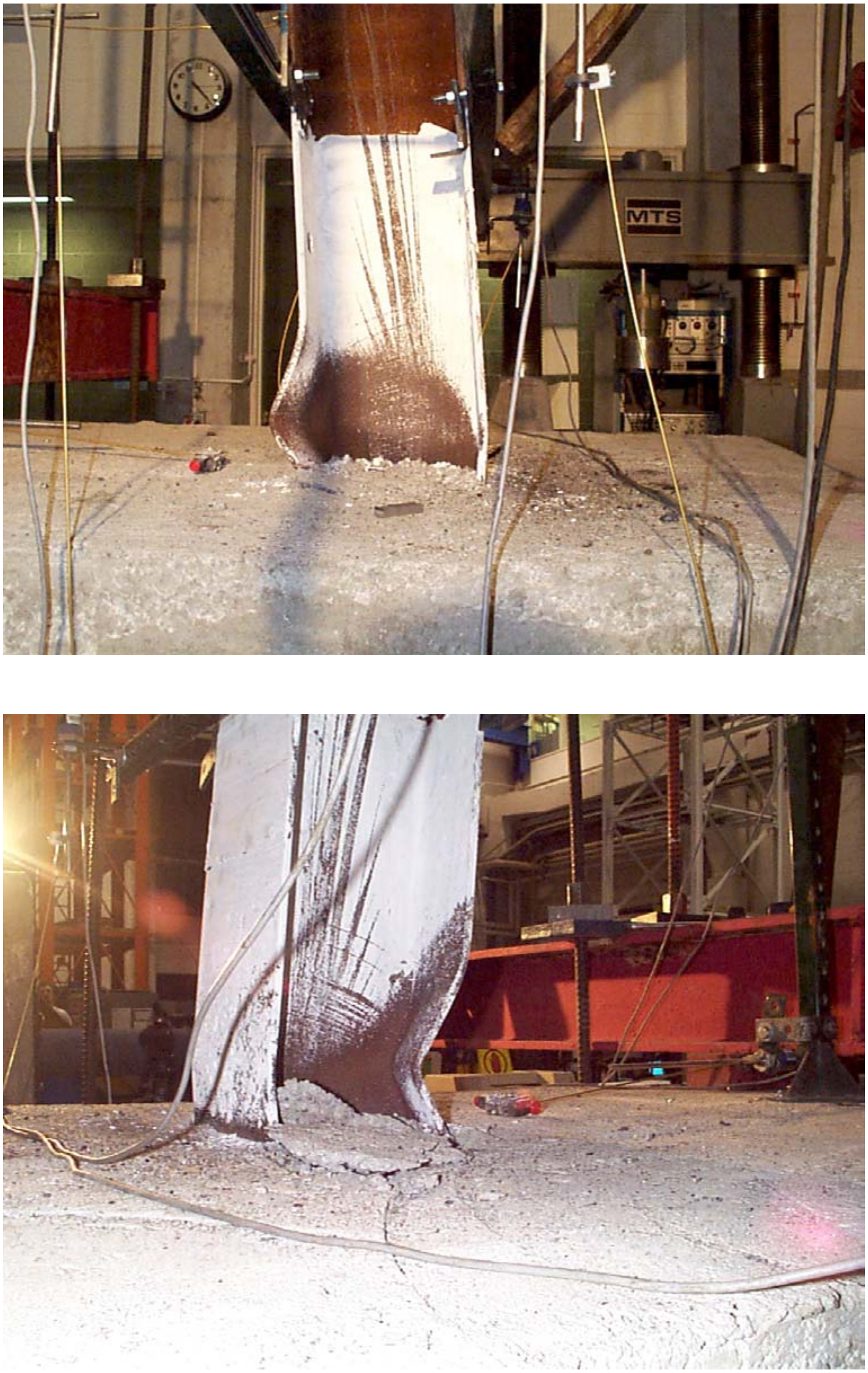

Figure 5.19 Photographs of Specimen *RePS* after the Test

this was not the same case for the retrofitted specimens, where the axial load had a minor influence on the strength of the connection. This was evidenced by the similar hysteretic respone behavior of specimens ReS1 and ReS2.

(iii) Based on the lateral force-displacement of the exterior pile bent specimen, before (S3) and after (ReS3) retrofit, one can realize the effectiveness of the retrofit strategy proposed in the present study. In the pre-retrofit test, the concrete cap beam sustained some limited cracking damage. This was characterized by the pinching in the lateral force-displacement loops. This pinching, however, did not occur for the retrofitted test specimen indicating that the connection behavior was governed by the ductile performance of the steel section with the joint remaining intact.

(iv) The experimental results presented in this section indicated that the retrofitted specimens possessed a superior performance in terms of ductility with respect to the as-built specimens. Therefore, it is considered that the conceptual elastic cap/elasto-plastic steel pile retrofit strategy proposed in this study is validated.

(v) It should be emphasized that the retrofitted pile-to-cap connections investigated in the present study were tested to high drift amplitudes ± 6%. In an actual earthquake, the structure may not exhibit such drifts. Therefore plastic hinging may be anticipated. Local buckling failure was attained in the experimental study as a result of low cycle fatigue under lateral loading, which may not happen during an actual seismic event.

SECTION 6
MODELING OF THE EXPERIMENTAL RESULTS

6.1 INTRODUCTION

The purpose of this section is to validate the theories developed in sections 2 and 3 for predicting the lateral force displacement relationship and ductility ratios for different pile-to-cap connections tested in the present study. Moreover, a fatigue theory is developed that predict the low cycle fatigue behavior of the specimens that failed in such failure mode. The predictive results are compared with experimental observations.

6.2 STRENGTH DEGRADATION AND ENERGY ABSORPTION CHARACTERISTICS OF BRIDGE PILED SUBSTRUCTURES

One useful way of assessing the seismic vulnerability of a structural system is through the identification of its energy absorption characteristics. This can be achieved by determining the cyclic energy absorption efficiency factor η and the effective viscous damping ratio, ξ_{eff} of the system. This empowers a comparison between the structural seismic capacity and the seismic demand. As mentioned in section 3, the efficiency factor η compares the energy absorbed by the structure to a 100% perfect elasto-plastic system. Therefore, this factor indicates the ability of the structure to absorb energy at a given drift level. The effective damping ratio, related to the structural efficiency factor through equation (3.25), is an important parameter in assessing the structural seismic vulnerability.

6.2.1 Energy Absorption Characteristics of As-Built Structures

6.2.1.1 Pile Bents Strong Axes Bending

The equivalent damping ratio calculated by equation (3.23) is plotted with respect to the displacement ductility factor for the specimens in figures 6.1(a),(b) and (c). The data for Pile

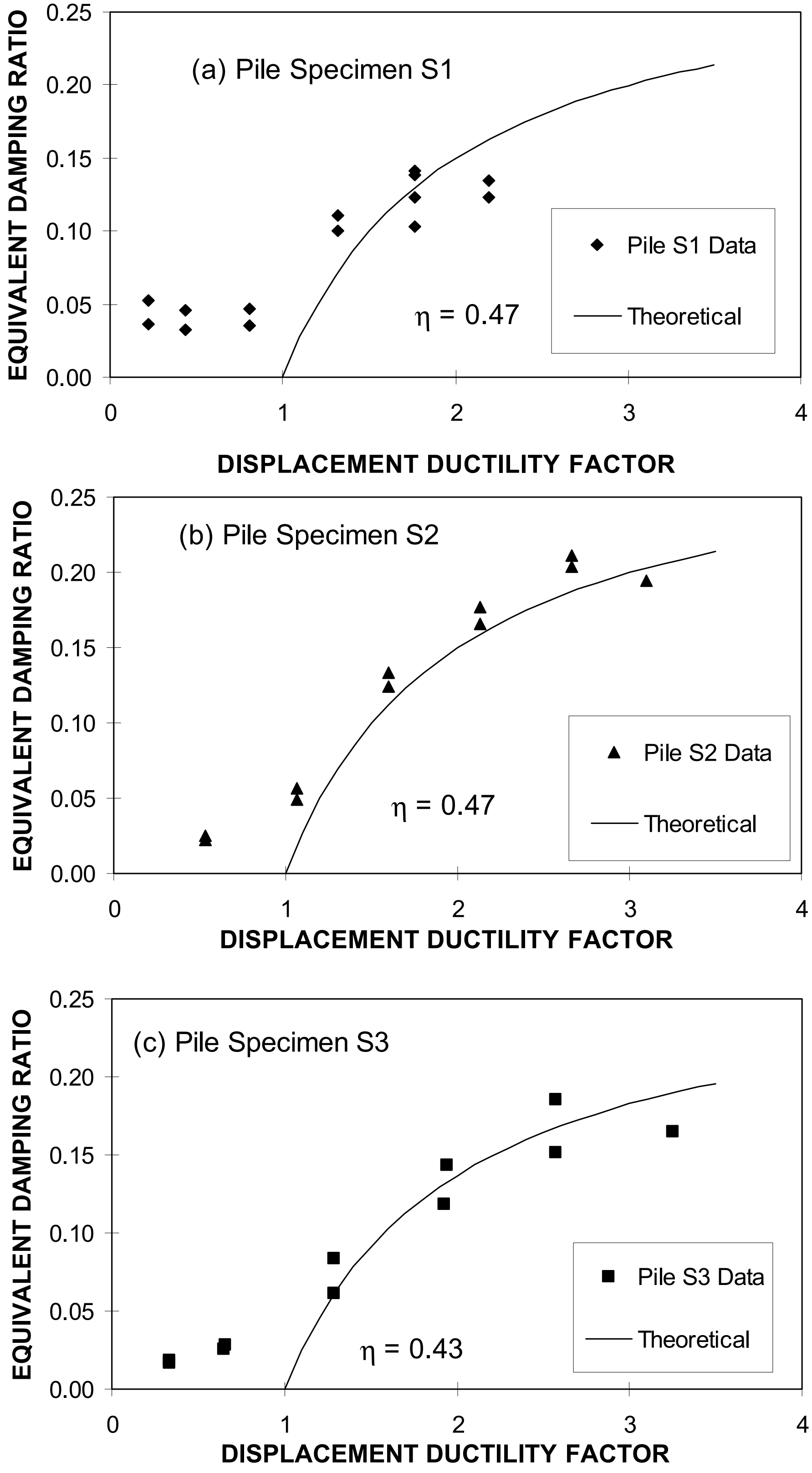

Figure 6.1 Energy Dissipation Characteristics of Pile Bents Tested Along its Strong Axes

Specimens S1 and S2, plotted in figure 6.1(a) and (b), is compared to the predicted behavior calculated by equation (3.23) with η = *47 %*. Similarly, the predicted behavior for Pile Specimen S3 is plotted in figure 6.1(c) with η= *43 %*.

6.2.1.2 Pile Bents Weak Axes Bending

Specimen W1 exhibited an extraordinary energy absorption capability. Therefore a *80%* average value for efficiency was taken for this specimen. Specimen W2 had a satisfactory performance too. It exhibited local buckling in the flanges, at *6%* drift, followed by the concrete failure during the last six cycles at *7.5%* drift. Therefore a value of 55 % efficiency was assigned to this specimen. Both specimens performed better than specimens S2, and S3 tested under similar conditions along the strong axis bending.

The efficiency values assigned for the two specimens were implemented in equation (3.23) to predict the theoretical ductility-damping ratio relationship. These relationships are plotted for the two specimens in figures 6.2a, and 6.2b. The experimental values for these relationships were plotted in both figures as dashed lines. The figures indicate satisfactory correlation between the theoretical and experimental relationships.

6.2.1.3 Pile Foundations Strong and Weak Axes Bending

Pile foundation specimens failed in a non-ductile brittle shear mode. Accordingly, one can deduce that they exhibited inferior energy absorption capabilities with respect to pile bent specimens. It is obvious from figure 4.17b that specimen PS had no post-yield stiffness, as the force deformation loops had a descending envelope, because the specimen failed suddenly in the concrete cap without exhibiting any ductility in the steel pile material. Specimen PW experienced some ductility in the steel pile material prior to failure. Therefore the theoretical ductility-damping ratio relationships are compared to the experimental values before connection fails and after failure. η was taken as 0.40 for specimen PS and 0.48 for specimen PW before the connection fails. Those values ,however, were reduced to 0.28 and 0.22 for the two specimens

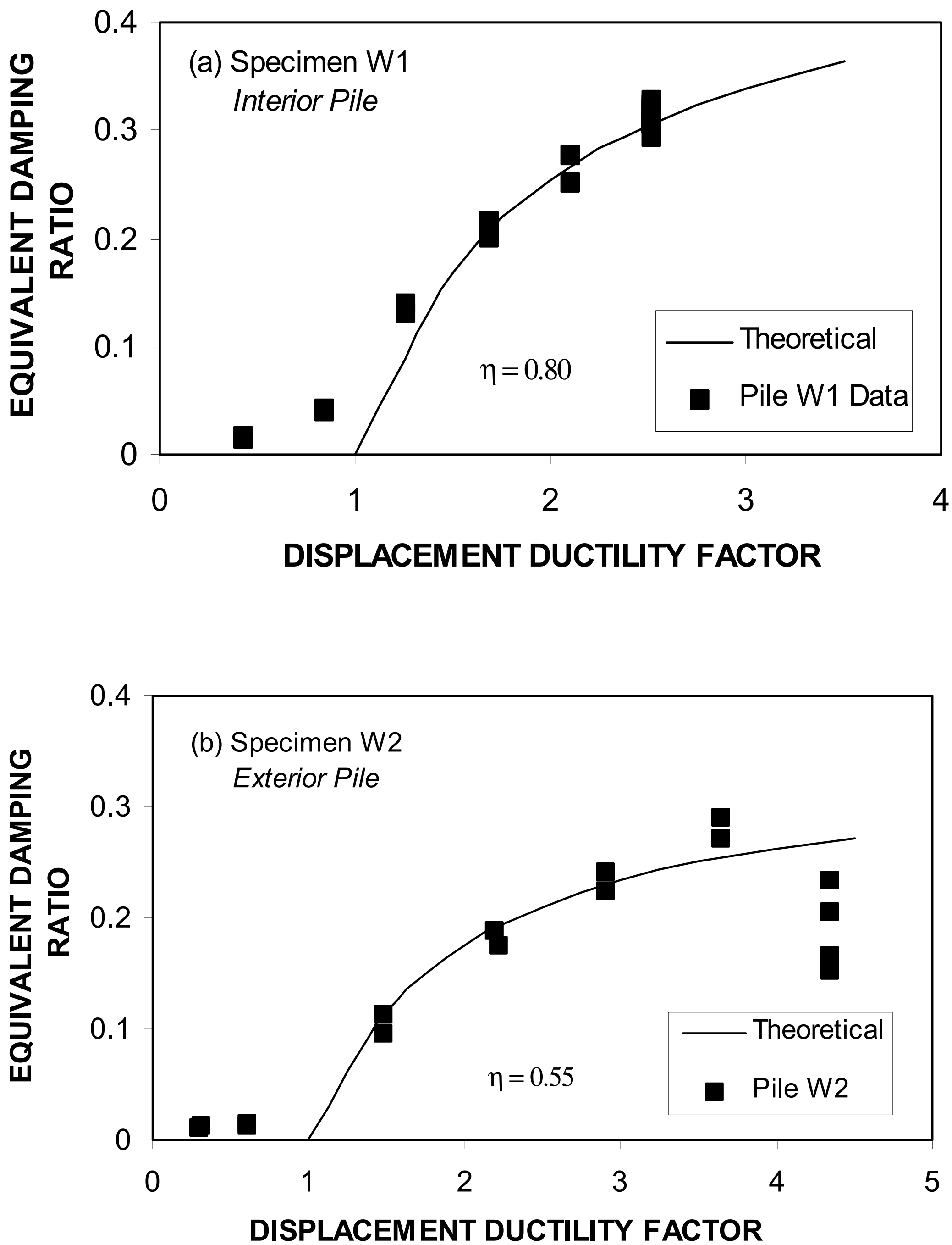

Figure 6.2 Energy Dissipation Characteristics of Pile Bents Tested Along its Weak Axes

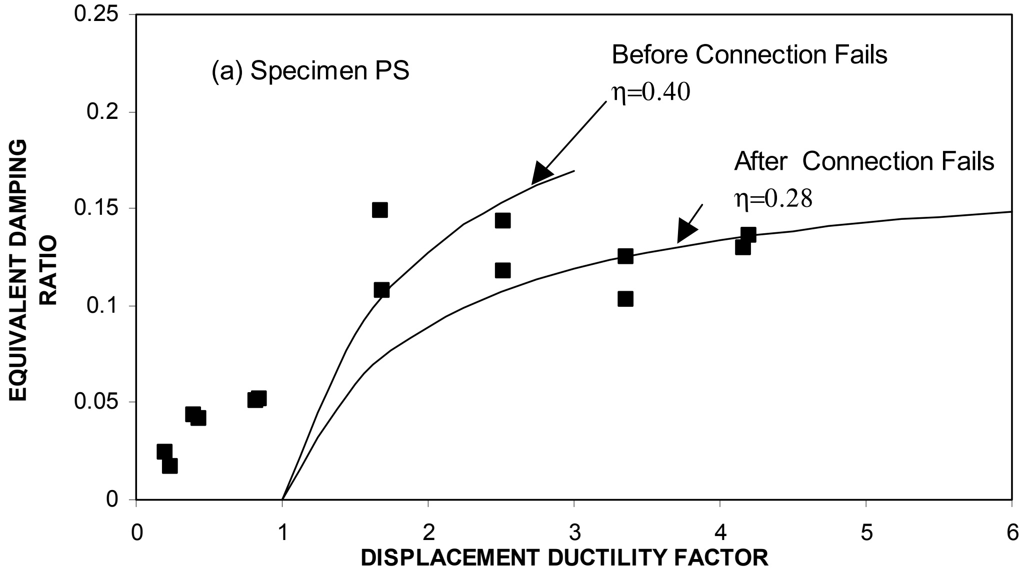

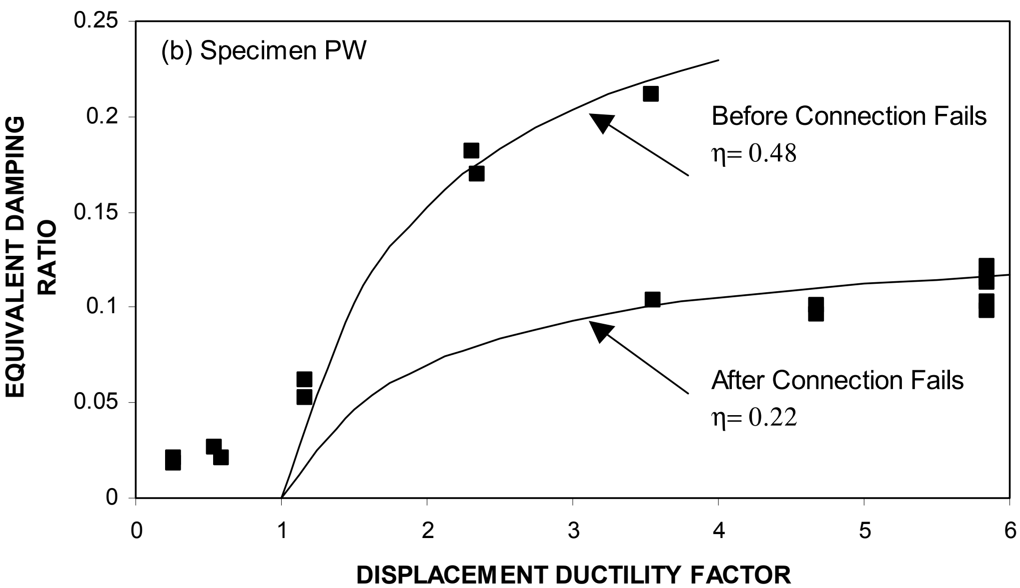

Figure 6.3 Energy Dissipation Characteristics of Piled Foundations Tested Along its Strong and Weak Axes

after failure. The efficiency values assigned for the two specimens were implemented in equation (3.23) to compare with the experimental values of the ductility-damping ratio relationships. These relationships are plotted for both specimens in Figures 6.3a and 6.36b respectively. Satisfactory convergence was achieved between the theoretical and experimental equivalent damping ratios

6.2.2 ENERGY ABSORPTION CHARACTERISTICS OF RETROFITTED STRUCTURES

6.2.2.1 Pile Bent Specimens

These specimens exhibited good energy absorption capabilities. Consequently a value of 80% is assigned for specimen ReS1 and 65% for both ReS2 and ReS3. The equivalent damping ratio calculated by equation (3.23) is plotted versus the displacement ductility factor for the specimens in figures 6.4a,6.4b and 6.4c. The experimental data for these specimens are shown in the figures too. Satisfactory agreement was achieved between the experimental and predicted values.

6.2.2.2 Piled Foundation Specimens

Both specimens PW and PS possessed high energy absorption capabilities. A values of η= 60% is assigned for both specimens. The equivalent damping ratio calculated using equation (3.23) is plotted versus the displacement ductility factor for the specimens in figures 6.5a and 6.5b. The experimental values are plotted in the same figure. The figures indicate good correlation between the theoretical and experimental relationships.

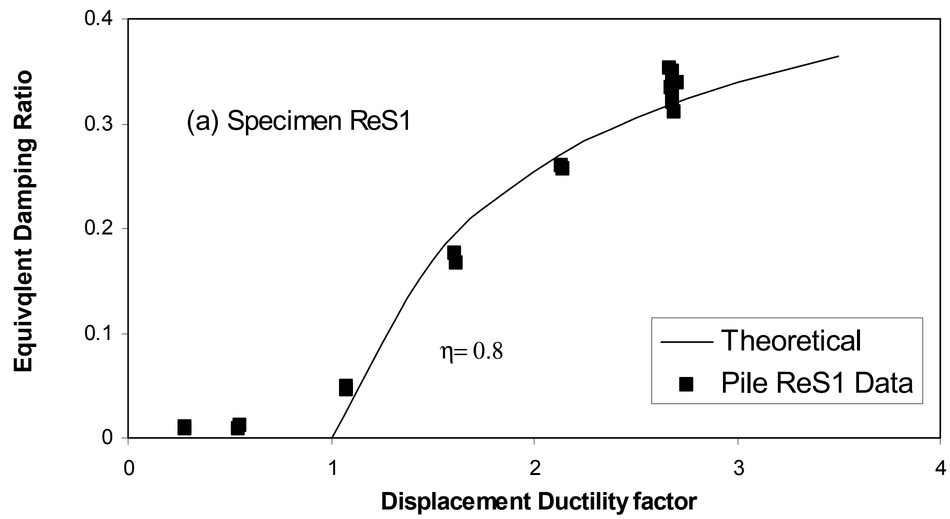

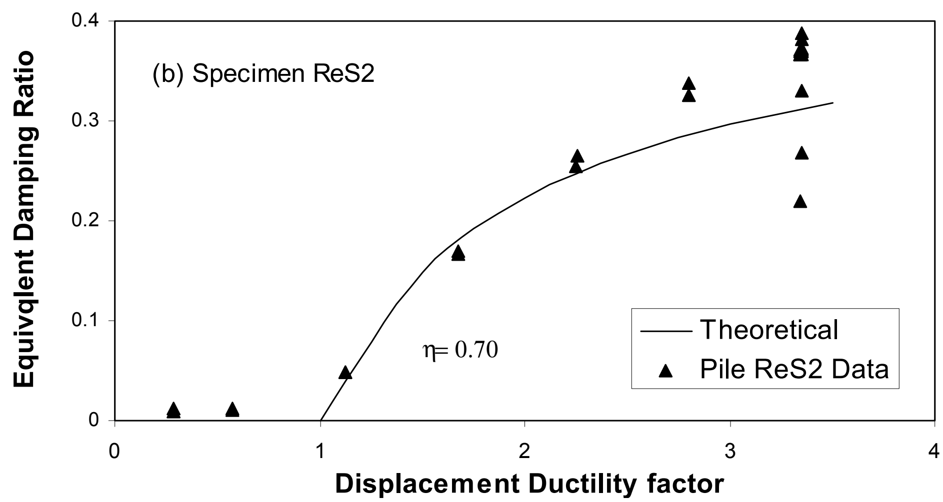

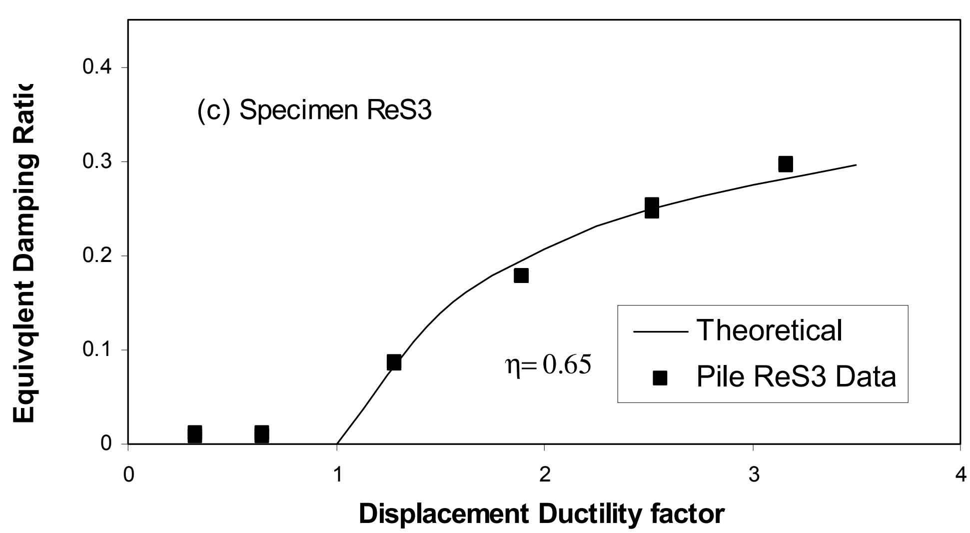

Figure 6.4 Energy Dissipation Characteristics of Retrofitted Pile Bents

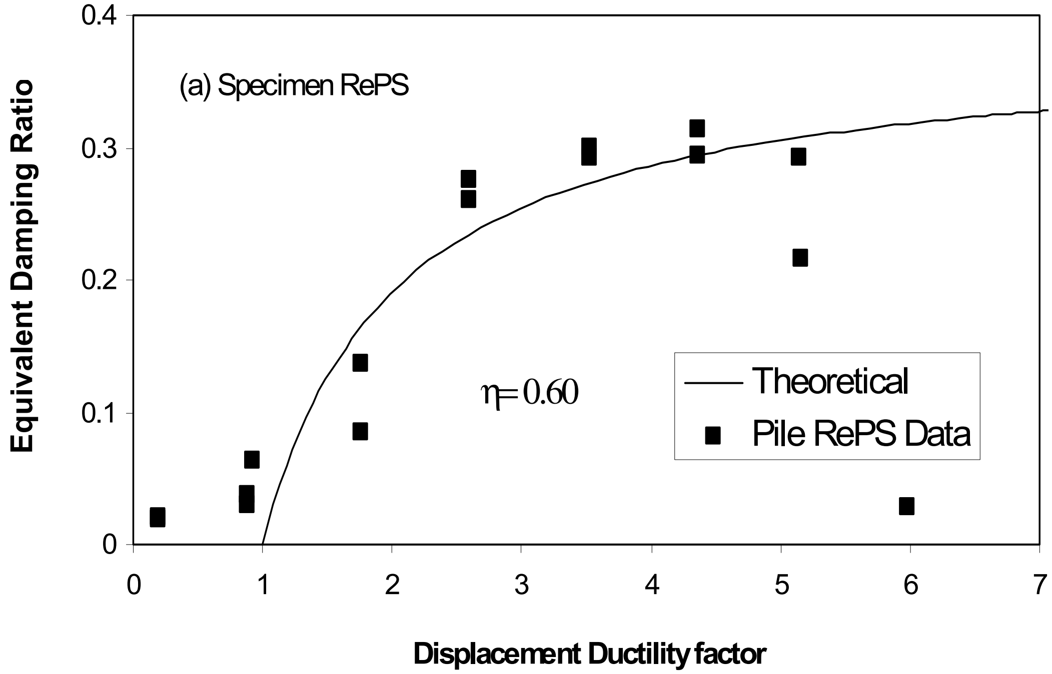

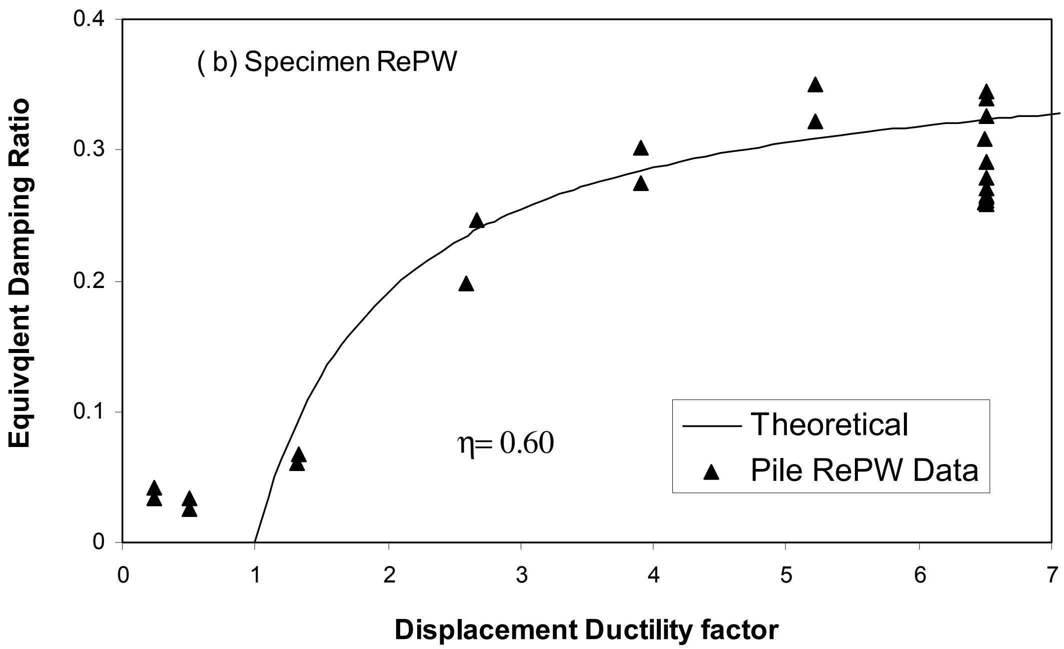

Figure 6.5 Energy Dissipation Characteristics of Retrofitted Piled Foundations

6.3 PUSHOVER MODELING OF AS-BUILT CONNECTIONS

Figures 6.6 through 6.8 show the cyclic normalized lateral force-drift relationships for as-built specimens. The theoretical monotonic pushover curves are also plotted in the same graphs with the experimental results. The figures demonstrate satisfactory agreement between the theoretical algorithm and the experimental results. The convergence in the case of strong axis experiments was slightly higher than in the case of weak axis experiments. This can be attributed to the extensive work hardening that the weak axis specimens exhibited during testing, which was not captured by the theoretical monotonic force-displacement algorithm.

Expectedly, the theoretical monotonic relationship overestimated the experimental one in the case of specimen PS (figure6.8a). This is attributed to the sudden brittle failure mode that this specimen experienced at the beginning of the 2% drift without any pronounced inelastic behavior in the steel.

6.4 PUSHOVER MODELING OF RETROFITTED CONNECTIONS

Figures 6.10 and 6.11 display the cyclic normalized lateral force-drift relationships for the retrofitted specimens. The theoretical relationships are also displayed in the graphs with experimental results. Again, one can observe satisfactory agreement between the theoretical prediction and experimental relationships.

To demonstrate the significance of considering the effect of the embedment depth in the analysis, figure 6.11 compares the experimental results to two theoretical cases for specimen RS1. Case 1 considers the steel pile fully fixed in the concrete base, and case 2 accounts for the embedment depth in the analysis. It is observed that ignoring the embedment depth in the analysis by considering the pile fixed to the cap beam does not represent the physical scenario.

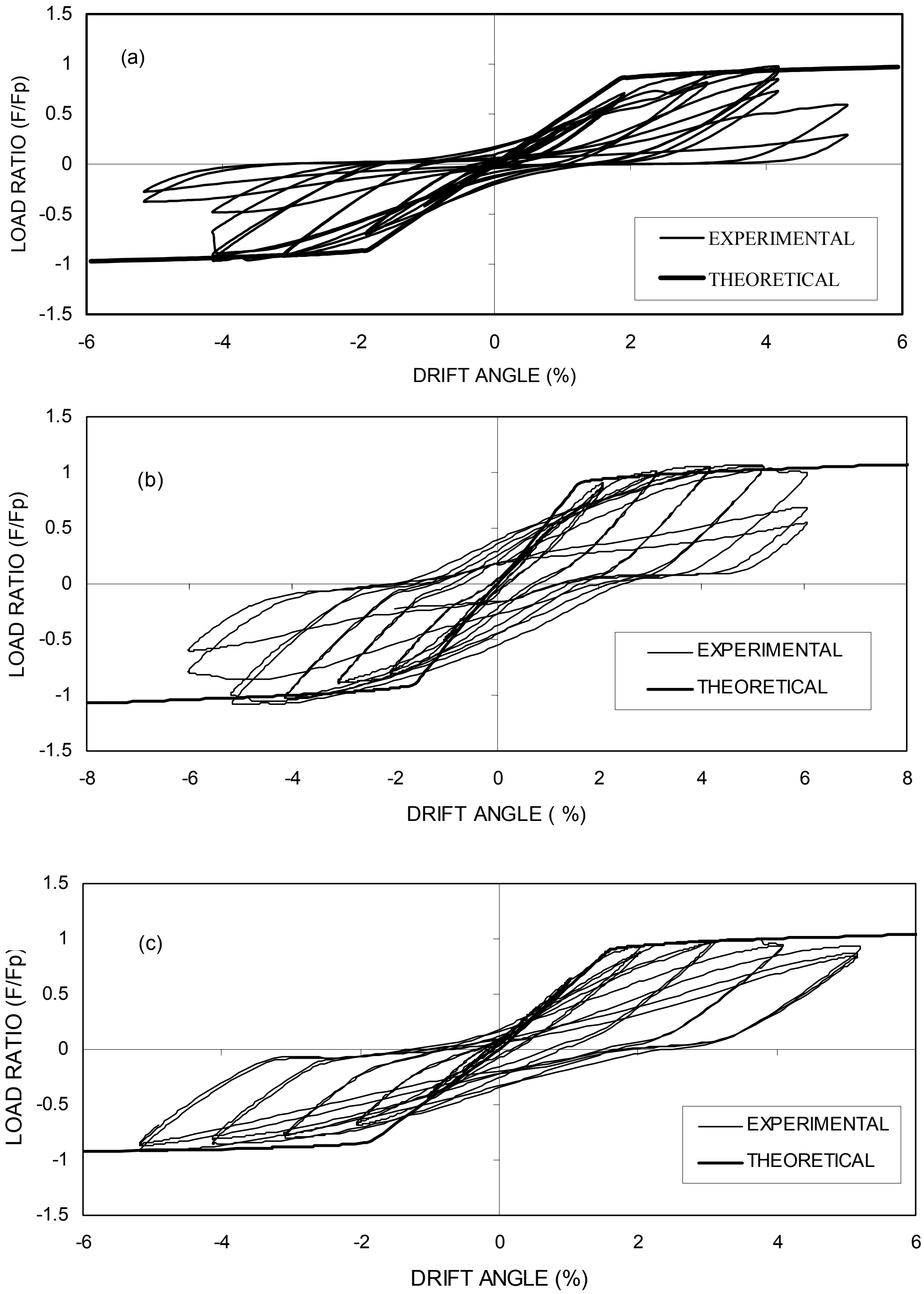

Figure 6.6 Comparison of The Theoretical Approach with Experimental Results For Strong Axis As-built Pile Bent Specimens : (a) Specimen S1; (b) Specimen S2; and (c) Specimen S3

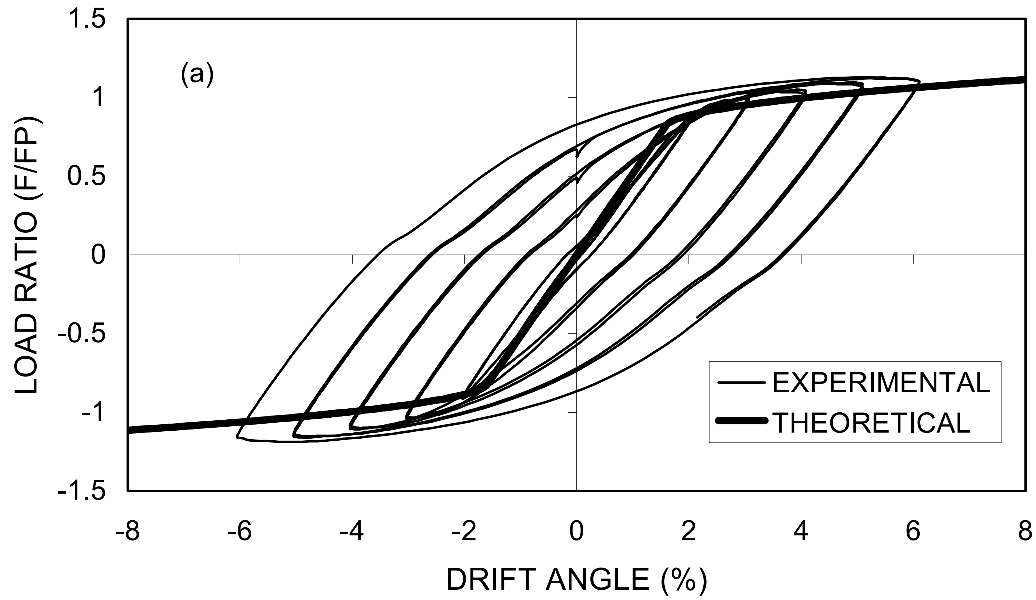

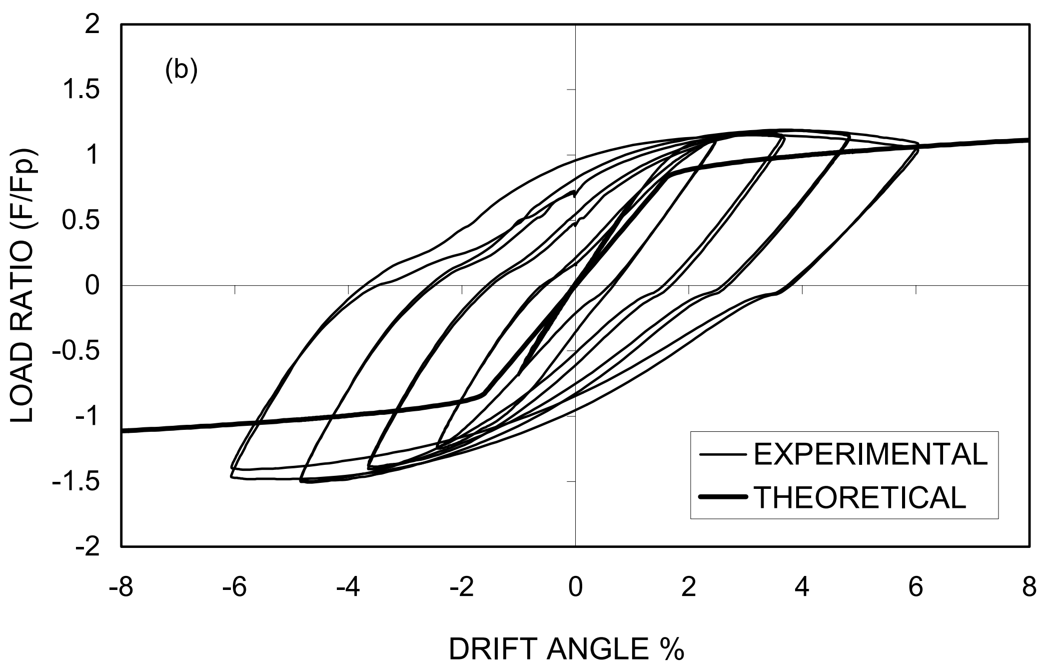

Figure 6.7 Comparison of The Theoretical Approach with Experimental Results For Weak Axis As-built Pile Bent Specimens : (a) Specimen W1; (b) Specimen W2

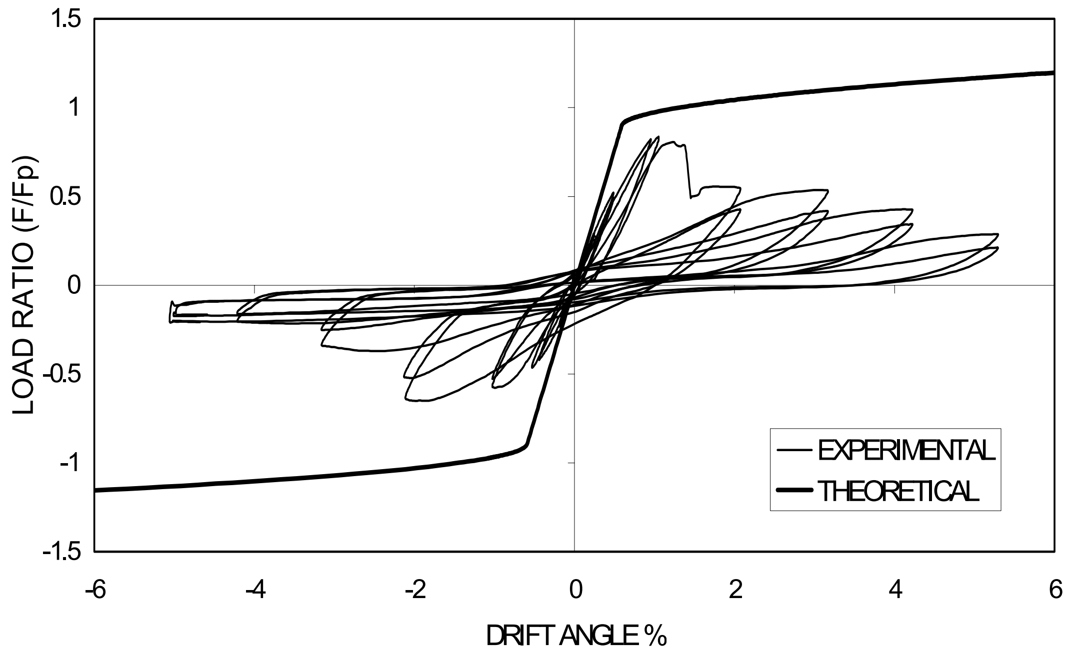

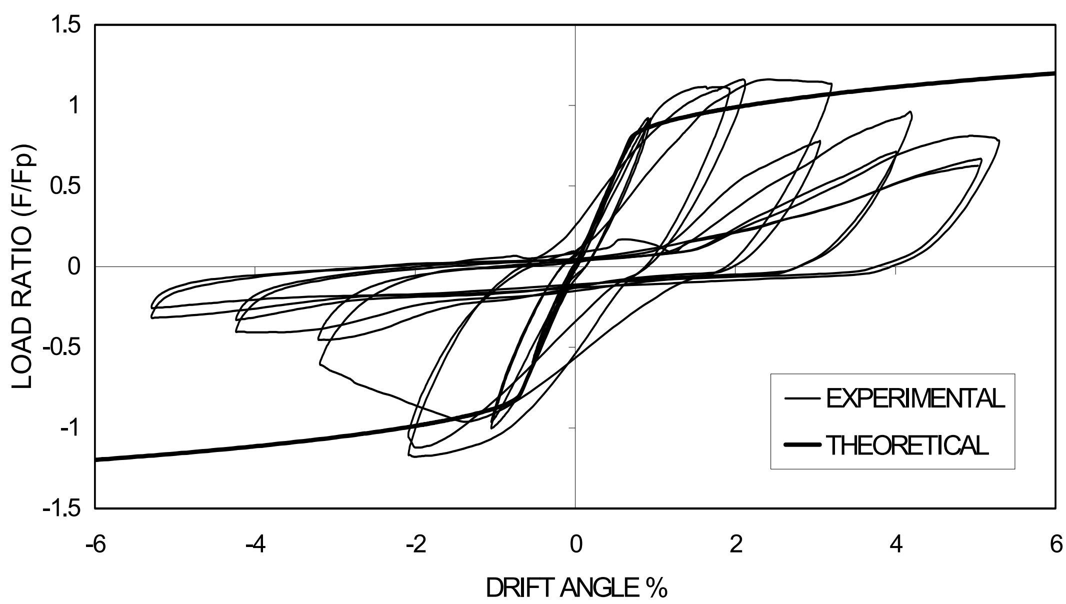

Figure 6.8 Comparison of The Theoretical Approach with Experimental Results As-built Piled Foundation Specimens : (a) Specimen PS;(b) Specimen PW

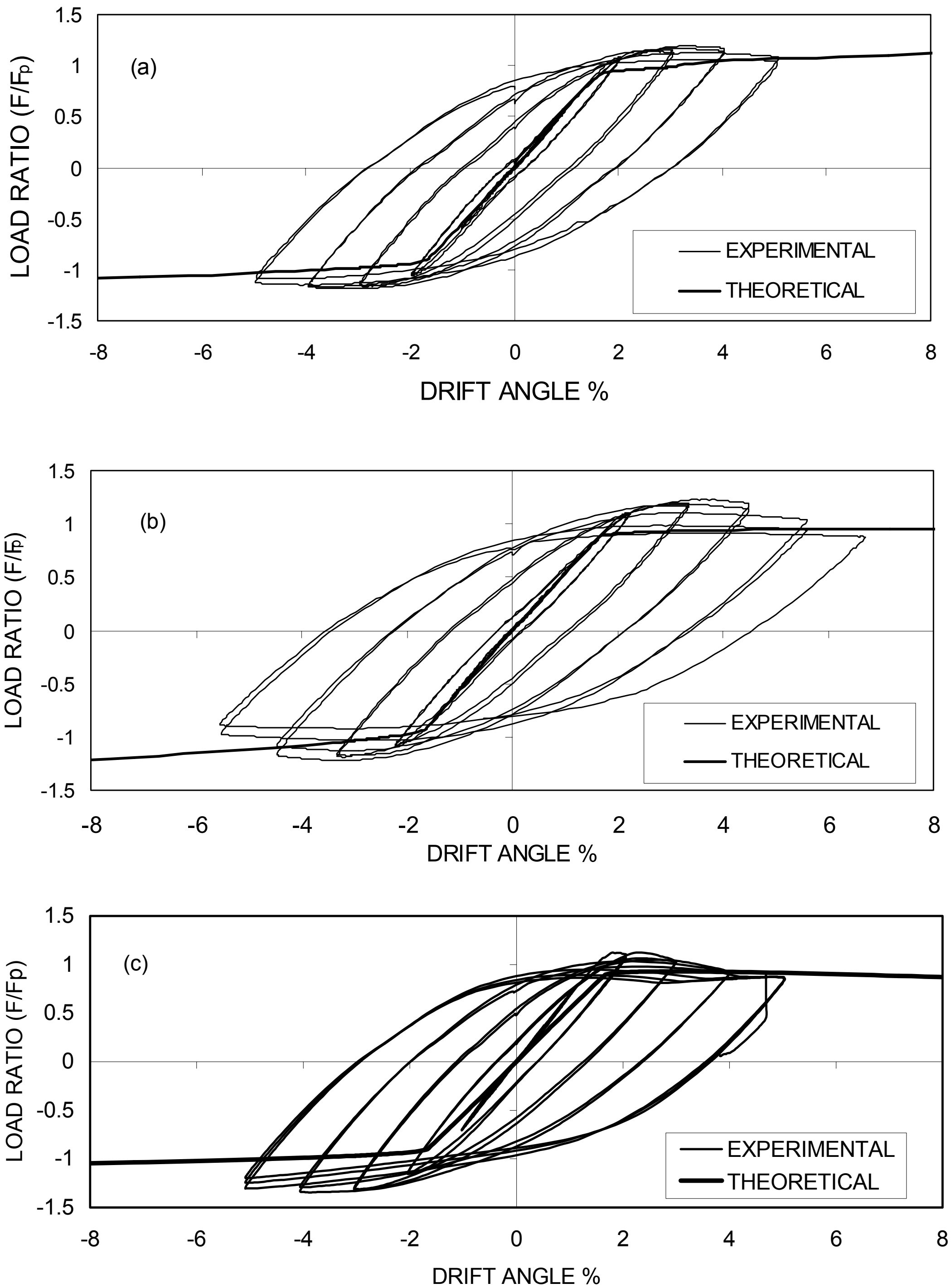

Figure 6.9 Comparison of The Theoretical Approach with Experimental Results For Strong Axis Retrofitted Pile Bent Specimens : (a) Specimen ReS1; (b) Specimen ReS2; and (c) Specimen ReS3

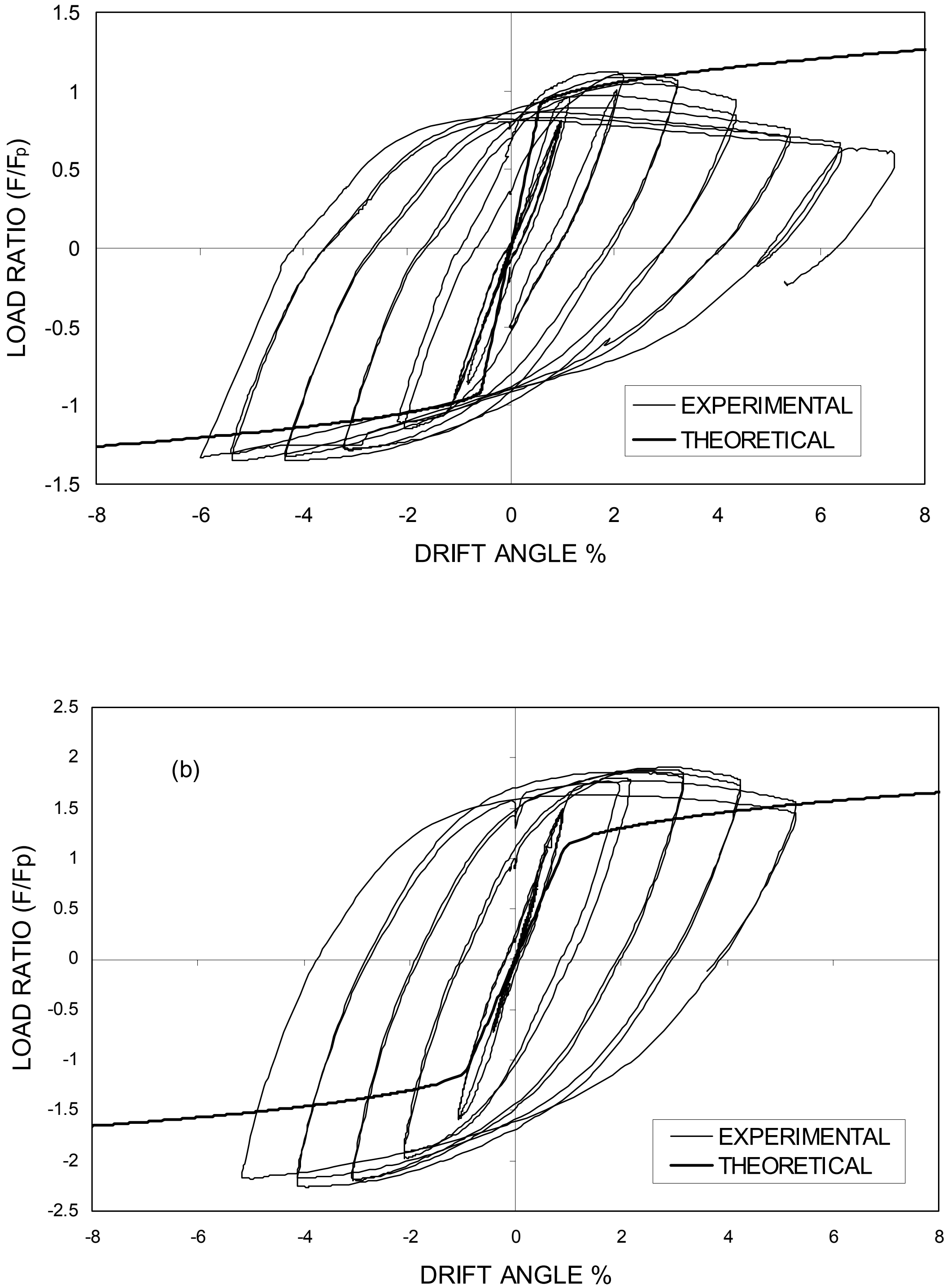

Figure 6.10 Comparison of The Theoretical Approach with Experimental Results ForRetrofitted Piled Foundation Specimens : (a) Specimen RePS;(b) Specimen RePW

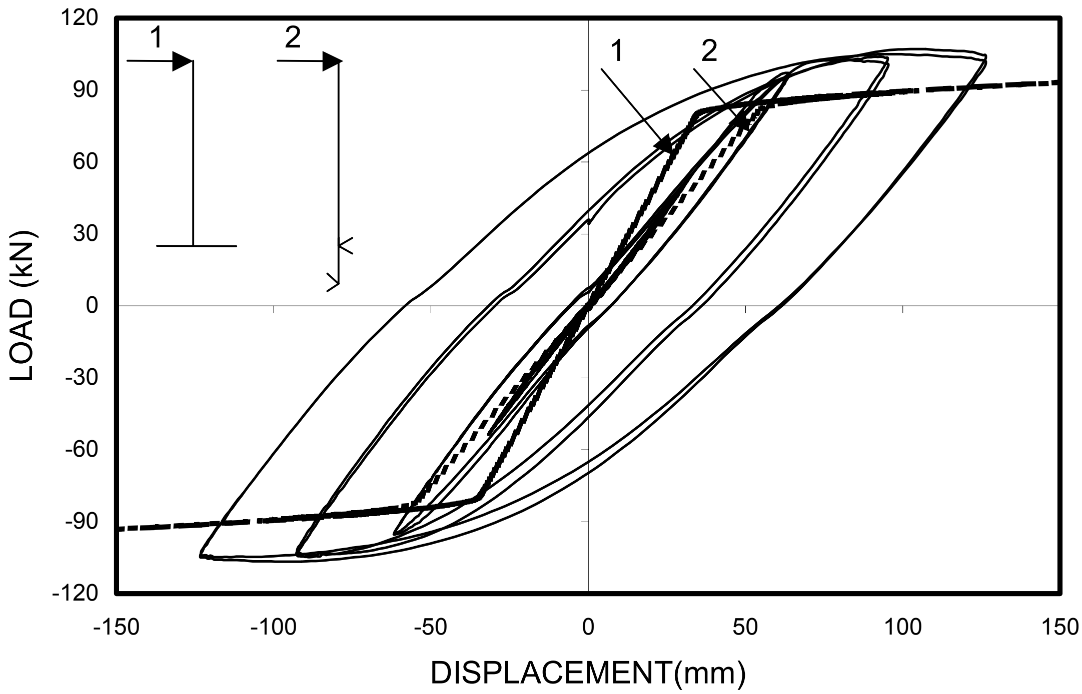

Figure 6.11 Illustrating the Importance of The Embedment Depth In Predicting The Theoretical Performance of Pile-to-Cap Connections

6.5 FATIGUE MODELING

The simplified procedure developed in section 2 to predict the seismic fatigue capacity of the retrofitted connections is employed in this section to determine such capacity of the specimens that exhibited a fatigue failure mode during the experiments (specimens ReS1, ReS2, RePW).

6.5.1 Comparison of the Theoretical with Experimental Results

6.5.1.1 Determination of Equivalent Cycling

An appropriate method for cycle counting should be employed for the experimental outcomes, in order to obtain results comparable with the theoretical model.

The equivalent number of cycles (N_{eq}) to failure is commonly obtained using Miner's linear damage accumulation rule (1945) which states that the damage accumulated up to the I-th loading cycle is given by:

$$D_i = \frac{1}{N_1} + \frac{1}{N_2} + \frac{1}{N_3} + ... + \frac{1}{N_i} \tag{6.1}$$

where N_1, $N_2, N_3, \ldots.., N_i$ are the total numbers of cycle to failure if all cycles are at plastic rotational amplitude θ_{pi}, thus it can be shown that:

$$N_{eq} = \sum n_i \left(\frac{\theta_i}{\theta_{max}} \right)^{-1/c} \tag{6.2}$$

where n_i = the number of cycles at each drift θ_i, θ_{max} = the maximum drift angle achieved, c = exponential constant.

For specimens governed by failure due to low-cycle fatigue of steel material, Mander et al(1994) showed that for steel fatigue, c = -0.33, thus -1/c = 3, and equation (6.2) becomes:

$$N_{eq} = \sum n_i \left(\frac{\theta_i}{\theta_{max}} \right)^3 \tag{6.3}$$

6.5.1.2 Comparison of Results

Equation (6.3) was employed to determine the equivalent cycle numbers for specimens ReS1, Res2 and W1. The results are presented in table 6.1 and compared to the exact relationship using the algorithm developed in section 2 as well as the simplified equation (2.129). It is shown that both the exact and the simplified relationships captured the experimental behavior with a satisfactory convergence. Figure 6.13 demonstrate such convergence through the linear log-log relationship.

Table 6.1 Comparison of the proposed fatigue models to the Experimental Results

Specimen ID	θ_p	$2N_f$		
		Experimental	Exact	Simplified
ReS1	0.038	27	14	17
ReS2	0.048	17	11	13
W1	0.05	12	11	13

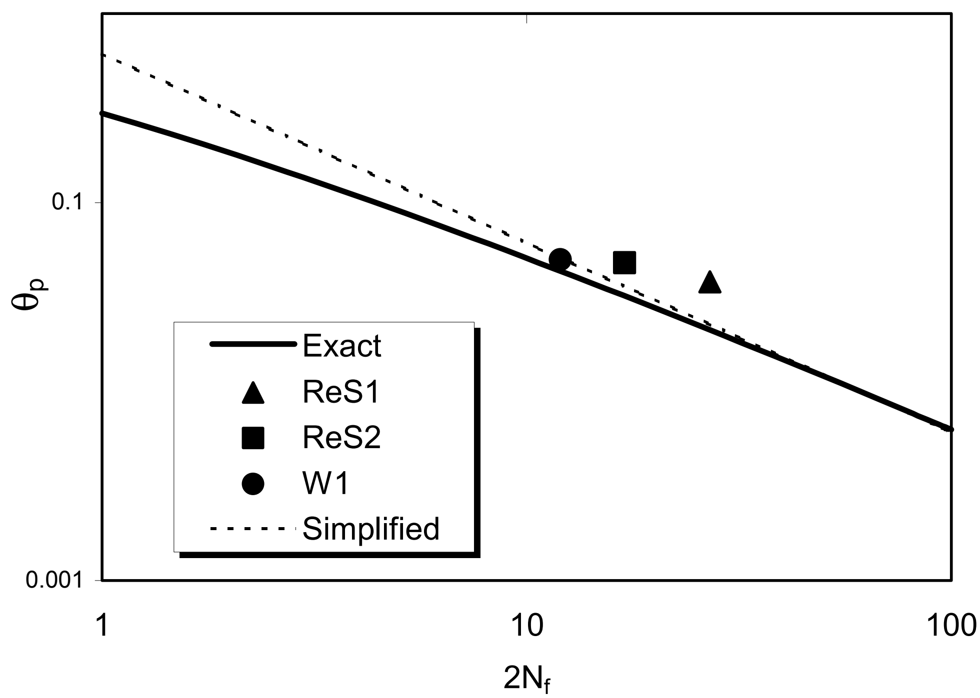

Figure 6.12 Connection Plastic Rotation vs. Fatigue Life

6.6 CLOSURE

The theory developed in section 2 for predicting the lateral force-displacement behavior of steel piles to cap connections was validated in this section by comparing its outcomes to the experimental results for all the specimens tested during the course of this study. Although some differences are observed due to the effects of cyclic loading not counted for in the theoretical model Satisfactory agreement was achieved between both cases.

The method outlined in section 3 for determining the equivalent damping ratio in terms of the displacement ductility factor for the pile cap system was verified by experimental results and hence values for the connection efficiency for different substructure conditions were evaluated. These values can be employed for the evaluation of the seismic vulnerability of bridges supported by such substructures.

Finally the fatigue life model, developed in section 2 was compared to the available experimental results. Hence, this model can be used in future studies to predict the fatigue life of these connections.

SECTION 7
CONCLUSIONS

7.1 EXCUTIVE SUMMARY

The present study investigated the performance and retrofit of bridge pile-to-cap connections that is representative of construction in the eastern and central US. Simplified theoretical concepts were developed to predict the connection behavior under different lateral and axial load patterns. Being compared to rigorous finite element analysis validated these simplified limit theories. On the basis of these theories, design guidelines and retrofit strategies for these connections were proposed.

A comprehensive experimental program was involved in the present study in order to determine the seismic behavior of bridge pile-to-cap connections. Seven test specimens, representing steel pile bents and pile foundations tested under different cyclic loading, were investigated to identify their seismic vulnerability.

Based on the experimental study for the as-built specimens, a conceptual elastic cap/elasto-plastic steel pile retrofit strategy was proposed in accordance with the design concepts advocated in this study. In order to assess this retrofit strategy, another experimental program consisted of testing five retrofitted test specimens was conducted .

An analytical approach for predicting the performance of these specimens under lateral load was compared to the experimental results. Finally, a fatigue life model based on a simplified approach was developed and compared to the available experimental results.

7.2 Concluding Remarks

Based on this experimental and analytical investigation reported herein, the following specific conclusions can be drawn:

1. The experimental program for existing pile-to-cap connections, characterized by small embedment depth of the pile inside the cap beam (300mm) indicated that pile and pile bent connections oriented along their strong axes of bending failed in a non-ductile manner within the concrete pile cap. Therefore these connections may be prone to damage under severe earthquake loads, and hence, may be in need of retrofit.
2. Due to their lesser strength, pile bent connections oriented along their weak axes of bending exhibited superior behavior with respect to strong axis connections, when tested under the same loading conditions.
3. The experiments showed that the theoretical predictions by both the cracked elastic and plastic theories developed in this study give an adequate representation of the joint strength range.
4. Compared to the as-built specimens, the retrofitted specimens exhibited superior energy absorption and stable hysteretic response loops.
5. On the basis of the performance of the specimens before and after retrofitting, it is considered that the conceptual elastic cap/elasto-plastic steel pile retrofit strategy proposed in this study is validated.
6. The analytical approach proposed in this study to simulate the monotonic force displacement for various specimens tested under different loading conditions compared favorably to the experimental back-bone curves for these specimens.
7. The fatigue life model proposed in the present study showed a satisfactory convergence to a limited number of experimental results and hence. This can be used in future studies to predict the fatigue-life of these connections.

7.3 RECOMMENDATIONS FOR FUTURE RESEARCH

1. In light of the information obtained from the comprehensive experimental program implemented in this study for as-built and retrofitted piled substructures, an overall seismic vulnerability study of bridges supported by steel piled substructures can be performed. Through this study, the likelihood of structural damage due to various levels of ground motions can be expressed by the aid of fragility curves.
2. The study needs to be extended to cover other types of piles such as timber piles, pipe piles, and precast-concrete piles.
3. In the present study, the experimental setups were devised to investigate the performance of individual pile bents. Future research may be extended to study the performance of pile bent subassemblies consisting of more than one pile. Other issues including the effect of bracing on the performance of timber pile bent subassemblies can be studied. Furthermore, different bracing configurations can be employed to enhance the performance of these subassemblies, and hence the need and/or effectiveness of retrofitting strategies.

SECTION 8

REFERENCES

"ABAQUS 5.7 User's Manual", (1998), Hibbitt, Karlsson and Sorensen, Inc.

ASCE-WRC (1971) "Plastic Design in Steel-A Guide and Commentary", Manual and Reports on Engineering Practice, No. 41, ASCE, New York, NY

Broms, B.B. (1964a), " Lateral Resistances of Piles in Cohesive Soils", ASCE Journal of Soil Mechanics and Foundation Division, Vol. 90, No. SM2, pp. 27-63.

Broms, B.B. (1964b), " Lateral Resistances of Piles in Cohesionless Soils", ASCE Journal of Soil Mechanics and Foundation Division, Vol. 90, No. SM3, pp. 123-156.

Chai, YH and Hutchinson, TC (1999) " Flexural Strength and Ductility of Reinforced Concrete Bridge Piles", Report No. UCD-STR-99-2, Dept. of Civil & Environmental Engineering University of California Davis, CA

Chang, G.A., Mander, J.B., (1994)" Seismic energy based fatigue damage analysis of bridge columns" Technical report (National Center for Earthquake Engineering Research); NCEER94-0013.

Chopra, A.K., (1995), " Dynamics of Structures Theory and Applications to Earthquake Engineering", 1st Ed., Prentice-Hall, Inc.

Cofin, L.F.Jr. (1954). " A study of the effects of cyclic thermal stresses on a ductile metal." Trans., American Society of Mechanical Engineers, New York, N.Y., 76, 931-950

Harries, K.A., Mitchell, D., Cook, W.D. and Redwood, R.G. (1993), " Seismic Response of Steel Beams Coupling Concrete Walls", Journal of Structural Engineering, Vol. 119, No. 12, Dec., pp. 3611-3629.

Pam, J.H. and Park, R. (1990) " Flexural Strength and Ductility Analysis of Spirally Reinforced Prestressed Concrete Piles", PCI Journal. V 35 n 4 Jul-Aug 1990 p 64-83

Pam, J.H. Park, R. (1990)" Simulated Seismic Load Tests on Prestressed Concrete Piles and Pile-Pile Cap Connections", PCI Journal. V 35 n 6 Nov-Dec 1990 p 42-61

Japan National Earthquake Engineering Commission (1965)"Nigata Earthquake of July 1964", Proceedings of 3rd World Conference on Earthquake Engineering

Kachadoorian, R.(1968)"Effects of The Earthquake of March 27, 1964, on The Alaska Highway System" Geological Survey Professional Paper 545-C

Mander, J.B., Dutta, A., and Goel, P. (1998), "Capacity design of bridge piers and the analysis of overstrength", Technical report (Multidisciplinary Center for Earthquake Engineering Research); MCEER-98-0003.

Mander, J.B., Panthaki, F.D., and Kasalanti, A., (1994), " Low Cycle Fatigue Behavior of Reinforcing Steel", Journal of Materials in Civil Engineering, Vol. 6, No. 4, p. 453-468.

Manson, S.S. (1953). " Behavior of materials under conditions of thermal stress." Heat Transfer Symp., University of Michigan Engineering Research Institute, Ann Arbor, Mich., 9-75

Marcakis, K. and Mitchell D. (1980), " Precast Concrete Connections with Embedded Steel Members", PCI Journal, Vol. 25, No. 4 July-August, pp. 88-116.

Matlock, H., Stephen, H.C., and Larry, M.B (1978) "Simulation of Lateral Pile Behavior Under Earthquake Motion" Proceedings of the ASCE Geotechnical Engineering Division Specialty Conference, Pasadena, CA, pp.600-619

Mattock, A.H. and Gaafar, G.H. (1982), " Strength of Embedded Steel Sections as Brackets", ACI Journal March-April 1982 pp. 83-93

Miner, M.A., (1945), " Cumulative Damage in Fatigue", Journal of Applied Mechanics, September 1945, pp. A159-A164

Poulos, H.G. (1982) " Developments in the Analysis of Static and Cyclic Lateral Response of Piles" Proceedings of the Fourth International Conference on Numerical Methods in Geomechanics/Edmonton, Canada pp1117-11135

Priestley, M.J, Seible, F., and Calvi, G.M. (1997), Seismic Design and Retrofit of Bridges, 1st Ed., John Wiley & Sons, Inc.

Raths, C.H. (1974), " Embedded Structural Steel Connections", PCI Journal, Vol. 19, No. 3, May-June, PP. 104-112

Shaffer, M.D. and Williams, F.M. (1947), Research Report No.1- Investigation of The Strength of The Connection Between a Concrete Cap and the Embedded End of a Steel H-pile, State of Ohio Department of Highways, 79 pgs.

Shama, A.A. (2000), "On the Seismic Analysis and Design of Pile-To-Cap Connections", Ph.D. Dissertation, State University of New York at Buffalo, Buffalo, NY.

Steunenberg, M. Sexsmith, R G. Stiemer, S F. (1998) "Seismic Behavior of Steel Pile to Precast Concrete Cap Beam Connections", Journal of Bridge Engineering. V 3 n 4 Nov 1998. P 177-185

Xiao, Y, Mander J.B., Wu, H. and Martin, G (1999) " Experimental Study on Seismic Behavior of Bridge Pile-to-pile Cap Connections", 15th U.S.-Japan Bridge Engineering Workshop November 9 and 10, 1999 Tsukuba City, Japan.

MCEER
MULTIDISCIPLINARY CENTER FOR EARTHQUAKE ENGINEERING RESEARCH
A National Center of Excellence in Advanced Technology Applications

University at Buffalo, State University of New York
Red Jacket Quadrangle ■ Buffalo, New York 14261-0025
Phone: 716/645-3391 ■ Fax: 716/645-3399
E-mail: mceer@acsu.buffalo.edu ■ WWW Site: http://mceer.buffalo.edu

University at Buffalo *The State University of New York*

ISSN 1520-295X